Multi-physics Large-Eddy Simulation of methane oxy-combustion in Liquid Rocket Engines

Simon Blanchard

To cite this version:

Simon Blanchard. Multi-physics Large-Eddy Simulation of methane oxy-combustion in Liquid Rocket Engines. Other. Institut National Polytechnique de Toulouse - INPT, 2021. English. NNT : 2021INPT0079 . tel-04171668

HAL Id: tel-04171668
https://theses.hal.science/tel-04171668v1

Submitted on 26 Jul 2023

THÈSE

En vue de l'obtention du

DOCTORAT DE L'UNIVERSITÉ DE TOULOUSE

Délivré par :

Institut National Polytechnique de Toulouse (Toulouse INP)

Discipline ou spécialité :

Dynamique des fluides

Présentée et soutenue par :

M. SIMON BLANCHARD

le mercredi 22 septembre 2021

Titre :

Multi-physics Large-Eddy Simulation of methane oxy-combustion in Liquid Rocket Engines

---

Ecole doctorale :

Mécanique, Energétique, Génie civil, Procédés (MEGeP)

Unité de recherche :

Centre Européen de Recherche et Formation Avancées en Calcul Scientifique (CERFACS)

Directrice de Thèse :

MME BENEDICTE CUENOT

Rapporteurs :

M. FABIEN HALTER, UNIVERSITE D'ORLEANS
M. PIERRE BOIVIN, UNIVERSITE AIX-MARSEILLE 1

Membres du jury :

M. FRANCK NICOUD, UNIVERSITE DE MONTPELLIER, Président
MME BENEDICTE CUENOT, CERFACS, Membre
M. MICHAEL PFITZNER, UNIVERSITAT DER BUNDESWEHR MUNICH, Membre
M. MIGUEL MARTIN-BENITO, CENTRE NATIONAL D'ETUDES SPATIALES CNES, Invité
M. PHILIPPE GRENARD, ONERA - CENTRE DE PALAISEAU, Invité
MI. THOMAS SCHMITT, CENTRALESUPELEC GIF SUR YVETTE, Membre

石の上にも三年 ("ishi no ue ni mo sannen")
Trois ans assis sur un rocher
Proverbe japonais

Résumé

La combustion dans les moteurs de fusée a lieu dans des conditions extrêmes qui impliquent plusieurs phénomènes multi-physiques. Pour cette raison la simulation numérique est utilisée afin de prédire et ainsi optimiser les performances et la durée de vie du moteur. Ces travaux de thèse se concentrent particulièrement sur deux aspects : l'oxy-combustion turbulente du méthane dans des flammes de diffusion haute pression et la prédiction des transferts thermiques pariétaux. Le code de Simulation aux Grandes Echelles (SGE) AVBP du CERFACS est utilisé.

Malgré ses performances moindres, le méthane est aujourd'hui favorisé par rapport à l'hydrogène pour les futurs moteurs-fusée en raison de ses coûts réduits et de sa praticité tant à l'utilisation que pour son stockage. En termes de simulation numériques, cet ergol amène de nouvelles questions concernant son allumage ou la stabilisation de sa combustion. Pour ce faire, le développement de modèles chimiques réalistes est une étape clé. Des schémas cinétiques réduits contenant une quinzaine d'espèces sont dérivés et testés dans des conditions de haute pression et haut étirement pour des flammes de diffusion à contre-courant. Cependant, ces chimies réduites restent coûteuses pour une utilisation industrielle de la SGE. Une nouvelle méthode d'intégration des termes sources chimiques est alors proposée avec pour objectif de faire fonctionner des simulations réactives avec un pas de temps proche du pas de temps de l'écoulement. Le coût de calcul est ainsi considérablement réduit, tout en gardant un résultat similaire à l'intégration classique. Enfin, avec pour futur objectif le développement d'un modèle de flamme de diffusion turbulente, une étude montrant l'impact de la résolution du maillage sur les flammes de diffusion est réalisée.

Le développement de ces chimies réduites permet alors d'étudier avec précision l'influence des réactions chimiques dans la région proche paroi d'un moteur-fusée sur le flux thermique pariétal. Des canaux turbulents périodiques sont simulés afin de comparer une couche limite turbulente résolue ou non, avec ou sans réactions chimiques. Les résultats montrent que ces réactions proche paroi peuvent avoir un impact significatif sur le flux thermique, et que le modèle de loi de paroi devrait prendre en compte cet effet dans le cadre d'une SGE non-résolue en paroi.
De plus une étude est menée afin de comprendre l'impact du couplage entre le modèle de sous-maille et la loi de paroi sur la prédiction des flux en paroi. On montre que le niveau de viscosité turbulente en paroi a une influence importante sur les flux. Un modèle stochastique est alors proposé dans le cas de simulations isothermes afin d'améliorer les résultats pour deux modèles de sous-maille usuels en SGE, WALE et Sigma.

Le développement de ces modèles et les résultats de ces analyses sont alors utilisés pour deux SGE de bancs d'essai : le cas supercritique à cinq injecteurs GCH4/GOx de l'ONERA et le cas sous-critique mono-injecteur GCH4/LOx de TUM. Ces études se concentrent en particulier sur le comportement de la flamme et la comparaison du flux de chaleur pariétal avec les résultats expérimentaux.

Mots clés: Simulation aux Grandes Échelles, moteur-fusée à ergol liquide, combustion turbulente, oxy-combustion du méthane, cinétique chimique, flamme de diffusion, modélisation de paroi, transfert de chaleur pariétal, injection liquide, super-critique, sous-critique

Abstract

Combustion in Liquid Rocket Engines (LRE) happens in extreme conditions which imply several multi-physics phenomena. For this reason, numerical simulation is used to predict and thus to optimize the engine performances and lifetime. In particular this thesis focuses on two main aspects: turbulent oxy-combustion in diffusion flames of methane at high pressure, and prediction of wall heat transfers. The Large Eddy Simulation (LES) code AVBP of CERFACS is used.

Despite its lower performances, methane is now preferred to hydrogen for future LRE because of its reduced cost and its practicality both for in terms of usage and storage. For numerical simulation, this propellant raises new questions about how to ignite and stabilize the flame. To do so, developing realistic chemistry is a key step. Reduced finite rate chemistry schemes with about 15 species are derived and tested for high pressure and highly strained counterflow diffusion flames. However, even reduced kinetic schemes are still expensive in the context of industrial LES simulations. Therefore a new integration method for the chemical source terms is proposed in order to run reactive simulations closer to the flow time step. It is found that significant computational cost is spared, while keeping the same result accuracy compared to the classical integration. Finally, in order to develop future turbulent diffusion flame modeling, a study on how the mesh resolution impacts diffusion flames is also performed.

The development of reduced chemistry allows to study precisely the influence of chemical reactions at the near-wall region in LRE conditions on the wall heat flux. Periodic turbulent channels are computed to compare the resolved and non-resolved turbulent boundary layer, with or without chemical reactions. Results show that the near-wall reactions may have a real impact on wall heat flux, and that wall models should take into account this effect in the context of wall-modeled LES.
Another study is conducted to determine the impact of the coupling between the sub-grid scale model and the wall-law on the wall fluxes prediction. It is shown that the amount of turbulent viscosity at the near-wall region greatly changes the fluxes. A stochastic-based model is proposed in the case of isothermal simulations, in order to improve the results for two common LES sub-grid scale models, WALE and Sigma.

The developed models and analyses of those test cases are then used for the LES simulation of two test rigs: the supercritical 5-injectors GCH4/GOx from ONERA and the subcritical single-injector GCH4/LOx from TUM. Their study particularly focuses on the flame behavior and the wall heat flux comparison with experiment.

Keywords: Large Eddy Simulation, liquid rocket engine, turbulent combustion, methane oxy-combustion, chemical kinetics, diffusion flame, wall modelling, wall heat transfer, liquid injection, supercritical, subcritical

Remerciements

Je remercie dans un premier temps les trois institutions qui m'ont permis de réaliser cette thèse. D'abord le CERFACS pour les excellentes conditions de travail fournies. Puis, c'est également une chance que d'avoir été financé et soutenu par deux acteurs majeurs du secteur spatial en France et en Europe: la Direction des Lanceurs du CNES et ArianeGroup.

Mes remerciements vont naturellement au jury qui a accepté d'évaluer mon travail, et ainsi de me conférer le grade de docteur. Plus spécifiquement, merci aux rapporteurs Fabien Halter et Pierre Boivin, pour leurs rapports très positifs sur ce travail tout en proposant des remarques justes sur les limites de l'étude et des axes d'amélioration. Cela a également été unique d'avoir pour rapporteur un de ses anciens prof de combustion qui m'a notamment donné envie de poursuivre sur l'apprentissage de cette science, merci Fabien! Merci aux examinateurs Franck Nicoud, Thomas Schmitt et Michael Pfitzner pour les discussions enrichissantes qui ont lieu lors de la soutenance. Merci à Franck pour m'avoir accompagné sur ce problème épineux de loi de paroi dans AVBP qui a donné lieu à une belle publication! Et merci à Thomas pour nos échanges réguliers sur des aspects scientifiques et coding (de l'expérience sur le LAD et le RG en échange d'expérience en chimie, le bon deal non?), toujours dans la bonne humeur. Bien sûr merci à mes deux encadrants industriels, Miguel et Didier, pour leur suivi des avancements de ma thèse de manière régulière et toujours pleines de bons conseils. Il m'a été également précieux d'avoir un point de vue côté applicatif/industriel sur ce travail, puisque j'aimerais me diriger vers cela plus tard. Merci aussi à Philippe pour avoir répondu à toutes mes questions sur la configuration CONFORTH.
Enfin je remercie évidemment mon encadrante Bénédicte pour m'avoir accompagné tout au long de ce travail. Cela a été un vrai plaisir de travailler avec toi, de part bien sûr tes apports scientifiques nombreux, mais également ta bonne humeur constante avec toujours une vision positive des choses, même quand cela ne me paraissait pas évident de l'avoir! Merci également d'avoir crû en mes capacités en me proposant des collaborations, à ma demande, avec nos voisins allemands notamment. Par ailleurs au délà du travail, je n'aurais pas pensé en signant le contrat jouer de la musique aux côtés de ma directrice de thèse dans l'orchestre de Météo France!

Ces trois années et demies au CERFACS ont été très plaisantes, de part à la fois la compétence et la sympathie des gens qui y travaillent. Merci notamment aux autres seniors comme Laurent, Nicolas et Davide pour vos apports en bonnes idées sur mon travail. Je n'oublie pas Eléonore pour nos discussions de couloirs pleines de "piques" certes, mais toujours sympathiques! Merci à l'équipe administration: Marie, Michèle, Chantal, Nicole... pour leur efficacité toujours au top, et bien sûr à l'équipe CSG pour leur réactivité et leur aide, sans quoi on n'aurait pas vu beaucoup de calculs! Dans le même registre, merci également à Gab, d'abord pour ton aide alors que je n'étais qu'un petit thésard de première année lâché sur le monstrueux calcul du Prometheus, et également pour avoir répondu à toutes mes difficultés pour pouvoir faire tourner sur les machines externes ("ça compile pas ... :'(").
Un grand merci à tous les thésards rencontrés au CERFACS. Au-délà d'être des collègues avec qui j'ai beaucoup échangé, nombre d'entre vous sont devenus des amis, ce qui a bien sûr compté pour moi le temps de ces années dans la ville rÔse. Donc merci pour tous les bons moments partagés, des dégustations au Biérographe aux fameux week-ends "Kayak-BBQ in da Gers", à ma "promo de docteurs": Quentin, Paul, Thomas, Willca, Etienne... sans oublier le seul, l'unique, le légendaire cobureau Julien, oscillant entre sa bonne humeur débordante (du genre

chanter à 17h pile tous les jours, magique) et ses "ça me saoûle...". Un petit coucou également à la future fournée de thésards (courage, bientôt votre tour!) comme Jonathan, Antoine, Théo, Thilbault, Felix, et enfin aux plus anciens, déjà partis, pour les bons moments partagés via notamment le jeu vidéo ou le sport: Soizic, Fabien, Matthieu, Charlélie, Frédéric... et d'autres, ils se reconnaîtront! Je n'oublierai pas mes prédécesseurs qui m'ont largement transmis leur savoir-faire des LES de moteurs-fusée, à savoir Luc, Dario, Lucas... Et, en plus à déjà tout ce petit monde, les copains/copines/ami(e)s rencontré(e)s pendant ces années, comme Clem, Masha, Léa, Arthur...

Und jetzt ein paar Worte auf Deutsch: ich möchte allen Personen danken, die ich während des TUM Sommer Programms 2019 getroffen habe. Danke an Oskar Haidn, der mich zu der einzigartigen Gelegenheit eingeladen hat, Forscher aus der ganzen Welt zu treffen. Danke an Andrej, Nikolaos, Patrick für die interessanten Diskussionen über unsere jeweiligen Simulationen. Danke dir Andrej für die Organisation der Wanderung in die schönen bayerischen Alpen! Schließlich danke an meinen Praktikanten Julian für den Gedankenaustausch bezüglich unserer gemeinsamen Problemstellung. Noch einmal "bravo" für deine Arbeit, die auch Teil meiner Thesis ist. Diese Begegnungen haben mir ermöglicht, zur Französisch-Deutschen Kooperation in der Raumfahrt beizutragen! Vielleicht bis bald!

Ces années de thèse seront pour toujours liées à ma vie à Toulouse, et donc je remercie également ma bande de colocs qui n'a cessé de s'étoffer d'année en année: Lucas, Clémentine, Lucie, Jeanne, Elliot, Mar(t)ine, Titaua, Léa, Elhadi... et par extension tous les autres rencontrés. Bien que non-liés directement à ce travail de thèse, nos nombreuses sorties (qui a dit Pub O Clock?), débats mouvementés sur des sujets plus ou moins farfelus et autres évènements rythmant la "vie de kolok", ont bien aidés à me changer les idées quand j'en avais besoin, en plus d'avoir des oreilles extérieures attentives. J'espère ne pas vous avoir trop embêtés avec mes problèmes de thésard - en tout cas ça m'a appris à vulgariser mon travail!

Finalement, je remercie ma famille qui m'a toujours soutenu dans les choix que j'ai fait y compris si ça implique de faire des choses difficiles, d'aller loin, et ce pendant longtemps (et c'est pas fini...). Merci à mes parents de m'avoir donné le goût et l'habitude de la reflexion, de m'avoir poussé jeune à la curiosité scientifique (j'en redemandais en même temps) qui m'a amenée là aujourd'hui. En tout cas le goût de l'aventure et de la découverte est toujours là, si bien qu'il m'emmène maintenant à l'autre bout du monde, au pays du soleil levant...

Contents

Nomenclature

Latin characters

Symbol	Description	SI unit
a	Strain rate	$[s^{-1}]$
A	Pre-exponential Arrhenius factor	[variable]
B_M	Spalding mass number	$[-]$
B_T	Spalding temperature number	$[-]$
C_p	Constant pressure heat capacity	$[J/K]$
C_v	Constant volume heat capacity	$[J/K]$
d_p	Particle diameter	$[m]$
d_{10}	Mean particle diameter	$[m]$
dt	Time step	$[s]$
D	Diffusion coefficient	$[m^2/s]$
D_l	Oxygen cone diameter	$[m]$
e	Internal energy	$[J]$
e_{kin}	Kinetic energy	$[J]$
E	Total energy	$[J]$
F	Rocket engine thrust	$[N]$
h	Enthalpy	$[J/kg]$
HR/HRR	Heat release rate	$[W/m^3]$
J	Momentum flux ratio	$[-]$
$J_{k,i}$	Species diffusion flux	$[kg/(m^2.s)]$
K	Arrhenius rate constant	[variable]
L	Oxygen cone length	$[m]$
L_v	Latent heat of evaporation	$[J/kg]$
M	Number of reactions in the chemical system	$[-]$
N_e	Number of elements in the chemical system	$[-]$
N_s	Number of species in the chemical system	$[-]$
m	Mass	$[kg]$
$\dot{m}$	Mass flow rate	$[kg/s]$
P	Pressure	$[Pa]$
q_i	Heat flux vector	$[W/m^2]$
$\dot{Q}_p$	Heat transfer source term	$[J/s]$
r	Mixture gas constant	$[J/(K.kg)]$
$\dot{r}_j$	Mass reaction rate	$[kg/(m^3.s)]$
s	Entropy	$[J/(K.kg)]$
S	Strain rate tensor	$[s^{-1}]$
S_{cone}	Oxygen cone section	$[m^2]$
t	Time	$[s]$

T	Temperature	$[K]$
u_i	Velocity vector	$[m/s]$
W	Molecular weight	$[kg/mol]$
X	Molar fraction	$[-]$
Y	Mass fraction	$[-]$
Z	Mixture fraction	$[-]$

Greek characters

Symbol	Description	SI unit
α_l	Liquid fraction	$[-]$
β	Arrhenius exponential factor	$[-]$
$\dot{\Gamma}_p$	Mass transfer source term	$[kg/s]$
δ_{th}	Thermal flame thickness	$[m]$
Δt	Simulation time step	$[s]$
Δx	Characteristic cell length	$[m]$
ζ	Takeno index	$[-]$
θ_{lip}	Injection angle of a particle at the lip	$[deg]$
κ	Ratio between the CFL time step and the effective simulation time step	$[-]$
λ	Thermal conductivity	$[W/(m.K)]$
μ	Dynamic viscosity	$[Pa.s]$
ν	Kinematic viscosity	$[m^2.s]$
ρ	Density	$[kg/m^3]$
τ	Characteristic time scale	$[s]$
τ_{ij}	Stress tensor	$[N/m^2]$
τ_w	Wall shear stress	$[Pa]$
ϕ	Equivalence ratio	$[-]$
χ	Scalar dissipation rate	$[s^{-1}]$
ψ	Ratio of turbulent over laminar viscosity	$[-]$
$\dot{\omega}_k$	Mass production rate	$[kg/(m^3.s)]$
$\dot{\omega}_T$	Energy source term	$[J/(m^3.s)]$

Special characters

Symbol	Description	SI unit
$\mathcal{P}$	Power	$[W]$
$\mathcal{R}$	Perfect gas universal constant	$[J/(mol.K)]$
$\mathcal{Z}$	Compressibility factor	$[-]$

Dimensionless numbers

Symbol	Description
Da	Damköhler number
Le	Lewis number
Nu	Nusselt number
Pr	Prandtl number
Re	Reynolds number
Sc	Schmidt number
Sh	Sherwood number
St	Stokes number
We	Weber number

Indices and superscripts

Symbol	Description
c	Critical quantity
e	e^{th} element
f/F	Fuel quantity
g	Gaseous phase quantity
i	i^{th} spatial component
j	j^{th} reaction
k	k^{th} species
l	Liquid phase quantity
o/O	Oxidizer quantity
p	Particle quantity
sgs	Sub-grid scale quantity
st	Stoichiometric quantity
t	Turbulent quantity
w	Wall quantity
ζ	Droplet surface quantity
τ	Friction quantity
$+$	Wall unit

Acronyms

Symbol	Description
ARC	Analytical Reduced Chemistry
ARCANE	Analytical Reduced Chemistry: Automatic, Nice and Efficient
AVBP	A Very Big Project
CERFACS	Centre Européen de Recherche et de Formation Avancée en Calcul Scientifique
CFD	Computational Fluid Dynamics
CFL	Courant-Friedrichs-Lewy
CNES	Centre National d'Études Spatiales
CNSA	China National Space Administration
CONFORTH	CONception et Fabrication d'un bOîtier Refroidi et d'une Tuyère - - Haut rapport de mélange
CPU	Central Processing Unit
DLR	Deutsches Zentrum für Luft- und Raumfahrt
DNS	Direct Numerical Simulation
DRGEP	Directed Relation Graph with Error Propagation
EoS	Equation of State
ESA	European Space Agency
GLOMEC	GLObal Oxygen MEthane MEChanism
HIT	Homogeneous and Isotropic Turbulence
HPC	High Performance Computing
HRR	Heat Release Rate
ICARE	Institut de Combustion, Aérothermique, Réactivité et Environnement
JAXA	Japan Aerospace Exploration Agency
LES	Large Eddy Simulation
LHV	Lower Heating Value
LRE	Liquid Rocket Engine
NASA	National Aeronautics and Space Administration
NIST	National Institute of Standards and Technology
NRI	Non-Reflective Inlet
NSCBC	Navier-Stokes Characteristic Boundary Conditions
ONERA	Office National d'Études et de Recherches Aérospatiales
PDF	Probability Density Function
QSSA	Quasi-Steady State Assumption
RAMEC	RAM accelerator MEChanism
RANS	Reynolds Average Navier-Stokes
RG	Real Gas
ROSCOSMOS	Gossoudarstvennaïa korporatsia po kosmitcheskoï deiatel'nosti
SGS	Sub-Grid Scale
SRK	Soave-Redlich-Kwong
TFLES	Thickened Flame model for Large Eddy Simulation
TUM	Technische Universität München
WMLES	Wall-Modeled Large Eddy Simulation
WRLES	Wall-Resolved Large Eddy Simulation

Part I

General introduction

Chapter 1

Context

Telecommunication, weather forecast, navigation systems, orbital stations, interplanetary probes... all of these space applications exist thanks to Mankind's capacity to send objects in space. At first only reserved for military and surveillance purposes, space is now accessible for a lot of civil applications thanks to our only mean to reach Earth's orbit so far: launchers.
This technology has existed for several decades now, with noticeable improvements through time in order to raise the ratio cost/efficiency in all fields: propulsion, materials, external aerodynamics, guidance systems... This thesis takes place in the continuity of the numerous developments concerning one of the main component of a launcher: the liquid cryogenic engine. This first part explains in which industrial context this research is conducted and introduces the work performed.

1.1 Current space sector landscape

From its beginning in the 1950s until today, space access was considered as a key point for states sovereignty (one talk about "space independence") and prestige, as showed during the Cold War. Its main stakeholders were and still are the governmental space agencies: NASA in USA, ROSCOSMOS in former USSR/Russia, CNES in France, or JAXA in Japan are some examples. ESA regroups now the European space agencies in a larger structure. These organizations led the sector for decades by proposing to their respective states the strategies to guarantee the access to space. However things have been changing since the 90s when private companies were created, often supported by governmental agencies. This is for example the case for the most well-known, SpaceX, founded in the early 2010s. There are now many of them like BlueOrigin, Virgin Galactic...

It is now admitted that these new stakeholders are clearly changing the rules of the space sector, which does not anymore belong only to states or militaries, but also to the private sector [Whealan George, 2019, Bryce Space and Technology, 2019b]. As their private status imposes, they must be profitable, contrary to agencies for which the main part of the budget comes from the states. It is in fact since the 90s that the space sector became profitable, which is largely due to the decrease of the launch cost per kilogram of load [Jones, 2018]. It could also be correlated to the rise of Internet, and therefore the explosion of possible applications for the space sector.
From this new situation came the designation "new space", referring to the cost competition, which until then was not really a central topic for the sector. One distinguishes the

"governmental-entity launches" from the "commercial launches", *i.e.*, a launch service provided to a private company. The rise of commercial launches involves imposes to space agencies to adapt their programs and services if they want to stay competitive.

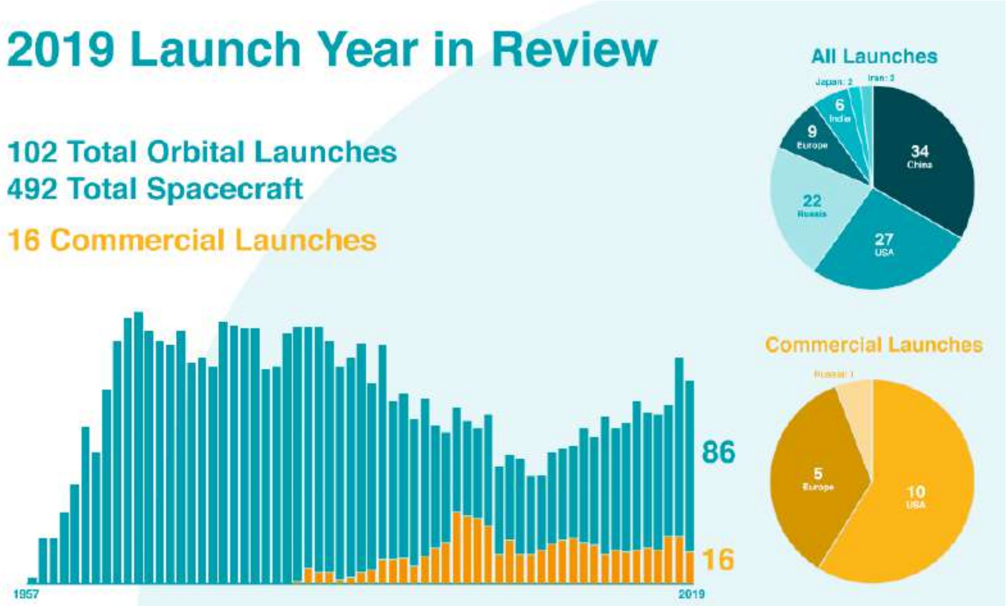

Figure 1.1: Commercial launches evolution [Bryce Space and Technology, 2019a].

1.1.1 A new stake: the reusable launcher

At the heart of this new cost competition era lies a largely mediatized topic: the reusable launcher. Indeed until recently, launchers were used only once: the first stage was dropped back on Earth while the upper parts remained in space (becoming then "space debris"). The idea of reusing some parts of the launcher was already considered in the 1990s by NASA [Freeman et al., 1997]. It was however determined that at that time the technological gap was still too large to go further into this technology [Powell et al., 1998]: a typical challenge is that the engines suffers extremely high heat flux which damage their walls irreversibly. Furthermore the idea, even if technically possible, was not considered very profitable as the number of launches per year was still limited, about a hundred overall (for all different types of rocket). The main attempt of reusability was the famous American space shuttle. Initially designed to reduce costs, at the end the contrary was observed [Jones, 2018].

However as the market of space applications grows, the demand of launchers increases in consequence, therefore the question of profitability is now reevaluated. Even if some concepts of reusability emerged in the 90s and 2000s, the technology really took another breadth with SpaceX and its Falcon 9, which managed (after some spectacular fails) to land its first stage on an offshore platform. The technology is now demonstrated, even if the cost gains still remain to be proven.
Meanwhile, Europe is making up the time by developing the LH2/LOX demonstrator Callisto (CNES/DLR/JAXA cooperation) [Tatiossian et al., 2017, Dumont et al., 2021] designed to fly 10 times, for which the first flight is foreseen in 2023. The objective is to test several technologies in order to be able in the future to develop heavy payload launchers. Finally, the

demonstrator program Themis has been recently signed between ESA and ArianeGroup, with the aim to provide valuable information on the economic value of reusability for Europe and prove technologies for a possible use in future European launch vehicles [Patureau de Mirand et al., 2020].

1.2 The space market

An overview of the current space market is here presented to show the spectrum of the main applications that are possible thanks to space access.

1.2.1 Satellites

Most space applications use satellites, which represent the wide majority of objects sent to space: about 77% of the turnover of space market relies on them [Bryce Space and Technology, 2017]. An overview of their use is presented in Fig. 1.2.

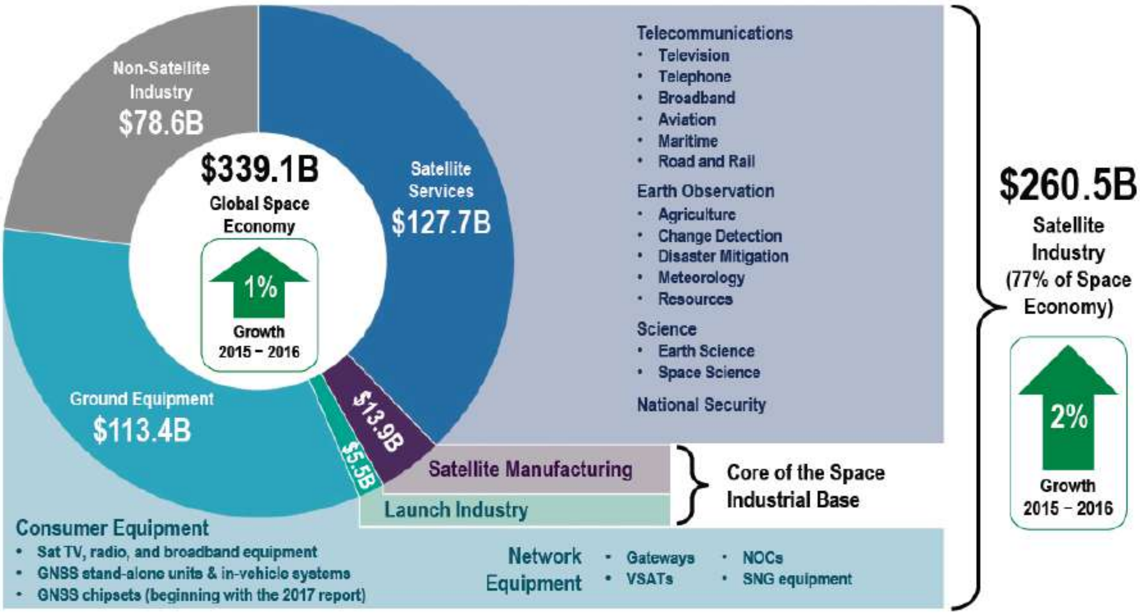

Figure 1.2: Overview of the satellite industry in 2016.

Noticeable applications to be cited are for example all the telecommunication services which we use everyday, including Internet and geolocalization. The "European GPS" Galileo, which consists of a constellation of 24 satellites is able to geolocalize with a precision of less than one meter, better than the American GPS. This upgraded precision is a real asset for applications which need it, like rescue missions in mountains or oceans.

As the climate change becomes a huge problem for humanity, many satellites are deployed to understand its effect, predict it, and therefore propose solutions to prevent it. Correlated to this, satellites can also help farmers by giving precious information about weather, soil composition and condition, and other exploitation parameters.

Today there is a particular emphasis on the market of nanosatellites, which can be put into orbit by dozens in a single launch. Their smaller size make them way more affordable for small companies, extending therefore their range of applications.

1.2.2 Probes, telescopes, rovers

Another important application of space is the understanding of our universe: from the formation of our solar system, Sun's influence on the Earth, black holes or dark matter, scientific devices are launched each year in order to try to answer these questions. A huge European achievement happened in 2014 with the Rosetta mission: the unprecedented successful landing of a probe on a comet, gave precious information about what comets are made of. Similar mission was more recently achieved by a partnership JAXA/CNES with the mission Hayabusa 2 which returned recently with asteroid samples.

Other recent missions to be cited are Solar Orbiter, launched in 2020 and resulting from a ESA/NASA cooperation to study solar winds and the magnetic field of our star. Another European mission will be in 2022 the launch of Euclide, a telescope which will study the origins of the Universe expansion and its source, commonly designated by the dark matter.

The hidden side of the Moon is currently explored for the first time by the Chinese space agency (CNSA) with their rover Chang'e-4. Finally, the red planet has been and is still a source of high interest for scientists, motivating the exploration missions with two American rovers Opportunity and Curiosity. The latter will soon be joined by the European rover ExoMars, initially foreseen for 2020 but reported to 2022.

1.2.3 Human exploration

The last (and maybe the most exciting) application is sending humans to space, other planets, and ultimately beyond our solar system. In this domain much experience has been accumulated through the Apollo program of NASA. Since the 90s the International Space Station prepares the future steps of human exploration. Understanding space biology and space medicine are crucial for the next generation of astronauts which will fly again to the Moon and travel for the first time to Mars. This was announced by NASA recently with the Artemis program, including a plan to return to the Moon by 2024, and later to establish a permanent human presence (Fig. 1.3[1]). Again in space history, human exploration is something really emphasized by the USA, Europe having more a support function, even though European astronauts will be part of these future missions. The goal is to learn and prepare a future departure for Mars within the next decades. It is to be noticed that the NASA foresees to employ a high number of commercial launches for these missions, showing a willingness to give more and more importance to the private sector in this domain. This in fact has already started as SpaceX is now resupplying regularly the ISS with its Dragon cargos.

1.3 Liquid Rocket Engine technology

As mentioned earlier, all these applications require launchers to put the required spatial instruments into orbit. On paper the principle of these vehicles is very simple and is a direct demonstration of the third fundamental dynamic law of Newton: apply a force on one side to obtain an acceleration opposed to this force. To create this force, rocket engines are used.

Rocket engines are divided into several categories. For the first (main) stage, both Solid Rocket Boosters and Liquid Rocket Engines (LRE) are employed to generate a gigantic amount of power in order to overcome Earth's gravity. This manuscript focuses on LRE, of which some key aspects of their operation are described here.

---

[1] Website NASA Artemis

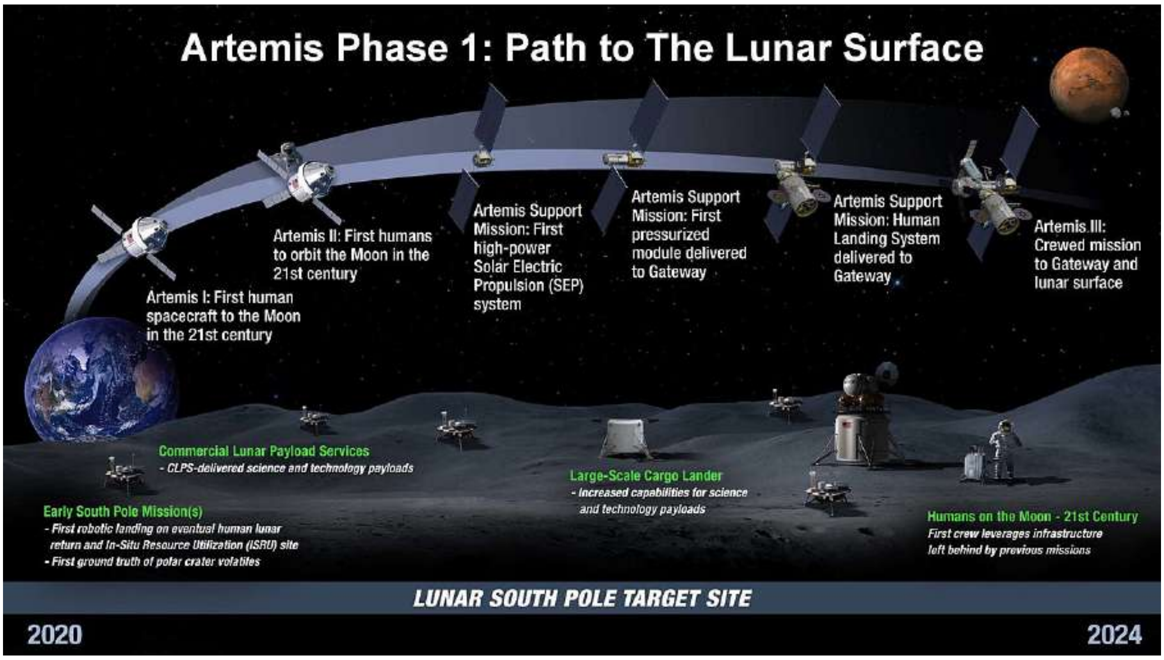

Figure 1.3: The Artemis program by NASA.

1.3.1 General principle

Liquid Rocket Engines convert chemical energy into thermal energy by burning fuel and oxidizer in a combustion chamber, which produces hot burnt gases. This thermal energy is then transformed into kinetic energy when these gases are ejected at a very high speed through a nozzle, generating thrust. The principle is summarized in Fig. 1.4[2].

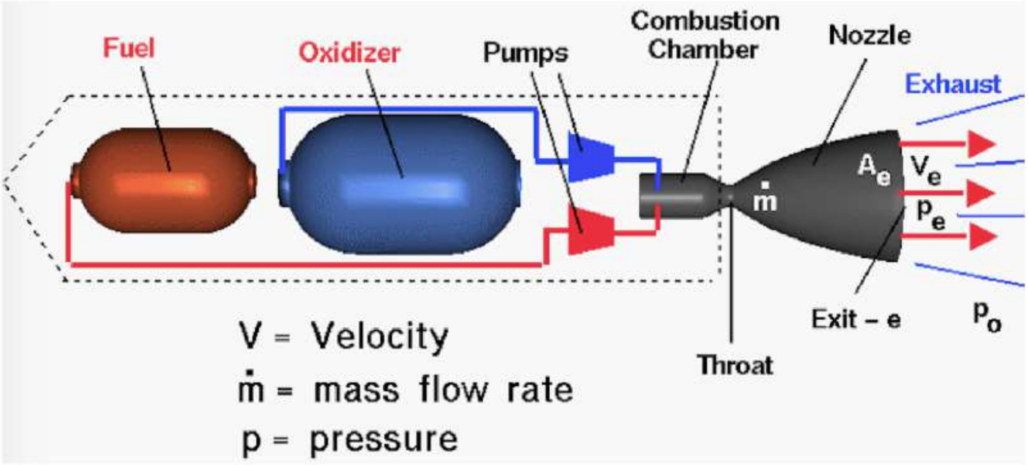

Figure 1.4: Liquid rocket engine schematic. This thesis focuses on the combustion chamber.

The thermal energy source, as for internal combustion engines, comes from the combustion of a fuel and an oxidizer, called in this context propellants. The fuel is generally liquid hydrogen because of its very high energetic density, but space kerosene is also employed for example in the Russian Soyuz rockets. The oxidizer is almost always oxygen, for two main reasons: in order to ensure oxidizer supply for the whole flight duration, it must be embarked as oxygen

---

[2] Website NASA Glenn Center

contained in the air rarefies as the rocket gains altitude; furthermore it is more efficient to embark pure oxygen rather than air, which contains a large amount of useless nitrogen.
Both propellants are stored in their liquid state, in order to reach sufficient density and therefore minimize the volume of the tanks. The fact is that except kerosene, classic propellants have a very low boiling temperature: 23K for hydrogen and 90K for oxygen (at one atmosphere), leading to the so-called cryogenic combustion: to be stored in their liquid state, propellants are cooled down to very low temperatures. They must then heat up and vaporize before burning in their gaseous state. In subcritical conditions, an atomization process takes place to form a spray.
The propellants are brought to the combustion chamber thanks to turbopumps: they pressurize the propellants, which arrive in the combustion chamber at a typical range of 30-300 bar. Turbopumps are integrating in the system following various thermodynamic cycles: expander, gas generator or staged combustion are the most common ones. A detailed description of the cycles can be found in [Yang et al., 2004]. Once the propellants enter in the combustion chamber, and depending on the thermodynamic regime (sub-, trans- or supercritical - described further), their mixing and burning behave differently.
The necessary amount of energy to ignite the flames is usually brought by a spark, a pyrotechnic charge or a torch of hot gas. Once the ignition phase is passed (it generally takes a few seconds), a stationary regime is reached in the combustion chamber. As the burnt gases resulting of the combustion are extremely hot (about 4200K for H2/O2), it is mandatory to cool down the combustion chamber walls, which would melt otherwise. The most usual way is too actively cool the walls by circulating the cold fuel in small channels inside them. The cold fuel is then pre-heated before being injected in the combustion chamber: this technique is called regenerative circuit.
The burnt gases are ejected through the nozzle, which has the role to expand them after their maximum compression at the throat, where the diameter of the device is the smallest. In these areas the flow becomes supersonic. The thrust resulting from the high gases momentum at the exhaust allows the rocket to lift off.

1.3.2 LRE performances

Knowing the main phenomena happening in a LRE, manufacturers seek the best performances when designing a product (for the best cost). The performances of a LRE are summarized by two main quantities: thrust and specific impulse (I_{sp}).

The thrust is expressed in Newton and is calculated, with the notation of Fig. 1.4, as:

$$F = \dot{m} V_e + (p_e - p_0) A_e \tag{1.1}$$

where $\dot{m}$ is the mass flow rate, and V_e, $p_e - p_0$ and A_e are respectively the velocity, the relative pressure and the nozzle area at the exhaust section. This equation highlights the importance of obtaining both a high speed flow and a large pressure at the exhaust to maximize the thrust.

The I_{sp} is a notion specific to air- and spacecrafts. It measures the force generated by the engine (the thrust) compared to its fuel consumption in time. It is therefore seen as a measurement of the engine efficiency: the higher the I_{sp}, the more efficient is the engine. It is expressed as a time:

$$I_{sp} = \frac{F}{\dot{m}g} \tag{1.2}$$

where g is the gravitational acceleration ($g = 9.81m/s^2$ at ground level on Earth). It means therefore that the I_{sp} changes during a flight, as g is varying: the I_{sp} of an engine is not the same considering a vacuum flight, an Earth take-off, or a take-off from another planet.

Typical values of thrust and I_{sp} for some main stage engines are reported in Table 1.1[3]:

Engine	Propellants	Scenario	Pressure in CC [bar]	Thrust [kN]	I_{sp} [s]
Vulcain 2.1	LOx/LH2	vacuum	120	1350	430
F-1	LOx/kero	vacuum	70	7770	304
F-1	LOx/kero	sea level	70	6770	263
RS-25	LOx/LH2	vacuum	210	2280	452
Raptor	LOx/LCH4	vacuum	300	2100	356
Prometheus	LOx/LCH4	vacuum(?)	110	1000	360

Table 1.1: Some typical values of chamber pressure, thrust and I_{sp}.

Some key characteristics of LRE are here highlighted. They all have in common a high pressure in the combustion chamber, which increases the obtained thrust. As shown in Eq. 1.1, the expansion ratio (ratio of exhaust area over throttle area) and the gases ejection speed play a major role as well, not detailed here.
The range of I_{sp} stands usually between 300s and 500s. It can be compared for example to engines used for satellite propulsion, such as Hall-effect thrusters which have typical I_{sp} range of 1000-8000s and 50mN-5N for thrust. The difference is huge because the use is completely different: launchers must overcome Earth's gravity while satellites only need to be regularly repositioned on their orbit, requiring very short and light impulsions.
The ideal spacecraft propulsion device would both dispose of high thrust and high I_{sp}, but it has not been discovered yet!

1.3.3 Towards methane propulsion

A current trend in the design of rocket engines in most space industry stakeholders is to switch from hydrogen to methane as fuel. At the first look, it could seem not really a good idea as methane is less energetic than hydrogen: a ratio of 3 exists between their lower heating value (*i.e.*, energy per unit of mass). However, methane offers many advantages which compensate this loss.
First, methane is about six times heavier than hydrogen. It means that more mass can be stored into the tank. Moreover the value of the product *density* × I_{sp} is higher than with hydrogen, making it possible to downsize the fuel tank and therefore the entire vehicle, and finally possibly decreasing its total mass.
Secondly, the boiling temperature of methane is 110K, higher than the hydrogen value of 23K. It means that it is way easier to store it in its liquid state, diminishing the loss caused by evaporation: a key aspect for long-duration missions. In addition, the close boiling temperatures of

---

[3] from Wikipedia

methane and oxygen (90K for the latter) is an asset for standardization of tanks manufacturing, diminishing the global cost.
As methane is less energetic than hydrogen, the temperatures reached in the combustion chamber are lower, typically about 3500K. In consequence, the wall heat flux are less intense, lowering therefore the margins for design of the cooling system. This leads also to a higher potential for reusability. Finally methane is less likely to transition to detonation because of its larger molecular weight than hydrogen, a good thing for safety issues.
From an environmental point of view and to the knowledge of the author, the advantages and drawbacks of choosing methane are not yet fully demonstrated. Today it is easier to produce methane compared to hydrogen for example, and it requires less energy to store it for the reasons mentioned above. However contrary to hydrogen its combustion produces CO and CO2. Even if gases emitted from rocket launches contribute less than 0.1% to the effect on the stratospheric ozone impact[4], this contribution may grow up as the number of launches per year will increase.
Finally in a more long-term vision, projects are emerging which aim to create methane during the missions in-situ, on the Moon or on Mars [Muscatello and Santiago-Maldonado, 2012].

All these aspects make the replacement of hydrogen by methane very interesting for the next LRE generation. Some projects already exist (Fig. 1.5).

Figure 1.5: Some methane-fed rocket engines. From left to right: Prometheus (ESA/CNES), Raptor (SpaceX), LNG (JAXA). Not at scale.

ESA/CNES/ArianeGroup is currently developing the Prometheus, a LOX/LCH4 with gas generator engine [Simontacchi et al., 2018]. In addition to the use of methane as fuel, its competitiveness is expected from innovative additive-manufacturing. Being less powerful than the current Vulcain 2.1 of Ariane 6, a higher number will be used and therefore produced, reducing the cost at the industrial scale. Prometheus will also equip Themis, the future European demonstrator for reusable rockets.

---

[4] https://ozone.unep.org/sites/default/files/2019-05/SAP-2018-Assessment-report.pdf

Other international examples of methane-fed engines are built by SpaceX developing the Raptor engine, which already flew on their super-heavy StarShip rocket, and the JAXA which has been developing for several years their own Liquid Natural Gas (LNG) engine family.

1.4 Tools to study and develop a LRE

As previously explained, European governmental agencies and industry must innovate to keep their space access independence and stay competitive on the market. The LRE manufacturers (ArianeGroup in Europe) need to have a detailed comprehension of the physical phenomena at play in order to design their product. To do so, they rely on both experiments and numerical simulations.

1.4.1 Experimental facilities

Most of the physical aspect happening in a LRE have been and are still studied thanks to experimental test benches, which are found worldwide. There are actually only a few because of the complexity and the costs they induce. Indeed the conditions are so extreme in the context of rocket engines that the test rigs for the full-size engines do not always reach them exactly. The power generated by such engines is so huge that a precise instrumentation is very difficult to set up. Thus, more compact test benches ("sub-scale" or "lab-scale") exist for easier experimental studies (and also for sake of security!).
In France, ONERA Palaiseau owns the Mascotte test bench which is equipped with multiple measurement techniques [Habiballah et al., 2006], used intensively to study wall heat fluxes [Pichillou et al., 2017, Grenard et al., 2019], sub- trans- and supercritical flames [Singla et al., 2005, Candel et al., 2006] and recently soot emissions [Vingert et al., 2019]. In Europe, Germany is also capable of such experiments at the DLR site of Lampoldshausen [Preuss et al., 2008, Preclik et al., 2005, Oschwald et al., 2006]. The Technical University of Munich uses different versions of test benches from 20 to 60 bar [Silvestri et al., 2014, Silvestri et al., 2016, Von Sethe et al., 2019, Perakis et al., 2017]. Italy conducts also its own experiments [Battista et al., 2015].

A lot has been learnt thanks to experiments, historically by NASA [NASA, 2004] and followed now by more actors, about many topics such as ignition, supercritical flows, wall heat transfers, nozzle flows... But a numerical simulation of a rocket engine allows to place a probe at any location in the discretized domain, giving access to information that is today impossible to obtain for experiment. However numerical codes are still young compared to the long experience acquired with test benches, and therefore still need validation by comparison with experiments. This is why experimental and numerical worlds are right now inseparable, as pointed out in [Slotnick et al., 2014].

1.4.2 Numerical modelling approaches

There are many ways to perform a numerical simulation. At its simplest, 0D simulations can be performed in order to get no more than budgets and performances of an engine. For more insights of each physical phenomenon, Computational Fluid Dynamics (CFD) is needed.

CFD is becoming a major tool in many indsutrial sectors to assist the design of new products. It consists of discretizing a given geometry, to solve a set of equations: in the case of CFD, the Navier-Stokes equations. A major issue when one wants to solve the Navier-Stokes equations is turbulence, because it is an unsteady, 3D, random phenomenon occurring at multiple scales. In a LRE the highly turbulent flow (Reynolds number of the order of $10^4 - 10^7$) makes the computation cost of a fully resolved simulation prohibitive. Thus several alternatives to compute a turbulent flow problem have been developed by the CFD community, which are grouped in three main categories (sum up by Fig. 1.6):

- Direct Numerical Simulation (DNS)
  Performing a DNS means that no model is used to compute the turbulence motions: they are all resolved from the integral length scale l_t to the Kolmogorov scale η_k. Since η_k can be very small, DNS requires a very high level of discretization. Therefore this kind of simulation is today only possible for simple academic cases, only when huge computational resources are available.

- Large Eddy Simulation (LES)
  LES is the "intermediate level" of CFD, because the smallest turbulent motions (lower than the discretization size k_Δ) are modelled thanks to sub-grid scale models, while the largest structures are computed. LES allows unsteady flow computations. It is today quite well-spreaded in the research world and becomes more and more accessible to industry.

- Reynolds Averaged Navier-Stokes (RANS)
  RANS simulations are the fastest CFD methods because here all the turbulent structures are modelled. RANS may give good tendencies but because of its formulation (the whole equation system is averaged) it is limited in the information it gives about the flow. Even though Unsteady-RANS allows unsteady computations, it does not reach the level of accuracy of LES.

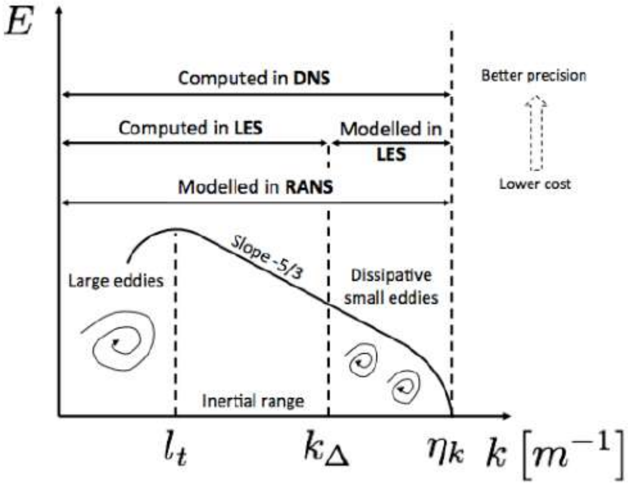

Figure 1.6: Turbulence modelling strategies (from [Potier, 2018]): depending on the chosen framework, turbulent motions are either fully computed (DNS), either fully modelled (RANS), or a mix (LES).

1.5 Scientific and technical challenges of LREs

Key aspects for the development of the next methane-fed LRE generations are reviewed in this section, focusing on critical design questions for the combustion chamber. A few modelling aspects are also mentioned but will benefit of more in-depth analysis further in the manuscript.

1.5.1 Ignition

The perfect control of ignition (and re-ignition when in space) phases are important because a failure can lead to malfunctioning or worse, the complete destruction of the engine. If too late, too much propellants are accumulated in the combustion chamber and the ignition can be too brutal. If too early, it possibly disrupts the burning process, leading to a thrust loss and a bad trajectory towards the target satellite orbit for example. In addition, much care must be put in the determination of the right amount of energy to be brought to ignite the chamber as it is prompt to trigger acoustic instabilities. Ignition can be obtained by various means, like a torch, electric spark, laser or additives into the propellants that allow them to auto-ignite [Yang et al., 2004]. Understanding the ignition process and how to model it numerically is still a challenge ([Lacaze, 2009, Dauptain, 2006]).

1.5.2 Injector design

The injectors are mainly responsible of the propellant mixing, so that they influence strongly the combustion performances. The most common injector types are shown Fig. 1.7.

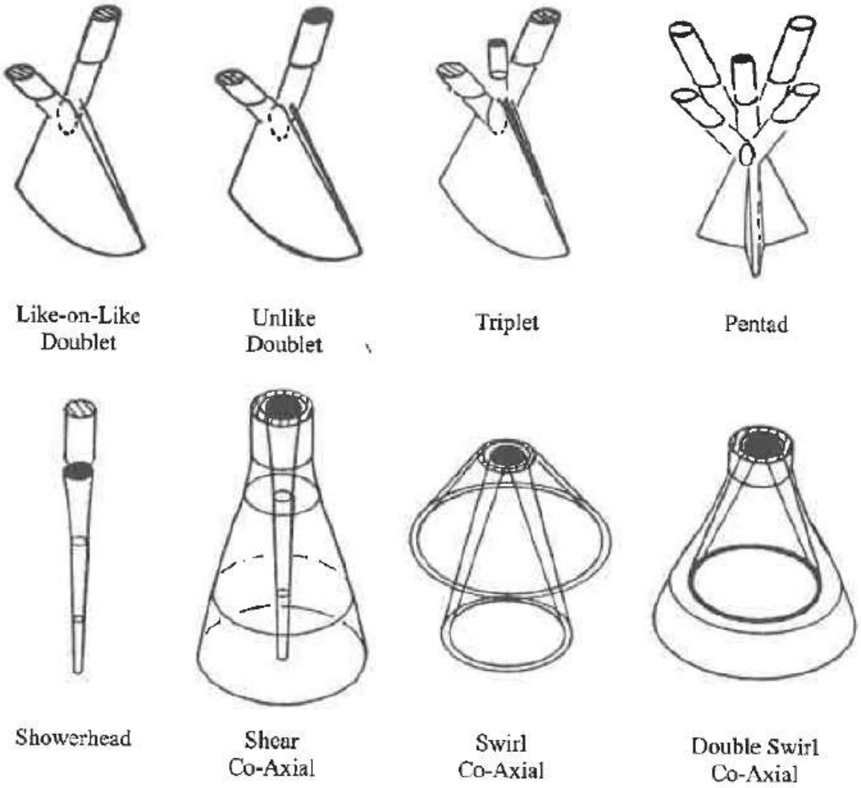

Figure 1.7: Common injector designs for LRE (from [Yang et al., 2004]).

In most of the applications, the shear coaxial injector is used: LOx is injected at the center and the fuel is injected around it, forming a shear layer between the two fluids.
It has been found that recess, which is the offset of the internal injector compared to the external one, is a major geometrical parameter having an important impact on the flame expansion in the chamber [Silvestri et al., 2017] (which could impact the wall heat flux).

1.5.3 Thermodynamics and two-phase flow

LREs are characterized by thermodynamic changes, and the conditions can cross the critical point. Figure 1.8 sums up the different states of a pure component in the (P-T) phase diagram. The propellants are usually injected sub- or transcritical, and as the pressure and temperature in the chamber increase, the supercritical state is reached in the flame and the burnt gases. Both propellants are not necessary in the same thermodynamic state at injection (like LOx/GCH4), with direct consequences on the flow dynamics. These different regimes are here characterized briefly.

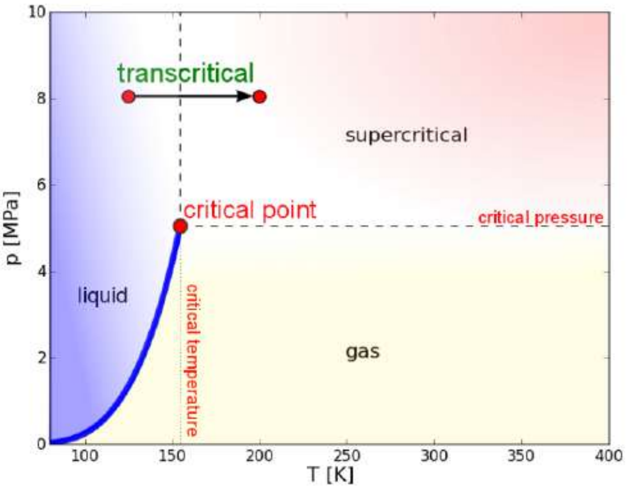

Figure 1.8: Phase diagram for O2 (from [Hickey and Ihme, 2013]).

- Subcritical
  In the subcritical regime, the liquid and gaseous phases are fully separated by a thin interface. The driving phenomena are atomization and evaporation, which control the flame length. At first long liquid ligaments appear along the liquid jet during the primary atomization, which then split into small droplets during the secondary atomization phase. This process depends on the ratio between the shear forces to the surface tension at the interface (characterized by the Weber number). Finally these droplets evaporate, a process accelerated by the hot surrounding environment when combustion has started. This atomization process is sketched in Fig. 1.9.

  Numerically, several techniques are available to describe a subcritical flow. In the non-dispersed phase, the gas-liquid interface and associated phenomena may be represented with accurate front-tracking approaches such as level-set [Desjardins et al., 2008] or Volume of Fluid [Hirt and Nichols, 1981], which are however CPU cost - prohibitive. Less demanding, but more approximate methods are multi-fluid techniques, either in the diffuse interface formulation [Pelletier, 2019, Jofre and Urzay, 2021], or second gradient

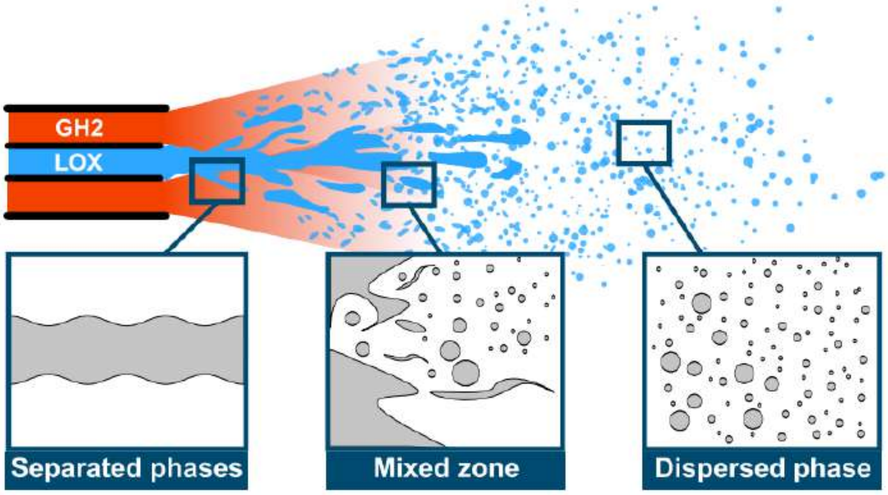

Figure 1.9: Schematic representation of the two-phase flow at the exit of a coaxial cryogenic injector for LRE in subcritical conditions (from [Le Touze et al., 2020]).

formulation [Jamet, 1995, Nayigizente et al., 2021].

The dispersed phase (non dense sprays) may be computed either with a statistical Eulerian approach or a Lagrangian approach tracking particle trajectories. The coupling of two models, one for the dense liquid phase and one for the spray, is still a challenge. An Eulerian-Eulerian coupling was made in [Le Touze et al., 2020], using a prescribed droplet-size distribution for the spray.

- Transcritical and Supercritical
  When pressure overcomes its critical value, the transcritical state is reached; supercritical state only happens if the temperature is above its critical value as well.
  Due to the high pressure, the repulsive atomic forces become important enough to overcome surface tension, leading to a single-phase fluid with both the properties of the gas and the liquid, *e.g.* high diffusivity and high density [Hickey and Ihme, 2013]. There is no atomization phenomenon, because there is no longer a clear liquid/gaseous interface.

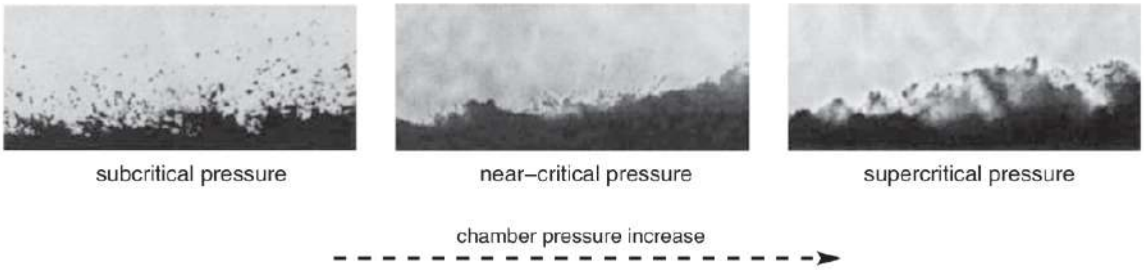

Figure 1.10: Cold nitrogen (105K, black area) injected into a 300K nitrogen environment from sub- to supercritical pressure (from [Jofre and Urzay, 2021]). The liquid-gas interface progressively disappears as the pressure grows up.

> In terms of experiment, trans- and supercritical flow visualizations are quite rare since they require high pressure test rigs and elaborated instrumentation. As an example, Fig. 1.10 gives an idea of how the pressure increase impacts the flow behaviour, in the case of a single component fluid.

Sub-, trans- or supercritical simulations can not anymore be described with the ideal equation of state, replaced with a cubic equation of states able to represent the higher density changes between the phases. Note a particularly difficult numerical issue raised by the critical point, where extremely high density changes occur and the heat capacity goes to infinity.

1.5.4 Thermoacoustic instabilities

Thermoacoustic instabilities are a complex phenomenon coming from the coupling of heat release from the flame and acoustics in the chamber. This coupling can amplify, leading to extremely high heat release rates which could lead to the engine destruction. As it is an unsteady phenomenon, LES is particularly suited to capture it with high fidelity, as for example in [Urbano et al., 2016, Kraus et al., 2018].

One of the most famous example about combustion instabilities in LRE is the F-1 engine that equipped the Saturn V rockets for the Apollo missions, which caused several catastrophic failures during its development in the late 1950s.

1.5.5 Turbulent combustion

Flames in LRE are characterized by their quasi-pure diffusion regime (propellants get into in the combustion chamber separated), on contrary to many other combustion devices.

In terms of simulation, flames are very thin (due to high pressure and high strain rate), so that it is generally not possible to fully resolve them on a LES mesh, therefore combustion models are needed to represent the sub-grid turbulence/chemistry interaction. For premixed flames in LES, the Thickened Flame model (TFLES) [Colin et al., 2000] has allowed to successfully predict a wide range of applications [Strakey and Eggenspieler, 2010, Kitano, T. and Kaneko, K. and Kurose, R. and Komori, S., 2016, Proch et al., 2017]. However this model is not directly applicable to diffusion flames which have different properties. Also, as TFLES only applies at the flame location [Legier et al., 2000], and its application to diffusion flames raises the question of which flame sensor to use [Rochette et al., 2020].

1.5.6 Chemistry

The sole change of propellant from hydrogen to methane raises a lot a questions. First, introducing the carbon atom in the system changes drastically the burnt gases, which are then mainly composed of H2O, CO, CO2, in different proportions depending on the stoichiometric ratio. The presence of C atom also brings the question of soot production in the chamber, which could impact the radiative heat transfer.

As LREs work at high pressure, chemical kinetics must be studied in the same condition. It is however difficult to obtain experimentally high pressure flames to study their kinetics. For methane oxy-combustion at high pressure, today no experiment studying the kinetics exist in realistic LRE conditions. Such work is in preparation at ICARE laboratory [Halter et al., 2020b].

As explained before, hydrogen is more energetic than methane and thus burns faster. So far, most chemical models for hydrogen oxy-combustion were rather simple, even considering infinitely fast kinetics, allowing significant simplification in CFD codes as it avoids to describe the chemical system. For methane however, the consumption speed is slower so that such approximation must be checked, and other model proposed.

1.5.7 Wall heat flux prediction and cooling

Last and not least, a critical aspect for the design of rocket engines remains the wall heat flux prediction. Indeed a precise idea of the thermal load on the structure is necessary in order to size the wall thickness and the cooling system. Cooling is essential as the burnt gases temperature exceeds the melting point of most typical steels and other alloys used in LRE.
On test rigs, wall heat flux is reconstructed from thermocouple measurements and serves often as reference or boundary condition for numerical simulations. In simulations, predicting accurate wall fluxes means to correctly compute the boundary layer. In RANS simulation, it is possible to refine the near-wall mesh to resolve the boundary layer. However in LES, resolving the boundary layer rapidly increases the cost above acceptable levels and wall-models are commonly used. Still, the question of coupling the wall-model with the external unsteady turbulent flow remains an open problem.

1.6 Organization of the manuscript

In this thesis, a few aspects of LRE combustion chamber numerical development are explored, related to combustion, chemistry and wall fluxes prediction. Each aspect is the subject of a more complete bibliographic analysis in its respective chapter. All topics are numerically studied with the LES code AVBP developed by CERFACS [Schönfeld and Rudgyard, 1999, Gourdain et al., 2009, Gicquel et al., 2011] and with the software CANTERA [Goodwin et al., 2017], an open source 0D and 1D chemistry solver.
In the next part, the governing equations considered in this work are presented for both gaseous (Chapter 2) and liquid (Chapter 3) phases, as well as some numerical aspects. The third part contains the developments brought to the code and is divided into two chapters: Chapter 4 is about combustion, including chemistry modelling and diffusion flame study; Chapter 5 describes wall modelling, on one hand linked to the choice of sub-grid scale model, on the other hand linked to the influence of a reactive multi-species mixture in the boundary layer. The fourth part contains the applications, that are all lab-scale test benches: Chapter 6 introduces the CONFORTH configuration from ONERA in supercritical conditions and Chapter 7 the single-injector from TUM in subcritical conditions. Finally a general conclusion on this work is proposed.

Part II

Governing Equations

Chapter 2

Gaseous phase

This chapter introduces the main equations used for reactive compressible flows. Their derivation is not detailed here and the reader is referred to textbooks [Poinsot and Veynante, 2012] for more details. In all the following, the Einstein index notation is used.

2.1 Thermodynamics

Reactive flows are composed of several species, which are taken into account in the thermodynamic state of the mixture. In a closed volume V, the following properties are defined:

- Density ρ
- Molar mass W
- Constant pressure and volume heat capacities C_p and C_v
- Enthalpy h and entropy s
- Internal energy e

In a mixture composed of N species denoted by their index k, the properties of the pure species are:

- Molar mass: W_k
- Mass fraction: $Y_k = m_k/m$ where m is the total mass of the mixture and m_k the mass of the species k.
- Molar fraction: $X_k = Y_k W/W_k$
- Molar concentration: $[X_k] = \rho X_k/W$
- Density: $\rho_k = \rho Y_k$

The links between the species constituting the mixture and the whole mixture are here introduced. The mixture molecular weight is:

$$\frac{1}{W} = \sum_{k=1}^{N} \frac{Y_k}{W_k} \text{ or } W = \sum_{k=1}^{N} X_k W_k \tag{2.1}$$

and its heat capacities are respectively:

$$C_p = \sum_{k=1}^{N} Y_k C_{p,k} \text{ and } C_v = \sum_{k=1}^{N} Y_k C_{v,k} \tag{2.2}$$

Still for a pure species k, enthalpy and internal energy take the following forms (as mass quantities):

$$h_k = h_{s,k} + \Delta h^0_{f,k} \tag{2.3}$$

$$e_k = e_{s,k} + \Delta h^0_{f,k} \tag{2.4}$$

with respectively $h_{s,k} = \int_{T_0}^{T} C_{p,k} dT$ and $e_{s,k} = \int_{T_0}^{T} C_{v,k} dT - RT_0/W_k$ the sensible enthalpy and the sensible energy, while $\Delta h^0_{f,k}$ is the standard enthalpy of formation of species k at the standard temperature T_0 (usually 0 or 298.15K).

For the mixture, the enthalpy and internal energy are simply:

$$h = \sum_{k=1}^{N} h_k Y_k,\; e = \sum_{k=1}^{N} e_k Y_k \tag{2.5}$$

Note that e denotes here the internal energy. It is also useful to recall the total energy E, which is the sum of all energies. In the following, only the internal and kinetic energy are accounted, so that:

$$E = e + e_{kin} = e + 0.5 u_i^2 \tag{2.6}$$

where u_i stands for the i^{th}-component of the flow velocity. The chemical energy is expressed through the chemical source terms introduced in Section 2.2.

2.1.1 Perfect gases

The perfect gas assumption is very common as it holds for most usual applications. The Perfect Gas equation of states writes for species k:

$$p_k = \rho_k \frac{\mathcal{R}}{W_k} T \tag{2.7}$$

where $\mathcal{R} = 8.314\ J.mol^{-1}.K^{-1}$ is the perfect gas universal constant and T is the mixture temperature.
For perfect gases the total mixture pressure P is simply the sum of the partial pressures p_k:

$$P = \sum_{k=1}^{N} p_k = \sum_{k=1}^{N} \rho_k \frac{\mathcal{R}}{W_k} T = \rho \frac{\mathcal{R}}{W} T = \rho r T \tag{2.8}$$

where

$$r = \frac{\mathcal{R}}{W} = \sum_{k=1}^{N} \frac{Y_k}{W_k} \mathcal{R} = \sum_{k=1}^{N} Y_k r_k \tag{2.9}$$

This equation of state is correct as long as the compressibility factor $\mathcal{Z}$ is close to one (typically $0.95<\mathcal{Z}<1.05$):

$$\mathcal{Z} = \frac{P}{\rho r T} \tag{2.10}$$

Otherwise it means that due to high density, the interaction between molecules is not anymore negligible, thus the perfect gas assumption does not hold anymore and a more complex equation of state must be used, like cubic laws. This is particularly the case in rocket engines where propellants are often injected at high pressure, cryogenic conditions.

2.1.2 Real gases

When the perfect gas assumption is not verified, one talk then about "real gas" (abbreviated as "RG"), introduced below.

The critical point

In Chapter 1 were introduced the three thermodynamic regimes for rocket engine combustion: sub- trans- and supercritical states. Figure 1.8 shows that these states are separated by the critical point, defined for a pure species with its critical temperature T_c and pressure P_c. Table 2.1 presents values for some common species used in this work.

Species	$T_c[K]$	$P_c[bar]$
CH4	190.564	45.992
O2	154.581	50.43
CO	133.0	34.987
CO2	304.128	73.773
H2O	647.096	220.64

Table 2.1: Values of critical temperature and pressure of main species considered in this work.

Reduced temperature and pressure are then defined as:

$$T_r = \frac{T}{T_c} \text{ and } P_r = \frac{P}{P_c} \tag{2.11}$$

The Soave-Redlich-Kwong equation

Two cubic equations may be used: the Peng-Robinson (PR) equation [Peng and Robinson, 1976] and the Soave-Redlich-Kwong (SRK) [Soave, 1972] equation. Only the second is presented here as it is known to be more accurate for cryogenic flows and was therefore used in this work [Ghanbari et al., 2017]. The SRK equation in mass units writes:

$$P = \frac{\rho r T}{1 - \rho b_m} - \frac{\rho^2 a_m(T)}{1 + \rho b_m} \tag{2.12}$$

where $a_m(T)$ and b_m are mass coefficients associated to the mixture which are computed following the mixture law of Van Der Walls [Kwak and Mansoori, 1986]: $a_m(T)$ represents the molecular attractive force while b_m is the repulsive force. Denoting with i and j two different species:

$$a_m(T) = \sum_{i=1}^{N} \sum_{j=1}^{N} a_{ij}(T) Y_i Y_j \tag{2.13}$$

$$b_m = \sum_{i=1}^{N} b_i Y_i \tag{2.14}$$

with

$$a_{ij}(T) = \sqrt{a_{ii}(T) a_{jj}(T)} \, (1 - k_{ij}) \tag{2.15}$$

where k_{ij} is the binary interaction coefficient. The quantities $a_{ii}(T)$ and b_i are the coefficients for a pure species. For SRK, they are written as:

$$a_{ii}(T) = \Phi_{C_i} \Psi(T)^2 \tag{2.16}$$

$$b_i = 0.08664 \frac{r_i T_{c_i}}{P_{c_i}} \tag{2.17}$$

with

$$r_i = \frac{\mathcal{R}}{W_i} \tag{2.18}$$

$$\Phi_{c_i} = 0.42747 \frac{(r_i T_{c_i})^2}{P_{c_i}} \tag{2.19}$$

$$\Psi(T) = 1 + c_i \left(1 - \sqrt{\frac{T}{T_{c_i}}} \right) \tag{2.20}$$

$$c_i = 0.48508 + 1.5517 \omega_i - 0.15613 \omega_i^2 \tag{2.21}$$

where ω_i is the acentric factor [Pitzer, 1955].

Calculation of the density

The density is obtained from the cubic equation of state, which induces to solve a third-order polynomial:

$$\rho^3 + (a_2)\, \rho^2 + (a_1)\, \rho + (a_0) = 0 \tag{2.22}$$

where for the SRK equation:

$$a_0 = \frac{P}{b_m a_m} \tag{2.23}$$

$$a_1 = -\frac{\bar{r} T}{b_m a_m} \tag{2.24}$$

$$a_2 = \frac{-P b_m^2 - \bar{r} T b_m + a_m}{a_m b_m} \tag{2.25}$$

The resolution of the above equation is made with the Cardano method[1]. Then, the enthalpy and heat capacities are also computed from the SRK equation.

2.2 Chemistry

The main principles of finite-rate chemistry, mostly used in this work, are presented.

2.2.1 Chemical kinetics

Consider a chemical system of N_s species associated with M reactions:

$$\sum_{k=1}^{N_s} \nu_{kj}^{'} S_k \rightleftharpoons \sum_{k=1}^{N_s} \nu_{kj}^{''} S_k \text{ for } j = 1, M \tag{2.26}$$

where S_k is the symbol for species k, $\nu_{kj}^{'}$ and $\nu_{kj}^{''}$ are the stoichiometric coefficients of species k in reaction j.

The forward rate constant, associated to reaction j, is computed using the Arrhenius law:

$$K_j^f = A_j^f T^{\beta_j} exp(-\frac{E_j}{\mathcal{R}T}) \tag{2.27}$$

with A_j^f the pre-exponential factor, β_j the temperature power and E_j the activation energy.

For reversible reactions, the equilibrium constant for a typical 2nd order reaction $A+B \rightleftharpoons C+D$ writes:

$$K_j = \frac{K_j^f}{K_j^r} \text{ with } K_j = \frac{[C][D]}{[A][B]} \text{ at equilibrium} \tag{2.28}$$

The forward and reverse rate constants are used to calculate the progress rates for each reaction:

$$Q_j = K_j^f \prod_{k=1}^{N_s} [X_k]^{\nu_{kj}^{'}} - K_j^r \prod_{k=1}^{N_s} [X_k]^{\nu_{kj}^{''}} \tag{2.29}$$

The reaction rates $\dot{r}_j$ are used to compute the production rates $\dot{\omega}_k$ for each species k:

$$\dot{\omega}_k = \sum_{j=1}^{M} \dot{r}_j = W_k \sum_{j=1}^{M} \nu_{kj} Q_j \tag{2.30}$$

Thus, mass conservation enforces that:

$$\sum_{k=1}^{N_s} \dot{\omega}_k = 0 \tag{2.31}$$

Knowing that $\nu_{kj} = \nu_{kj}^{''} - \nu_{kj}^{'}$, it is also possible to get the production rate for specie k in the reaction j:

$$\dot{\omega}_{kj} = Q_j W_k \nu_{kj} \tag{2.32}$$

---

[1] https://brilliant.org/wiki/cardano-method/

These production rates are necessary to then compute the heat release rate $\dot{\omega}_T$ (or energy source term):

$$\dot{\omega}_T = -\sum_{k=1}^{N_s} \Delta h^0_{f,k} \dot{\omega}_k \tag{2.33}$$

2.2.2 Chemical time scale

To understand the role of chemistry in CFD, it is important to introduce the chemical characteristic time scale τ_c. This scale can be determined by several ways [Wartha et al., 2020], and one of the most common, used in this work, is to use the inverse Jacobian analysis method [Caudal et al., 2013].

The Jacobian matrix J is composed of the source term derivatives and writes for species k and l:

$$J = \frac{\partial \Omega_k}{\partial Y_l} \text{ for } k = 1, ..., N \text{ and } l = 1, ..., N \tag{2.34}$$

with $\Omega_k = \dot{\omega}_k / \rho$ and Y_l is the mass fraction of species l. J is homogeneous to the inverse of a time, and to simplify, the characteristic time scales are often considered as the inverse of the diagonal terms λ_{kk} of J:

$$\tau_{c,k} = \frac{1}{\lambda_{kk}} \tag{2.35}$$

Another chemical time is used in practice in simulations, $dt_{c,k}$, to prevent negative mass fraction values and ensure stability. In AVBP this time expresses the maximum time step corresponding to the maximum allowed species mass fraction change.

$$dt_{c,k} = \frac{[Y_k]}{\dot{\omega}_k} \tag{2.36}$$

The final chemical integration time is simply the minimum of $dt_{c,k}$ over all species:

$$dt_c = min\left(\frac{[Y_k]}{\dot{\omega}_k}\right) \tag{2.37}$$

2.3 Navier-Stokes equations

For fully compressible, reactive flows the conservation equations for mass, momentum, energy and species are:

$$\frac{\partial \rho}{\partial t} + \frac{\partial}{\partial x_i}(\rho u_i) = 0 \tag{2.38}$$

$$\frac{\partial \rho u_j}{\partial t} + \frac{\partial \rho u_i u_j}{\partial x_i} + \frac{\partial P \delta_{ij}}{\partial x_i} = -\frac{\partial \tau_{ij}}{\partial x_i} \tag{2.39}$$

$$\frac{\partial \rho E}{\partial t} + \frac{\partial \rho u_i E}{\partial x_i} + \frac{\partial u_j P \delta_{ij}}{\partial x_i} = -\frac{\partial q_i}{\partial x_i} + \frac{\partial u_j \tau_{ij}}{\partial x_i} + \dot{\omega}_T \tag{2.40}$$

$$\frac{\partial \rho Y_k}{\partial t} + \frac{\partial \rho u_i Y_k}{\partial x_i} = -\frac{\partial J_{k,i}}{\partial x_i} + \dot{\omega}_k \quad \text{for } k = 1, N \tag{2.41}$$

where u_i stands for the i^{th}-component of the velocity, τ_{ij} is the viscous stress tensor, E the total energy, q_i the i^{th}-component of the heat flux (by conduction and species diffusion), $\dot{\omega}_T$ the energy source term, $J_{k,i}$ the i^{th}-component of the diffusive flux of species k, and $\dot{\omega}_k$ the chemical source term of species k. δ_{ij} is the Kronecker symbol, equal to 1 if $i = j$ and 0 otherwise. All these terms are detailed below, except $\dot{\omega}_T$ and $\dot{\omega}_k$ which were already introduced in Section 2.2.

2.3.1 Diffusion fluxes

Viscous stress tensor

The viscous stress tensor is written as:

$$\tau_{ij} = 2\mu \left(S_{ij} - \frac{1}{3}\delta_{ij} S_{ll} \right) \tag{2.42}$$

with μ the dynamic viscosity and S_{ij} the deformation tensor:

$$S_{ij} = \frac{1}{2}\left(\frac{\partial u_j}{\partial x_i} + \frac{\partial u_i}{\partial x_j} \right) \tag{2.43}$$

Species diffusion flux

For multi-species flows, the diffusive flux of species k in the mixture is often calculated using the Hirschfelder and Curtiss approximation [Hirschfelder et al., 1969], considering only diffusion of a species in the mixture without detailing species-to-species binary diffusion:

$$J_{k,i} = \rho Y_k V_{k,i} = -\rho \left(D_k \frac{W_k}{W} \frac{\partial X_k}{\partial x_i} - Y_k V_i^c \right) \tag{2.44}$$

where D_k is the diffusion coefficient of species k in the mixture, and $V_{k,i}$ is the i^{th}-component of the diffusion velocity of species k, to which a correction velocity V_i^c is added to ensure mass conservation as:

$$V_i^c = \sum_{k=1}^{N} D_k \frac{W_k}{W} \frac{\partial X_k}{\partial x_i} \tag{2.45}$$

Heat diffusion flux

The energy flux q_i is the sum of the Fourier flux (heat diffusion) and the enthalpy flux via species diffusion, taking into account with the velocity correction:

$$q_i = -\lambda \frac{\partial T}{\partial x_i} + \sum_{k=1}^{N} J_{k,i} h_k = -\lambda \frac{\partial T}{\partial x_i} - \rho \sum_{k=1}^{N} \left(D_k \frac{W_k}{W} \frac{\partial X_k}{\partial x_i} - Y_k V_i^c \right) h_k \tag{2.46}$$

2.3.2 Transport properties

Viscosity

The dynamic viscosity $\mu = \rho\nu$, may be expressed with different laws which are presented here.

The power law writes:

$$\mu = c_1 \left(\frac{T}{T_{ref}} \right)^b \tag{2.47}$$

where c_1 and b are constants.

The Sutherland law writes:

$$\mu = c_1 \left(\frac{T}{T_{ref}} \right)^{3/2} \frac{T_{ref} + c_2}{T + c_2} \tag{2.48}$$

where c_1 and c_2 are constants determined to best fit the real viscosity of the mixture.

Molecular diffusion

The diffusion coefficient of species k in the mixture is written as:

$$D_k = \frac{1 - Y_k}{\sum_{j \neq k} X_j / D_{jk}} \tag{2.49}$$

with D_{jk} the binary diffusion coefficient of species j in species k.

The binary coefficients D_{jk} are complex functions implying collision integrals. The above formulation is used in detailed chemistry 0D-1D flame codes such as CANTERA but is too complex for CFD. In AVBP, a simplification is made taking the form of constant Schmidt numbers for each species Sc_k. This way, the diffusion coefficients are computed as:

$$D_k = \frac{\mu}{\rho \, \mathrm{Sc}_k} \tag{2.50}$$

Note that the Soret effect (molecular species diffusion due to temperature gradient) is neglected here, following the conclusions of [Giovangigli, 1999, Ern and Giovangigli, 1994].

Conduction

The heat conduction λ of the mixture is computed thanks to:

$$\lambda = \frac{\mu C_p}{\mathrm{Pr}} \tag{2.51}$$

where Pr is the constant Prandtl number of the mixture, supposed constant for a given mixture in this work.

The Dufour effect (heat flux due to species mass fraction gradients) is as well neglected here ([Giovangigli, 1999, Ern and Giovangigli, 1994]).

Comment: for real gas, the Chung method [Chung et al., 1988] allows to compute more precisely the viscosity and the thermal conductivity at high pressure, as it takes into account RG properties of the species. It is however not employed in this work, as for several intermediate species the RG properties are uncertain and could alter the accuracy of the mixture properties.

2.4 Large Eddy Simulation (LES)

2.4.1 The LES concept

The main LES concepts are here described in order to understand the derivation of the filtered Navier-Stokes equations that are resolved in this work. The literature is vast on this topic and the reader is advised to refer to textbooks [Sagaut, 2006] for more details.

A key quantity in industrial flows is the Reynolds number, which is the ratio of inertial forces over viscous forces, and is written as:

$$\mathrm{Re} = \frac{\rho u L}{\mu} \tag{2.52}$$

where u and L are the characteristic velocity and length of the flow. When Re is large enough (typically above 2500 for channel flows), the flow is considered as turbulent: viscous forces are low compared the inertial forces, and vortical structures appear. These structures are of various sizes, from the integral length scale l_t (largest eddies) to the smallest dissipative Kolmogorov scale η_k. Turbulence is described by the famous energy cascade theory theoretized by Kolmogorov [Kolmogorov, 1941].

As already introduced in Section 1.4.2, in LES the smallest eddies are filtered out and modelled. Therefore, a LES code solves *filtered* equations, in which the modelled part is represented thanks to *subgrid-scale* model terms. Using the notation $\bar{f}$ for filtered quantities, f being any flow quantity, the following definition is used:

$$\overline{f}(x) = \int f(x')F_{\Delta}(x - x')dx' \tag{2.53}$$

where F_{Δ} is the LES filter (which can be a cut-off, box filter, etc...) of size Δ.

The unresolved subgrid scales f' therefore read as:

$$f'(x,t) = f(x,t) - \bar{f}(x,t) \tag{2.54}$$

For variable density flows, a mass-weighted Favre filtering is used:

$$\bar{\rho}\tilde{f}(x) = \int \rho f(x')F_{\Delta}(x - x')dx' = \overline{\rho f} \tag{2.55}$$

so that:

$$\tilde{f} = \frac{\overline{\rho f}}{\bar{\rho}} \tag{2.56}$$

Note that one shall distinguish between two types of LES: the "explicit" LES, where the filter is explicitly built and applied to the conservation equations which are then solved numerically, and the "implicit" LES, where the conservation equations are implicitly filtered by the grid, acting as a low-pass filter. The large majority of LES codes, including AVBP, use implicit filtering, while explicit filtering is used for dynamic models and allows to better control the numerical error, but is more expensive [Sagaut, 2006, Lund, 2003].

2.4.2 Filtered conservation equations

The Favre filter is now applied to the conservation equations, which gives:

$$\frac{\partial \bar{\rho}}{\partial t} + \frac{\partial \bar{\rho}\tilde{u}_i}{\partial x_i} = 0 \tag{2.57}$$

$$\frac{\partial \bar{\rho}\tilde{u}_j}{\partial t} + \frac{\partial \bar{\rho}\tilde{u}_i\tilde{u}_j}{\partial x_i} + \frac{\partial \bar{P}\delta_{ij}}{\partial x_i} = \frac{\partial}{\partial x_i}\left[\bar{\tau}_{ij} - \bar{\rho}\left(\widetilde{u_iu_j} - \tilde{u}_i\tilde{u}_j\right)\right] \tag{2.58}$$

$$\frac{\partial \bar{\rho}\tilde{E}}{\partial t} + \frac{\partial \bar{\rho}\tilde{u}_i\tilde{E}}{\partial x_i} + \overline{\frac{\partial u_iP\delta_{ij}}{\partial x_i}} = \frac{\partial}{\partial x_i}\left[\overline{q_i} - \bar{\rho}\left(\widetilde{u_iE} - \tilde{u}_i\tilde{E}\right)\right] + \overline{\tau_{ij}\frac{\partial u_i}{\partial x_j}} + \bar{\dot{\omega}}_T \tag{2.59}$$

$$\frac{\partial \bar{\rho}\tilde{Y}_k}{\partial t} + \frac{\partial \bar{\rho}\tilde{u}_i\tilde{Y}_k}{\partial x_i} = \frac{\partial}{\partial x_i}\left[\bar{J}_{k,i} - \bar{\rho}\left(\widetilde{u_iY_k} - \tilde{u}_i\tilde{Y}_k\right)\right] + \bar{\dot{\omega}}_k \quad \text{for } k = 1, N \tag{2.60}$$

This set of equations is the one actually solved in AVBP. The filtered and subgrid-scale fluxes must now be detailed.

2.4.3 Filtered diffusion fluxes

The filter applied to the different fluxes leads to the following expressions.

Filtered viscous stress tensor

$$\overline{\tau_{ij}} = \overline{2\mu\left(S_{ij} - \frac{1}{3}\delta_{ij}S_{ll}\right)} \tag{2.61}$$

is approximated by:

$$\overline{\tau_{ij}} \simeq 2\bar{\mu}\left(\tilde{S}_{ij} - \frac{1}{3}\delta_{ij}\tilde{S}_{ll}\right) \tag{2.62}$$

with:

$$\tilde{S}_{ij} = \frac{1}{2}\left(\frac{\partial \tilde{u}_j}{\partial x_i} + \frac{\partial \tilde{u}_i}{\partial x_j}\right) \tag{2.63}$$

and

$$\bar{\mu} \simeq \mu(\tilde{T}) \tag{2.64}$$

Filtered species diffusion flux

$$\bar{J}_{k,i} = -\overline{\rho\left(D_k\frac{W_k}{\bar{W}}\frac{\partial X_k}{\partial x_i} - Y_kV_i^c\right)} \tag{2.65}$$

is approximated by:

$$\bar{J}_{k,i} \simeq -\bar{\rho}\left(\bar{D}_k\frac{W_k}{\bar{W}}\frac{\partial \tilde{X}_k}{\partial x_i} - \tilde{Y}_k\tilde{V}_i^c\right) \tag{2.66}$$

with:

$$\tilde{V}_i^c = \sum_{k=1}^{N} \bar{D}_k \frac{W_k}{\bar{W}} \frac{\partial \tilde{X}_k}{\partial x_i} \tag{2.67}$$

and

$$\bar{D}_k \simeq \frac{\bar{\mu}}{\bar{\rho} Sc_k} \tag{2.68}$$

Filtered heat diffusion flux

$$\overline{q_i} = -\overline{\lambda \frac{\partial T}{\partial x_i}} + \overline{\sum_{k=1}^{N} J_{k,i} h_k} \tag{2.69}$$

is approximated by:

$$\overline{q_i} \simeq \bar{\lambda} \frac{\partial \tilde{T}}{\partial x_i} - \sum_{k=1}^{N} \bar{J}_{k,i} \tilde{h}_k \tag{2.70}$$

with:

$$\bar{\lambda} \simeq \frac{\bar{\mu} \overline{C_p}(\tilde{T})}{\mathrm{Pr}} \tag{2.71}$$

2.4.4 Subgrid-scale fluxes

Applying filtering to non-linear terms leads to unclosed terms which are linked to subgrid-scale phenomena. To describe the interaction between the non-resolved and resolved quantities, subgrid-scale (SGS) models are used and detailed below.

SGS viscous stress tensor

$$\bar{\tau}_{ij}^{sgs} = -\bar{\rho}(\widetilde{u_i u_j} - \tilde{u}_i \tilde{u}_j) \tag{2.72}$$

is modelled following the Boussinesq assumption, which says that the subgrid turbulent stresses can be modelled thanks to a subgrid-scale turbulent viscosity ν_t:

$$\bar{\tau}_{ij}^{sgs} = 2\bar{\rho}\nu_t \left(\tilde{S}_{ij} + \frac{1}{3}\delta_{ij}\tilde{S}_{ll} \right) \tag{2.73}$$

ν_t can be computed by various subgrid-scale models: this is explained in Section 2.4.5.

SGS species diffusion flux

$$\bar{J}_{k,i}^{sgs} = -\bar{\rho} \left(\widetilde{u_i Y_k} - \tilde{u}_i \tilde{Y}_k \right) \tag{2.74}$$

is modelled by:

$$\bar{J}_{k,i}^{sgs} = -\bar{\rho} \left(\bar{D}_k^t \frac{W_k}{\bar{W}} \frac{\partial \tilde{X}_k}{\partial x_i} - \tilde{Y}_k \tilde{V}_i^{c,t} \right) \tag{2.75}$$

which introduces the turbulent diffusion velocity:

$$\tilde{V}_i^{c,t} = \sum_{k=1}^{N} \bar{D}_k^t \frac{W_k}{\bar{W}} \frac{\partial \tilde{X}_k}{\partial x_i} \tag{2.76}$$

and the turbulent diffusivity:

$$\bar{D}_k^t = \frac{\bar{\mu}}{\bar{\rho} Sc_k^t} \tag{2.77}$$

where Sc_k^t is the turbulent Schmidt number of species k. It is usually assumed that all species Schmidt numbers are equal: $Sc_k^t = Sc_t$. In AVBP, the standard value is $Sc_t = 0.7$.

SGS heat diffusion flux

$$\bar{q}_i^{sgs} = -\bar{\rho}\left(\widetilde{u_i E} - \tilde{u}_i \tilde{E}\right) \tag{2.78}$$

is modelled following the same idea, introducing a turbulent thermal conductivity:

$$\bar{q}_i^{sgs} = -\lambda_t \frac{\partial \widetilde{T}}{\partial x_i} - \sum_{k=1}^{N} \bar{J}_{k,i} \tilde{h}_k \tag{2.79}$$

with:

$$\lambda_t = \frac{\bar{\mu}_t \overline{C_p}(\widetilde{T})}{\mathrm{Pr}^t} \tag{2.80}$$

where Pr^t is the turbulent Prandtl number, also supposed constant. In AVBP, its standard value is 0.7.

2.4.5 Turbulent viscosity models

The previous equations introduced the dynamic turbulent viscosity $\mu_t = \bar{\rho}\nu_t$. Various sub-grid scale models can be used to compute it. Three of them, widely used in the community and implemented in AVBP, are presented below: the Smagorinsky, WALE and Sigma models. Most of the time, the role of ν_t is only to dissipate energy, therefore a majority of subgrid-scale models make the hypothesis that there is no backscatter phenomenon (*i.e.*, an energy transfer from the smallest to the largest scales) [Piomelli et al., 1991].

Smagorinsky model [Smagorinsky, 1963]

$$\nu_t = (C_S \Delta)^2 \sqrt{2 \tilde{S}_{ij} \tilde{S}_{ij}} \tag{2.81}$$

where Δ denotes the filter characteristic length (cube-root of the node volume in implicit grid filtering) and C_S is a constant of the model with $0.1 \leq C_S \leq 0.18$.
This model was one of the first to be developed and therefore has been widely used in the LES community. It was however originally designed for homogeneous isotropic turbulent flows, and is therefore not well adapted for wall-bounded flows (where turbulence is anisotropic). It is known to be overall too dissipative, a major problem for turbulent flows.
An extension of the model exists where C_S is not anymore a constant but is calculated in the simulation using the dynamic Smagorinsky model.

WALE model [Nicoud and Ducros, 1999]

$$\nu_t = (C_w \Delta)^2 \frac{\left(s_{ij}^d s_{ij}^d\right)^{3/2}}{\left(\widetilde{S}_{ij} \widetilde{S}_{ij}\right)^{5/2} + \left(s_{ij}^d s_{ij}^d\right)^{5/4}} \tag{2.82}$$

with

$$s_{ij}^d = \frac{1}{2}\left(\widetilde{g}_{ij}^2 + \widetilde{g}_{ji}^2\right) - \frac{1}{3}\widetilde{g}_{kk}^2\delta_{ij} \tag{2.83}$$

where $C_w = 0.4929$ is a model constant and $\widetilde{g}_{ji}$ is the resolved velocity gradient. The model was developed to recover a correct scaling law in near wall regions for wall bounded flows.

Sigma model [Nicoud et al., 2011]

$$\nu_t = (C_\sigma \Delta)^2 \frac{\sigma_3(\sigma_1 - \sigma_2)(\sigma_2 - \sigma_3)}{\sigma_1^2} \tag{2.84}$$

where $C_\sigma = 1.5$ and $\sigma_1 \geq \sigma_2 \geq \sigma_3 \geq 0$ are the singular values of the resolved velocity gradient tensor.
This model, similar to the WALE model, recovers the proper y^3 damping scaling of eddy viscosity at walls. It has been developed for resolved boundary layers and is therefore very well adapted for wall-resolved LES ($y^+ < 5$), and less efficient in wall-modeled LES.

2.5 Combustion

Two main combustion modes exist:

- in premixed flames, the fuel and oxidizer are mixed before ignition.
- in diffusion flames, the fuel and oxidizer are injected separately, and burn along the stoichiometric line that establishes between the two streams.

In liquid rocket engines, flames burn mostly in the diffusion (or "non-premixed") regime, as a consequence of the high reactivity of fuels with oxygen. This indeed avoids premixing which could also lead to safety issues. Indeed even if premixed flames are usually more powerful than diffusion flames, their drawback is that in case of malfunctioning, the flame could be subjected to flashback, propagating back into the injectors and igniting the whole tank leading to spectacular explosions. Therefore only diffusion flames are described here, as they are at the heart of this work.
Note that only flame structure aspects are described here, the chemical features are treated in Chapter 4.

2.5.1 Laminar diffusion flames

Even if the vast majority of industrial applications, including rocket engines, work by burning in turbulent regime, it is useful to introduce the main properties of laminar diffusion flames which are helpful to understand, analyse and even model the turbulent flames.

As their name indicates, diffusion flames are mainly piloted by diffusion effects provided that chemistry is fast enough. Fuel and oxidizer (denoted afterwards by indices "f" and "o") diffuse towards each other and, after ignition, are separated by the reaction zone, situated along the stoichiometric line where the combustion products appear. The diffusion flame structure is sum up on Fig. 2.1.

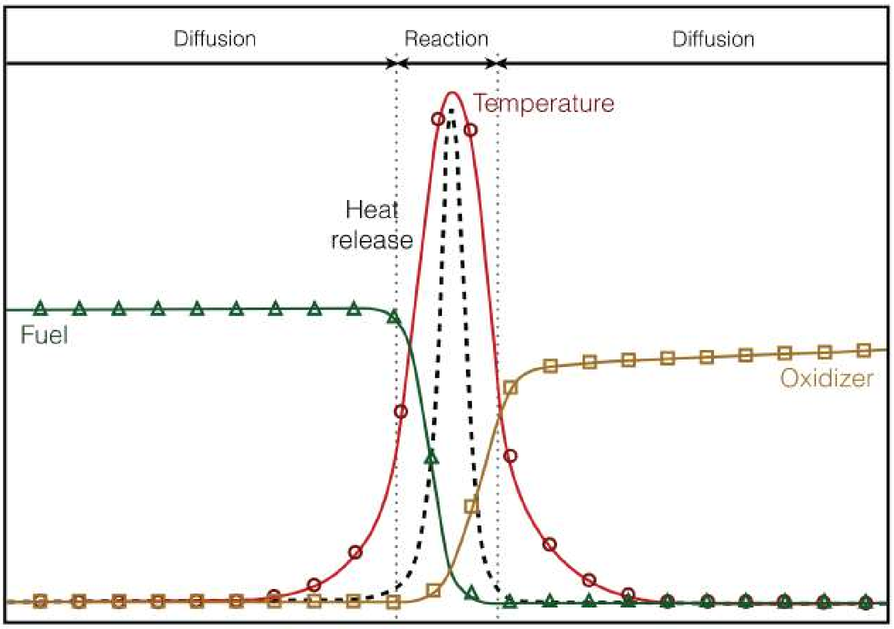

Figure 2.1: Schematic description of a laminar diffusion flame structure (from [Esclapez, 2015]).

Diffusion enhances the mixing process, leading to higher heat release rate. The mixing level is quantified by the scalar dissipation rate, expressed as the inverse of a time:

$$\chi = 2D(\nabla Z)^2 \tag{2.85}$$

where D is the mixture diffusion coefficient (under the unity Lewis number assumption) and Z is the mixture fraction. The definition of Bilger is used in this work [Bilger, 1989], as it is defined considering the atom mass fractions and not the species: it is therefore well adapted for complex chemistry, used in this work. Bilger defines:

$$\beta = \sum_{e=1}^{N_e} \gamma_e \sum_{k=1}^{N_s} N_{e,k} \frac{W_e Y_k}{W_k} \tag{2.86}$$

where $N_{e,k}$ is the number of elements e in species k and N_e is the number of element in the chemical system. γ_e represents the weights, with $\gamma_C = 2/W_c$, $\gamma_H = 1/(2W_H)$ and $\gamma_O = -1/W_O$, as defined by Bilger. β is then normalized:

$$Z = \frac{\beta - \beta_o}{\beta_f - \beta_o} \tag{2.87}$$

Thus, $Z = 1$ for pure fuel, $Z = 0$ for pure oxidizer, and in-between lies the stoichiometric mixture fraction Z_{st}, its value depending on the reactants. For example for methane oxy-combustion, studied in this work, $Z_{st} = 0.2$ (still under the unity Lewis assumption, which is used in Bilger's definition).

In strained diffusion flames, the scalar dissipation rate is related to the strain rate a with the relation [Poinsot and Veynante, 2012]:

$$\chi = \frac{a}{\pi}(-2[erf^{-1}(1-2Z)]^2) \tag{2.88}$$

where a is defined here as the local velocity gradient along the flame and erf the error function. Thanks to these definitions, some length scales are here useful to introduce:

- The diffusion layer thickness (δ_d) corresponds to the whole zone between pure fuel and pure oxidizer
- The thermal flame thickness (δ_{th}) corresponds to the zone where the temperature gradient changes rapidly
- The reaction zone thickness (δ_r) is defined where reactions occur and is located around the line Z_{st}. It is usually much smaller than δ_{th}

Due to their boundary conditions, diffusion flames always burn at stoichiometry. Note that complex chemistry and transport properties may stabilize the flame slightly aside the stoichiometric location. However it is useful to define a global equivalence ratio inside a burner ϕ_g, computed as [Poinsot and Veynante, 2012]:

$$\phi_g = sY_f/Y_o \tag{2.89}$$

where Y_f and Y_o are the fuel and oxidizer mixture fractions in the injections streams and s is the stoichiometric mixture ratio ($s = 4$ for methane oxy-combustion).

The flamelet formalism

Visualizing diffusion flames in the mixture fraction space is quite common and is widely used in the following work. Indeed a change of variables from the physical space x to the mixture fraction Z space leads to a simplified 1D formulation of the mass and energy equations, describing the flame in a framework decoupled from the transport phenomena induced by the flow, itself represented by the mixture fraction equation [Poinsot and Veynante, 2012]. This derivation requires some assumptions that are recalled here:

- Constant thermodynamic pressure and small Mach number.
- All the diffusion coefficients D_k of chemical species equal to D_{th}, *i.e.*, unity Lewis number for all species. The Fick's law, without velocity correction, is used for diffusion velocities.
- Equal and constant heat capacities $C_{p,k} = C_p$ of chemical species. In particular C_p is independent of temperature.

Note that these assumptions are rarely verified in a real flame. However they allow to study way more easily diffusion flames and to develop models for them.

After the variable change, the mass and energy equations in the mixture fraction space write respectively:

$$\rho \frac{\partial Y_k}{\partial t} = \dot{\omega}_k + \rho \mathcal{D} \left(\frac{\partial z}{\partial x_i} \frac{\partial z}{\partial x_i} \right) \frac{\partial^2 Y_k}{\partial z^2} = \dot{\omega}_k + \frac{1}{2} \rho \chi \frac{\partial^2 Y_k}{\partial z^2} \tag{2.90}$$

$$\rho \frac{\partial T}{\partial t} = \dot{\omega}_T + \frac{1}{2} \rho \chi \frac{\partial^2 T}{\partial z^2} \tag{2.91}$$

If combustion is fast enough, the flamelet unsteadiness in the Z-space may be neglected [Cuenot and Poinsot, 1994] and the above equations reduce to:

$$\dot{\omega}_k = -\tfrac{1}{2} \underbrace{\rho\chi}_{\text{mixing}} \underbrace{\frac{\partial^2 Y_k}{\partial Z^2}}_{\text{reaction}} \quad \text{and} \quad \dot{\omega}_T = -\tfrac{1}{2} \underbrace{\rho\chi}_{\text{mixing}} \underbrace{\frac{\partial^2 T}{\partial Z^2}}_{\text{reaction}} \tag{2.92}$$

The two expressions of Eq. 2.92 are largely used in the following work when using CANTERA and ARCANE in order to derive new reduced chemical schemes. Indeed even if the few assumptions are not true in a real context (and furthermore, in AVBP), they are considered acceptable when deriving the chemical scheme with diffusion flames (see Section 4.3.1 and C.). It is computationally very efficient to use such framework compared to resolving the equations in the physical space: solving a flame in the mixture fraction space requires less grid points than in the physical space due to the very thin flames. As many flame computations are required by the ARCANE process, typically a gain in computing time of a factor 5 to 100 is observed when using flamelet equations.

2.5.2 Turbulent diffusion flames

When the flow is turbulent, vortices interact with the flame and possibly alter combustion phenomena. The Damköhler number $Da = \tau_f/\tau_c$ which compares the flow and flame timescales, allows to evaluate the turbulence-flame interaction (TCI) in diffusion flames. Using the flamelet formulation, Da is expressed with $\tau_f \simeq 1/\chi_{st}$:

$$Da^{fl} = \frac{1}{\chi_{st}\tau_c} \tag{2.93}$$

For large Damköhler numbers, chemistry is very fast compared to the flow, while for small Damköhler numbers this is the contrary. This gives the possibility to classify the diffusion combustion regimes, as presented in Fig. 2.2.

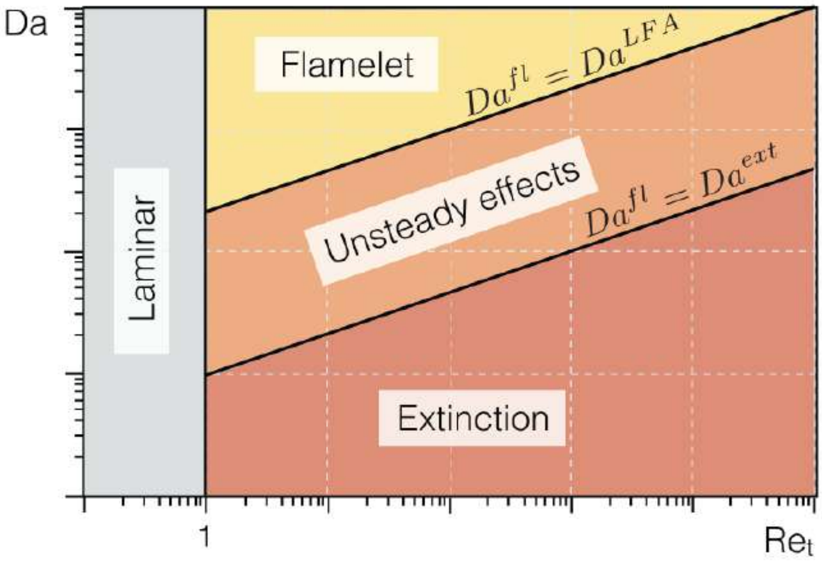

Figure 2.2: Diffusion flame regimes described as functions of the Damköhler number against the turbulent Reynolds number (from [Esclapez, 2015], adapted from [Cuenot and Poinsot, 1994]).

Depending on the flame Damköhler number Da^{fl}, the various encountered regimes are:

- Very high Da^{fl} numbers ($\tau_f >> \tau_c$) mean that the burning is not influenced by the flow. One talks then of the Laminar Flamelet Assumption ("LFA"), where all single flame elements can be assimilated to a laminar diffusion flame ($Da^{fl} > Da^{LFA}$).
- For moderate Da^{fl} numbers, the flow and chemical time scales are sufficiently close to allow direct interaction between turbulence and combustion, therefore unsteady effects appear.
- Low Da^{fl} numbers ($\tau_f << \tau_c$) mean that turbulence is very intense with high strain rates. Therefore the flame comes closer to extinction, occurring at $Da^{fl} = Da^{ext}$.

2.6 Numerics

The main aspects of the numerical framework of AVBP is described here. More details can be found in [Gicquel and Poinsot, 2011] and [Lamarque, 2007].
AVBP is a massively-parallel LES code made for the simulation of compressible reacting flows [Schönfeld and Rudgyard, 1999, Gicquel et al., 2011, Gourdain et al., 2009] developed by CERFACS. It solves the compressible Navier-Stokes equations explicitly on unstructured and hybrid grids. The code uses a Cell-Vertex Finite-Volume method (CVFV), meaning that the conservation relations are applied at the cell centers, whereas the solution data are stored at the grid nodes.

2.6.1 Numerical schemes

For explicit time integration, a 3rd order Runge-Kutta scheme is used. There is only one diffusion scheme used in this work, the 2Δ Galerkin operator (see [Lamarque, 2007]).

The main convective schemes available in AVBP are here described:

- The Lax-Wendroff (LW) scheme [Lax and Wendroff, 1960]
  It is a finite volume centered scheme using an explicit time integration with a single Runge-Kutta step. Being 2nd-order in time and space, it has the advantage of a moderate computational cost for satisfying accuracy. However, it is known to be overall too dissipative and dispersive. On the other hand, it allows to avoid the use of too much artificial viscosity (see below).
- Taylor Galerkin schemes (TTGC and TTG4A) schemes [Colin and Rudgyard, 2000]
  These schemes are 3rd order finite element centered schemes, which benefit of low dispersion and dissipation properties. TTG4A has also the particularity to dissipate high frequencies (generating wiggles, see below). They are therefore recommended in LES to get a more accurate solution, however their cost is more than twice the one of LW. Because of the long residence time and high computational cost of the 3D simulations in this work, the TTG schemes family was not used.

2.6.2 Artificial viscosity

Because the numerical schemes used in AVBP are spatially centered, they are prompt to create "wiggles", *i.e.*, point-to-point oscillations, in locations where strong gradients occur. To limit this effect, artificial viscosity can be added to the discretized equations, but must be used with caution to avoid altering too much the solution accuracy. Several models exist and two of them used in this work are presented here.

The Colin-ρu-species operator

This operator consists of two artificial viscosity terms: a 2nd order term that smoothes the gradients (bringing therefore artificial dissipation), and a 4th order hyperviscosity term to limit the wiggle amplitude. These terms are only applied where needed, and to do this, a sensor based on both the momentum and the species gradients is used.

Localized Artificial Diffusivity (LAD)

For real gas simulations the LAD is preferred because it has a sensor based on the density gradients, which can be very stiff in the cases presented in this thesis. The version used is the one presented in [Schmitt, 2020], based on the strategy of [Mathew et al., 2003]. It is very efficient to stabilize RG simulations, but can quickly results in over-diffusion if too much is applied.

Chapter 3

Liquid phase

The following work includes a simulation where liquid oxygen is present (subcritical regime), leading to two-phase flow ("TPF") simulations. In the subcritical regime, an interface is present between the gaseous and the liquid phases. There are several numerical strategies to describe this interface, like sharp-interface (Level-Set [Desjardins et al., 2008], Volume of Fluid [Hirt and Nichols, 1981] for example) or diffuse interface methods for which a recent work and wide review can be found in [Pelletier, 2019]. For the development of AVBP, many research efforts are currently devoted to the diffuse interface methods. However at the time of this work, these developments were not yet operational and their use for rocket engine simulations is left for future work. As a consequence, liquid injection and atomization is here described with phenomenological and empirical models, described in Section 7.2.2.

After atomization, a spray composed of very small droplets is formed. There are currently two ways to describe such spray in AVBP: the Eulerian and the Lagrangian approaches. The Eulerian approach considers a continuous description of the liquid statistical moments, while the Lagrangian formulation tracks discrete particle trajectories. The advantage of the Eulerian framework is that it leads to a very similar set of equations as for the gaseous phase, allowing to use the same numerical approach and sparing both computational cost and numerical difficulties. However its formulation complexity and associated computing cost increases drastically as soon as the spray is no more considered locally mono-disperse, *i.e.*, when the droplet size follows a non-Dirac distribution inside a grid cell.
In this work, the Lagrangian approach has been chosen as polydispersity is a key point and is easier and faster to handle with this formulation. Indeed the injection model, taken from [Potier, 2018] and fully described in Section 7.2.2, introduces a size distribution which was shown to have first order effects on the subsequent flame.
Therefore in this chapter, only the equations for the Lagrangian formalism are presented. In the following indices g and l indicate gaseous and liquid quantities, respectively.

3.1 Lagrangian formalism

In the Lagrangian formalism each particle represents one or several liquid droplets, subjected to mechanical forces and thermodynamic laws. In AVBP, some assumptions are made:

- The particles are considered spherical of diameter d_p, cannot be deformed, and are not subject to breakup.

- The only force applied by the gaseous flow on the droplets is drag. Gravity forces are neglected.
- The liquid spray is diluted: the liquid volume fraction $\alpha_l < 0.01$. It means also that interactions between particles are neglected (*e.g.* they do not collide).
- The temperature is uniform inside the droplets.
- The droplets are small compared to the mesh cells ("point source approximation").

Each particle p is described with a trajectory equation as formulated below, giving its position $x_{p,i}$, mass m_p, momentum $\rho_l u_{p,i}$ and temperature T_p at each instant t. Note that only single-component droplets are considered here, but that more complex modelling can take into account multi-component liquids (each particle being composed of several species).

$$\frac{dx_{p,i}}{dt} = u_{p,i} \tag{3.1}$$

$$\frac{d}{dt}(m_p u_{p,i}) = F_{p,i} \tag{3.2}$$

$$\frac{dm_p}{dt} = \Gamma_p = \dot{m}_p \tag{3.3}$$

$$\frac{d}{dt}(m_p C_{p,l} T_p) = \dot{Q}_p \tag{3.4}$$

where $C_{p,l}$ is the liquid specific heat, $F_{p,i}$ are the external forces, Γ_p the mass evaporation source term and $\dot{Q}_p$ the heat flux. These terms are described in the following section.

3.1.1 Droplet interactions with boundary conditions

The particles require specific rules at the boundary conditions. For inlet, they enter the domain with a given velocity and diameter. For outlets, they simply leave the computational domain. When droplets hit a wall, several physical phenomena can happen, known as droplet-wall interactions. The droplets can either bounce on the wall, splash on it (dividing the droplet into other smaller droplets), or create a liquid film on it [Frohn and Roth, 2000]. In this work, only elastic rebound on walls is considered (mass-conservative condition). Although other droplet-wall interaction behaviours may occur, there study is beyond the scope of the present work. It is expected anyway that a vast majority of droplets evaporate before reaching a wall and that their interactions with the wall surface does not impact significantly the result. This assumption will be verified *a posteriori* in the simulation.

3.2 Exchange between phases

The exchanges between the liquid and the gaseous phases are made via source terms which are applied in both sets of equations (gaseous and dispersed phases). To simplify the writing, only one direction is considered in the following.

3.2.1 Drag

The drag force represents the resistance opposed by the gas (of velocity u_g) on a droplet, and is expressed as a force obtained here by a simplification of the Basset-Boussinesq-Oseen equation [Clift et al., 1978]:

$$\frac{F_p}{m_p} = \frac{(u_g - u_p)}{\tau_p} \tag{3.5}$$

where τ_p is the relaxation time of the particle expressed as:

$$\tau_p = \frac{\tau_p'}{1 + 0.15\,\mathrm{Re}_p^{0.687}} \quad \text{with} \quad \tau_p' = \frac{\rho_l d_p^2}{18\mu_g} \tag{3.6}$$

with Re_p the Reynolds number of the particle:

$$\mathrm{Re}_p = \frac{|u_g - u_p|\, d_p}{\nu_g} \tag{3.7}$$

The effect of drag on the dispersed phase can be evaluated thanks to the Stokes number which compares the particle relaxation time to the flow time scale:

$$\mathrm{St} = \frac{\tau_p}{\tau_f} \tag{3.8}$$

with $\tau_f = L/u_g$, L being the characteristic length scale of the gaseous flow. When $St >> 1$ the particle is not influenced by the surrounding gaseous flow. On the contrary when $St << 1$, the flow dictates to the particle its trajectory and dynamics.

In this work the two-way coupling is applied, meaning that the droplet also opposes a resistance to the surrounding gas: this is valid for moderately dense sprays ($1e^{-6} < \alpha_l < 1e^{-3}$). For sake of conservativity, the exact opposite force of Eq. 3.5 is applied to the gas.

3.2.2 Evaporation

The evaporation process of a droplet leads to both mass and energy transfer to the gas. Several evaporation models are available in AVPB, among which the Spalding model [Spalding, 1953], where the gas and the droplet are considered at rest, and the Abramzon-Sirignano model [Abramzon and Sirignano, 1989], where a relative velocity is considered between the phases. Both are analytical models considering isolated spherical droplets of radius $r_p = d_p/2$ moving in a far-field defined at ∞. A uniform temperature is supposed inside the droplet, from its center to its surface ζ as sketched in Fig. 3.1.
Note that the use of the isolated droplet model is a strong assumption if the local liquid fraction is high, *i.e.* a dense zone. This will be checked in Chapter 7.

To find the source terms of mass and energy, spatial conservation equations for momentum, mass and enthalpy of a droplet are written:

$$\rho_g u_g r_p^2 = \text{ constant } = \frac{\dot{m}_p}{4\pi} \tag{3.9}$$

$$\rho_g u_g r_p^2 \frac{dY}{dr} = \frac{d}{dr}\left(r_p^2 \rho_g D \frac{dY}{dr}\right) \tag{3.10}$$

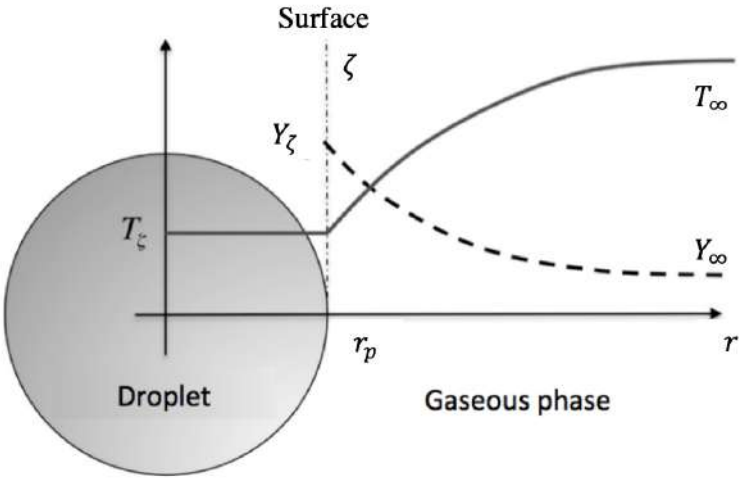

Figure 3.1: Radial profile of temperature T and mass fraction Y of the evaporated species around a droplet. Adapted from [Collin-Bastiani, 2019].

$$\rho_g u_g r_p^2 \frac{dC_{p,g}T}{dr} = \frac{d}{dr}\left(r_p^2 \frac{\lambda_g}{C_{p,g}} \frac{dC_{p,g}T}{dr}\right) \tag{3.11}$$

These equations do not make the point source approximation as they show a droplet-size dependency. However by combining them with Eq. 3.1 to Eq. 3.4, and integrating them leads to the droplet mass and heat source terms.

Mass transfer

Under quasi steady-state assumption, the mass transfer source term $\dot{\Gamma}_p$ from a liquid droplet p evaporating into gas is written:

$$\dot{\Gamma}_p = -\rho_l \alpha_l \, \pi d_p \, \mathrm{Sh} \, D \, \ln(1 + B_M) \tag{3.12}$$

where Sh is the Sherwood number, which represents the ratio between the mass transfer by convection and the transfer by diffusion. It is here convenient to use the correlation proposed by Ranz and Marshall [Ranz and Marshall, 1952] which considers the Reynolds number of the particle Re_p and the Schmidt number of the considered species:

$$\mathrm{Sh} = 2 + 0.55 \, \mathrm{Re}_p^{1/2} \, \mathrm{Sc}^{1/3} \tag{3.13}$$

B_M is the Spalding mass number which uses the vapor mixture fraction at the droplet surface ζ and in the far field ∞:

$$B_M = \frac{Y_\zeta - Y_\infty}{1 - Y_\zeta} \tag{3.14}$$

These mixture fractions are computed by solving Eq. 3.10. Under the point source assumption Y_∞ is simply the mixture fraction of the considered species in the gaseous control volume containing the droplet, and Y_ζ is computed as:

$$Y_\zeta = \frac{P_\zeta W_p}{P_\zeta W_p + (P_g - P_\zeta) W_g F_{corr}} \tag{3.15}$$

where P_ζ is the vapor pressure, P_g the pressure of the gaseous phase, W_p and W_g the molecular weight of the particle and the gas respectively and:

$$F_{corr} = \frac{1 - Y_{fuel}}{(1 - Y_{fuel})W_g/W_p} \tag{3.16}$$

Heat transfer

The heat transfer source term is calculated by integrating Eq. 3.11 in Eq. 3.4:

$$\dot{Q}_p = \dot{m}_p L_v\left(T_p\right) - 2\pi r_p \,\mathrm{Nu}\, \frac{\lambda_g}{C_{p,g}(T_p)} \left(C_{p,g}(T_p)T_p - C_{p,g}(T_\infty)T_\infty\right) \frac{\ln\left(B_T + 1\right)}{B_T} \tag{3.17}$$

where $L_v\left(T_p\right) = h_{s,g}\left(T_p\right) - h_{s,l}\left(T_p\right)$ is the latent heat of evaporation and $B_T = (1 + B_M)^{\frac{1}{Le}} - 1$ is the Spalding temperature number.

Again a correlation from Ranz and Marshall [Ranz and Marshall, 1952] is used to compute Nu:

$$\mathrm{Nu} = 2 + 0.55\,\mathrm{Re}_p^{1/2}\,\mathrm{Pr}^{1/3} \tag{3.18}$$

Note that in AVBP, there is a slight difference compared to the theory. The heat capacity is taken at a temperature $T_{ref} = (1/3)T_g + (2/3)T_p$. Therefore Eq. 3.17 becomes:

$$\begin{aligned} \dot{Q}_p &= \dot{m}_p L_v\left(T_p\right) - 2\pi r_p \,\mathrm{Nu}\, \frac{\lambda_{ref}}{C_{p,g}(T_{ref})} \left(C_{p,g}(T_{ref})T_p - C_{p,g}(T_{ref})T_\infty\right) \frac{\ln\left(B_T + 1\right)}{B_T} \\ &= \dot{m}_p L_v\left(T_p\right) - 2\pi r_p \,\mathrm{Nu}\, \lambda_{ref}(T_p - T_\infty)\frac{\ln\left(B_T + 1\right)}{B_T} \end{aligned} \tag{3.19}$$

Abramzon-Sirignano correction

Taking into account a non-zero relative velocity between the liquid droplet and the gas, Abramzon & Sirignano proposed modified Sherwood and Nusselt numbers:

$$\mathrm{Sh}^* = 2 + (\mathrm{Sh} - 2)/F_M \tag{3.20}$$

$$\mathrm{Nu}* = 2 + (\mathrm{Nu} - 2)/F_T \tag{3.21}$$

with

$$F_M = (1 + B_M)^{0.7} + \frac{\ln(1 + B_M)}{B_M} \tag{3.22}$$

$$F_T = (1 + B_T)^{0.7} + \frac{\ln(1 + B_T)}{B_T} \tag{3.23}$$

3.2.3 Characteristic evaporation time

Finally it is useful to introduce the characteristic evaporation time, usually computed as:

$$\tau_{ev} = \frac{\rho_l d_p^2}{8\rho_g D \ln\left(1 + B_M\right)} \tag{3.24}$$

where $D = \nu/Sc$ is the molecular diffusion coefficient and B_M the Spalding mass number. This characteristic evaporation time is to be compared to a characteristic residence time of the droplet, indicating therefore if the droplet has enough time to evaporate before reaching the flame for example.

3.3 Numerics

A full numerical description of the Lagrangian solver in AVBP can be found in [Martinez, 2009]. Some elements are here mentioned.

In order to interact with the gaseous fields, the dispersed phase equations must be brought back to the Eulerian grid, meaning a projection of the Lagrangian quantities on the Eulerian grid. Because of the two-way coupling (due to drag), the inverse is also necessary, *i.e.*, evaluating gaseous quantities at the droplet location. This is done through interpolations operators.

The interpolation of a quantity f from the gaseous field at the particles location is made through:

$$f_{g\to p} = \sum_{n\in X_C} I\left(x_{p,i}, x_{n,i}\right) \bar{f}_{g,n} \tag{3.25}$$

where n are the nodes contained in the vertex X_C of the cell C, and I is an interpolation function.

A source term S_p of a particle is interpolated on the Eulerian grid, giving S_n, as:

$$S_n = \frac{1}{V_n} \sum_{p\in\mathcal{D}_n} S_p \Theta^C_{n,p} \tag{3.26}$$

where V_n is the nodal volume, $\mathcal{D}_n$ the domain containing the particle p, and $\Theta^C_{n,p}$ the weights applied to each particle p. These weights are computed as the ratios of the inverse distances to the target node n and the sum of all inverse distances to the nodes m of the cell C in which the particle is located.

$$\Theta^C_{n,p} = \frac{1}{\left|x_{p,i} - x_{n,i}\right|} \sum_{m\in C} \frac{1}{\left|x_{p,i} - x_{m,i}\right|} \tag{3.27}$$

These operations are sum up by Fig. 3.2. Because the Eulerian and Lagrangian equations are coupled through these interpolation operations, it means that all the numerical methods introduced earlier (schemes, artificial viscosity...) are applied by taking into account the Lagrangian influence on the gaseous phase.

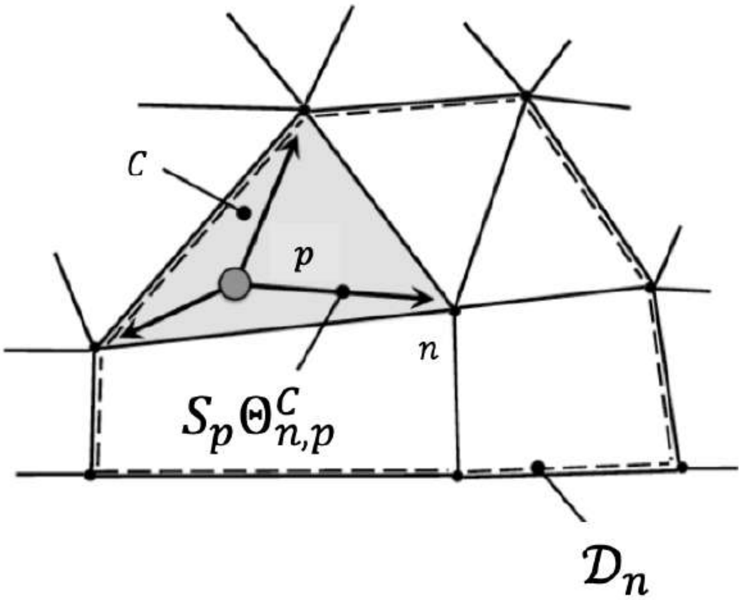

Figure 3.2: Distribution of the source terms generated by a Lagrangian particle p (located in the cell C highlighted in grey) to the Eulerian grid. Adapted from [Potier, 2018].

Part III

Model developments

Chapter 4

Turbulent combustion for methane oxy-combustion

This chapter is about several aspects needed to be studied for comprehension of methane oxy-combustion in Liquid Rocket Engines. After a reminder of chemical kinetics description in CFD in Section 4.1, emphasis is put on chemical aspects, by studying the specificity of this reactant couple in LRE conditions in Section 4.2, and chemical schemes are derived in consequence in Section 4.3. Then a new integration method is developed in order to reduce the computational cost in Section 4.4. A part is also dedicated to a preliminary analysis of the resulting flames computed on coarse grids, Section 4.5.

4.1 Description of chemistry in CFD

As seen in the previous chapters, reacting flows require to use a chemical scheme (or "kinetic scheme") in order to represent the chemical reactions (or "reactive paths") which convert the fuel and oxidizer into burnt gases. Chemical kinetics is the science of describing these chemical reactions and their rate constants. Large and complete chemical schemes, containing generally hundreds to thousands of species and reactions, are developed by specialized laboratories, usually with experimental means. Because of their huge size, such schemes can only be used in small numerical problems like 0D reactors or 1D flames. They are completely out of reach for 3D CFD simulations with the current available computational power: if directly integrated in the simulation, it is important to remind that each chemical species represents an additional differential equation to solve. It is therefore needed to simplify these detailed schemes, while keeping sufficient accuracy, and there are actually several ways to do so.

The most simple chemical models are composed of only few species (4 to 6 in general) involved in one or two reactions, and are called global schemes. Example for methane or kerosene combustion can be found in [Franzelli et al., 2010], and for oxy-fuel combustion in [Frassoldati et al., 2009]. These one-/two-steps schemes are designed to reach a good final equilibrium, known from prior equilibrium calculations performed with chemical codes like CHEMKIN or CANTERA, within the correct time scale thanks to tuned kinetic parameters. Another method is to pre-tabulate chemical solutions corresponding to flames or reactors, and parameterized with flow or scalar quantities which are computed in the CFD simulation. In the case of diffusion flames, the solutions are tabulated as functions of the mixture fraction and possibly the scalar dissipation rate. Such method allows a more detailed description of chemistry than global schemes, including pollutants, and can be combined with a probability density function (PDF) of the mixture fraction to describe turbulence-chemistry interaction (TCI). Presumed shape PDFs may be used, usually of the form of a β-PDF [Poinsot and Veynante, 2012]. Tabulated chemistry combined with a mixture fraction PDF applied to rocket combustion simulations were recently assessed in [Zips et al., 2019], where the capability of the method was shown in various conditions (adiabatic/non-adiabatic flamelets for example), as well as in [Ribert et al., 2017], where sub-grid scale contributions to the filtered equation of state was evaluated. A great advantage of such method is the computational cost reduction, as only the mixture fraction is calculated instead of all species mass fractions. If the infinitely fast chemistry assumption is made, the tabulated chemistry may be reduced to equilibrium, and the chemical source term in the species and energy equations is simply expressed as a relaxation toward equilibrium (IFCM model) [Schmitt, 2020]. Other techniques are available to build specific chemical schemes like the virtual chemistry [Cailler et al., 2017, Maio et al., 2017], where the principle is to set "fake" species with optimized thermodynamic properties and Arrhenius parameters in order to fit certain conditions (laminar flame speed, adiabatic flame temperature etc...) on a larger range of equivalence ratio than global schemes. Finally, the possibility of applying neural network to many scientific domains has been tested for chemical kinetics [Chen et al., 2000, Betelin et al., 2021].

Global chemistry and infinitely fast chemistry were the modeling techniques mostly used until recently in AVBP and other LES codes because they are computationally affordable, provide satisfactory results for the prediction of the heat release rate spatial distribution for example and quite easy to build. However, they lack precision when it comes to describe the true flame structure, the turbulence-chemistry interaction, or the flame-wall interactions. As LES is able to reach high accuracy in the prediction of unsteady turbulent flows, it is natural and useful to include realistic chemistry. To do so, and as the computational power rises each year, the tendency in LES is more and more to make use of Analytical Reduced Chemistry (ARC), which represents a good compromise between fully detailed and global chemistry.

An ARC is a reduced kinetic scheme derived from a detailed scheme, containing typically 10 to 50 species only. To reach this more affordable size, a reduction procedure is applied to the detailed scheme, keeping only the most relevant species and reactions. Furthermore, the remaining fastest species are treated with the Quasi-Steady State Approximation (QSSA), assuming them as steady [Lu and Law, 2006]. This brings the advantage to avoid a prohibitive simulation cost due to short-time species (typically radicals) inducing stiffness. This is particularly problematic for explicit time integration using time steps at the minimum of all characteristic times. Stiffness may be enhanced by the high temperature, pressure, and strain rate encountered in LRE flames.

Considering methane oxidation, the literature already provides some ARC schemes for methane combustion like [Sankaran et al., 2007], however with air as oxidizer and usually for pressure reaching no more than 20 bar. Therefore, they are not directly applicable to combustion with pure oxygen and at higher pressure levels. Furthermore, any fuel burns way faster with pure oxygen than air (the nitrogen contained in the air having an endothermic effect), leading to higher reaction rates. For these reasons a first objective is to derive ARC schemes adapted to the specific cases targeted in this work, and presented in Part IV.

4.2 Study of methane oxy-combustion in LRE conditions

Methane combustion in rocket engines is studied now more and more intensively as the following examples show.
The flame structures obtained for fuel burning with pure oxygen or air are different, and for methane it has been analysed both experimentally and numerically in [Joo et al., 2013] from 1 to 60 bar. The authors point out that the methane-oxygen flame exhibits a two-zones structure, also retrieved in this work as shown in Sections 4.3.1 and 6.3.2. Soot production is also impacted by oxy-combustion. Test rigs have been cited in the introduction (Section 1.4.1), and focus is made here on numerical works. In [Laurent et al., 2018] the effects of flame-wall interaction on the flame root stabilization mechanisms was studied in a doubly-transcritical LO2/LCH4 cryogenic flame. Thanks to a coupled conjugate heat transfer strategy the importance of using adiabatic or non-adiabatic wall condition at the injector lip was demonstrated. The flame response to acoustic modulation was studied in [Laurent et al., 2021] to evaluate the possible occurrence of thermo-acoustic instabilities. Other coupled simulations were carried out by [Maestro et al., 2019] and [Song and Sun, 2016], proving that using a coupled heat transfer framework (i.e. with a heat conduction solver in the solid parts), even if more costly, allows a better agreement with experimental data. Apart from combustion chambers, nozzle flows are also studied for example in [Zhukov, 2019] where frozen and reactive flows are compared to check the influence of kinetics in this zone of a rocket engine, showing a larger impact with methane than with hydrogen combustion. Numerical study of methane injection was also carried out by [Son et al., 2017], as well as experimentally with added acoustic pulsation in [Ge et al., 2019].

4.2.1 Kinetics

All the above behaviours strongly depend on methane oxy-combustion chemical kinetics at high pressure. From this point of view, flames in rocket engines can be characterized by two main aspects:

- High strain rate/scalar dissipation rate:
  The strain rate is a measure of the mixing speed between the propellants: the higher it is, the faster will be mixing and therefore combustion (*i.e.* high heat release rate). The limit to this phenomenon is reached when the combustion is not fast enough to consume all the reactants which are brought to the stoichiometric line, eventually leading to quenching. This is illustrated by Fig. 4.1:

  In practice, even if flames in LREs exhibit quite high strain rates due to the mass flow rates in the injectors, the propellants are so reactive that the extinction is not likely to happen.
  There are two main outcomes for a highly strained flame: as the heat release rate is high, the chemical stiffness is strong as well, which also means a thin flame, *i.e.*, a more demanding spatial resolution.

- High pressure:
  High pressure combustion has been a wide topic of study for many years and impacts several aspects of the process, like thermodynamics and transport [Foster and Miller, 2010], mixing [Oefelein and Yang, 1998], and kinetics [Carstensen and Dean, 2007]. Thermody-

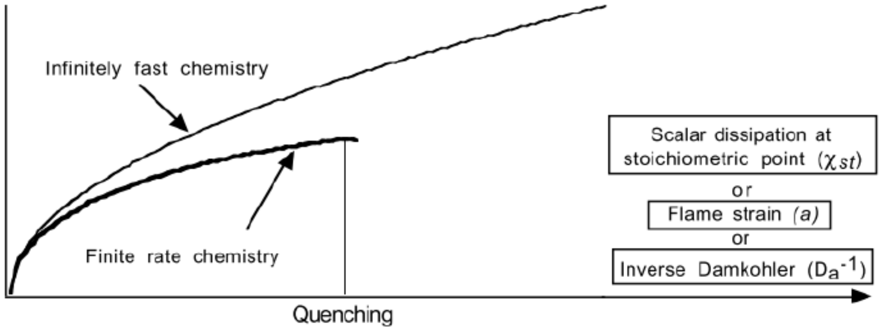

Figure 4.1: Integrated reaction rate as a function of strain rate, stoichiometric scalar dissipation rate or inverse of the Damköhler number for infinitely fast and finite rate chemistry (from [Poinsot and Veynante, 2012]). A square root relation is found between the quantities.

namics tell that if the pressure increases, the temperature does the same (in a constant volume). Therefore, recalling the Arrhenius form for the forward chemical rate constant:

$$K_j^f = A_j^f T^{\beta_j} exp(-\frac{E_j}{\mathcal{R}T}), \tag{4.1}$$

it is clear that a higher flame temperature leads to higher reaction rates, so are the chemical source terms. Numerically, this also means more stiffness.

More specifically, fall-off reactions are chemical reactions that are particularly dependant to pressure. They behave like three-body reactions at low pressure (a non-reactive collision partner brings the necessary energy to trigger the reaction), and as elementary reactions at high pressure. This happens because at high pressure, the concentration of all species are higher, therefore more species can act as a third body to trigger a reaction path. At lower pressure only collision partners are important. To describe the fall-off regime, a set of two rate constants k_0 and k_{inf} is used for respectively low and high pressure. The rate constant for the fall-off regime takes the following form, for reaction j:

$$K_j = K_{inf}\left(\frac{P_r}{P_r+1}\right)F(P_r,T) \tag{4.2}$$

where $P_r = k_0[M_j]/k_{inf}$ is the reduced pressure, $[M_j]$ the concentration of the collision partner, and $F(P_r,T)$ the fall-off function, described in CANTERA with the Troe formulation [Gilbert et al., 1983].

At first a study is proposed in order to identify which critical aspects must be taken into account when derivating a CH4/O2 ARC in given conditions. To do so, 0D reactors and 1D flame analysis are performed with CANTERA.
First a detailed kinetic scheme with the ability to describe methane oxy-combustion at high pressure must be chosen. The RAMEC mechanism [Petersen et al., 1999] was chosen because it was validated against experimental data of methane-oxygen flames in low-diluted shock tube experiments (aiming therefore ignition delay times) from 40 to 270 bar. Other mechanisms were as well considered such as the classic GRI3.0 [Smith et al., 1999], but it was not chosen because it was designed mainly for air as oxidizer. The FFCM-1 [Smith et al., 2016] could have

been a good candidate as it was validated against experiments of laminar flames up to 60 bar and shock tubes up to 86 bar, but was not known at the beginning of this work. Other possible schemes were those developed by the Technical School of Milan (POLIMI) like the POLIMI C1-C3 [Ranzi et al., 2014], but it is quite complex with many species (114) and reactions (1999), meaning very long calculation times of reduction steps.

It is to be noticed that in all the following, the RAMEC mechanism will be now taken as a reference (to derive ARCs mainly), even for 1D diffusion flames although it was experimentally not validated for such case. It is however considered as the best known reference for high pressure methane oxy-combustion. Indeed high pressure test rigs are complex and costly, and very few are found in the literature: [Mazas, 2010] drove experiments of premixed CH4/O2 flames, and recently other laboratories developed experimental facilities dedicated to methane-oxygen combustion [Meyer et al., 2017], [Tancin et al., 2019]. Currently the ICARE laboratory of Orléans is working with a high-pressure experiment (up to 100 bar) for methane-oxygen premixed flame speed measurements in order to validate detailed chemical schemes. The experimental test rig is presented in [Halter et al., 2020a] and its recent use can be found in [Halter et al., 2020b]. This will potentially improve detailed kinetics schemes for CH4/O2 combustion that could be used for future work.

4.2.2 Species selection

The number of species of an ARC is a first order parameter which drives its computational cost. The objective is to reach the smallest number of transported species. A first constraint is to guarantee the correct final equilibrium. Indeed, [Mari, 2015] demonstrated that oxy-combustion of methane is quite sensitive to the number of species used in the reduced mechanism and how, if they are not sufficient, the equilibrium state of the burnt gases is not at all retrieved compared to the detailed mechanism.

The test to identify the species required for the equilibrium is simply to remove species from the detailed scheme (RAMEC), and check the equilibrium obtained without these species. Three sets of species are considered here: the original RAMEC-orig, RAMEC-bis and RAMEC-ter. The two latter have less species, as sum up by Table 4.1:

RAMEC-orig	RAMEC-bis	RAMEC-ter
38 species	H2O CO CO2 CH4 H2 H O O2 OH	H2O CO CO2 CH4 H2 O2 OH

Table 4.1: Considered species for equilibrium study.

Basically RAMEC-ter is the RAMEC-bis without H and O atoms, so they contain respectively 9 and 7 species. Constant-pressure and constant-enthalpy equilibrium is computed for the conditions of Table 4.2, for which the mixture ratio is close to the simulated applications of the next chapters.

The results are presented in Table 4.3: the RAMEC-bis with 9 species allows to retrieve exactly the same equilibrium than the original RAMEC with its 38 species. Interestingly, the H and O are present in the final equilibrium. Despite their low mass fraction quantity (less than 0.5% in the final equilibrium), they actually play a major role. Otherwise, as shown by the computation with RAMEC-ter, the equilibrium temperature is overestimated of about 100K, and O2 and

Pressure	[bar]	100
YCH4	[-]	0.25
YO2	[-]	0.75
Mixture ratio	[-]	3.0
Initial temperature	[K]	300

Table 4.2: Conditions for equilibrium computations.

	RAMEC-orig	RAMEC-bis (9S)		RAMEC-ter (7S)	
	Value	Value	Error	Value	Error
$T\ [K]$	3604.42	3604.7	≈ 0%	3701.61	+2.69%
$\rho\ [kg/m^3]$	6.77	6.77	≈ 0%	6.67	-1.48%
$C_p\ [J/kg/m^3]$	2435.5	2435.5	≈ 0%	2440.1	+0.19%
$YH2$	0.0125941	0.0125923	≈ 0 %	0.0136639	+8.51%
YH	0.00132376	0.00132449	≈ 0%	-	-
YO	0.0045804	0.00458787	≈ 0%	-	-
$YO2$	0.0129675	0.0129918	≈ 0%	0.0167488	+28.92%
YOH	0.0401163	0.0401546	≈ 0%	0.0489535	+21.91%
$YH2O$	0.415795	0.41584	≈ 0%	0.41344	-0.58%
YCO	0.303412	0.303419	≈ 0%	0.312724	+3.07%
$YCO2$	0.209041	0.20909	≈ 0%	0.19447	-6.99%
$YCH4$	0.0	0.0	0%	0.0	0%
$YHO2$	0.000103732	-	-	-	-

Table 4.3: Comparison of equilibriums obtained with the different sets of species.

OH are largely overestimated. For these species it may seem not that crucial, however for CO2 the difference of about -7% may actually become important in particular for quantities such as heat fluxes.

This means that the ARCs to be derived must at least contain the species of RAMEC-bis, *i.e.* 9 species which are now identified: CH4, O2, H2O, CO, CO2, H2, OH, H, O. Note that although not shown here, this criterion is independent of pressure.

4.2.3 Pressure influence

Figure 4.2 shows the evolution of the maximum temperature and the integrated heat release rate for different pressure values. As expected, both rise as the pressure increases, following a square root law. Typical maximum temperature values of methane oxy-combustion are found between 3300 and 3800K for the considered pressure range.

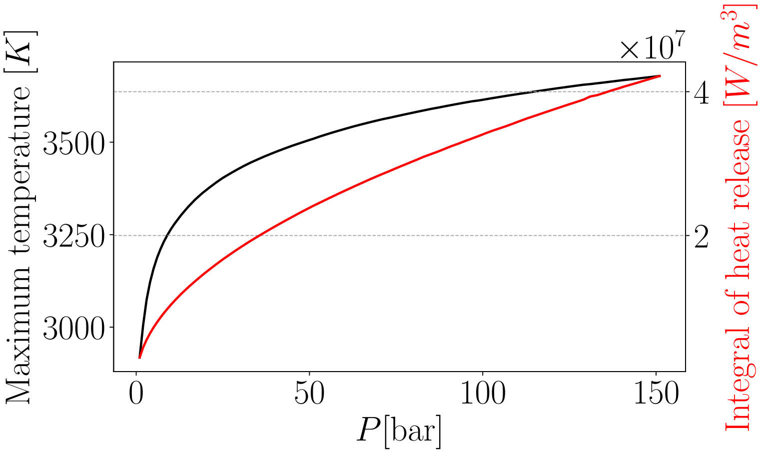

Figure 4.2: Evolution of maximum temperature and integrated heat release rate depending on pressure. $a_{mean} = 1312s^{-1}$.

Figure 4.3 shows the impact of increasing pressure on the main species contribution to the integrated heat release rate. Species that only have minor contributions are not presented here, therefore the shown species can be considered of primary importance for an ARC derivation. It can be observed that as the pressure is higher, H2O and CO2 are contributing less to the flame power, while it is the contrary for CO. Overall this means a loss of positive heat release (exothermic) which does not seem to be compensated by other species. Indeed at high pressure, the endothermic part of the flame takes a bigger importance, as it can be seen in Fig. 4.4: the endothermic peak is narrower for high pressures. Note also the shift of the main exothermic zone from $Z = 0.3$ to $Z = 0.27$, which could be driven by different reaction paths.

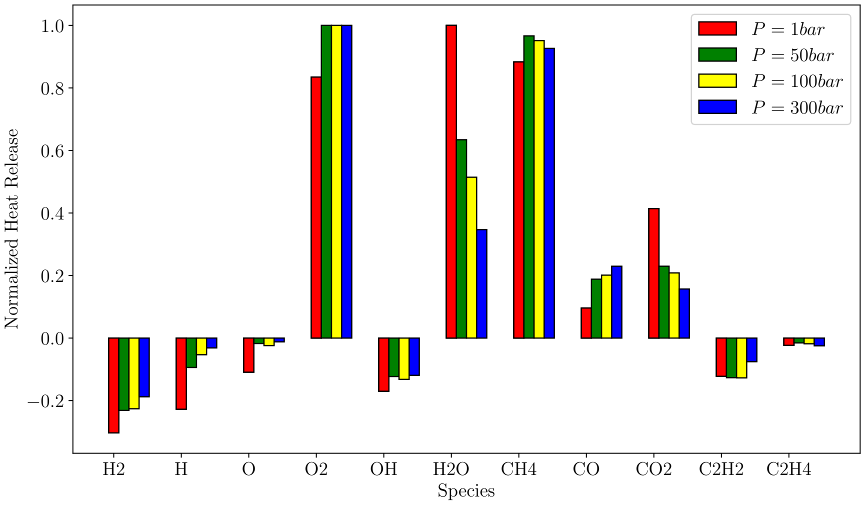

Figure 4.3: Species contribution to the integrated heat release rate in 1D counterflow diffusion flames for several pressure values. $\chi_{st} = 1000s^{-1}$.

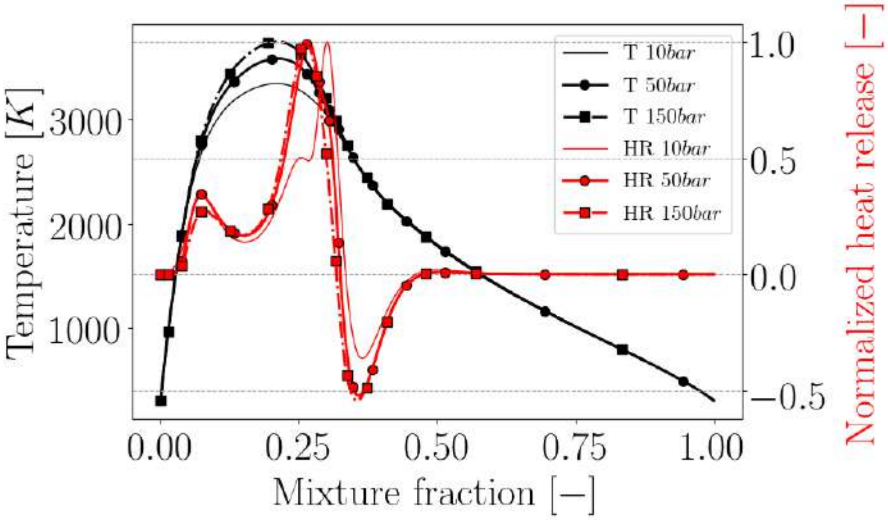

Figure 4.4: Flame structure (temperature and normalized heat release rate profiles) at various pressures. $\chi_{st} = 1000 s^{-1}$.

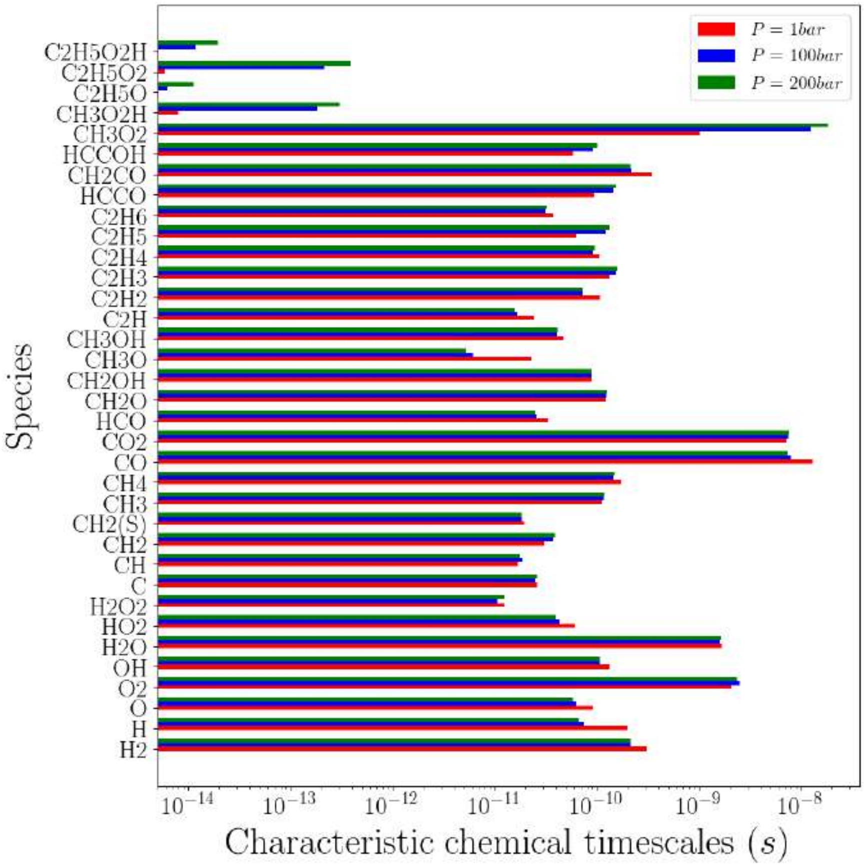

Figure 4.5: Evolution of characteristic species chemical timescales depending on pressure. $\chi_{st} = 1000 s^{-1}$.

Finally Fig. 4.5 exhibits the characteristic chemical time scales (computed with the inverse Jacobian analysis method, Eqs. 2.34 and 2.35) of the RAMEC scheme at 1, 100 and 200 bar.

Most of them lie between 10^{-11} and $10^{-8}s$. Interestingly the change of pressure does not affect significantly most of the species times, even though the majority of the species have a slightly diminished time scale at higher pressure. However for some of them it is the contrary, as a result of pressure-dependent reaction pathways. The difference is almost not anymore perceptible at 200 bar. It is to be noticed that a group of particularly stiff species is present, namely C2H5O2H, C2H5O2, CH3O2H: these must be absolutely removed during the ARC derivation to avoid too small time steps.

It is also possible to analyse reaction and species paths through graphics, as in Fig. 4.6 which shows the integrated paths through atom O that bring from the reactant O2 to the production of the main products H2O, CO and CO2. This graph clearly illustrates how the pressure increase changes the reaction paths leading to the production of H2O and CO2. At 100 bar, an important path involving HO2 is present, as shown on the right side of the figure (block "R"). On the other hand, going to high pressure can diminish the importance of chemical pathways as for example the path from O, then CH2O to H2O that goes below 10% at 100 bar (block "L"). This example shows how, when reducing a chemistry, the choice of the range of derivation will affect the result of reduction algorithm by keeping or not specific reaction paths.

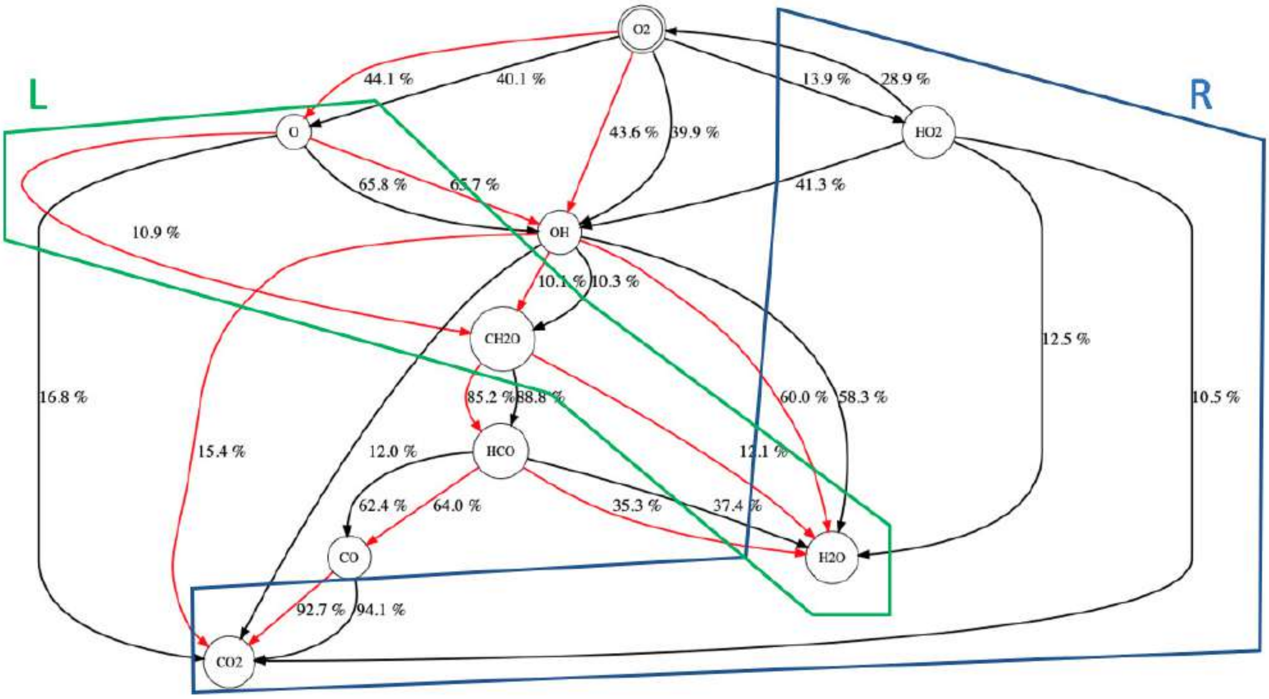

Figure 4.6: Integrated fluxes through atom O starting from O2 and leading to the production of H2O, CO and CO2, for 1 bar (red arrows) and 100 bar (black arrows). The values indicate the percentage of atom flux leaving a species. Fluxes under 10% are not shown for clarity.

4.2.4 Strain rate influence

Figure 4.7 shows that the maximum temperature decreases slightly with the scalar dissipation rate (equivalently the strain rate, see Eq. 2.88) at stoichiometry, while the integrated heat release rate increases as $\sqrt{a_{st}}$, *i.e.*, as predicted by theory.

On Fig. 4.8 showing the species contributions to the heat release, it is interesting to see the exact opposite behaviour compared to the pressure influence. Here when the scalar dissipation rate increases, the contribution to the flame heat release rate of H2O and CO2 increases, while it is the contrary for CO. Also as the global heat release increases, the part of exothermic reactions takes more importance. For extremely high values of χ_{st}, as presented in Fig. 4.9, it is interesting to notice that the endothermic zone completely disappears, as well as the minor exothermic peak around $Z = 0.1$. Actually the very high strain rate leads to a very thin flame in which the various peaks tend to merge.

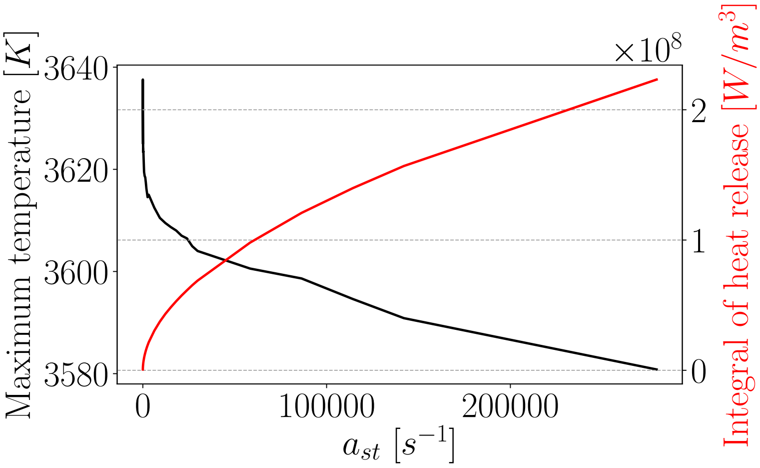

Figure 4.7: Evolution of maximum temperature and integrated heat release rate depending on the stoichiometric strain rate. $P = 100bar$.

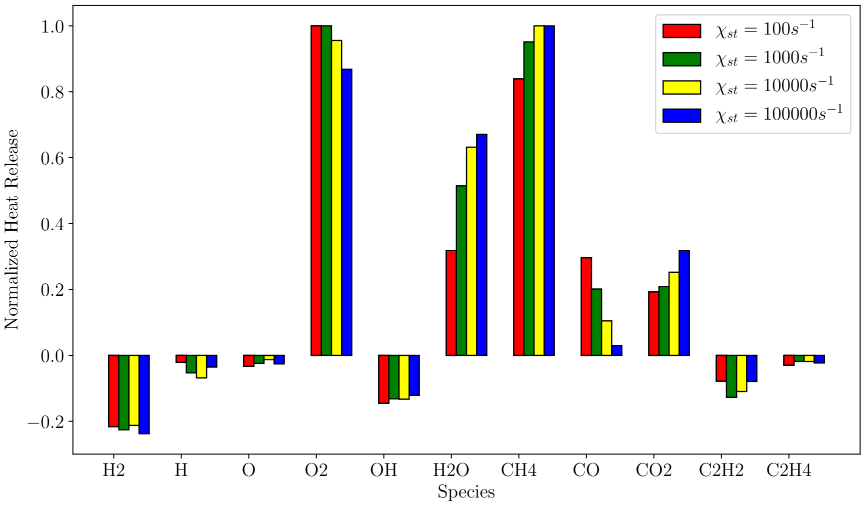

Figure 4.8: Species contribution to the integrated heat release rate in 1D counterflow diffusion flames for several scalar dissipation rate values. $P = 100bar$.

Concerning time scales, Fig. 4.10 shows that the increase of scalar dissipation rate changes almost nothing in the range 100 or 10000 s^{-1}. This is explained by the fact that as long as the flame remains controlled by diffusion, the kinetics are fast enough to consume the reactant fluxes and do not change much. For extreme values like 1000000 s^{-1}, chemistry starts to be a limiting process and differences of time scales appear, increasing for almost all species consistently with the slower chemistry.

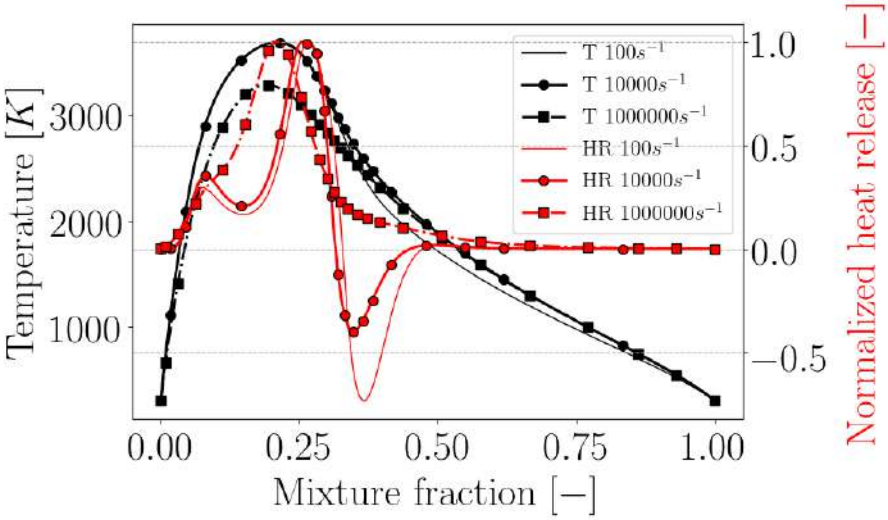

Figure 4.9: Flame structure (temperature and normalized heat release rate) for various scalar dissipation rated. $P = 100bar$.

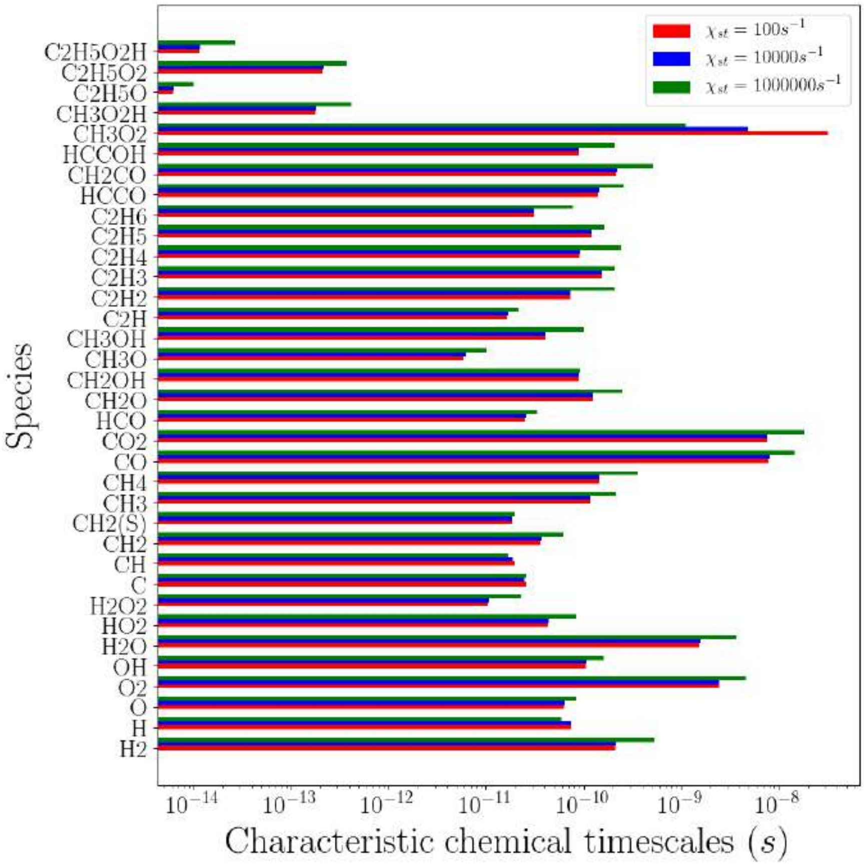

Figure 4.10: Evolution of characteristic species chemical timescales depending on scalar dissipation rate. $P = 100bar$.

4.3 Towards semi-complex chemistry

With this first analysis of CH4/O2 combustion in mind, two ARCs are derived and used in this thesis: one for the 54 bar five-injectors CONFORTH test bench (Chapter 6), another for the 20 bar single-injector TUM test bench (Chapter 7). The Section 4.3.1 contains the ARC mechanism derivation for the CONFORTH test bench, which is an extract from the paper *"Chemical modelling for methane oxy-combustion in Liquid Rocket Engines"* [Blanchard et al., 2022] published in *Acta Astronautica*. The derivation of the ARC mechanism for the TUM test bench is very similar and therefore can be found in Annex C..

4.3.1 Derivation of Analytical Reduced Chemistry for methane oxy-combustion

Methodology

Measurements of chemical kinetics in CH_4/O_2 flames at high pressure induce complexity and safety issues which make them rare, if not inexistant and there is no reference detailed scheme available for these conditions. Among the chemical schemes found in the literature, GRI3.0 [Smith et al., 1999], RAMEC [Petersen et al., 1999] and Slavinskaya [Slavinskaya et al., 2016] are good candidates. As RAMEC (38 species, 190 reactions), initially coming from the GRI1.2, was specifically made for methane oxy-combustion at high pressure by adding several reactions specific of such condition, and was validated against low-diluted CH_4/O_2 shock tubes experiments, it seems the most appropriate for the present study.

To target LRE conditions, the reduction is performed for pressure in the range $49 < P < 59\ bar$, *i.e.*, above the critical pressure of both propellants and sufficient to reach the supercritical combustion regime with injection temperatures of $280K$. Using diffusion flames as target flames, the range of strain rate a_{st} (or equivalently scalar dissipation rate χ_{st}, recalled in Eq. 4.3 [Poinsot and Veynante, 2012]) must be defined. It is here taken quite large, representative of conditions met in lab-scale LRE [Preclik et al., 2005, Ordonneau et al., 2016]: $100 < \chi_{st} < 1500 s^{-1}$. This corresponds to strain rates in the range $650 < a_{st} < 9500 s^{-1}$, of the same order of magnitude as in [Maestro et al., 2019].

$$\chi_{st} = 2D \left(\frac{\partial Z}{\partial x} \right)^2_{st} \tag{4.3}$$

In the equation 4.3, D is the diffusion coefficient of methane and Z the mixture fraction with Bilger's definition [Bilger, 1989].

The chemistry reduction process goes through several steps which are realized within an automatic algorithm implemented in the numerical platform ARCANE [Cazères et al., 2021]. First, Direct Relation Graph with Error Propagation (DRGEP) is performed several times on the detailed mechanism to keep only the most relevant species and reactions. Chemical lumping is then applied to remove the isomeric molecules. Finally, a Level Of Importance (LOI) criterion is applied on the remaining species to select the ones to be treated with the QSSA. An overview of these methods are described in [Cazères et al., 2021, Løvås, 2012].

The primary target flame property used to control the reduction process is the total heat release rate, with a maximum tolerance of 5%. This quantity, linked to the consumption speed,

is indeed the first property to preserve as, similarly to premixed flames, it controls the flame stabilisation and flame length which are used for engine design.
With these constraints, a reduced mechanism with 14 transported species, 4 QSS species (listed in Table 4.4) and 68 reactions was obtained with ARCANE.

Transported	QSS
H_2 H O O_2 OH H_2O HO_2	HCO CH_2O
CH_3 CH_4 CO CO_2	C_2H_3 C_2H_5
C_2H_2 C_2H_4 C_2H_6	

Table 4.4: Species contained in the derived ARC mechanism for high pressure methane oxy-combustion.

Validation

The ARC scheme is validated on laminar diffusion flames (computed with CANTERA [Goodwin et al., 2017]) in the target conditions that are solved following the steady flamelet equations for mass and temperature, recalled here [Poinsot and Veynante, 2012]:

$$\dot{\omega}_k = -\tfrac{1}{2}\rho\chi\tfrac{\partial^2 Y_k}{\partial Z^2} \text{ and } \dot{\omega}_T = -\tfrac{1}{2}\rho\chi\tfrac{\partial^2 T}{\partial Z^2} \tag{4.4}$$

where $\dot{\omega}_k$ is the chemical source term of species k and $\dot{\omega}_T$ is the energy source term. Overall five test cases are considered to cover all the range of values of P and χ_{st}. The obtained relative errors, shown in Tab. 4.5, never exceed 0.83% for the maximum temperature and 1.62% for the total (integral) heat release rate, indicating a very good agreement with the RAMEC detailed mechanism.

Case	Conditions	T_{max}	$\int \dot{\omega}_T$
A	49 bar, $\chi_{st} = 100s^{-1}$	-0.75%	+1.29%
B	49 bar, $\chi_{st} = 1500s^{-1}$	-0.83%	+1.62%
C	54 bar, $\chi_{st} = 1000s^{-1}$	-0.80%	+1.36%
D	59 bar, $\chi_{st} = 100s^{-1}$	-0.77%	+1.55%
E	59 bar, $\chi_{st} = 1500s^{-1}$	-0.83%	+1.50%

Table 4.5: Validation cases: relative errors of the ARC scheme compared to the RAMEC detailed mechanism, on the maximum temperature (T_{max}) and the total heat release rate ($\int \dot{\omega}_T$).

Cases A and E are illustrated on Figs. 4.11 and 4.12 respectively. In both cases an excellent agreement is observed for the temperature and heat release rate profiles. With a limited number of species and reactions, even the complex flame structure typical of the LRE conditions is retrieved. This also means that the intermediate species profiles are globally well retrieved, as shown Fig. 4.13. Slight deviation is observed on the heat release rate profile for case E but without significant impact on the integral of heat release rate.
Figure 4.14 shows the response of ARC flames to strain. Even if derived over a limited range of χ_{st}, the ARC exhibits a very good agreement with the RAMEC over a larger range: below $\chi_{st} = 20000s^{-1}$, the error keeps lower than 2.5% on maximum temperature, and lower than 2% on the total heat release rate. It never exceeds 5% on the latter quantity until extinction.

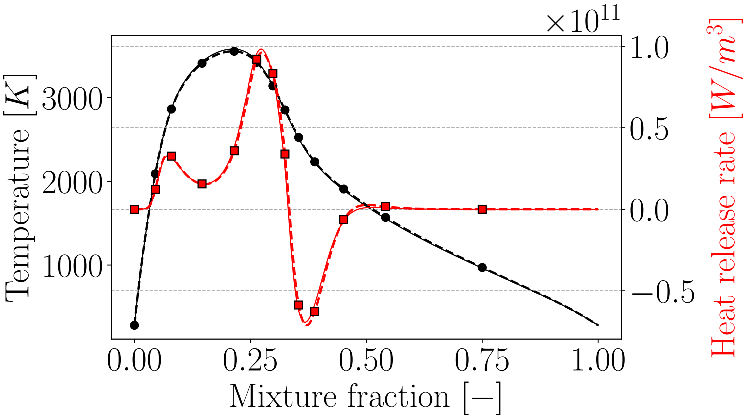

Figure 4.11: 1D strained diffusion flame: evolution with mixture fraction of the temperature (black) and the heat release rate (red). Thick lines: RAMEC. Dashed lines with markers: ARC. Case A: $P = 49bar$, $\chi_{st} = 100s^{-1}$.

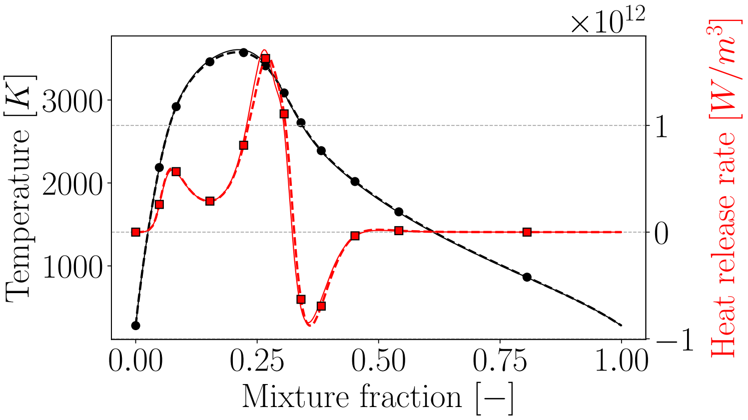

Figure 4.12: 1D strained diffusion flame: evolution with mixture fraction of the temperature (black) and the heat release rate (red). Thick lines: RAMEC. Dashed lines with markers: ARC. Case E: $P = 59bar$, $\chi_{st} = 1500s^{-1}$.

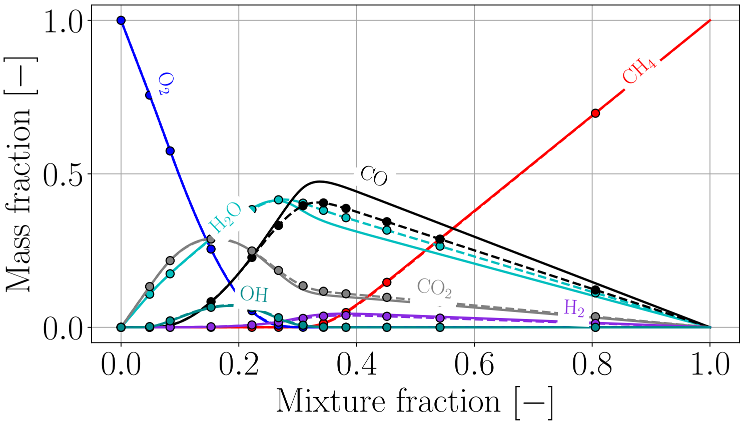

Figure 4.13: 1D strained diffusion flame: evolution with mixture fraction of the main species. Thick lines: RAMEC. Dashed lines with markers: ARC. Case C: $P = 54bar$, $\chi_{st} = 1000s^{-1}$.

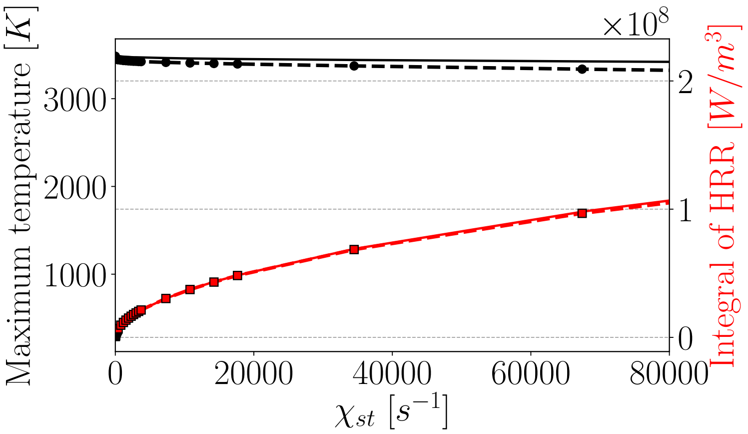

Figure 4.14: Evolution with scalar dissipation rate of the maximum temperature (black) and the total heat release rate (red) at $P = 54bar$. Thick lines: RAMEC. Dashed lines with markers: ARC.

Finally Fig. 4.15 shows the evolution with P of the same quantities over the whole pressure range for which it was derived. The ARC mechanism reproduces well the increase with P of both quantities in excellent agreement with the RAMEC detailed scheme. Only a slightly lower maximum temperature ($\approx$ -1.0%) and very similar total heat release rate ($\approx$ -2.0%) are observed for all pressures.

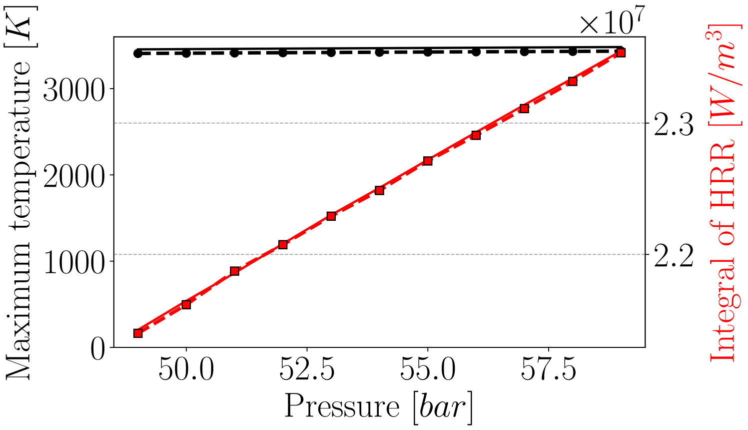

Figure 4.15: Evolution with pressure of the maximum temperature (black) and the total heat release rate (red) at $\chi_{st} = 1000s^{-1}$. Thick lines: RAMEC. Dashed lines with markers: ARC.

The reduced chemistry has been validated in the case of laminar flames, although its final use is for turbulent flows (Chapter 6). Note that turbulence modifies combustion processes via mixing only, and does not affect chemistry. Of course it could happen that this reduction procedure ignores some chemical phenomena which may occur due to turbulent mixing, leading to reacting mixtures of fresh gas with burnt gas and intermediate species that are not encountered in the 0D and 1D cases. These chemical processes are however assumed negligible and are indeed not represented in most turbulent combustion models, such as flamelet-based approaches for example. Moreover, these processes are much sensitive to the turbulent flow and ensuring to describe them in all cases with the same ARC scheme would be impossible.

4.3.2 Discussion

The target cases chosen to derive the ARC have been only chosen as 1D diffusion flames, as rocket engines mostly work in pure diffusion combustion regime. This is different from many ARCs found in the literature which were mainly derived with 1D premixed flames as references. In practice in chemistry codes like CANTERA, it was observed that diffusion flames are generally more complicated to converge, but it is worth the effort for the present case of LRE flames. It also has the advantage of directly taking into account the whole range of mixture ratio in one flame, as the mixture ratio of diffusion flames spans from zero in the oxidizer side to infinite in the fuel side. Thus, the ARCs derived in this work are very likely to be valid for premixed flames, and this is one of the known advantage of ARCs [Felden, 2013, Cazères, 2021].

Similarly the choice of the derivation range (pressure and scalar dissipation rate) was made to target the operating point of the application. Concerning pressure, the range of + or - 10% around the target operating point of the test bench seems quite obvious, taking into account potential mean pressure deviation of small acoustic instabilities. Concerning the scalar dissipation rate, the range of $100 - 1500 s^{-1}$ first coincides with previous AVBP computations in the same type of cases [Maestro et al., 2019], but also comes from early computation of the target CONFORTH configuration where χ_{st} was found mostly within this range. Actually, in LES the scalar dissipation may reach much higher values (typically $5000 - 10000 s^{-1}$). Extending the range of scalar dissipation rate to higher values for the reduction procedure leads to less transported species in the ARC, but at the cost of decreased accuracy at lower χ_{st}. As low values are found far more probable along the turbulent flame, the chemistry reduction focuses on this range. Finally, in order to guarantee a correct equilibrium state, the necessary 9 species identified in the analysis of equilibrium with RAMEC, presented in Section 4.2.2, were the primary target during the reduction process.
Note also that the perfect gas equation of state has been used during the reduction process. There are two reasons for that. The first one is about the code itself: at the time when it was performed, CANTERA could only solve 1D problems with the perfect gas EoS. Some cubic EoS were available but only for 0D problems (auto-ignition...). Secondly, the use of a real gas framework means that some more properties must be added to the species, namely their coefficients a, b, ω described in Section 2.1.2. If they are known for the main species, many others (mainly radicals, atoms) were not found, for example in the NIST database. It is possible that the real gas properties of short-times existence molecules are difficult to get or verify experimentally. Despite this, it is very likely that the reduction process would have been the same anyway the EoS used, because most of the chemical processes under consideration happen at high temperatures, and therefore quite far from conditions where a real gas EoS would have been needed (typically at cryogenic temperatures).

The tolerance on the error of integral of heat release rate is actually lower than 5%. In fact, as the derivation of the ARC is split in several consecutive steps, it allows to adapt the error tolerance of all values at each step. The choice of these tolerances is quite empirical and is made to reach a satisfying number of species while keeping a reliable ARC. At the end the maximum error on the integral heat release rate was set to 2% for the species removal step, 0.5% for the reaction removal step, 2% for the lumping step and 5% for the QSSA step, explaining finally the maximum 5% error presented in the paper. The 0.5% error for the reaction removal step explains why the final ARC still has a quite large number of reactions compared to its parent mechanism, the RAMEC. This is however not a problem for the simulations in which the main part of the computational cost comes from the number of transported species while the number of reactions involving simple algebraic operations, are not critical. Note that experience has shown that these error thresholds have more influence on the final number or species and reactions than the range of derivation.

4.4 Accelerating chemistry integration

In rocket engines as in many combustion devices, the flow time scales (convection, diffusion) are generally much higher than the chemical time scales: this is what makes the chemical process *stiff* compared to the other physical phenomena. In an *explicit* time integration framework as in AVBP, numerical stability imposes to use a time step corresponding to the fastest phenomenon, *i.e.*, with the smallest timescale. In the precise case of chemistry, a time-explicit computation with a too large time step can lead to non-positive mass fractions as was already observed in AVBP, and also mentioned in [He et al., 2011] for example.

Even if most of the stiffness induced by chemistry is removed in ARCs thanks to the QSSA, some may remain and increases the LES computational cost. This can be the case when for example the fuel or oxidizer themselves are sources of stiffness, or if other minor stiff species could not be removed or treated as QSS during the ARC derivation process. This may be reinforced by high pressure and strain rate, which both increase the reaction rates. Early tests using the ARC derived in Section 4.3.1 showed that the integration of chemistry accounts for up to 50% of the total simulation time.

Implicit time integration methods are a solution to leverage this timescale constraint in numerical simulations and are often used to solve stiff problems. The general difference between explicit an implicit integration is recalled below.

For an Ordinary Differential Equation (ODE) $\partial y / \partial t = \phi(y)$, explicit integration consists in computing the solution y at the next time step $t + \Delta t$ from the current value at instant t only, in the form:

$$y(t + \Delta t) = \phi(y(t))\Delta t + y(t) \tag{4.5}$$

for 1^{st} order time integration. Typically, if Δt is chosen too large, this inevitably leads to an unstable or at least non-physical solution, and possibly a simulation failure.
An implicit integration makes use of the solution at both the current instant $y(t)$ and the next instant $y(t + \Delta t)$ to compute the solution at $t + \Delta t$ by solving the ODE as:

$$y(t + \Delta t) = \phi(y(t + \Delta t))\Delta t + y(t) \tag{4.6}$$

By construction implicit methods are stable for large time steps, whatever the characteristic time scale of the studied phenomenon, which drastically decreases the number of iterations needed to converge a simulation. However one iteration with implicit integration is much more demanding in computational time than one iteration with explicit integration, so that at the end the gain depends on the time step ratio between the two methods. It is usually concluded that if the full implicit integration of chemistry is worth in implicit incompressible (or low-Mach) flow solvers, the gain in time step is not enough compared to the cost of implicit integration in explicit compressible flow solvers which run with already very small time steps.

In addition, even if numerically stable it is not recommended to increase too much the implicit time step above the characteristic chemical time scales in order to keep a correct description of the unsteady behavior of the system.

The problem of dealing with stiff chemical source terms is not new in the literature. An overview can be found in [Kee et al., 1985], where the authors introduce the main stakes and techniques to solve stiff ODEs. For recent work on implicit solvers one can cite [Savard et al., 2015] where the authors compute premixed and non-premixed turbulent flames with semi-implicit preconditioning of chemistry, or [Wasserman, 2018] using implicit methods in a RANS framework.

As AVBP is an explicit compressible code, the full implicit integration of chemistry is not efficient. However some species of ARC schemes still have a too short time scale compared to the flow time scale, imposing a significant decrease of the simulation time step. To avoid this, a common technique is to use a "semi-implicit" integration for these few stiff species, as for example in [Felden, 2013] where this method is applied to H2O. This technique (ODEPIM) is also found in [Yang et al., 2017] where it was applied to a chemical scheme, reduced on-the-fly using a criterion based on both thermodynamic variables and species mass fractions, allowing to accelerate DNS of turbulent premixed flames. In the present work, a novel approach called "exponential chemistry" is proposed to integrate the chemical source terms, based on an analytical guess of the solution at time $t + \Delta t$. It can be therefore assimilated to an implicit method for chemistry integration, allowing to recover the compressible flow time step of the explicit compressible LES. In addition the method improves the quality of the solution at low temporal resolution. Its principle and applications are described in the Section 4.4.1, which is another extract from [Blanchard et al., 2022], with a few modifications to better fit in this manuscript.

4.4.1 The exponential integration

In Section 4.3.1, although the strongest stiffness has been removed thanks to the QSSA applied to the fastest radicals, very small chemical time scales remain as methane oxy-combustion at high pressure is a very fast oxidation process. Explicit time integration then requires a time step at least of the order of the shortest chemical time step Δt_{chem}, calculated in the simulations as:

$$\Delta t_{chem} = min\left(\frac{\rho Y_k}{\dot{\omega}_k}\right), \tag{4.7}$$

with $\dot{\omega}_k$ the source term of the species k and ρ the mixture density. The ARC scheme presented in the previous sections leads to a integration time step of the order of 1×10^{-10}s due mainly to the radicals (detailed in Fig. 4.17), which may therefore considerably increase the computing time. This time step is to be compared to the flow time step Δt_{CFL}, imposed by the CFL number (fixed at 0.7) as:

$$\Delta t_{CFL} = \frac{\Delta x \, CFL}{u + u_a}, \tag{4.8}$$

with u the flow velocity, u_a the acoustic velocity and Δx the characteristic mesh size. With typical mesh sizes used in 3D LES of LRE, Δt_{CFL} is found of the order of 5×10^{-9}s. As a consequence, the use of ARC in reactive simulations leads to a decrease of the time step typically by a factor 50, which directly impacts the computational cost: explicit computation of the chemical source term is usually one of the most expensive part in a LES code.

With the ultimate goal to run the reactive simulations with the CFL time step, a new time integration method for the chemistry is proposed here. The idea is to take advantage of the simple form of elementary reactions composing the ARC scheme to make an analytical integration of the source terms over the time step. This leads to a time evolution of the concentrations in the form of an exponential function, hence the name of "exponential method", and allows to substantially increase the time step.

Principle of the exponential integration

For all what follows, one only considers mass quantities (for source terms, concentrations, etc...). Consider a species k which is produced and consumed only by elementary first order irreversible chemical reactions. Its total source term $\dot{\omega}_k$ may be recast in the form:

$$\frac{\partial c_k}{\partial t} = \dot{\omega}_k = A_k c_k + B_k, \tag{4.9}$$

with c_k the concentration of the species k. The functions $A_k c_k$ and B_k are the sum of the contributions to destruction and creation respectively, of the reactions j involving species k:

$$\begin{aligned} A_k c_k &= \sum_{j=1}^{M} \nu'_{kj} \dot{r}_j \\ B_k &= \sum_{j=1}^{M} \nu''_{kj} \dot{r}_j \end{aligned} \tag{4.10}$$

where ν'_{kj}, ν''_{kj} are the stoichiometric coefficients of species k in reaction j and $\dot{r}_j$ the reaction rate.
Assuming A_k^n and B_k^n constant during iteration n, the integration of Eq. 4.9 is easily found to give at time iteration $n+1$:

$$c_k^{n+1} = \left(c_k^n + \frac{B_k^n}{A_k^n} \right) e^{A_k^n \Delta t} - \frac{B_k^n}{A_k^n} = \frac{B_k^n}{A_k^n} \left(e^{A_k^n \Delta t} - 1 \right) + c_k^n e^{A_k^n \Delta t} \tag{4.11}$$

where Δt is the time step of the iteration. The obtained solution is correct as long as the assumption of constant A_k^n and B_k^n in the time step stays valid. This introduces a new time step limit, still much higher than the chemical time step, as will be seen in the next sections.

For very small values of A_k^n, i.e., species creation only or non-reacting zone, in order to avoid numerical error, Eq. 4.11 is rewritten with the second order approximation as:

$$c_k^{n+1} = B_k^n \left(\Delta t + \frac{A_k^n \Delta t^2}{2} \right) + c_k^n \tag{4.12}$$

The value c_k^{n+1} can then be used to evaluate the source term to be integrated in the equation of transport of c_k as:

$$\dot{\omega}_k = \frac{c_k^{n+1} - c_k^n}{\Delta t} \tag{4.13}$$

Note that the expression for c_k in Eq. 4.11 is always positive (provided c_k^0 is positive), so that the approach guarantees positivity of all concentrations. Notice also that this expression exactly holds for first order species only. For second order species, the analytical integration of the source term is still possible but is more complex. As only few reactions involve second order species (10 over 136 in the previously derived ARC), the impact of using first order solution for them is considered negligible and Eq. 4.11 is still taken as a good approximation.

The calculation of the source term as in Eq. 4.13 does not guarantee atom conservation, which must be then enforced in a second step. The principle is to correct at each iteration and at each grid point the error on the total mass of each element, by modifying accordingly the local concentrations at iteration $n+1$. To minimize the impact of this correction, it is made on the species of largest concentration. In methane-oxygen flames, three elements are present (H, O, C) and it is chosen to distribute the associated mass corrections among only three species having locally the highest concentration (identified as c_{k_1} to c_{k_3} below).
The mass excess/loss is computed for each element e between iteration n and $n+1$ as:

$$dm_e = \sum_{k=1}^{N_s} (c_k^{n+1} - c_k^n) N_{e,k} \tag{4.14}$$

where $N_{e,k}$ is the number of element e in species k, and N_s the number of species in the chemical system. Then the corrections $c_{k_e}^{corr}$ of species k_e are calculated by solving the linear system:

$$\begin{pmatrix} n_{H,k_1} & n_{H,k_2} & n_{H,k_3} \\ n_{O,k_1} & n_{O,k_2} & n_{O,k_3} \\ n_{C,k_1} & n_{C,k_2} & n_{C,k_3} \end{pmatrix} \times \begin{pmatrix} c_{k_1}^{corr} \\ c_{k_2}^{corr} \\ c_{k_3}^{corr} \end{pmatrix} = \begin{pmatrix} -dm_1 \\ -dm_2 \\ -dm_3 \end{pmatrix} \tag{4.15}$$

The corrections c^{corr,k_e} are then used to update the source term in Eq. 4.13. The linear system may be solved with a simple Gaussian elimination process for example.

The exponential integration algorithm can be summarized as follows:
1 - Compute c_k^{n+1} with Eq. 4.11 or Eq. 4.12, where A_k^n, B_k^n use the standard Arrhenius reaction rates.
2 - Compute element mass error dm_e.
3 - Compute concentration corrections c_k^{corr}, for as many species as elements in the chemical system.
4 - Compute the source terms as:

$$\dot{\omega}_k = \frac{c_k^{n+1} + c_k^{corr} - c_k^n}{\Delta t} \tag{4.16}$$

Validation in laminar counterflow diffusion flame

The ARC scheme for methane-oxygen combustion of Section 4.3.1, combined with the exponential time integration method is applied here to a laminar 2D counterflow diffusion flame, now computed with the CFD solver AVBP. A second order in time and space Lax-Wendroff scheme [Lax and Wendroff, 1960] is used. The perfect gas equations of state is used. The power-law function is utilized for the molecular viscosity, and constant Schmidt and Prandtl numbers are used for species molecular diffusion and thermal conductivity. The conservation equations for mass, momentum, energy and species were already presented (Eqs. 2.57 to 2.60). For the following laminar flame computations, all the sub-grid scale terms are zero.

The opposed jets configuration is set with mass flow rates leading to equal momentum at both sides in order to get the stagnation plane at the center of the domain, where the mesh is the most refined. A small distance ($H = 1mm$) between both injectors is used to obtain a strain rate in the range of the derived ARC while keeping the flow laminar. With this setup, the targeted mean strain rate is, with $u_F = 0.54$ and $u_O = 0.27m/s$ the fuel and oxidizer velocities respectively:

$$a_{mean} = \frac{u_F + u_O}{H} = 809s^{-1}. \tag{4.17}$$

Figure 4.16 illustrates the obtained flame for the Fine mesh (see below). Due to the velocity difference of both streams, it is not planar and the solution will be analyzed only along the central axis.

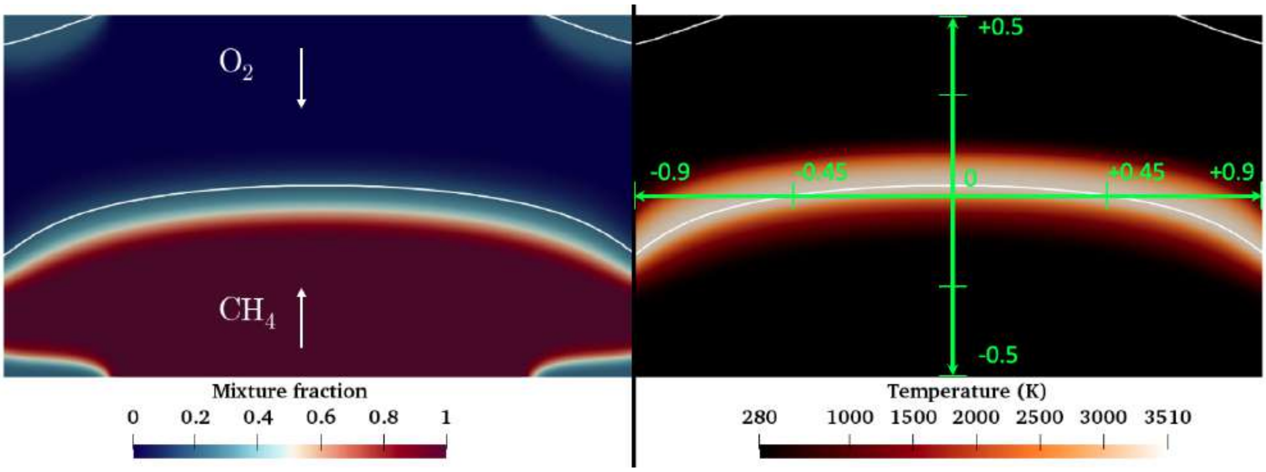

Figure 4.16: Laminar counterflow flame in AVBP. Left: mixture fraction field. Right: temperature field. The white line corresponds to the stoichiometric line ($Z_{st} = 0.2$). Axes in millimeter.

A fine mesh (about $\Delta x = 1\mu m$ cell characteristic size at the stagnation plane) is first used to assess the accuracy of the exponential integration. Then coarser meshes are used, listed in Table 4.6, to be more realistic of LES and to demonstrate the capacity of the exponential integration to increase the computational time step. Reference solutions computed with CANTERA are also reported for comparison.

Case	$\Delta x[\mu m]$	$\Delta t_{CFL}[ns]$
Fine	1	0.194
Coarse 1	10	2.50
Coarse 2	30	5.28

Table 4.6: Mesh characteristics for the 2D counterflow flame.

The mesh grid size can be compared to the theoretical thermal flame thickness of a diffusion flame, computed as:

$$\delta_{th} = \sqrt{\frac{\pi D_{th}}{2a_{mean}}} \tag{4.18}$$

In the present case, $\delta_{th} = 0.298mm$, so that meshes from Fine to Coarse 2 contain respectively about 300, 30 and 10 points in the thermal flame thickness.

The characteristic chemical time scales $\tau_{chem,k}$ of each species k of the ARC scheme in a diffusion flame at the specified strain rate $a_{mean} = 809s^{-1}$ are presented in Fig. 4.17. They are computed as introduced by Eq. 4.7. It is found that C_2H_6 is the stiffest species with $\tau_{chem,C_2H_6} = 6.8e^{-9}s$. Other radicals are stiff as well, and as already mentioned the fuel itself, CH_4, is also among the stiffest species. Note that these time scales tend to decrease rapidly as the strain rate grows, reaching values about 10e^{-10} - 10e^{-11}s. In practice in the LES code, it is needed to use typically a 1000 times smaller time step than presented in Fig. 4.17, i.e., much smaller than the time steps Δt_{CFL} for Coarse 1 and Coarse 2 cases of Table 4.6.

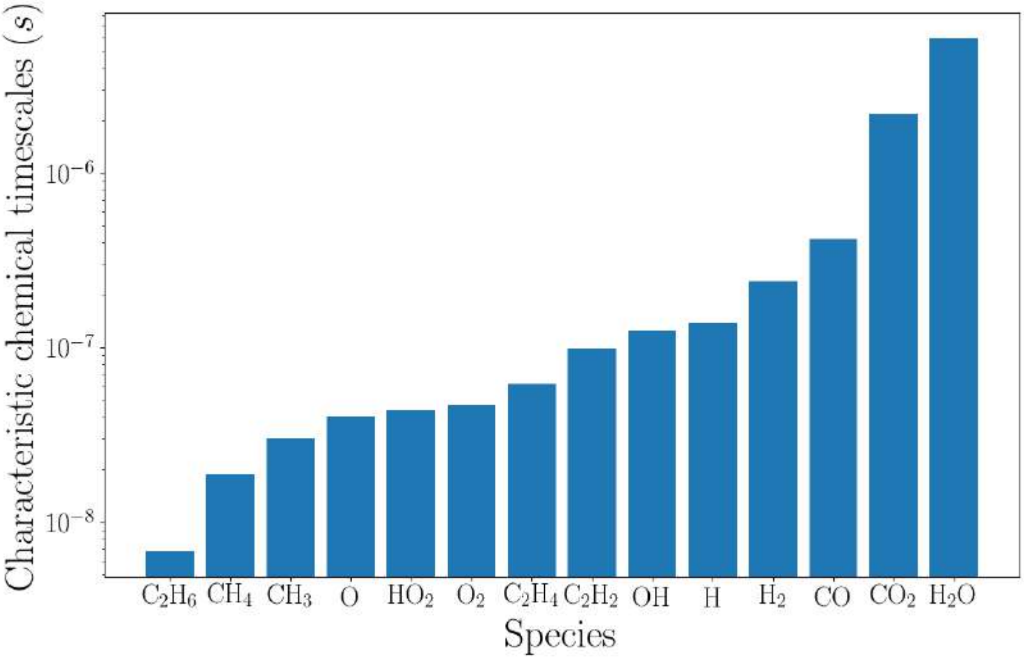

Figure 4.17: Characteristic chemical timescales of the methane-oxygen ARC, in the counterflow diffusion flame conditions.

Fine mesh case

Figure 4.18 shows the temperature and heat release rate profiles for the fine mesh case, obtained with standard explicit Arrhenius form (referred as "classic") and exponential time integration. An excellent agreement is observed, with exactly the same flame structure. The temperature profiles match perfectly. The difference of total heat release rate is only of 0.11% between the two AVBP computations, and about 2.6% between AVBP and CANTERA simulations. The latter may be attributed to the different numerical solvers and slightly different local strain rate.

Some species profiles, shown in Fig 4.19, confirm the excellent behavior of the exponential time integration against the classic one and the excellent agreement with CANTERA. The species profiles perfectly match, with only a slight deviation for CO between AVBP and CANTERA.

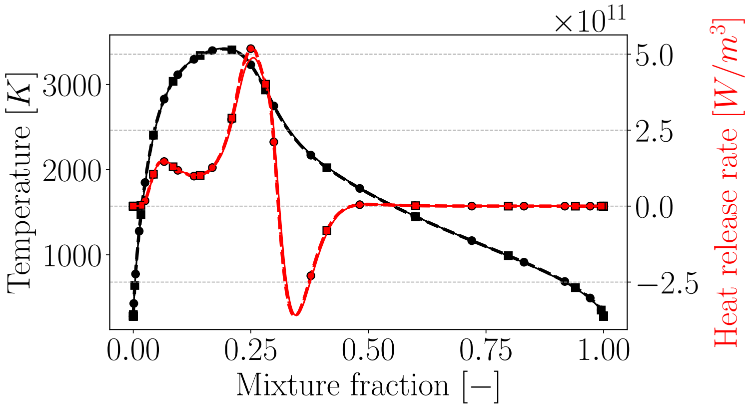

Figure 4.18: Strained diffusion flame: evolution with mixture fraction of the temperature (black) and the heat release rate (red). Solid lines: CANTERA ($a_{mean} = 809s^{-1}$). Dashed lines with circle markers: classic time integration. Dotted lines with square markers: exponential time integration. Fine mesh case.

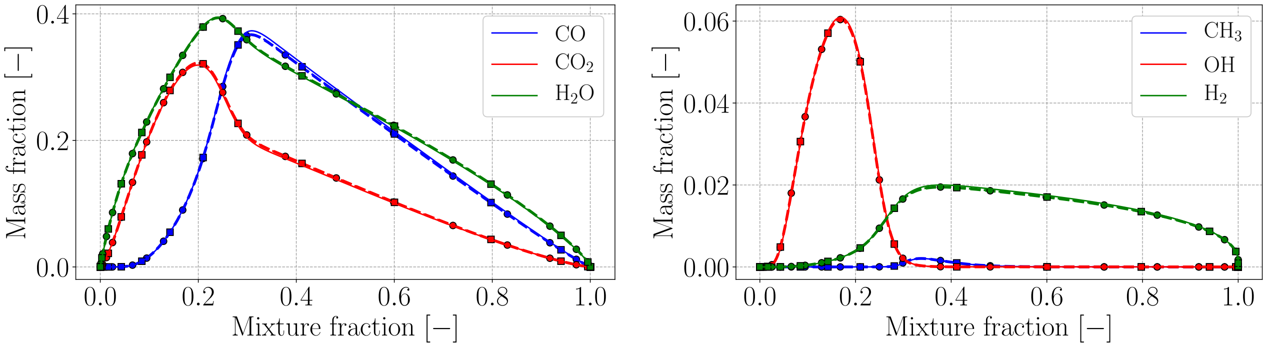

Figure 4.19: Strained diffusion flame: evolution with mixture fraction of some species profiles. Solid lines: CANTERA ($a_{mean} = 809s^{-1}$). Dashed lines with circle marker: classic time integration. Dotted lines with square markers: exponential time integration. Fine mesh case.

In this particular case, it was found that $\Delta t_{chem} > \Delta t_{CFL}$ so that the exponential time integration is not useful. The Fine mesh case was only considered for validation of the exponential time integration. The computational gain is presented in the next section with cases Coarse 1 and Coarse 2 where $\Delta t_{chem} < \Delta t_{CFL}$.

Coarse mesh cases and computational gain

Coarse meshes induce numerical diffusion which adds to the laminar diffusion, and artificially increases the scalar dissipation rate at the flame location. This phenomenon, beyond the scope of the present analysis, was highlighted in [Shum-Kivan, 2017] and explored in Section 4.5. The comparison with CANTERA must be at the same scalar dissipation rate, found to be $\chi_{st} = 146s^{-1}$ and $\chi_{st} = 209^{-1}$, or equivalently in terms of strain rate $a_{st} = 930s^{-1}$ and $a_{st} = 1335s^{-1}$ for Coarse 1 and Coarse 2 cases, respectively.

To measure the efficiency of time integration, the quantity κ is introduced as the ratio between the CFL time step and the effective simulation time step:

$$\kappa = \frac{\Delta t_{CFL}}{\Delta t} \tag{4.19}$$

For both integration methods, coarse mesh cases run with the chemical time step ($\Delta t = \Delta t_{chem}$), leading to κ above 1 as shown in Table 4.7. Using classic time integration, a reference solution is obtained with a time step 25 times smaller than the CFL time step. The value κ_{min} corresponds to the maximum time step keeping a correct time resolution. As the flow time step Δt_{CFL} is proportional to Δx, κ_{min} increases from 4 for the Coarse 1 case to 10 for the Coarse 2 case. In comparison, the exponential time integration method allows to increase Δt_{chem} (and therefore decrease κ) up to half and fourth the CFL time step for Coarse 1 and Coarse 2 cases, respectively. A reference case with $\kappa = 25$ is also computed for exponential integration. As explained in Section 4.4.1, the constant reaction factors assumption does not allow larger time steps for the exponential method. With the exponential method, the obtained solution has the same accuracy as the solution obtained with the classic approach. This means, concerning the chemical time step, an acceleration factor of 2 and 2.5 for Coarse 1 and Coarse 2 reference solutions, respectively.

Mesh	κ_{ref} (classic)	κ_{min} (classic)	κ_{ref} (expo)	κ_{min} (expo)
Coarse 1	25	4	25	2
Coarse 2	25	10	25	4

Table 4.7: Efficiency of time integration κ (Eq. 4.19) for the classic and exponential time integration for the coarse mesh cases.

Figures 4.20 and 4.21 compares the solutions obtained with the classic and exponential method, with κ_{ref} and κ_{min}, as well as with the CANTERA solution taken at the appropriate strain rate, for the two coarse meshes.

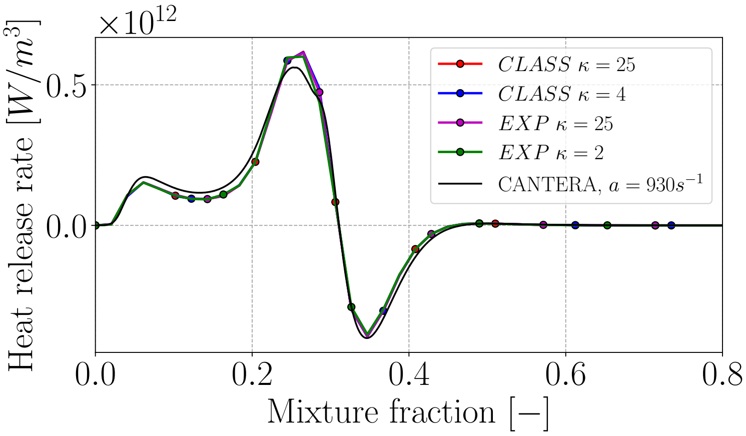

Figure 4.20: 1D strained diffusion flame: evolution with mixture fraction of the heat release rate for different time integration methods. Coarse 1 case.

For Coarse 1 case, the heat release rate profile shows less than 1% discrepancy between all AVBP simulations, and about 2% difference with the CANTERA flame. Discrepancies are larger for Coarse 2 case, linked to the very poor grid resolution with about 10 points to describe the three-peaks flame reaction zone. They stay however very small between all AVBP

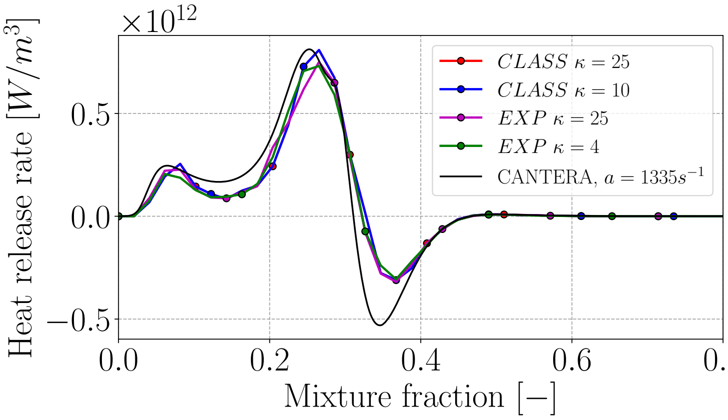

Figure 4.21: 1D strained diffusion flame: evolution with mixture fraction of the heat release rate for different time integration methods. Coarse 2 case.

cases, and are more noticeable in the comparison with the CANTERA solution, which does not have this mesh effect. Interestingly, the classic and exponential methods do not respond similarly to the time step increase. While in the classic approach, the solution stays unchanged until the simulation crashes, the increased robustness of the exponential method allows to converge solutions at large time steps, but with an increased error.

The non-conservation of mass of the exponential time integration, described in Section 4.4.1 is quantified for each element as:

$$dm_{e,rel} = \frac{\sum_{k=1}^{N_s}(c_k^{n+1} - c_k^{n})N_{e,k}}{\sum_{k=1}^{N_s} c_k^{n+1} N_{e,k}} \tag{4.20}$$

In all fine and coarse mesh cases, $dm_{e,rel}$ is found to stay always below 1% in each cell and for all elements, which results in a maximum correction of $\mathcal{O}(1\%)$ on species concentrations. These are maximum values, and most of the simulation does not require such correction. Therefore it is verified *a posteriori* that the mass correction proposed in Section 4.4.1 remains low and has a very limited impact on the final results. As expected, the mass deviation is directly linked to the temporal resolution: for example in Coarse 1 case with $\kappa = 2$, the maximum correction is about $\mathcal{O}(1\%)$ but with $\kappa = 25$, it decreases down to $\mathcal{O}(0.1\%)$.

Finally, Fig. 4.22 shows the temperature and the CH_3 mass fraction profiles for the different meshes. The cases Fine, Coarse 1 and the CANTERA reference, all curves almost perfectly match, proving the mesh convergence. The Coarse 2 case logically deviates a bit from the others due its poorer resolution.

4.4.2 Discussion

The exponential integration introduced in the paper shows promising results in terms of stability and gain in computational cost. This result is further demonstrated in Chapter 6 dedicated to the CONFORTH test bench. Actually the computational gain depends of the chemical scheme, the application, and the ratio of characteristic time scales $\kappa = \tau_{CFL}/\tau_{chem}$. For example the chemical time step was multiplied by 50 in the simulation of low-pressure ignition in [Pestre et al., 2021]. This led to a global computational speed 19 times faster thanks to the

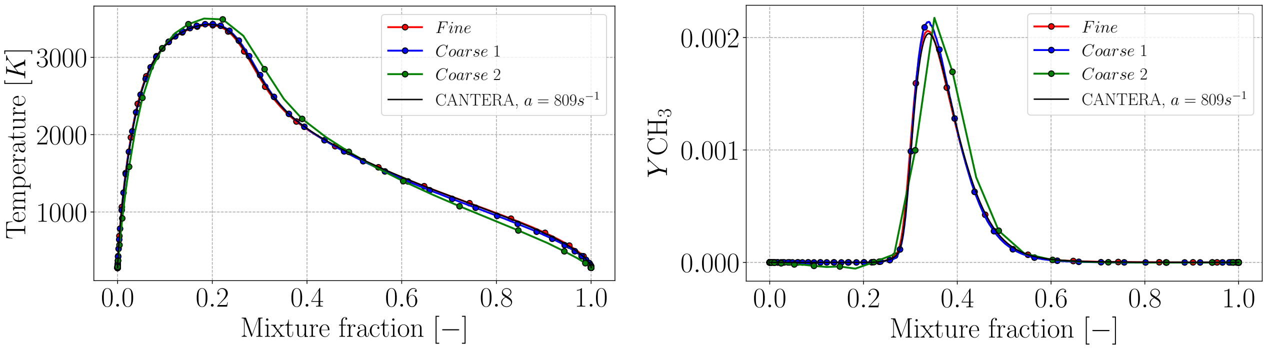

Figure 4.22: Strained diffusion flame: evolution with mixture fraction of the temperature and CH_3 mass fraction for the considered meshes compared to CANTERA.

exponential integration without loss of accuracy. It seems therefore that the exponential integration is particularly efficient in the case of non-stationary cases, where the chemical constraint is usually even stronger due to the presence of many different radicals, and therefore, timescales.

In practice it was found that even though the chemical time step can be significantly increased with the use of exponential integration, numerical instability in mixture fractions resulting in some local heat release and pressure peaks, could still appear. This is attributed to the mass conservation algorithm, which may change too much some species concentrations if the time step is too large. Other mass conservation strategies are possible but are left to future work.

As introduced earlier, one of the main problem of explicit integration with non-positive numerical schemes is the possibility to generate non-physical negative mass fractions. By construction the exponential integration is positive, *i.e.*, does not change the sign of the solution. However negative mass fractions can still appear from the convective scheme.

Finally to further reduce the CPU cost of chemistry in AVBP, the application of subcycling could be improved. Currently the number of chemical subcycles κ is imposed in the whole computational domain. However, the chemical time step constraint only concerns the stiffest reaction zones, usually around the stoichiometric line in the case of diffusion flames, where the reaction rates are the highest. Typically it is not necessary to subcycle the chemistry in the burnt gases, in the injection zone, or in the less reactive parts of the flame. In the application cases of Chapters 6 and 7, these non-stiff zones correspond to about 80% of the grid points. An efficient way that is proposed here for future work, would be to apply local subcycling only to the stiff zones, identified with a criterion based on the local heat release rate or κ value for example. This would also require some HPC work to avoid processor load imbalance.

4.5 Turbulent diffusion flame modelling

4.5.1 The Thickened Flame model for diffusion flames

The Thickened Flame Model for LES (TFLES) [Colin et al., 2000] is now widely used by the LES community to get around the high spatial resolution needed to compute premixed flames. In the context of diffusion flames, as found in rocket engines, the impact of the grid is different as previously highlighted in the theses of Shum-Kivan [Shum-Kivan, 2017] and Rocchi [Rocchi, 2012].

In their theses, considering high-Damköhler flames, *i.e.*, controlled by diffusion, they explain that the thickening factor of the TFLES approach should be applied to the diffusion coefficient only (contrary to premixed flames for which it is applied also to the reaction rates), to represent three contributions to the turbulent flame consumption rate:

- Mesh filtering: F_M
  In the case of a diffusion flame, under-resolution does not lead to a crash, but in over-diffusion of the flame structure: a coarse mesh acts as a supplementary diffusion, which may be therefore cancelled with a "counter-diffusion" correction. Therefore $F_M < 1$.
- Sub-grid scale strain rate: F_Λ
  Because of under-resolution, the smallest flow structures are not represented, and the corresponding highest strain rates are ignored. As the strain rate directly acts on the consumption rate of diffusion flames, a factor $F_\Lambda > 1$ must be introduced.
- Sub-grid scale wrinkling: F_Π
  Similarly to premixed flames sub-grid scale wrinkling acts on the flame surface, enhancing the combustion rate. Thus, $F_\Pi > 1$.

These three effects are combined in the turbulent diffusion thickened flame model, multiplying species and heat diffusion coefficients by:

$$F = \underbrace{F_{\mathrm{M}} F_\Lambda F_\Pi}_{F_{\mathrm{tot}}} \tag{4.21}$$

As in premixed flames, this modified diffusion coefficients $D_k \times F$ and $\lambda \times F$ should only be applied in the flame zone. A simple flame sensor θ has been proposed by Shum-Kivan, especially made for diffusion flames as it is centered on the stoichiometric mixture fraction Z_{st}:

$$\theta = min(A \times exp(-B \times (Z - Z_{st})^2, 1) \tag{4.22}$$

where A and B are user-defined constants and Z the local mixture fraction. A more advanced sensor has been recently developed at CERFACS that is applicable to both premixed or non-premixed flames independently of the flame structure [Rochette et al., 2020].

4.5.2 Paper published in *Combustion & Flame*

To make first steps in the demonstrations and validation of the method, a first work was performed on laminar flames to investigate F_M only, the mesh under-resolution effect on the flame. Turbulent subgrid-scales contributions are left to future work.
This work ([Cuenot et al., 2021]) is now published in *Combustion & Flame*. The paper included below reports the effect of mesh coarsening on 1D counterflow diffusion flames computed with CANTERA, and extends the first analysis of Shum-Kivan for simple chemistry (also included in the paper) to detailed kinetics in the form of the ARC scheme derived in Section 4.3.1.

Combustion and Flame xxx (xxxx) xxx

Contents lists available at ScienceDirect

Combustion and Flame

journal homepage: www.elsevier.com/locate/combustflame

The thickened flame approach for non-premixed combustion: Principles and implications for turbulent combustion modeling

B. Cuenot[a,*], F. Shum-Kivan[a], S. Blanchard[a,b]

[a] CERFACS, 42 Av. G. Coriolis, 31057 Toulouse, France
[b] CNES, Launchers Directorate, 52 rue Jacques Hillairet, 75612 Paris Cedex, France

ARTICLE INFO

Article history:
Received 31 March 2021
Revised 4 August 2021
Accepted 6 August 2021
Available online xxx

Keywords:
Non-premixed combustion
Laminar flame
Turbulent combustion modeling

ABSTRACT

Modeling turbulent non-premixed combustion remains a challenge in the context of Large Eddy Simulation (LES) in complex geometries and for realistic conditions, taking into account all physical phenomena impacting the flame such as heat loss, dilution, or liquid fuel atomization and evaporation. In this work, the Thickened Flame concept, which allows to resolve the flame front on the LES grid while preserving the consumption speed, and initially derived for premixed combustion, is adapted to diffusion flames. It is demonstrated that the concept holds for these flames, with however, a different formulation of the model due to but their specific nature and properties. In particular, in the high-Damköhler regime, the thickening factor is applied only to the diffusion coefficients. The behavior of thickened diffusion flames is illustrated on laminar steady strained flames for both simple and complex chemistry, showing how the Thickened Flame concept applies. Based on these results, an expression for the thickening factor related to mesh coarsening is derived. For a complete turbulent combustion model, the thickening factor should also describe the sub-grid scale flame-turbulence interaction, which is left for future work.

1. Introduction

Because it induces locally high temperatures, non-premixed combustion is usually avoided in practical systems. Indeed, on top of thermal fatigue issues, high temperatures greatly favor nitrogen oxidation and soot production which, in the current context of control and possibly reduction of pollutants, is not acceptable [1]. In the vast majority of gas-fed industrial burners, combustion occurs however, in a partially premixed regime characterized by reactant premixing at various levels. In such burners, the equivalence ratio is not uniform but the occurrence of non-premixed combustion stays very low [2]. The situation is different in systems burning liquid fuel injected in the form of a spray. In this case, droplets may evaporate in zones free of oxidizer and the produced fuel vapor may burn in a non-premixed mode with recirculation or dilution air, or with the excess oxygen in the lean burnt gas [3]. Although this combustion regime is rarely prevalent, it may induce significant increase of pollutant production in aeronautical gas turbines, or in direct injection IC engines [4], where the spray flame may locally induce non-premixed combustion in overall highly stratified mixtures. Pure diffusion flames are found only in very specific devices, such as liquid rocket engines [5] or industrial furnaces, in particular with oxygen-fuel burners [6]. In these systems highly flammable reactants raise critical safety issues, and the burner geometry is designed to avoid premixing, leading to a flame attached to the separator between the two reactant streams.

Despite the above-mentioned dominant premixed mode in practical systems, the accuracy level required to address current industrial challenges makes it essential to account for the specific structure of diffusion flames in system analysis. Contrary to premixed flames which exhibit intrinsic space and time scales in the form of fixed flame thickness and flame speed, diffusion flames do not have such properties and reach a steady state only in the presence of a flow. The simplest reference configuration allowing theoretical studies of diffusion flame is the pseudo-1D counterflow configuration, in which two opposed jets meet at a stagnation plane. Following the pioneer work of Peters [7], non-premixed turbulent combustion has been much successfull with the flamelet concept, taking advantage of the flame properties in the mixture fraction space. Combined with a probability density function (PDF) to account for turbulence intermittency, the pre-tabulated flamelet approach allows to compute turbulent flames with detailed chemistry at a reasonable computational cost [8–12]. The main drawback of this type of model is the loss of direct interaction between the local flame structure and the flow. To describe this interaction, direct integration of the chemistry is required, which implies the

---

[*] Corresponding author.
E-mail address: cuenot@cerfacs.fr (B. Cuenot).

https://doi.org/10.1016/j.combustflame.2021.111702
0010-2180/© 2021 The Combustion Institute. Published by Elsevier Inc. All rights reserved.

Please cite this article as: B. Cuenot, F. Shum-Kivan and S. Blanchard, The thickened flame approach for non-premixed combustion: Principles and implications for turbulent combustion modeling, Combustion and Flame, https://doi.org/10.1016/j.combustflame.2021.111702

resolution of a transport equation for each species and a model for the associated chemical source term. The latter may be described with simple mixing-controlled models such as Eddy Break-Up (EBU) [13], or later Eddy Dissipation Model (EDM) [14]. More sophisticated techniques use transported PDF or solve the flame quantities conditioned on the mixture fraction as in the Conditional Moment Closure (CMC) [15] or the Multiple Mapping Conditioning (MMC) models [16]. All these models have been extensively validated in turbulent adiabatic gaseous combustion, and were found to predict the flame structure with good accuracy. Their extension to non-adiabaticity [17–19], two-phase combustion [20–22], multiple injection and dilution [23,24], has been proposed in the literature. Although their rigorous derivation makes them attractive, their application to validation test cases led to various levels of success. This is due to the increased complexity of the physics involved which demands additional modeling, weighs down the model formulation and significantly increases the computational cost.

In the framework of Large Eddy Simulation (LES), which has become a standard in the research community for the study of realistic turbulent flows, the Thickened Flame (TF) concept [25] has gained much interest as it takes full benefit of the spatial filtering of the formulation. Note that although they are not strictly identical, the grid filter usually serves as the LES filter and both filters are equivalently used in model derivations and analyses. Only the subfilter, or subgrid smallest dissipative scales of the turbulent field are modeled so that, provided that the smallest resolved scales are sufficiently close to the premixed flame scale, a good part of the flame front is directly resolved by LES. To make it fully resolved, the flame is artificially thickened while keeping its flame speed unchanged. Introducing a sub-grid efficiency model to take into account the unresolved filtered flame front wrinkling, this approach then allows to solve unsteady turbulent flames taking into account heat losses, liquid fuels or dilution without further modeling. The TF approach may be combined to various descriptions of the flame structure, such as direct chemistry integration [26,27], tabulated flamelets [28–30] or equilibrium [31]. It represents the flame-turbulence interaction with the resolved contribution and a subgrid-scale contribution in the form of an efficiency function, i.e., totally different from pdf-based or viscosity-based (ILES) methods. The TF model has been applied with success to a large variety of configurations and to study many complex phenomena such as thermo-acoustic instabilities [32,33], ignition and extinction [34–36], and pollutant formation [26,37]. Its simplicity makes it easy to implement in industrial CFD codes for the prediction of real industrial systems with complex geometries and varying operating conditions. In its original version, the TF model is however, limited to premixed combustion as it is based on particular properties of premixed flames. If directly applied to non-premixed flames, it may lead to a significant modification of the turbulent flame consumption speed and finally incorrect flame shape and behavior. A literature search combining the keywords 'thickened flame' and 'non premixed' reveals very few references [38–42]. All cases refer to non premixed injection, leading to a partially premixed flame, i.e., a premixed flame with variable equivalence ratio, and a rare occurrence of true non-premixed combustion which does not significantly impact the result. The key point was then to avoid thickening outside the reaction zone in order to ensure correct mixing prior to combustion. This was obtained with the Dynamic TF (DTF) model based on a flame sensor [38]. However, modeling pure diffusion flames with a TF approach remains an open question. If the TF concept, i.e., making the flame resolvable on the grid still holds for non-premixed combustion, it must be adapted to it. This question is crucial for extending the TF model to LES of purely non-premixed combustion, partially premixed combustion or two-phase combustion in real systems. Indeed, even though computational resources today allow to come close to flame resolution in ambient conditions and in simple geometries, there are still conditions such as high pressure, oxycombustion or very intense turbulence which induce very thin flames requiring modeling.

In order to make first steps in this direction, the present paper aims to demonstrate how laminar non-premixed flames can be artificially thickened while preserving their main properties. Aiming to allow the direct resolution of combustion chemistry, the TF model answers two related major questions. First, artificial flame thickening allows to compute a thin flame on a coarse grid, ensuring numerical robustness and physical validity. Second, the subgrid scale flame-turbulence interaction is modeled by describing the sub-grid scale wrinkling. The first question is addressed here for non-premixed combustion, based on the properties of laminar diffusion flames. This first step allows then to derive a theoretical formulation of the TF approach for LES of turbulent non-premixed and partially premixed combustion. This theoretical formulation is however not complete, as it introduces sub-grid scale models which still need to be derived. The objective of the present work is only to demonstrate the theoretical validity of the TF concept adapted to non premixed combustion, and therefore the study does not include turbulent flame cases.

The paper is organized as follows. In Section 2, the properties of laminar diffusion flames are recalled and the implications for their artificial thickening and resolution on coarse grids are detailed. These findings are illustrated on a series of numerical test cases, first using simple chemistry and summarized in Section 3 together with the numerical method. Results are then presented and analyzed in Section 4. They are extended to more complex chemistry flames in 5. Finally the formulation of a Thickened Flame approach for non-premixed combustion is given in Section 6.

2. Strained diffusion flames

Contrary to premixed flames, laminar diffusion flames do not have a steady structure in a quiescent environment. The reason is that the flame is fed by both sides and therefore can not propagate in a direction or the other, but naturally stabilizes at locations of stoichiometric conditions. While the convective-diffusive-reacting balance is reached in the propagating premixed flame as soon as it propagates at the flame speed, the similar balance can be reached in diffusion flames only if convective transport is forced by an external flow. Thus, two types of laminar flames may be defined: (i) unsteady unstrained flames, which widen indefinitely in the absence of a flow, and (ii) steady strained flames, which are subjected to a velocity strain rate and reach a stationary structure. It was shown in Cuenot et al. [43] that an unsteady unstrained flame at time t after the moment when the reactants are put into contact, has the same structure as a steady strained flame with an equivalent strain rate $a = 1/2t$. More complex flames resulting from a varying strain rate have been studied in Cuenot et al. [43] and were also shown to have the same structure than of a steady strained flames with a so-called equivalent strain rate, taking into account the strain rate variation in time. Therefore in the following only steady strained flames will be considered.

The most simple configuration which allows to establish a steady diffusion flame is the counterflow configuration (Fig. 1) where the fuel and oxidizer streams are injected with two opposed jets. Although the real counterflow geometry is axisymmetric, it is often considered as a planar 2D configuration for simplicity in both theoretical and numerical studies. In this case the velocity field corresponds to the simple potential flow defined by $u = ay$ and $v = -ax$, where u and v are the two velocity components and the strain rate a is the constant velocity gradient which depends only on both injection velocities u_O and u_F and the distance between the injector planes L as $a = |u_O - u_F|/L$. Note that in the presence

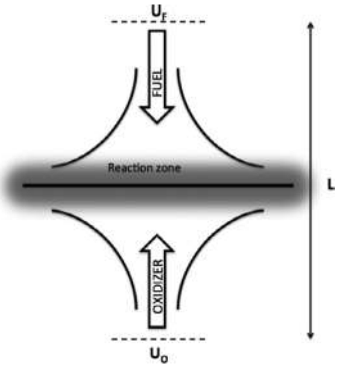

Fig. 1. Counterflow configuration for the study of laminar diffusion flames.

of a flame the velocity field is perturbed by the varying density so that the true strain rate applied to the flame is slightly different from the constant value of the non-reacting flow. However, even in that case the velocity field may be approximated by $\rho u = \rho_0 ay$ and $\rho v = -\rho_0 ax$ where ρ_0 is a reference density, and the strain rate a corrected with the density ratio can be again considered constant [44].

Thanks to symmetry and the simple 2D velocity fields, the problem may be described with a pseudo-1D set of equations along the axial x-direction, which in the steady case take the general form:

$$\rho u \frac{\partial var}{\partial x} = D \frac{\partial^2 var}{\partial x^2} + \dot{\omega}_{var} \tag{1}$$

where var represents any species mass fraction or temperature and $\dot{\omega}_{var}$ is the associated chemical source term. For simplicity the same diffusion coefficient D is used here for all variables, but it can be easily extended to different diffusivities following [45]. It will be shown in Section 5 that the conclusions obtained with this simplified transport properties model still hold for different diffusivities.

The steady solution obtained for the mixture fraction, which follows Eq. (1) without the chemical source term, writes [45]:

$$Z(x) = \frac{1}{2}(1 - \mathrm{erf}(\eta(x))) \tag{2}$$

with

$$\eta(x) = \frac{\zeta(x)}{\sqrt{2D/a}} \quad \text{and} \quad \zeta(x) = \int_0^x \frac{\rho}{\rho_0} dx \tag{3}$$

where Z is the non-dimensional mixture fraction, taking values of 1 in the fuel stream and 0 in the oxidizer stream. In the above equation, erf is the error function and the quantity ζ is introduced to take into account the varying density through the flame. The coordinate origin $x = 0$ is taken at the point of zero velocity, and ρ_0 denotes the density at this point.

It is easily demonstrated that a change of variable from x to Z applied to Eq. (1) leads to:

$$-\chi \frac{\partial^2 var}{\partial Z^2} = \dot{\omega}_{var} \tag{4}$$

where $\chi = 2D(\partial Z/\partial x)^2$ is the scalar dissipation rate. Outside the reaction zone, i.e., where $\dot{\omega}_{var}$ is zero, the solution of Eq. (4) is a simple linear function. Assuming that the gradient of Z is close to constant inside the reaction zone, χ is often taken also constant at its value at stoichiometry χ_{st}. From Eq. (2), one obtains $\chi_{st} = C_{st}^2 a/\pi$, where $C_{st} = \exp(-\eta_{st}^2)\rho_{st}/\rho_0$ is a constant linked to the position of the flame ($C_{st} = \rho_{st}/\rho_0$ if the flame is located at $x = 0$). With this expression of χ_{st}, it can be observed that the solution of Eq. (4) in the mixture fraction space is insensitive to diffusion coefficients for steady strained flames.

Eq. (4) clearly highlights the reactive-diffusive balance in the Z-space, which controls the flame structure and its response to scalar dissipation or equivalently to strain rate. Two different combustion regimes may be introduced here, depending on this reactive-diffusive balance and distinguished with the Damköhler number $\mathrm{Da} = 1/\tau_c\chi_{st}$ where τ_c is the flame chemical time scale. For high Da, combustion is very fast while flow transport processes are slow: the chemistry completely consumes reactants as soon as they reach the stoichiometric zone and the flame consumption rate is limited by diffusion. On the contrary for low Da, the flame is fed too fast compared to what it can burn: the combustion is limited by chemistry, and leakage of unburnt reactants occurs. Below a certain value of Da, the consumption rate starts to decrease until extinction is reached at the quenching value Da_q. The analysis performed in the following holds for the high-Da regime which is encountered in most practical systems. Low-Da flames being controlled by slow chemistry, have a higher thickness and are therefore less demanding in numerical resolution.

In view of elucidating the mesh requirements for diffusion flames, the same quantities of interest used for premixed flames, namely consumption speed and thickness which also hold for diffusion flames, are used to characterize the flame.

2.1. Flame consumption speed

As for premixed combustion, a major quantity of interest is the flame consumption speed which controls the flame surface and is critical for the design of combustion chambers. This quantity can be calculated first in the mixture fraction space from any flame variable, by integrating Eq. (4):

$$\dot{\Omega}^Z_{var} = \int_{-\infty}^{+\infty} \dot{\omega}_{var} dZ = -\chi_{st} \left[\frac{\partial var}{\partial Z} \right]_{-\infty}^{+\infty} \tag{5}$$

As all flame variables (mass fractions and temperature) are linear functions of Z where the reaction rate is zero, and replacing χ_{st} with the strain rate, one gets:

$$\dot{\Omega}^Z_{var} = -\frac{a}{\pi} \left(\frac{var_{+\infty} - var_{st}}{1 - Z_{st}} - \frac{var_{st} - var_{-\infty}}{Z_{st}} \right) \tag{6}$$

Note again that in the Z-space, the flame consumption speed is independent of the diffusion D and only depends on the strain rate a. Going back in the physical space, the consumption speed writes:

$$\dot{\Omega}_{var} = \frac{\dot{\Omega}^Z_{var}}{\partial Z/\partial x} \tag{7}$$

As done previously for the scalar dissipation rate, and because reaction source terms are non zero only near stoichiometry, the passive scalar gradient is considered constant ant taken at the stoichiometric value:

$$\left(\frac{\partial Z}{\partial x} \right)_{st} = C_{st} \sqrt{\frac{a}{2\pi D}} \tag{8}$$

This finally gives the following expressions for the consumption speed:

$$\dot{\Omega}_{var} = -\frac{1}{C_{st}} \sqrt{\frac{2aD}{\pi}} \left(\frac{var_{+\infty} - var_{st}}{1 - Z_{st}} - \frac{var_{st} - var_{-\infty}}{Z_{st}} \right) \tag{9}$$

The above expression can be applied to the fuel, oxidizer or temperature. In this paper the heat release rate will be used to measure the flame consumption speed:

$$\dot{\Omega}_T = \frac{1}{C_{st}} \sqrt{\frac{2aD}{\pi}} \frac{C_p(T_{st})T_{st} - C_p(T_0)T_0}{Z_{st}(1 - Z_{st})} \tag{10}$$

where for simplicity the same initial temperature T_0 is taken for both reactant streams, T_{st} is the temperature at stoichiometry and

$C_p(T)$ is the heat capacity. Note that the flame consumption speed scales as a diffusive flux, therefore leading to the same flame location as the stoichiometric line which is also controlled by the same diffusive flux.

2.2. Flame thickness

The second important quantity to evaluate is the flame thickness, which in principle controls the spatial resolution of numerical simulations. In diffusion flames, the thermal thickness may be expressed as the inverse of the mixture fraction gradient:

$$\delta_f = \frac{1}{C_{st}}\sqrt{\frac{2\pi D}{a}} \tag{11}$$

Of course, the thickness of the reaction zone is smaller and depends on chemistry. However, in the considered high-Da diffusion flame regime, chemistry is not the limiting phenomenon and the reaction zone thickness is not as important as it is for premixed flames. Therefore it is ignored in this analysis and it will be confirmed in the simulations of Sections 4 and 5 that this quantity is not a controlling parameter.

The two above expressions in Eqs. (10) and (11) show that in diffusion flames, the consumption speed scales as $\sqrt{aD}$ while the flame thickness scales as $\sqrt{D/a}$. This immediately shows that modifying the chemical source term has no effect on high-Da diffusion flames properties, which can only be altered by modifying either the diffusion coefficient D or the strain rate a. This is to be compared to the scaling laws of the same quantities in premixed flames, which are $\propto \sqrt{RD}$ for the consumption speed (or equivalently the flame speed) and $\propto \sqrt{D/R}$ for the thermal flame thickness, where $1/R$ is a chemical time scale. Therefore, the Thickened Flame concept as formulated for premixed flames, i.e., multiplying D and dividing R by the same thickening factor F, can not be applied to diffusion flames. For these flames, preserving the consumption speed while thickening the flame front requires to multiply D and divide a by the same thickening factor F.

Another important difference with the premixed flame is that a diffusion flame does not have any fixed, intrinsic thickness. Instead, the diffusion flame thickness adjusts to the local velocity gradient, as the result of the convection-diffusion balance of the mixture fraction. This property of diffusion flames has a direct consequence for their numerical simulation: the resolution requirements are directly linked to the resolved flow. In other words, when applying grid filtering as is done in LES, the resolved strain rate decreases which automatically thickens the flame. This effect may even be enhanced by possible numerical diffusion which adds to the physical diffusion and further thickens the flame front. This of course depends on the numerical method used in the solver, but a direct consequence is that, contrary to premixed flames, simulating diffusion flames on LES grids does not need any explicit artificial thickening. The question is then to evaluate if the grid resolution is sufficient, i.e., if the LES mesh is not too coarse for the thickened flame corresponding to the resolved flow, which is the first objective of the present study. Whereas the obtained solution is correct or not, and what it implies for turbulent combustion modeling, are two other questions which are also addressed in this paper.

3. Test cases and numerical set-up

In order to illustrate and evaluate the effect of grid resolution on diffusion flames, a methane-air counterflow configuration is computed with different meshes. The advantage is that in this particular case, thanks to the very simple flow the strain rate does not change with the mesh and the flame has a fixed thickness. It is then possible to analyse the effect of mesh resolution on the flame only, whatever it means for the flow. As a consequence, and following Eq. (4) the theoretical solution in the mixture fraction space does not change. According to the findings of the previous Section, in this particular case where a is kept constant, the impact of grid filtering on both the flame consumption speed and flame thickness is only related to the diffusion coefficient seen by the flame, i.e., including numerical diffusion induced by both filtering and numerical schemes.

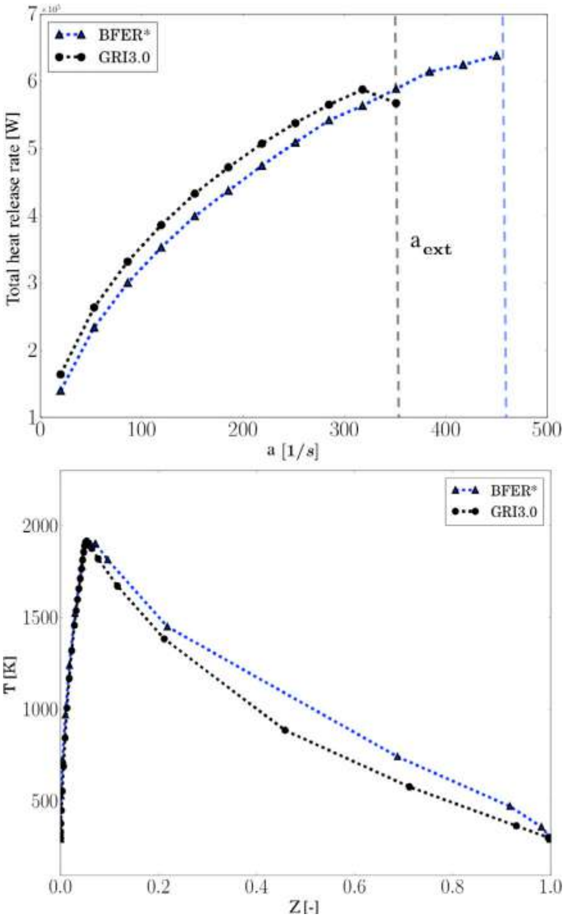

Fig. 2. Comparison of the 2-steps chemistry with GRI3.0: total heat release rate $\dot{\Omega}_T$ of strained methane-air flames as function of the strain rate (left) and temperature profile in the mixture fraction space for $a = 250$ s^{-1} (right).

Simulations are performed with the open source solver CANTERA [46]. For simplicity and easier analysis, a simple 2-steps chemical scheme is used first. Extension to more complex chemistry will be addressed in Section 5. The 2-steps scheme (denoted BFER*) is taken from [47], adapted to diffusion flames in Franzelli [48] by using non-unity Lewis numbers to recover the correct flame response to strain rate. The kinetic scheme writes:

$$CH_4 + 1.5O_2 \rightarrow CO + 2H_2O \tag{12}$$

$$CO + 0.5O_2 \leftrightarrow CO_2 \tag{13}$$

In the approach of [47], the pre-exponential constant of both reactions is a polynomial function of the equivalence ratio, fitted on measured flame speed values. All reaction constants and correction functions may be found in Franzelli et al. [47], Franzelli [48]. It has been verified that the 2-steps scheme correctly reproduces the diffusion flame structure and properties at initial ambient temperature and pressure. This is illustrated in Fig. 2 showing the comparison with the reference GRI3.0 [49] of the total heat release rate $\dot{\Omega}_T$ computed from the heat release rate integrated through the

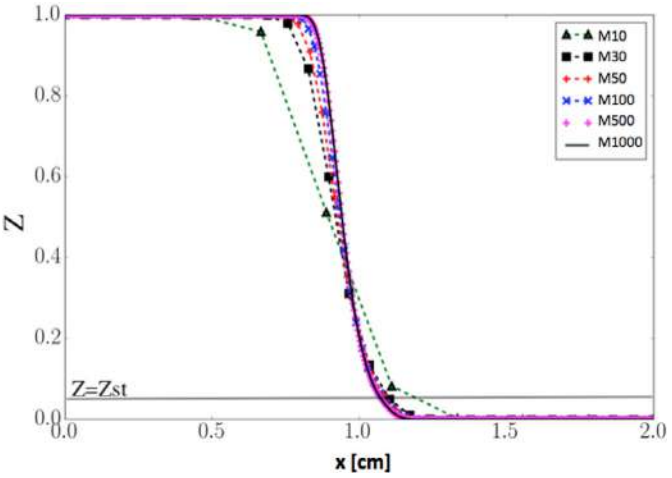

Fig. 3. Mixture fraction profiles obtained for the various meshes of Table 1, $a = 100\ s^{-1}$.

Table 1
List of test cases.

Name	Number of points	Δx [mm]	*RR*
M1000	1000	0.02	200
M500	500	0.04	100
M100	100	0.2	20
M50	50	0.4	10
M30	30	0.67	6
M10	10	2	2

flame front, as a function of the strain rate, and the temperature profile in the mixture fraction space for a strain rate of 250 s^{-1}. Both curves show that the 2-steps chemistry correctly predicts the flame shape and its response to strain, with only minor deviations from the reference case. The main difference is the value of the extinction strain rate, found to be higher with the 2-steps chemistry. However, the present study is restricted to the high-Da regime, i.e., far from extinction.

The test cases are summarized in Table 1. The distance between the two injection planes is 2 cm and the reactants are initially taken at ambient temperature and pressure. Pure methane and pure air are injected with velocities of 1.2 m s^{-1} and 0.8 m s^{-1} respectively, leading to a global equivalence ratio of about 15 and a strain rate of 100 s^{-1}. In these conditions the flame thickness δ_f, computed from the mixture fraction profile, is about 4 mm and the total heat release rate is 323 kW. Due to a low strain rate, this flame thickness is quite larger than what would be found in LES of real systems, but it features the same behavior if related to the flame resolution for a given flow resolution. Therefore, up to 6 different meshes are used, all with a uniform step size Δx, corresponding to a resolution ratio $RR = \delta_f / \Delta x$ in the range [2–200].

4. Results and analysis

Figure 3 shows the mixture fraction profile obtained for the different meshes. The flame is located at $Z = 0.05$, i.e., very close to the air stream. Even with only 10 points in the domain, a stable solution is obtained. As expected, the mixture fraction is filtered by the grid and the numerical evaluation of its gradient decreases with mesh coarsening. Note that CANTERA uses a first-order upwind discretization scheme, which introduces a dissipation error of the form $sin(k\Delta x)/k\Delta x$ for a harmonic function, where k is the wave number. The discretization error on derivatives then adds to the filtering effect, with a maximum of $2/\pi$ factor for the maximum discrete wave number. To better understand the flame response, Fig. 4 shows the corresponding heat release rate profiles. Here also the impact of grid filtering is very clear, with the decrease of the peak value and increase of the reaction zone width with mesh coarsening. Note that in case M10, the reaction zone is described with 1 point only, which confirms that the resolution of the reaction zone is not critical. The reason for this somewhat surprising, very robust behavior is linked to the specific property of diffusion flames of always burning at stoichiometry, i.e., at fixed stoichiometric values of temperature and reactant mixture fractions which, according to Eq. (4), only depend on the strain rate. Note that the reaction rate has a peaked profile and that its integral, not its derivative, are relevant. This explains why it may be represented with very few points, contrary to the thermal thickness which is based on a gradient and requires more points. Therefore, and contrary to premixed flames, a converged filtered solution may be obtained for any grid resolution, provided that the stoichiometric location is captured. This is indeed what can be observed in Fig. 4, where the peak of heat release rate is always close to the stoichiometric point.

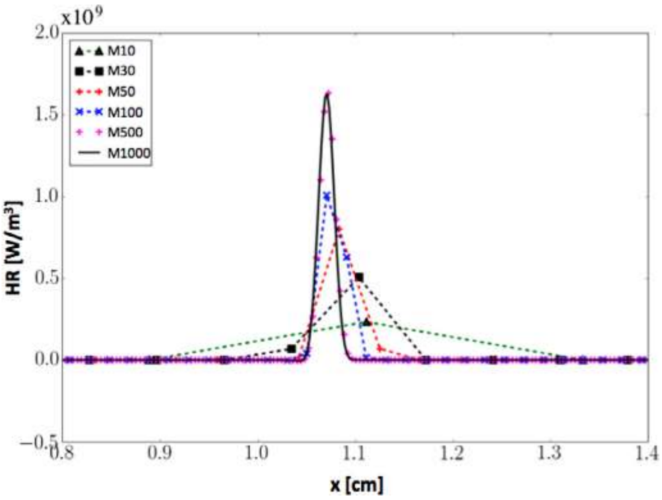

Fig. 4. Heat release rate profiles obtained for the various meshes of Table 1, $a = 100\ s^{-1}$.

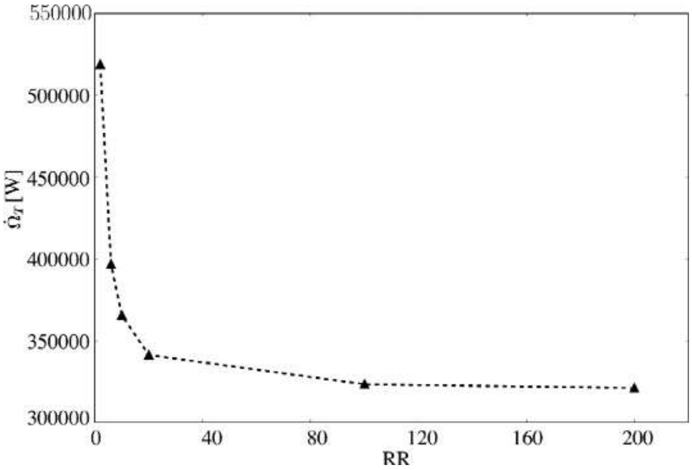

Fig. 5. Total heat release rate obtained for the various meshes of Table 1, as a function of *RR*.

The accuracy of the solution is now evaluated with the flame consumption rate (or equivalently total heat release rate $\dot{\Omega}_T$), plotted as function of the ratio *RR* in Fig. 5. Even if the simulation leads to a stable solution, deviations with the reference value appear already for $RR = 20$ and below. This is due to the under-estimation of

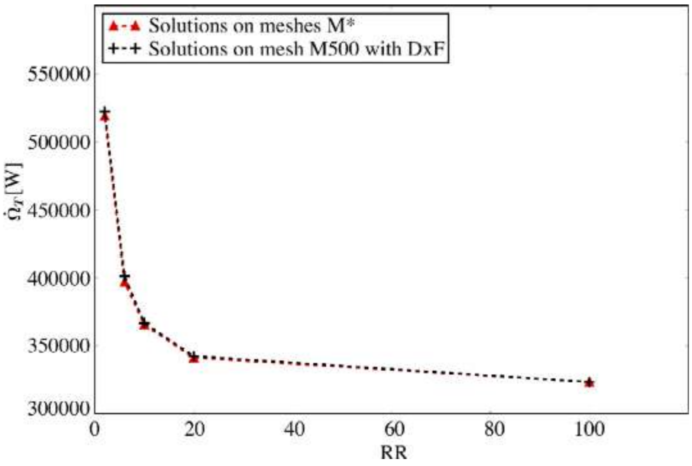

Fig. 6. Total heat release rate obtained on mesh M500 with the correction factor F, as a function of RR.

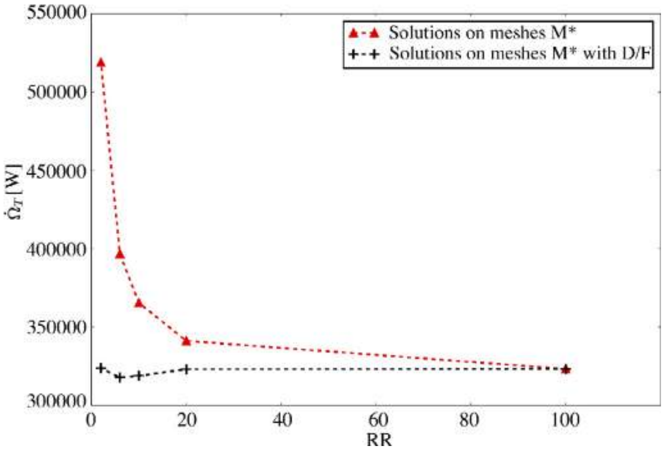

Fig. 7. Total consumption rate obtained for the various meshes of Table 2 with the correction factor $1/F$, as a function of RR.

the mixture fraction gradient, which can be interpreted as numerical over-diffusion. Consistently with Eq. (10), this over-diffusion leads to an increased consumption rate, up to a relative increase of 65% for mesh M10 ($RR = 2$).

To verify the assumption that the over-estimation of the flame consumption rate is solely due to numerical diffusion, the effect of mesh coarsening is now mimicked by introducing an effective diffusion coefficient D^* in the simulation with the reference fine mesh M1000. Following Eq. (10), the value of D^* is estimated from the solution obtained on the coarse meshes as:

$$F = \frac{D^*}{D} = \left(\frac{\dot{\Omega}_{T,M^*}}{\dot{\Omega}_{T,M1000}}\right)^2 \tag{14}$$

where M^* stands for the various meshes of Table 1. Taking mesh M1000 as the reference, the values of F obtained for the coarser meshes are summarized in Table 2, with a maximum of 2.57 for mesh M10. Multiplying all diffusivities by the same factor F and using the refined mesh, i.e., without numerical diffusion, the results of Fig. 6 are obtained. They show that indeed, changing diffusivities not only changes the consumption rate, but the behavior of the coarse mesh solutions is exactly retrieved.

The inverse exercise can then be performed, i.e., simulating the flame on the coarse meshes with modified diffusion coefficients to recover the reference consumption speed. This time all diffusion coefficients are divided by the factor F. Results plotted in Fig. 7 show that indeed the correct reference consumption rate is well retrieved. If the accuracy slightly decreases at low RR, the deviation never exceeds 3%, which is remarkable for $RR = 2$ for example. Again, this is due to the fact that the flame consumption rate is only driven by the diffusive flux at stoichiometry, which can be corrected even with only two points in the reaction zone provided that one point is close to stoichiometry.

Table 2
Values of the correction factor F for the meshes of Table 1.

Name	M500	M100	M50	M30	M10
F	1	1.113	1.27	1.505	2.575

5. Impact of thickening on the chemical structure of the flame

All calculations in the previous sections have been performed with a simple two-steps chemical scheme. It is therefore important to determine if the conclusions obtained for simple chemistry sill hold for more detailed chemistry. In particular, it can be questioned if mesh coarsening alters the chemical inner flame structure. Another possible issue is the stiffness of intermediate species which may raise difficulties if their diffusion coefficient is further decreased by F. In order to study these possible effects, another series of counterflow flames has been computed with semi-detailed, so-called Analytically Reduced Chemical (ARC) scheme. The conditions here correspond to high-pressure, methane-oxygen combustion encountered in rocket engines. In such conditions the flame is extremely thin, leading to small values of RR in LES of rocket engine combustion chambers.

ARC schemes are built from detailed chemistry, following several reduction steps starting with DRGEP, then lumping and finally applying the Quasi-Steady-State Assumption (QSSA) to decrease chemical stiffness. ARC schemes offer a good compromise between accuracy and computational cost and are well adapted to LES. All details may be found in Pepiot-Desjardins and Pitsch [50], Felden [51]. In the present case the ARC scheme was specifically derived for methane oxy-combustion. Starting from the Ramec [52] detailed scheme, a 14 transported species-, 4 QSS species- and 136 reactions-mechanism was obtained and validated on laminar diffusion flames at various strain rates with an error on the consumption rate staying below 1.5%. As in the previous section, counterflow flame simulations have all been performed with the solver CANTERA [46].

The distance between the two injection planes is here 1 cm. Pure methane and pure oxygen are injected at 280 K with the same mass flow rate, leading to a strain rate of 810 s^{-1} and a global equivalence ratio of 4. The pressure is set at 54 bar. In these conditions the flame thickness is 300 μm and the total heat release rate is 2020 kW. Up to 9 different uniform meshes have been used, with the number of points ranging from 30 to 1500, i.e., with RR, ranging from 0.9 to 45, respectively (see Table 3). All cases led to a converged flame solution, demonstrating that diffusion flames may be stably computed on very coarse meshes even with detailed chemistry.

Figure 8 shows the mixture fraction profiles obtained with the different meshes of Table 3. The mesh-filtering effect appears clearly, similarly to what was observed in simple chemistry cases. Two additional observations can be made, which are also true but less visible in the simple chemistry cases. First, it can be seen that the profiles are less steep on the fuel (left) side due to larger diffusion coefficients in this stream compared to the fuel stream, and as a consequence this zone is less sensitive to filtering. Second, note that all profiles except the M50 case, have a grid point close to stoichiometry. As explained in the previous section, this should impact the accuracy of the flame consumption rate prediction.

Table 3
Values of the correction factor *F* for ARC flames.

Name	M1500	M1000	M700	M500	M300	M200	M100	M50	M30
RR	45	30	21	15	9	6	3	1.5	0.9
F	1	1.01	1.03	1.04	1.08	1.12	1.19	1.25	1.46

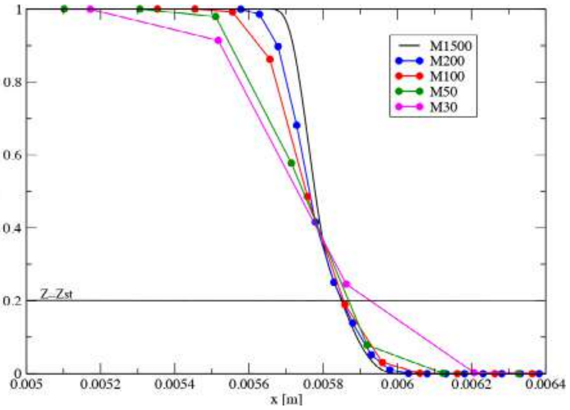

Fig. 8. Diffusion flames with ARC chemistry: mixture fraction profiles for the various meshes of Table 3.

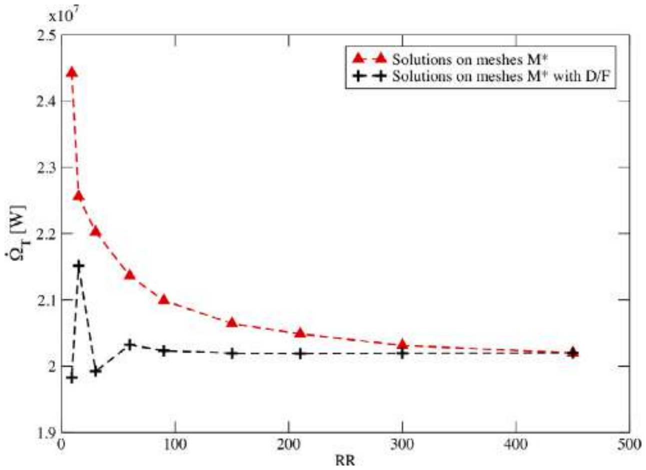

Fig. 9. Diffusion flames with ARC chemistry: total heat release rate obtained for the various meshes of Table 3, as a function of *RR*.

The total heat release rate obtained with the different meshes is shown in Fig. 9. Similarly to the simple chemistry cases, numerical diffusion due to mesh coarsening leads to an increase of the total heat release rate which is multiplied by about 1.46 for the coarsest mesh. The same correction is then applied, dividing all diffusion coefficients by a correction factor *F* calculated with Eq. (14), in order to compensate for the numerical diffusion. Table 3 gives the values of *F* for all cases. Compared to the simple chemistry cases, the *F* factors are slightly higher for equivalent *RR* values. Results are compared to the simulations without correction in Fig. 9. Similarly to the simple chemistry cases, the reduced diffusion coefficients allow to recover the correct heat release rate. Except for M50, the corrected consumption rate is recovered with less than 2% error. Case M50 is particular in the sense that it is the only one with no grid point close to stoichiometry: as explained in the previous Section, it is then impossible to obtain a correct evaluation of the reaction rate. In other words, using the same mesh resolution but with a point close to stoichiometry would allow to well predict the flame consumption speed with the *F* correction.

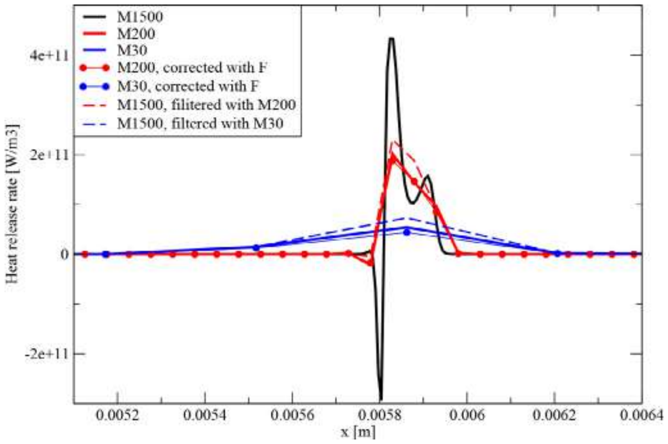

Fig. 10. Diffusion flames with ARC chemistry: heat release rate profiles for meshes M1500, M200 and M30.

These results indicate that the theoretical expressions derived in Section 2 still hold for more detailed chemistry diffusion flames, which may be controlled by acting on diffusion coefficients. They also confirm that a good prediction of the flame consumption rate can be obtained even on very coarse meshes, provided that a grid point is placed close to stoichiometry.

The final question to answer is about the description of the inner chemical structure of the flame. Indeed, ensuring an accurate prediction of the flame consumption rate is critical and a must for any model, but using detailed chemistry is useless if the chemical structure of the flame is not preserved. To elucidate this question, the flame structure obtained with M200 having $RR = 6$, and $M30$ having $RR = 0.9$ are compared to the reference flame computed on M1500.

The complex structure of methane-oxygen flames is first illustrated with the profile of the heat release rate, shown in Fig. 10. Three zones can be identified. On the methane side (left side in the plot), an endothermic zone marks dissociation of methane before entering the exothermic, double peak oxidation zone. The highest peak, close to stoichiometry, corresponds to the oxidation of the fuel species and the production of the major products, while the second lower peak on the oxygen side is related to the recombination of OH and O into H_2O.

The heat release rate obtained on meshes M200 and M30 appear much filtered by the coarse grid, with only 4 points and 1 point respectively in the profile. Despite this very low resolution, the heat release rate profile on M200 keeps the endothermic - exothermic double structure. It is slightly widened and all peaks are much lowered, but as reported in Table 3, the integral is only 1.12 higher than the reference value and the *F*-corrected profiles are very close to the non corrected ones. On mesh M30, the shape of the heat release rate is lost and the profile exhibits one single peak, which is the only possible structure with 1 point in the reaction zone. However, here again, and as demonstrated previously, the integral is not so far from the reference value and can be corrected. To elucidate this behavior, top-hat filters of size 50 μm, i.e., the step size of mesh M200 and 333 μm, i.e., the step size of mesh M30, have been applied to the reference solution and are compared to the M200 and M30 solutions in Fig. 10. In both cases, the filtered M1500 solutions appear to be remarkably close to the M200 and M30 profiles which confirms that the reaction rate, being evaluated around stoichiometry, does not introduce strong non-linearity.

The chemical structure of the flame is finally investigated with the species mass fraction profiles in the mixture fraction space, for the same 3 cases M1500, M200 and M30 in Fig. 11. The major species (Fig. 11, top) are very close for all cases, the deviations being mostly the result of mesh sampling. In Fig. 11, bottom, intermediate species are still very well captured with M200: although some species like O, H or HO2 have only one non-zero point, the peak location and value is correctly predicted for all species. The agreement is not so good with mesh M30, with deviations in peak level for H and H2, and peak location for HO2, OH and O. However, the OH species, often used as the flame marker, is reasonably well captured.

From the above simple and detailed numerical simulations, the following conclusions can be drawn:

- for a given strain rate, the flame solution in the mixture fraction space is insensitive to diffusion, and therefore to mesh filtering,
- because the flame thickness adapts to the numerically resolved strain rate, the numerical simulation of diffusion flames stays robust on coarse meshes even with *RR* below 1, without further artificial thickening,
- the error on flame consumption speed due to numerical diffusion may be corrected by acting on the diffusion coefficients,
- to correctly capture the inner chemical structure of the flame, about 5 grid points are needed to describe the reaction zone.

It must be reminded that the above conclusions only hold for high-Da flames, while low-Da flames do not raise such numerical issues. Note that the correction by *F* does not modify Da, i.e., preserves the flamelet regime.

6. Implications for turbulent combustion modeling

The properties of diffusion flames described in the above section allow to derive a Thickened Flame Approach for the modeling of turbulent non-premixed combustion in LES. As explained in the Introduction, the model must ensure that:

- the LES of the turbulent diffusion flame is numerically stable,
- the consumption speed, which controls the flame length and combustor efficiency, is predicted with sufficient accuracy,
- the inner chemical flame structure is correctly described for the prediction of pollutants or fuel effects.

Concerning numerical stability, the conclusions drawn in the previous Section bring the answer. It has been demonstrated that the simulation always leads to a stable solution even for very low mesh resolutions with *RR* below 1. Note that with the LES grid acting as a filter on the flow, the resolved strain rate decreases with mesh coarsening and consequently the flame thickness, which adapts to the resolved filtered flow, increases.

Concerning the accuracy of the prediction of the consumption speed, it has been demonstrated in the previous Sections that it can be recovered by applying a factor *F* on the diffusion coefficients. The remaining question is now about the determination of the value of *F*. To answer it, it is useful to come back to the sources of error on the consumption speed. They are of two kinds: the numerical error (ε_{num}) due to numerical diffusion as observed in the previous Sections, and the modeling error (ε_{sgs}) due to subgrid-scale flame-turbulence interaction.

The numerical error $\varepsilon_{num} = \dot{\Omega}_{T,num} - \dot{\Omega}_{T,exact}$ is easy to evaluate in the LES. Indeed, it is directly related to the ratio $F = D^*/D$ in-

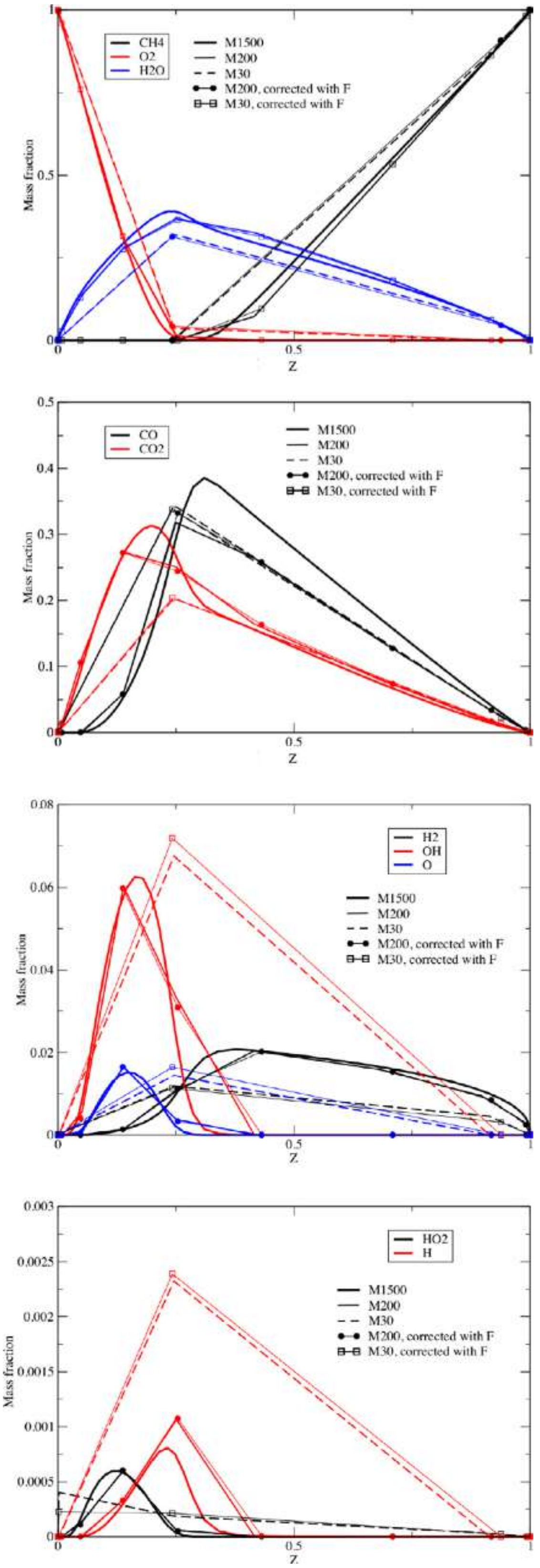

Fig. 11. Diffusion flames with ARC chemistry: species mass fraction profiles in the mixture fraction space, for meshes M1500, M200 and M30.

troduced in Eq. (14) as $\varepsilon_{num} = (F_{num}^2 - 1)\dot{\Omega}_{T,exact}$. To evaluate F_{num}, the relation between the resolved strain rate and the scalar dissipation at stoichiometry $\chi_{st} = C_{st}^2 a/\pi$ is used. As χ_{st} is proportional to the diffusion coefficient D, the correction factor F_{num} can be determined as:

$$F_{num} = \frac{C_{st}^2 a^{LES}/\pi}{\chi_{st}^{LES}} \tag{15}$$

where the superscript *LES* refers to values measured in the LES. If the mesh is sufficiently fine, $\chi_{st}^{LES} = C_{st}^2 a^{LES}/\pi$ and $F_{num} = 1$. If numerical diffusion appears, χ_{st}^{LES} decreases and $F_{num} < 1$.

The modeling error ε_{sgs} is more difficult to evaluate. It is the result of two subgrid-scale effects. First the subgrid-scale strain rate, which may be higher than the filtered strain rate, may increase the flame consumption rate. Second the subgrid-scale flame front wrinkling, by increasing the flame surface area, may also increase the flame consumption rate. Ignoring both effects leads to an underestimation of the flame consumption rate, which should be corrected by the application of a factor $F_{sgs} \leq 1$. The determination of F_{sgs} is a complex modeling question and is left for future work, which could be inspired by subgrid-scale modeling for premixed combustion.

While the numerical error depends on the already defined RR ratio measuring the flame resolution, the modeling errors depends on the Kolmogorov turbulent scale η resolution $RR_\eta = \eta/\Delta x$. For a given flame, high turbulence intensity leads to $RR_\eta \leq RR$, i.e., dominant modeling error, while in weakly turbulent flows $RR_\eta \geq RR$, i.e, dominant numerical error. The limit between the two situations is modulated by the flame scale which in the case of non-premixed combustion is driven by diffusion. This is also nuanced by the fact that diffusion flames may not adapt to the smallest scales of turbulence, when these are too fast compared to the flame time scale, as shown in Cuenot et al. [43].

The Thickened Flame model for non-premixed turbulent combustion finally consists in dividing all diffusion coefficients by $F_{LES} = F_{num} \times F_{sgs}$. Note that depending on the relative importance of the numerical and modeling errors, F_{LES} may be above or below 1, i.e., diffusion may be decreased or increased. It may also happen that $F_{LES} \approx 1$, which means in that case that numerical diffusion compensates subgrid-scale effects. This has been observed for example in Breda et al. [53] where LES with and without sub-grid scale turbulent combustion model gave similar results.

This approach will give an approximate description, considered acceptable in the context of LES, of the chemical structure of the flame provided that about 5 points are located in the reaction zone with one point close to stoichiometry. Whereas this resolution can be achieved or not depends on the Damköhler number of the filtered flame, possibly corrected with F_{LES}.

7. Conclusions

The specific properties of diffusion flames give them a very different behavior compared to premixed flames when computed on coarse meshes. Because they do not have any intrinsic thickness nor consumption speed, diffusion flames are more difficult to control. In the high-Damköhler regime, and for a given strain rate, the only controlling parameter is the diffusion coefficient. One positive consequence is that diffusion flames adapt to the resolved flow, i.e., to the mesh and do not require artificial thickening to stay numerically stable. Interestingly, and again due to the particular mixing and reacting process of diffusion flames, the consumption speed is found relatively insensitive to the mesh resolution and the error becomes significant for very low resolution only. These properties and flame behavior may be used to build a Thickened Flame concept for the modeling of non-premixed turbulent combustion in the framework of LES, ensuring flame resolution while preserving the combustion speed. The formulation is different from the premixed combustion Thickened Flame model, which will require to identify the flame regime in partially premixed combustion. Next step is now to determine and model the sub-grid scale flame-turbulence interaction, which is left for future work.

Declaration of Competing Interest

The authors declare that they have no known competing financial interests or personal relationships that could have appeared to influence the work reported in this paper.

Acknowledgments

This work was partly supported by the ANR under the project TIMBER ANR-14-CE23-0009.

References

[1] IEA, Energy Technology Perspectives 2020, IEA Paris https://www.iea.org/reports/energy-technology-perspectives-2020(2020).
[2] L.Y. Gicquel, G. Staffelbach, T. Poinsot, Large eddy simulations of gaseous flames in gas turbine combustion chambers, Prog. Energy Combust. Sci. 38 (2012) 782–817.
[3] F. Shum-Kivan, J.M. Santiago, A. Verdier, E. Riber, B. Renou, G. Cabot, B. Cuenot, Experimental and numerical analysis of a turbulent spray flame structure, Proc. Combust. Inst. 36 (2) (2015) 2567–2575.
[4] Y. Pei, S. Som, P. Kundu, G.M. Goldin, Large eddy simulation of a reacting spray flame under diesel engine conditions, SAE Tech. Paper (2015) 2015–01–1844.
[5] C.M. Roth, O.J. Haidn, A. Chemnitz, T. Sattelmayer, G. Frank, H. Frank, J. Zips, R. Keller, P.M. Gerlinger, D. Maestro, B. Cuenot, H. Riedmann, L. Selle, Numerical investigation of flow and combustion in a single element GCH4/GOx rocket combustor, 52nd AIAA/SAE/ASEE Joint Propulsion Conf. (2016). paper AIAA 2016–4995
[6] C.E. Baukal Jr, V.J. Gershtein, L. Xianming, Computational Fluid Dynamics in Industrial Combustion, CRC Press, 2000.
[7] N. Peters, Laminar diffusion flamelet models in non-premixed turbulent combustion, Prog. Energy Combust. Sci. 10 (1984) 319–339.
[8] S.K. Liew, K.N.C. Bray, J.B. Moss, A stretched laminar flamelet model of turbulent nonpremixed combustion, Combust. Flame 56 (2) (1984) 199–213.
[9] D.C. Haworth, M.C. Drake, R.J. Blint, Stretched laminar flamelet modeling of a turbulent jet diffusion flame, Combust. Sci. Tech. 60 (4–6) (1988) 287–318.
[10] D. Bradley, P.H. Gaskell, A.K.C. Lau, A mixedness-reactedness flamelet model for turbulent diffusion flames, Symp. (Int.) Combust. 23 (1) (1991) 685–692.
[11] H. Pitsch, E. Riesmeier, N. Peters, Stretched laminar flamelet modeling of a turbulent jet diffusion flame, Combust. Sci. Tech. 158 (1) (1988) 389–406.
[12] P.D. Nguyen, L. Vervisch, V. Subramanian, P. Domingo, Multidimensional flamelet-generated manifolds for partially premixed combustion, Combust. Flame 157 (1) (2010) 43–61.
[13] B.F. Magnussen, B.H. Hjertager, On mathematical modeling of turbulent combustion with special emphasis on soot formation and combustion, Symp. (Int.) Combust. 16 (1977) 719–729.
[14] I.S. Ertesvag, B.F. Magnussen, The eddy dissipation turbulence energy cascade model, Combust. Sci. Tech. 159 (2000) 213–235.
[15] A.Y. Klimenko, R.W. Bilger, Conditional moment closure for turbulent combustion, Prog. Energy Combust. Sci. 25 (1999) 595–687.
[16] M.J. Cleary, A.Y. Klimenko, A generalised multiple mapping conditioning approach for turbulent combustion, Flow, Turb. Combust. 82 (2009) 477.
[17] P.A. Libby, F.A. Williams, Strained premixed laminar flames under non adiabatic conditions, Combust. Sci. Tech. 31 (1–2) (1983) 1–42.
[18] P. Pantangi, A. Sadiki, J. Janicka, M. Mann, A. Dreizler, LES of premixed methane flame impinging on the wall using non-adiabatic flamelet generated manifold (FGM) approach, Flow, Turb. Combust. 92 (4) (2014) 805–836.
[19] P.C. Ma, H. Wu, M. Ihme, J.P. Hickey, Non adiabatic flamelet formulation for predicting wall heat transfer in rocket engines, AIAA J. 56 (6) (2018) 2336–2349.
[20] Y. Hu, R. Kurose, Non premixed and premixed flamelets LES of partially premixed spray flames using a two-phase transport equation of progress variable, Combust. Flame 188 (2018) 227–242.
[21] B.T. Bojko, P.E. DesJardin, On the development and application of a droplet flamelet-generated manifold for use in two-phase turbulent combustion simulations, Combust. Flame 183 (2017) 50–65.
[22] A. Andreini, D. Bertini, B. Facchini, S. Puggelli, Large-eddy simulation of a turbulent spray flame using the flamelet generated manifold approach, Energy Procedia 82 (2015) 395–401.
[23] M. Ihme, Y.C. See, LES flamelet modeling of a three-stream mild combustor: analysis of flame sensitivity to scalar inflow conditions, Proc. Combust. Inst. 33 (1) (2011) 1309–1317.
[24] J. Lamouroux, M. Ihme, B. Fiorina, O. Gicquel, Tabulated chemistry approach for diluted combustion regimes with internal recirculation and heat losses, Combust. Flame 161 (8) (2014) 2120–2136.

[25] O. Colin, F. Ducros, D. Veynante, T. Poinsot, A thickened flame model for large eddy simulations of turbulent premixed combustion, Phys. Fluids 12 (2000) 1843–1863.

[26] T. Jaravel, E. Riber, B. Cuenot, G. Bulat, Large eddy simulation of an industrial gas turbine combustor using reduced chemistry with accurate pollutant prediction, Proc. Combust. Inst. 36 (2017) 3817–3825.

[27] A. Felden, P. Pepiot, L. Esclapez, E. Riber, B. Cuenot, Including analytically reduced chemistry (ARC) in CFD applications. acta astronautica, Acta Astronaut. 158 (2019) 444–459.

[28] C. Fureby, A comparative study of flamelet and finite rate chemistry LES for a swirl stabilized flame, J. Eng. Gas Turbines Power 134 (4) (2012).

[29] F. Proch, A.M. Kempf, Modeling heat loss effects in the large eddy simulation of a model gas turbine combustor with premixed flamelet generated manifolds, Proc. Combust. Inst. 35 (3) (2015) 3337–3345.

[30] B. Fiorina, R. Mercier, G. Kuenne, A. Ketelheun, A. Avdic, J. Janicka, D. Geyer, A. Dreizler, A. Alenius, C. Duwig, P. Trisjono, K. Kleinheinz, S. Kang, H. Pitsch, F. Proch, F. Cavallo Marincola, A. Kempf, Challenging modeling strategies for LES of non-adiabatic turbulent stratified combustion, Combust. Flame 162 (11) (2015) 4264–4282.

[31] L. Hakim, T. Schmitt, S. Ducruix, S. Candel, Dynamics of a transcritical coaxial flame under a high-frequency transverse acoustic forcing: influence of the modulation frequency on the flame response, Combust. Flame 162 (10) (2015) 3482–3502.

[32] P. Wolf, G. Staffelbach, A. Roux, L. Gicquel, T. Poinsot, V. Moureau, Massively parallel LES of azimuthal thermo-acoustic instabilities in annular gas turbines, C. R. Méc. 337 (2009) 385–394.

[33] E. Lo Schiavo, D. Laera, E. Riber, L. Gicquel, T. Poinsot, Effects of liquid fuel/wall interaction on thermo-acoustic instabilities in swirling spray flames, Combust. Flame 219 (2020) 86–101.

[34] M. Philip, M. Boileau, R. Vicquelin, E. Riber, T. Schmitt, B. Cuenot, D. Durox, S. Candel, Large eddy simulations of the ignition sequence of an annular multiple-injector combustor, Proc. Combust. Inst. 35 (2015) 3159–3166.

[35] F. Collin-Bastiani, E. Riber, B. Cuenot, Study of inter-sector spray flame propagation in a linear arrangement of swirled burners, Proc. Combust. Inst. 38 (4) (2021) 6299–6308.

[36] Q. Malé, G. Staffelbach, O. Vermorel, A. Misdariis, F. Ravet, T. Poinsot, Large eddy simulation of pre-chamber ignition in an internal combustion engine, Flow, Turbul. Combust. 103 (2019) 465–483.

[37] L. Gallen, A. Felden, E. Riber, B. Cuenot, Lagrangian tracking of soot particles in LES of gas turbines, Proc. Combust. Inst. 37 (2019) 5429–5436.

[38] J.P. Légier, T. Poinsot, D. Veynante, Dynamically thickened flame LES model for premixed and non-premixed turbulent combustion, Proc. Summer Prog. 12 (2000) 157–168.

[39] J.P. Légier, T. Poinsot, B. Varoquié, F. Lacas, D. Veynante, Large eddy simulation of a non-premixed turbulent burner using a dynamically thickened flame model, IUTAM Symp. on Turbulent Mixing and Combustion (2002), pp. 315–326.

[40] B. Varoquié, Légier, F. J. P. Lacas, D. Veynante, T. Poinsot, Experimental analysis and large eddy simulation to determine the response of non-premixed flames submitted to acoustic forcing, Proc. Combust. Inst. 29 (2) (2002) 1965–1970.

[41] M.T. Shang, W.P. Zhang, K. Zhang, J.R. Fan, Three-dimensional full compressible large-eddy simulation of non-premixed combustion using dynamically thickened flame model, J. Combust. Sci. Tech. 16 (6) (2010) 496–502.

[42] J. Yang, L. Yubing, G. Apeng, LES of the ignition process of non-premixed CH_4based on dynamic thickened flame model, Adv. Eng. 126 (2017) 219–226.

[43] B. Cuenot, F.N. Egolfopoulos, T. Poinsot, An unsteady laminar flamelet model for non-premixed combustion, Combust. Theory Model. 4 (1) (2000) 77–97.

[44] U. Niemann, K. Seshadri, F.A. Williams, Accuracies of laminar counterflow flame experiments, Combust. Flame 162 (2015) 1540–1549.

[45] B. Cuenot, T. Poinsot, Asymptotic and numerical study of diffusion flames with variable Lewis number and finite rate chemistry, Combust. Flame 104 (1996) 111–137.

[46] D.G. Goodwin, Cantera C++ User's Guide, California Institute of Technology, 2002.

[47] B. Franzelli, E. Riber, M. Sanjosé, T. Poinsot, A two-step chemical scheme for kerosene-air premixed flames, Combust. Flame 157 (2010) 1364–1373.

[48] B. Franzelli, Impact of the Chemical Description on Direct Numerical Simulations and Large Eddy Simulations of Turbulent Combustion in Industrial Aero-engines, Univ. Toulouse, 2011 Doctoral dissertation.

[49] G.P. Smith, D.M. Golden, M. Frenklach, N.W. Moriarty, B. Eiteneer, M. Goldenberg, C.T. Bowman, R.K. Hanson, S. Song, W.C. Gardiner Jr., V.V. Lissianski, Z. Qin, GRI-Mech 3.0, http://www.me.berkeley.edu/gri_mech/, 2021.

[50] P. Pepiot-Desjardins, H. Pitsch, An efficient error-propagation-based reduction method for large chemical kinetic mechanisms, Combust. Flame 154 (2008) 67–81.

[51] A. Felden, Development of Analytically Reduced Chemistries (ARC) and Applications in Large Eddy Simulations (LES) of Turbulent Combustion, Univ. Toulouse, 2017 Doctoral dissertation.

[52] E.L. Petersen, D.F. Davidson, R.K. Hanson, Kinetics modeling of shock-induced ignition in low-dilution CH_4/O_2 mixtures at high pressures and intermediate temperatures, Combust. Flame 117 (1999) 272–290.

[53] P. Breda, M. Hansinger, M. Pfitzner, Chemistry computation without a sub-grid PDF model in LES of turbulent non-premixed flames showing moderate local extinction, Proc. Combust. Inst. 38 (2) (2021) 2655–2663.

4.5.3 Application in AVBP

The behaviour obtained for both simple and complex chemistry in 1D CANTERA flames, in agreement with theory, is now checked in AVBP. The F expression is recalled here (note the different writing conventions for F in Section 4.5.1 and F_M in the paper: $F = 1/F_M$, so that $F > 1$):

$$F = \frac{D^*}{D} = \left(\frac{\dot{\omega}_{M^*}}{\dot{\omega}_{REF}}\right)^2 \tag{4.23}$$

In his thesis work, Shum-Kivan suggested that the behaviour would be the same in AVBP. However the numerics employed in both solvers are rather different and may act differently on the solutions. In the following the numerical schemes used for convection and diffusion are respectively Lax-Wendroff [Lax and Wendroff, 1960] and the 2Δ Galerkin, which are 2nd order in space and are known to be quite dissipative.

The same numerical setup as in Section 4.4.1, for the simulation of 2D counterflow diffusion flames with the same strain rate of $a_{mean} = 809 s^{-1}$, is used along with the ARC chemistry derived for the CONFORTH configuration in Section 4.3.1 (note that is is also the same ARC scheme as presented in the paper section 5 "Impact of thickening on the chemical structure of the flame"). No SGS model is activated as laminar flames are considered and, as the study focuses on diffusion, no artificial viscosity is applied in the flame zone.
As in CANTERA, several meshes are considered, from the reference refined case where the thermal flame thickness is resolved until a very coarse mesh, close to the crash limit. Table 4.8 sums up the obtained integrated heat release rate depending on the mesh resolution, and the subsequent F factor calculated with Eq. 4.23.

Case	$\Delta x [\mu m]$	Normalized $\dot{\omega}_T$	F
REF	1	1	1
COARSE_5	5	0.997	0.994
COARSE_10	10	1.04	1.077
COARSE_20	20	1.40	1.971
COARSE_30	30	1.79	3.200

Table 4.8: Integrated heat release rate normalized with the reference value, obtained in AVBP 2D counterflow diffusion flames depending on the mesh resolution.

A similar behaviour as in the CANTERA simulations is obtained: the mesh under-resolution induces numerical diffusion which increases the integral of the heat release rate. Notice that case COARSE_5 exhibits a really similar total heat release rate compared to the reference case, demonstrating mesh convergence. This case does not need any F correction and is omitted in the following.
The correction factors F computed with Eq. 4.23 (denoted F_5, F_{10}... afterwards) can then be applied directly through the Schmidt and Prandtl numbers of the species and mixture. As the objective is to counter-diffuse, Sc_k and Pr are multiplied by F, which is equivalent to decrease the diffusive fluxes. Results from simulations run with the modified Sc_k^* and Pr^* numbers are reported in Table 4.9.
It seems that in AVBP the application of F does not fully have the expected effect. Even though it improves the results (normalized integral of heat release rate are lower than without

Case	$\Delta x[\mu m]$	Normalized $\dot{\omega}_T$
REF	1	1
COARSE_10_F	10	1.01
COARSE_20_F	20	1.24
COARSE_30_F	30	1.65

Table 4.9: Integrated heat release rate normalized with the reference value, obtained in AVBP 2D counterflow diffusion flames depending on the mesh resolution, after application of the F factors of Tab. 4.8 to the diffusion fluxes.

correction), the flames are still over-diffused and their consumption rate is not well recovered, contrary to what was found with CANTERA. The explanation comes from the numerics in AVBP which induce more numerical diffusion and counteract the F correction.

To verify this explanation, the effect of F is tested the other way around, applying over-diffusion with $1/F < 1$ to flames resolved on the reference mesh, *i.e.*, with minimum numerical error. The case named REF_F_30 uses $F_{30} = 3.2$ of case COARSE_30, now dividing the original Sc_k and Pr number by F_{30}. This gives the results presented in Table 4.10.

Case	$\Delta x[\mu m]$	Normalized $\dot{\omega}_T$
REF	1	1
COARSE_30	30	1.79
REF_F_30	1	1.98

Table 4.10: Integrated heat release rate normalized with the reference value, obtained in AVBP 2D counterflow diffusion flames on meshes REF, COARSE_30 and REF after application of $1/F_{30}$ factor to the diffusion fluxes.

Here the effect of over-diffusion is indeed well recovered, as the normalized integral of the heat release rate on the reference mesh is well increased with the application of $1/F_{30}$, and close to the case COARSE_30 although slightly higher. This means that the effect of applying the thickening factor F to diffusion only is well recovered in AVBP and consistent with theory, provided that the numerical error stays limited. It can be therefore concluded that in order to apply counter-diffusion in AVBP, as possibly demanded by the thickened flame approach, it is necessary to use numerical schemes with limited numerical diffusion.
This was tried with the TTGC scheme (introduced in Section 2.6.1) which is known to be less dissipative than Lax-Wendroff, but however in absence of artificial viscosity, it led quickly to a crash. Therefore finding the good balance between numerical stability and not too much dissipation is quite tough and should be a main concern to develop a diffusion flame model.
Note however that the full model, including also F_Λ and F_Π will rarely lead to an overall F factor higher than 1, *i.e.* to counter-diffusion in 3D turbulent diffusion flames, as tested in [Maestro et al., 2019].

Chapter 5

Wall-modelled LES for heat transfer prediction

Heat transfer occurring at the walls is one of the critical parameters in the design of a rocket engine. Indeed, the extreme temperature and pressure resulting from the propellant combustion induce very high temperature at the engine walls. Standard materials used in rocket engines cannot withstand these extreme conditions and require either cooling, using for example regenerative cooling systems, or wall protection with for example layers of ablative material.

To size efficiently these thermal management techniques during the design phase, one must predict with precision the friction and the heat flux at the wall. This can be achieved with numerical simulation with good accuracy provided that the mesh is sufficiently refined in the near-wall region. However the boundary layer found in most turbulent reacting flows of interest is very thin with sharp gradients at the wall, requiring a very refined mesh in the near-wall region which usually leads to unacceptable computing costs in LES [Piomelli, 2008, Chapman and Kuhn, 1986, Choi and Moin, 2012].

The alternative is to use wall models (WMLES) allowing to avoid the mesh refinement near the wall by applying a wall-law describing analytically the velocity and temperature profiles in the boundary layer. Two main families of modeling techniques are commonly distinguished, as recalled in [Larsson et al., 2016]. The first one is the hybrid LES/RANS approach, where the inner turbulent boundary layer is refined and solved with RANS equations (less expensive), while the external part of the boundary layer is solved with the LES formulation. The second one is the wall-stress-models, where only LES equations are solved, and a model is applied in the first wall cell (sometimes beyond) in order to determine the fluxes. Wall-stress-models are often based on RANS-like models. The first approach is not investigated in this work, so that in the following WMLES denotes only wall-stress-models.

Many still open questions make the modeling of the boundary layer a challenging topic in LES. Depending of the nature of the problem, various wall-laws already exist which go beyond the standard wall-law (an algebraic model). For example, the axial pressure gradient driving the flow, is often considered negligible. In the context of LRE, this is usually an acceptable assumption in the combustion chamber, but not in the nozzle. In this context, other models such as the Afzal's law (widely developed and implemented in AVBP in [Zhang, 2019], or more recent models [Wilhelm et al., 2021] are better suited.

Other phenomena that are of interest for the modeling and prediction of wall fluxes are developed in this chapter. After a sum up of the boundary layer theory and wall-law concepts in Section 5.1, a study concerning the coupling between the sub-grid scale model and the standard wall-law is proposed in Section 5.2. Finally the impact of the presence of a reacting multi-species mixture in the boundary layer and the subsequent wall fluxes, a topic directly linked to the previous chapters about chemistry and to the applications presented in Part IV, is explored in Section 5.3.

5.1 Wall-Modelled LES (WMLES)

Before describing the work that was conducted on this topic, some key theoretical elements are introduced. This section is not intended to be exhaustive but aims to introduce the main concepts of boundary layer theory [Schlichting and Gersten, 1979] and wall-laws, which will be useful in the next sections.

5.1.1 Turbulent boundary layer theory

In a flow constrained by solid walls, the turbulent boundary layer ("TBL") is the near-wall region of thickness δ. This boundary layer is itself divided into the external zone and the internal zone, the second one being also divided into three others: the viscous sub-layer, the buffer layer and the inertial or more often called logarithmic sub-layer. Figure 5.1 sums up these different zones within the TBL.

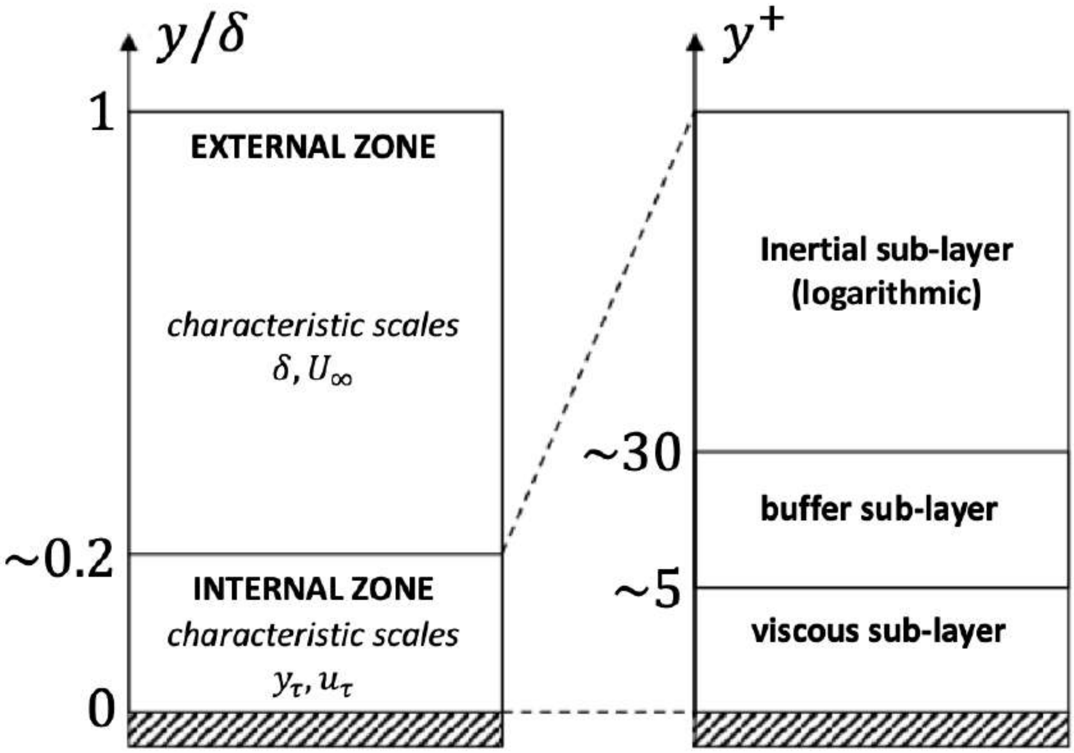

Figure 5.1: General description of the turbulent boundary layer (translated from [Cabrit, 2010])

In boundary layer theory, wall-units are often used for sake of scaling the problem to provide a universal vision of the flow behaviour in the near-wall region.

The characteristic scales of the internal zone of the boundary layer are the viscous (or friction) scale δ_v, the friction velocity u_τ and the friction temperature T_τ:

$$\delta_v = y_\tau = \frac{\nu_w}{u_\tau}, u_\tau = \sqrt{\frac{\tau_w}{\rho_w}}, T_\tau = \frac{q_w}{\rho_w C_{p,w} u_\tau} \tag{5.1}$$

where the subscript "w" denotes wall quantities. Then, the physical values of wall distance y, velocity u and temperature T are turned into wall-units, written with the superscript "+":

$$y^+ = \frac{y}{\delta_v} = \frac{\rho_w u_\tau y}{\mu_w}, u^+ = \frac{u}{u_\tau}, T^+ = \frac{T_w - T}{T_\tau} \tag{5.2}$$

The friction flux is computed as:

$$\tau_w = \mu_w \left.\frac{\delta u}{\delta y}\right|_w \tag{5.3}$$

Similarly, the heat flux reads:

$$q_w = \lambda_w \left.\frac{\delta T}{\delta y}\right|_w \tag{5.4}$$

5.1.2 Wall-law concepts

As already introduced, the idea behind the use of a wall-law is to avoid mesh refinement (directly related to the computation cost) that a fully resolved (*i.e.* without model) boundary layer would require. Instead, a wall-law can accommodate a relatively coarse mesh at the near-wall region with typical values of y^+ for the first off-wall grid point from 50 to 200. The whole stake of the wall-laws is to return the correct fluxes (friction and heat) that would have been returned by the direct integration of the Navier-Stokes equations on a fine near-wall grid (WRLES).

Most of the wall-law models are based on algebraic relations linking the flow quantities at the first off-wall node with the chosen boundary condition at the wall. Other visions also exist, for example a mix between RANS and LES (ZDES for example), but they are not investigated in this work. Figure 5.2 shows the general principle of a wall-law.

The model uses both values of the outer flow (at the first off-wall node denoted by subscript "1") and at the wall: temperature, velocity either for slip or no-slip condition, mass fractions (Y_k)... A slip condition means that a non-physical tangential velocity exists at the wall, while a no-slip condition means that all velocity components are null (it is physically true) at the wall and is therefore used in WRLES.

The standard two-layers velocity wall-law [Launder and Spalding, 1974] is here recalled:

$$\begin{aligned} u^+ &= y^+ && \text{if } y^+ < y_c^+ \\ u^+ &= \frac{1}{\kappa}\ln(y^+) + B && \text{if } y^+ > y_c^+ \end{aligned} \tag{5.5}$$

with B the Van Driest constant, $B = 5.2$ for external flows and $B = 5.5$ for internal flows and $\kappa = 0.41$ is the Von Kármán constant.

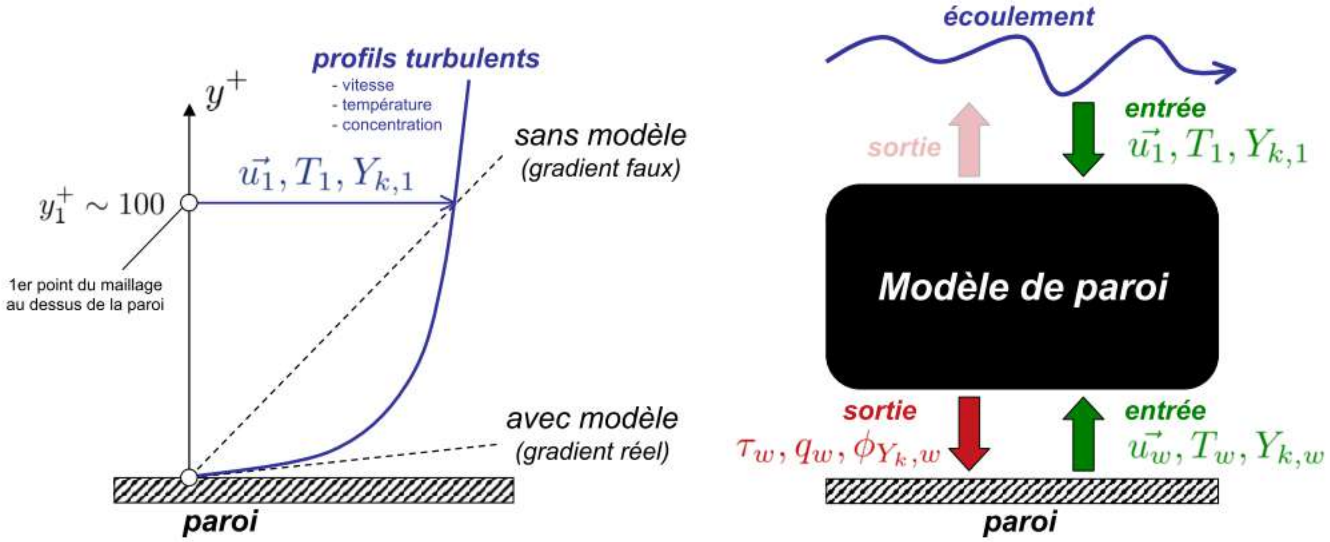

Figure 5.2: Wall-law principle (from [Cabrit, 2010]).

For the thermal boundary layer, one of the most usual is the Kader law [Kader, 1981], which reads:

$$\begin{aligned} T^+ &= y^+ && \text{if } y^+ < y_c^+ \\ T^+ &= 2.12\ln(y^+) + \beta && \text{if } y^+ > y_c^+ \end{aligned} \tag{5.6}$$

with β a function of the Prandtl number:

$$\beta = (3.85\,\mathrm{Pr}^{\;1/3} - 1.3)^2 + 2.21\ln(\mathrm{Pr}) \tag{5.7}$$

In AVBP, the switch between the linear and logarithmic laws is done at the critical value $y_c^+ = 11.445$.

From u^+ and T^+, Eq. 5.2 is used to find u_τ and T_τ. Finally, the wall fluxes are computed thanks to Eq. 5.1 as:

$$\tau_w = \rho_w u_\tau^2 \tag{5.8}$$

$$q_w = \rho_w C_{p,w} u_\tau T_\tau \tag{5.9}$$

In the LES framework, a recurrent topic is the determination of the best adapted internal flow quantities to be linked to the wall law. Indeed the LES velocity contains the resolved part of the turbulent fluctuation, which depends strongly on the subgrid-scale turbulent model, whereas wall laws describe boundary layers in steady state. This aspect is specifically addressed in Section 5.2.

The coupled wall-law

The standard wall-law was built for standard cases and mainly in the framework of isothermal flows. However in combustion chambers high temperature burnt gases reach the walls which are cooled, therefore at much lower temperature inducing strong temperature gradients at the walls. Furthermore this temperature gradient may trigger chemical reactions in the multi-species mixture reaching the wall. A direct consequence of the high temperature gradient is a high density gradient, inducing flow motion under the effect of dilatation, *i.e.*, a modified velocity profile at the wall. At the end, both temperature and velocity wall profiles are strongly coupled and Cabrit ([Cabrit and Nicoud, 2009]) developed a coupled wall law which is used in this work. It is notably able to take into account significant density/temperature variations, molecular Prandtl number effects and chemical reactions. However in its current implementation in AVBP and to spare computational cost, the chemical reactions are not taken into account in the coupled wall law.

The main features of the coupled wall-law, as implemented in AVBP, are recalled here.

Equations 5.5 and 5.6 are replaced by:

$$\left\{\begin{array}{ll} \left\{\begin{array}{ll} u^+ = y^+ & \text{if } y^+ < y_c^+ \\ \frac{2}{Pr_t B_q}\left(\sqrt{1-K)B_q} - \sqrt{\frac{T}{T_w}}\right) = \frac{1}{\kappa}\ln y^+ + B & \text{if } y^+ > y_c^+ \end{array}\right. & \\ T^+ = (\mathrm{Pr}\, y^+)\exp(\Gamma) + (\mathrm{Pr}_t\, u^+ + K)\exp(1/\Gamma) & \forall y^+ \end{array}\right. \tag{5.10}$$

with $B_q = T_\tau / T_w$ and Γ is a damping function (to smooth the T^+ profile in the buffer layer) written as:

$$\Gamma = -\frac{10^{-2}(\mathrm{Pr}\, y^+)^4}{1 + 5\,\mathrm{Pr}^3\, y^+} \tag{5.11}$$

and K writes:

$$K = \beta - \mathrm{Pr}_t\, B\left(\frac{\mathrm{Pr}_t}{\kappa} - 2.12\right)(1 - 2\ln(20)) \tag{5.12}$$

where β was previously introduced with Eq. 5.7. The system of Eq. 5.10 is solved thanks to a Brent algorithm RE [Brent, 1993].

The improvement of wall fluxes prediction brought by the coupled wall-law was already demonstrated in the framework of AVBP in [Potier, 2018], and is therefore not shown again here. In this work, we focus however on the influence of chemical activity on the wall fluxes, which was not investigated so far. This aspect is developed in Section 5.3.

5.2 Influence of the sub-grid scale turbulence model

It was previously observed in recent work at CERFACS ([Potier, 2018], [Maestro, 2018]) that in the framework of WMLES, the choice of the SGS turbulence model may impact the predicted wall fluxes, both friction (τ_w) and heat (q_w). This is also reported in the literature as in [Rezaeiravesh et al., 2019] or [Bae et al., 2019]. Models that are considered as "best practice" in AVBP, like WALE [Nicoud and Ducros, 1999] and Sigma [Nicoud et al., 2011], were developed for resolved boundary layers with a turbulent viscosity built to vanish when approaching the wall as the inner boundary layer is a laminar pure-shear flow. However this behaviour is not valid anymore for WMLES, which represents the vast majority of computations of industrial flows due to the lower computational cost. Therefore the impact of part of the turbulent structures which are neither solved by the grid nor modeled by the SGS model, is missing. From this observation the idea of creating a "wall-law with sub-grid scale model" has emerged.

This topic is developed in the next section, which reproduces the article *"Stochastic forcing for Sub-Grid Scale models in Wall-Modeled Large Eddy Simulation"* [Blanchard et al., 2021], now published in the journal *Physics of Fluids*.

5.2.1 Paper published in *Physics of Fluids*

Physics of Fluids

Stochastic forcing for sub-grid scale models in wall-modeled large-eddy simulation

Cite as: Phys. Fluids **33**, 095123 (2021); https://doi.org/10.1063/5.0063728
Submitted: 16 July 2021 . Accepted: 06 September 2021 . Published Online: 24 September 2021

S. Blanchard, N. Odier, L. Gicquel, B. Cuenot, F. Nicoud, et al.

AIP Publishing

Physics of Fluids ARTICLE scitation.org/journal/phf

Stochastic forcing for sub-grid scale models in wall-modeled large-eddy simulation

Cite as: Phys. Fluids **33**, 095123 (2021); doi: 10.1063/5.0063728
Submitted: 16 July 2021 · Accepted: 6 September 2021 ·
Published Online: 24 September 2021

S. Blanchard,[1,2,a)] N. Odier,[2] L. Gicquel,[2] B. Cuenot,[2] and F. Nicoud[3]

AFFILIATIONS
[1]CNES, Launchers Directorate, 52 rue Jacques Hillairet, 75612 Paris Cedex, France
[2]CERFACS, 42 Avenue Gaspard Coriolis, Toulouse Cedex 1 31057, France
[3]IMAG, University of Montpellier, CNRS, 34090 Montpellier, France

[a)]Author to whom correspondence should be addressed: blanchard@cerfacs.fr

ABSTRACT

In the framework of wall-modeled large-eddy simulation (WMLES), the problem of combining sub-grid scale (SGS) models with the standard wall law is commonly acknowledged and expressed through multiple undesired near-wall behaviors. In this work, it is first observed that the static Smagorinsky model predicts efficiently the wall shear stress in a wall-modeled context, while more advanced static models like wall-adapting local eddy (WALE) viscosity or Sigma with proper cubic damping fail. It is, however, known that Smagorinsky is overall too dissipative in the bulk flow and in purely sheared flows, whereas the two other models are better suited for near-wall flows. The observed difficulty comes from the fact that the SGS model relies on the filtered velocity gradient tensor that necessarily comes with large errors in the near-wall region in the context of WMLES. Since the first off-wall node is usually located in the turbulent zone of the boundary layer, the turbulent structures within the first cell are neither resolved by the grid nor represented by the SGS model, which results in a lack of turbulent activity. In order to account for these subgrid turbulent structures, a stochastic forcing method derived from Reynolds-averaged Navier–Stokes (RANS) turbulence models is proposed and applied to the velocity gradients to better estimate the near-wall turbulent viscosity while providing the missing turbulent activity usually resulting from the WMLES approach. Based on such corrections, it is shown that the model significantly improves the wall shear stress prediction when used with the WALE and Sigma models.

I. INTRODUCTION

In fluid dynamics, turbulence is a complex phenomenon characterized by the motion, the creation, and the dissipation of different scales, from the largest to the smallest eddies. Today, direct numerical simulation (DNS) allows one to numerically study with the highest precision turbulence because the mesh is fine enough to capture the smallest eddies (Kolmogorov scale) without any need of modeling. However, this requires huge computational resources: DNS is therefore restricted to academic cases like homogeneous isotropic turbulence (HIT) or channel flows at moderate Reynolds numbers. When dealing with industrial applications, DNS is too expensive and modeling is needed. In this specific context, the large-eddy simulation (LES) modeling approach has shown successes by resolving the largest structures while modeling the smallest ones that are spatially filtered by the grid size and known to be computationally expensive to resolve.[1] The smallest eddies are therefore modeled by a so-called sub-grid scale (SGS) model to close the problem, which accounts for the energy transfer between the resolved and the modeled scales, following the well-known Kolmogorov energy cascade theory.[2]

Even if LES has proved its capability to compute complex turbulent flows,[3,4] wall-bounded flows remain a challenge and induce a large computational cost. Indeed, with increasing Reynolds numbers, small turbulent structures in the near-wall region still lead to strong mesh requirements, and the cost of LES approaches the cost of DNS. Chapman[5] estimated that the inner layer of the boundary layer (about 20% of its height) scales with $Re^{1.8}$. This order of magnitude has been updated by Choi and Moin,[6] where the authors suggest even a higher cost. In industrial flows where the Reynolds number can easily reach 1×10^6, this makes LES unaffordable to accurately resolve the boundary layer characteristic dynamics, that is, with the so-called wall-resolved LES (WRLES) approach.

To alleviate the cost induced by this specific flow region, the concept of wall-modeled LES (WMLES) is often put forward. Several ways currently exist to model wall flows, and the reader is refereed to

Larsson *et al.*[7] and Bose and Park[8] for recent overviews of the available methods. Among them, a widely used approach is the wall stress model, where LES is used everywhere in the domain with dedicated wall functions and models. Wall stress models can be developed in a physical sense, trying to reproduce the real fluid behavior known thanks for experiments or DNS, such as the classic log-law.[9] However, the context of WMLES is also prone to numerical errors, and mathematical-based models are developed to circumvent this problem, like in Nicoud *et al.*[10] This article focuses on wall stress models, which we refer to as WMLES from here on.

This latter framework however leads to specific difficulties related to the coupling between wall laws and SGS models. This point has been recently discussed in Rezaeiravesh *et al.*,[11] Bae *et al.*,[12] and Vanna.[13] In those works, the authors indicate that the SGS contribution must be non-zero for a coarse grid at the wall. This means that the choice of the SGS model is a crucial parameter for the wall stress prediction and has consequences on the so-called log-layer mismatch problem.[14–16] This well-known phenomenon leads to potentially large errors on the prediction of the wall shear stress and can indeed come from not only SGS influence, but also numerical scheme choice[17] or the treatment of the boundary condition.[18] In the present study, one focuses on SGS models making use of the gradient hypothesis and more specifically the static Smagorinsky,[19] wall-adapting local eddy viscosity (WALE),[20] and Sigma[21] models. The static Smagorinsky model has been derived for isotropic turbulence, while WALE and Sigma have been derived in a wall-resolved context, to provide an accurate turbulent viscosity behavior close to the wall. In a wall-modeled context, Jaegle *et al.*[22] however indicated that the standard wall law gives better results in combination with the Smagorinsky model because it provides more turbulent viscosity at the wall. On the contrary, WALE and Sigma both have the property to vanish for pure shear flows and follow the physical y^3 damping function near the wall.

However, although the Smagorinsky model has the desired property of providing a non-zero viscosity at the wall in WMLES, it is known to be too dissipative in the bulk flow, decreasing the overall LES quality in either WRLES or WMLES context. WALE and Sigma on the other hand show usually good results in the bulk flow, in both non-reactive and reactive cases whenever subject to pure shear, rotation, and contraction. In order to provide accurate LES results both in the bulk flow and in the near-wall region in a wall-modeled context, consistent SGS models, and wall-law coupling procedures must therefore be developed. This idea is not new, and the literature provides several examples investigating this problem.[13,23–26] Note also that the coupling of SGS models with other kind of physics is a general concern in LES, for example, in the case of particle-laden flows (including the near-wall problematic), as suggested by Marchioli,[27] Bassenne *et al.*,[28] and Johnson *et al.*[29]

This paper proposes a coupling strategy to improve the behavior of existing advanced static models when used in a WMLES context. Main ideas for this work come from stochastic forcing methods as proposed in Mason and Thomson,[30] Piomelli *et al.*,[31] or Keating and Piomelli.[32] Their original purposes were however in the context of Reynolds-averaged Navier–Stokes (RANS)/LES boundary layer modeling to represent backscatter or to decrease the transition region between the RANS and LES zones. The goal is here different and is to generate stochastic fluctuations of velocity gradients that feed the SGS models, as a correction for the incompatibility between SGS models with the proper near-wall asymptotics and the WMLES framework.

The paper is organized as follows. In Sec. II, the methodology including the test case and the numerics is described. A brief comparative study between Smagorinsky, WALE, and Sigma models is then proposed to illustrate the identified weaknesses of the default coupling strategy. In Sec. III, the development of a dedicated stochastic forcing is introduced and applied to the different SGS models and results are discussed. Finally, Sec. IV concludes and provides some perspectives.

II. PRESENTATION OF THE PROBLEM

A. Numerical framework

The LES code AVBP developed by CERFACS[33–35] is used in this study. In its original form, it solves the compressible Navier–Stokes equations for unstructured meshes with a finite volume cell-vertex formalism. Although mainly dedicated to compressible applications such as combustion, the code has been validated in incompressible framework such as two-phase flow problems[36,37] and is therefore adapted for the present work dealing with incompressible test cases (Sec. II B). A Lax-Wendroff[38] (second order in space and time) numerical scheme coupled to a third-order Runge–Kutta procedure for time advancement is applied. The filtered equations for mass, momentum, and energy are written below:

$$\frac{\partial \bar{\rho}}{\partial t} + \frac{\partial \bar{\rho}\widetilde{u}_i}{\partial x_i} = 0, \tag{1}$$

$$\frac{\partial \bar{\rho}\widetilde{u}_j}{\partial t} + \frac{\partial \bar{\rho}\widetilde{u}_i\widetilde{u}_j}{\partial x_i} + \frac{\partial \bar{P}\delta_{ij}}{\partial x_i} = \frac{\partial}{\partial x_i}\left[\bar{\tau}_{ij} - \bar{\rho}\left(\widetilde{u_i u_j} - \widetilde{u}_i\widetilde{u}_j\right)\right], \tag{2}$$

$$\frac{\partial \bar{\rho}\widetilde{E}}{\partial t} + \frac{\partial \bar{\rho}\widetilde{u}_i\widetilde{E}}{\partial x_i} + \frac{\overline{\partial u_i P\delta_{ij}}}{\partial x_i} = \frac{\partial}{\partial x_i}\left[\overline{q_i} - \bar{\rho}\left(\widetilde{u_i E} - \widetilde{u}_i\widetilde{E}\right)\right] + \overline{\tau_{ij}\frac{\partial u_i}{\partial x_j}}, \tag{3}$$

where ρ is the mixture density, u_i stands for the ith component of the velocity, P the pressure, τ_{ij} the viscous stress tensor, E the total non-chemical energy, q_i the ith component of the heat flux, and δ_{ij} is the Kronecker symbol, equal to 1 if $i=j$ and 0 otherwise. In these notations, the operator $\bar{\cdot}$ represents a Reynolds-filtered variable and the operator $\widetilde{\cdot}$ denotes the mass-weighted Favre averaging.

The term $\bar{\tau}_{ij}^{sgs} = -\bar{\rho}(\widetilde{u_i u_j} - \widetilde{u}_i\widetilde{u}_j)$ is the sub-grid scale viscous stress tensor and is modeled following the Boussinesq assumption, where the subgrid stresses are modeled thanks to a subgrid scale viscosity $\nu_t = \mu_t/\rho$ (with the hypothesis of having only a dissipative role on the larger structures),

$$\bar{\tau}_{ij}^{sgs} = 2\bar{\rho}\nu_t\left(\widetilde{S}_{ij} + \frac{1}{3}\delta_{ij}\widetilde{S}_{ll}\right), \tag{4}$$

where

$$\widetilde{S}_{ij} = \frac{1}{2}\left(\frac{\partial \widetilde{u}_j}{\partial x_i} + \frac{\partial \widetilde{u}_i}{\partial x_j}\right). \tag{5}$$

The turbulent viscosity ν_t is computed depending on the chosen subgrid scale model, being in this paper Smagorinsky,[19] WALE,[20] or Sigma.[21]

Since the overall context of work is WMLES, wall modeling has to be introduced to complement the above equations in the near-wall region. Variables expressed in wall units (superscript "+") are useful to express a unified vision of the turbulent boundary layer. Based on the friction velocity u_τ and the viscous length scale δ_ν, the wall distance and the velocity are normalized as

$$y^+ = \frac{y}{\delta_\nu} = \frac{\rho_w u_\tau y}{\mu_w}, \quad u^+ = \frac{u}{u_\tau}, \tag{6}$$

where the subscript "w" stands for wall values (in the cell-vertex formalism, variables are stored at nodes). The classic two-layer logarithmic law distinguishes the viscous sub-layer from the log-layer with $y_c^+ = 11.445$ as the cutoff value so that

$$u^+ = \frac{1}{\kappa}\ln\left(y^+\right) + C \;\text{ if } y^+ > y_c^+, \tag{7}$$

$$u^+ = y^+ \text{ otherwise}, \tag{8}$$

where $\kappa = 0.41$ is the Von Kármán constant and $C = 5.5$ for internal flows. Note that this classic wall law is used in this work in a local and instantaneous way, even though it has been originally developed for RANS;[9] however, it has been commonly used in LES as well. More advanced wall laws exist but are not considered in this work as the classic wall law is still largely used in industrial LES that is the target of this study, and the cases described further fit the assumptions made for the derivation of the classic wall law.

The friction flux is computed as

$$\tau_w = \rho_w u_\tau^2, \tag{9}$$

with

$$u_\tau = \sqrt{(u_1\mu_w)/(y_1\rho_w)}, \tag{10}$$

where the subscript "1" indicates the first off-wall node value (cf. Fig. 1).

From the friction flux predicted by the wall law and imposed as a Neumann boundary condition, the wall velocity gradient is expressed as

$$\left.\frac{\partial u}{\partial y}\right|_{w,wall-law} = \frac{\tau_w}{\mu_w + \mu_{t,w}}, \tag{11}$$

with $\mu_{t,w}$ the wall turbulent dynamic viscosity. Equation (11) leads to a non-zero slip velocity u_{slip} as illustrated in Fig. 1. This is actually where the coupling between the wall law and the sub-grid scale model appears: At the next iteration, u_{slip} (which is unphysical but still results from the convective scheme) and u_1 are used to compute the wall velocity gradient that feeds the SGS model. Then, μ_t acts directly on the next evaluation of the exact wall velocity gradient through Eq. (11): high values of μ_t will lead to a moderate velocity gradient, while low values of μ_t induce steep wall velocity gradient, as observed in Jaegle *et al.*[22] and can lead to reversed slip velocities and spurious oscillations.

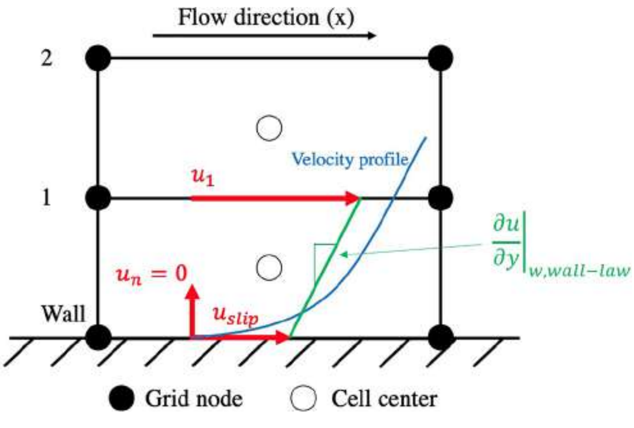

FIG. 1. Near-wall velocities scheme.

B. Numerical setup

The simple bi-periodic turbulent channel flow configuration[39] of half-height h as sketched in Fig. 2 is used hereafter to illustrate the issue and test the coupling strategy. In this specific case, the problem is statistically steady and the average flow can be considered one-dimensional, meaning that $\partial/\partial t = 0$, $\partial/\partial x = 0$, $\partial/\partial z = 0$. Under these conditions, the momentum equation, Eq. (2), reduces to

$$\frac{\partial}{\partial y}\left(\mu\overline{\frac{\partial u}{\partial y}} - \bar{\rho}\widetilde{u''v''} + \mu_t\overline{\frac{\partial u}{\partial y}}\right) = -S_x, \tag{12}$$

where $\bar{\rho}\widetilde{u''v''}$ is the LES resolved turbulence contribution and S_x is a source term needed to equilibrate the wall shear as the mean pressure gradient is zero due to periodicity. This source term can be evaluated using the Kármán–Nikuradse correlation[40] (abbreviated "KNc" hereafter) that predicts a friction coefficient $C_{f,KNc}$, based on the bulk Reynolds number and hydraulic diameter $Re_{b,Dh}$,

$$C_{f,KNc} = 0.046\, Re_{b,Dh}^{-0.2}, \tag{13}$$

$$\tau_{w,KNc} = 0.5\, C_{f,KNc}\, \rho u^2. \tag{14}$$

This source term is imposed dynamically to maintain the target mass flow rate (or equivalently, the bulk Reynolds number),

$$S_x^{t+\Delta t} = \frac{(\rho u)_{\text{target}} - \frac{1}{V}\iiint_{\Omega}(\rho u)^t dV}{\tau_{\text{relax}}}, \tag{15}$$

where t denotes the current time step, Δt is the computational time step, V is the integration volume in the domain Ω, and τ_{relax} is a relaxation time coefficient, taken to $\tau_{relax} = 1/3 \times h/u_\tau$ in this study.

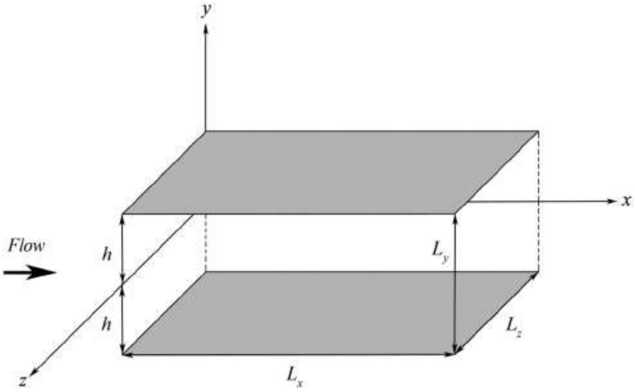

FIG. 2. Turbulent channel geometry. Gray surfaces represent wall boundary conditions (making use of the wall law), while the other pairs of faces are periodic.

Following the DNS of Hoyas and Jimenez,[41] two cases are considered at $Re_\tau = 547$ and $Re_\tau = 934$ (with $Re_\tau = u_\tau h/\nu_w$), as test cases for analyzing and developing the wall-law/SGS model coupling strategy. The WMLES cases are built with meshes, respectively, satisfying $y^+ \approx 55$ and $y^+ \approx 95$, ensuring that the wall nodes are in the log zone of the boundary layer. Note that for these cases, meshes are regular and fully made of hexaedra (of dimensions $\Delta x^+, \Delta y^+, \Delta z^+$), while the channels have the same dimensions as indicated by Hoyas and Jimenez[41] (cf. Table I for mesh characteristics).

To finish, although the solver is fully compressible, the operating mean flow pressure is fixed at 1 MPa so that $M < 0.05$ in both cases, ensuring that no compressible effect is present. The wall boundary condition relies on a slip formalism ($u_n = 0$ with a slip velocity $u_{slip} \neq 0$, cf. Fig. 1 and Jaegle *et al.*[22] for the implementation) and the standard law of the wall, used with an isothermal condition that is also the flow temperature. The flow is thus virtually isothermal, and the interest is put on the viscous flux of momentum through the solid wall: the wall shear stress. Also, the heat generated by viscous dissipation is clearly negligible given the Mach number considered. As a consequence, density and viscosity are nearly constant in the whole channel.

All simulations are performed with the Smagorinsky, WALE, and Sigma models and are time-averaged over at least 100 diffusive times ($100 \times h/u_\tau$) to ensure statistical convergence.

C. Comparison between SGS models for wall shear stress prediction

The wall shear stress obtained by using the different SGS models within the WMLES framework described in Sec. II A are displayed in Tables II and III. Although the following focuses on case $Re_\tau = 547$, the comments are valid for the case $Re_\tau = 934$. In the results presented below, the friction flux computed with the Kármán–Nikuradse correlation ("KNc"), Eq. (14), is taken as the reference. Note that the incompressible nature of the simulations has been checked following the Morkovin hypothesis that has been verified in past studies,[42,43] stating that the compressibility effects on turbulent statistics are limited to the mean density variations (here below 0.003% in space and time) as long as the fluctuating Mach number is small.

The results clearly show that the Sigma and WALE models fail to accurately predict the wall shear stress in this WMLES context, with about $\approx +20\%$ and $\approx +25\%$ for $Re_\tau = 547$, and $\approx +22\%$ and $\approx +28\%$ errors, respectively, for $Re_\tau = 934$ for the friction flux. Contrarily, the Smagorinsky model gives a good prediction by providing an error of only $\approx +3$–4%. Such differences can be effectively related to the fact that u_τ is over-predicted with Sigma and WALE, the first off-wall velocity u_1 being clearly overestimated with these models as observed from Fig. 3(a) contrarily to the Smagorinsky SGS closure. This specific overestimation of τ_w then expresses in reduced slopes of the log-law velocity profiles as shown by Fig. 3(b) for Sigma and WALE.

TABLE I. Meshes used for the channel flow test cases considered.

Case	Re_b	L_x/h	L_z/h	$N_x \times N_y \times N_z$	Δx^+	Δy^+	Δz^+
Re_τ 547	10450	$8\,\pi$	$4\,\pi$	$201 \times 21 \times 101$	69	55	69
Re_τ 934	18950	$8\,\pi$	$3\,\pi$	$201 \times 21 \times 101$	117	95	88

TABLE II. Comparison of the wall shear stress in the turbulent channel flow for $Re_\tau = 547$. Errors are relative to the KNc.

	KNc	Smagorinsky		Sigma		WALE	
	Value	Value	Error	Value	Error	Value	Error
τ_w (Pa)	2.59	2.69	+3.77%	3.11	+19.97%	3.24	+24.98%

The over-prediction of the effective turbulent Reynolds number and wall friction can be explained as follows. Since all SGS models are gradient diffusion-based models making use of a turbulent viscosity, their physical action is purely dissipative when it comes to energy and purely diffusive when it comes to momentum. However, by construction Sigma and WALE provide a turbulent viscosity that is linked to the near-wall velocity gradient, which itself depends on the wall distance. The near-wall velocity gradient being under-resolved and the near-wall velocity fluctuation being too weak, and it results a streamwise off-wall velocity value u_1 that is overestimated compared to what it should be. Indeed, its coupling with the wall law relying on Eq. (10), an overestimation of $\tau_w = \rho_w u_\tau^2$, is found as reported by Tables II and III. Note that in such a scheme, a good prediction of τ_w requires a good first off-wall streamwise velocity u_1 estimation (like in the Smagorinsky case) or conversely a good turbulent SGS viscosity and velocity gradient. This last critical issue is of particular importance as emphasized in Sec. III.

In a wall-resolved context, the Smagorinsky model is known to induce overestimated turbulent viscosity in the near-wall region, because of its response to the wall shear stress. To address this issue, WALE and Sigma have been developed to induce a turbulent viscosity that follows a y^3 damping when approaching the wall. This intends to comply with the wall-resolved physics,[44] where no turbulent activity exists in the viscous sub-layer. However, in a WMLES context, this y^3 damping function is no longer relevant since the first off-wall node is located in the logarithmic region, which contains turbulent activity. Still, Fig. 3(d) shows that this asymptotic behavior also occurs in WMLES, meaning that it is independent of the y^+ or τ_w values.

Figure 3(a) shows that the choice of SGS model also affects the wall slip velocity: $u_{slip} \approx 5.8$ m/s using a Smagorinsky model, while $u_{slip} \approx 1.6$ m/s with WALE of Sigma. Although unphysical and artificially resulting from the law of the wall implementation,[22] this wall velocity impacts the code evaluation of the normal streamwise velocity gradient that then propagates to the near-wall nodes through the diffusion process (either SGS or laminar process) as shown in Fig. 3(c). A direct consequence of the small slip velocity produced by WALE of

TABLE III. Comparison of the wall shear stress in the turbulent channel flow for $Re_\tau = 934$. Errors are relative to the KNc.

	KNc	Smagorinsky		Sigma		WALE	
	Value	Value	Error	Value	Error	Value	Error
τ_w (Pa)	7.57	7.82	+3.33%	9.22	+21.83%	9.70	+28.17%

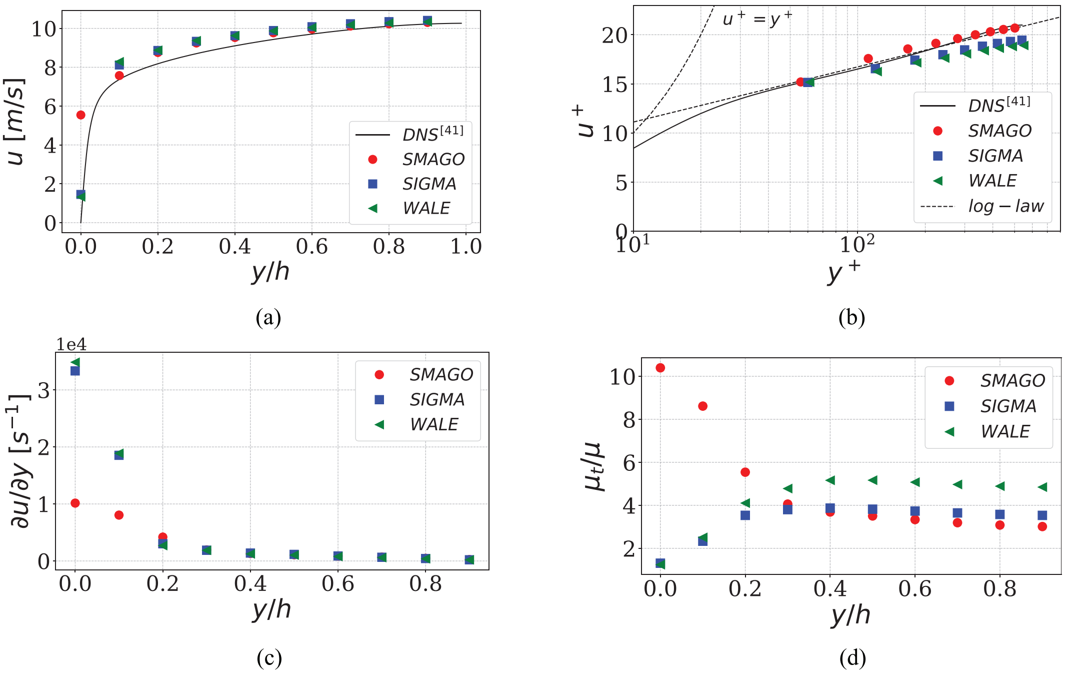

FIG. 3. Comparison between the different SGS models for the channel flow $Re_\tau = 547$. (a) Streamwise velocity. (b) Streamwise velocity in wall units. (c) Streamwise velocity gradient. (d) Dynamic viscosity ratio.

Sigma is to generate higher velocity gradients than Smagorinsky at the first two nodes.

The limitations of WMLES and more specifically the coupling scheme adopted between the law of the wall and any SGS model have been evidenced. WALE and Sigma near-wall behavior is physically justified in WRLES, but fails to characterize the near-wall region in WMLES where the first off-wall node lies in the logarithmic region. Contrarily, although the Smagorinsky model is known, in a wall-resolved context, to have physical limitations especially in sheared flows, its coupling with a law of the wall appears satisfying in the WMLES context. Because these SGS models rely on the filtered velocity gradient, which is wrong in the framework of WMLES, the choice of the SGS model in a WMLES context may significantly impact the wall shear stress prediction.

III. PROPOSED WMLES/SGS COUPLING FRAMEWORK

The problem of WMLES and the coupling with different SGS models has been evidenced in the specific cases of the Smagorinsky, WALE, and Sigma models. The following discussion therefore proposes a correction framework to facilitate the coupling between a law of the wall and WALE or Sigma models while guaranteeing robust near-wall flow predictions. The idea followed in this paper is to artificially generate the missing turbulent activity in the first cell of the wall-modeled mesh, so that the velocity gradients feeding these SGS models would be representative of the actual physics. Indeed, SGS models build the turbulent viscosity operator with the assumption of a turbulent physical property, generally presuming a velocity gradient of the resolved field sufficiently representative of the true SGS turbulent activity. Adding fluctuations to the velocity gradients of the resolved field can therefore help meeting initial goal that is to manipulate a locally turbulent field, which is not guaranteed if a law of the wall is used.

The general idea of the proposed approach is therefore to keep the WALE and Sigma models untouched in the bulk flow while modifying the velocity gradients in the near-wall region. The goal is to recover a corrected turbulent viscosity value in this region of the flow to ensure an accurate wall shear stress prediction.

A. Development of the stochastic forcing approach

This subsection intends to relate the expected velocity gradient near-wall activity to the available LES variables. To reach this objective, a Reynolds-averaged Navier–Stokes approach, for which the logarithmic region is valid, is followed in a first step. This first step evaluates the expected turbulent kinetic energy within the first cell, on the basis of the filtered LES quantities within the outer layer. This turbulent kinetic energy is then recast in terms of fluctuating velocity gradients and complies with the unsteady LES context. This fluctuating velocity gradients are finally generated using a stochastic approach and added within the first LES cell to correct the predicted velocity gradient, to account for the missing turbulent activity.

In order to relate the turbulent kinetic energy with the external LES velocity, both a mixing-length algebraic model and a turbulent kinetic energy model[45] are used. On one hand, the mixing-length algebraic model writes

$$\nu_t = l_m^2 \frac{\partial u}{\partial y}, \tag{16}$$

where l_m is the mixing length.[46] It can be shown that in the overlap region ($50\delta_\nu < y < 0.1\delta$), as well in the log region, the mixing length writes[47]

$$l_m = \kappa y, \tag{17}$$

where κ is the von Kármán constant. Furthermore at high Reynolds number, within the log-zone,[45]

$$\frac{\partial u}{\partial y} = \frac{u_\tau}{\kappa y}. \tag{18}$$

The mixing-length model can therefore be recast into

$$\nu_t = u_\tau \kappa y. \tag{19}$$

On the other hand, the turbulent kinetic energy evolution model[45] follows:

$$\nu_t = C_\mu^{1/4}\sqrt{k}l_m, \text{ with } C_\mu = 0.09, \tag{20}$$

where k stands for the turbulent kinetic energy. Hence, combining Eqs. (16), (18), and (20), one gets across the log-region,

$$\nu_t = C_\mu^{1/4}\sqrt{k}l_m = l_m^2\frac{u_\tau}{\kappa y}. \tag{21}$$

Injecting Eq. (17) into Eq. (21) allows to establish

$$C_\mu^{1/4}\sqrt{k} = u_\tau, \tag{22}$$

so that the kinetic energy within the log region finally writes

$$k = \frac{u_\tau^2}{\sqrt{C_\mu}} = \frac{\tau_w}{\rho_w\sqrt{C_\mu}}. \tag{23}$$

Note that this last expression provides an evaluation of the local turbulent kinetic energy based on the wall variables τ_w and ρ_w.

The next step is to evaluate the velocity gradient activity: the turbulent kinetic energy dissipation rate ε within the log law framework is used.[45] Using Eq. (19), one can write

$$\varepsilon = \frac{C_\mu k^2}{\nu_t} = \frac{C_\mu k^2}{u_\tau \kappa y}, \tag{24}$$

or, using the wall units $y^+ = y/\delta_\nu$ and $\delta_\nu = \nu_w/u_\tau$,

$$\varepsilon = \frac{C_\mu k^2}{u_\tau \kappa y^+ \delta_\nu} = \frac{C_\mu k^2}{\kappa y^+ \nu_w}. \tag{25}$$

The assumption of homogeneous isotropic turbulence (HIT) is now called upon. Although it might appear as a strong assumption considering wall-bounded flows, Schlichting[48] argued that even if strictly speaking isotropic turbulence does not exist in nature, Eq. (26) hereafter enjoys a very wide applicability if one considers locally isotropic turbulence, that is, large gradients of the fluctuating velocity field $(\partial u_i'/\partial x_j)$, which is exactly the context adopted here. With this assumption, Taylor[49] demonstrated that

$$\varepsilon = 15\nu\overline{\left(\frac{\partial u'}{\partial x}\right)^2}, \tag{26}$$

where u' denotes the turbulent velocity fluctuation.

Using Eqs. (25) and (26), the gradient of the fluctuating velocity follows:

$$\overline{\left(\frac{\partial u'}{\partial x}\right)^2} = \frac{C_\mu k^2}{15\kappa y^+ \nu_w^2}. \tag{27}$$

Then using Eq. (23) to substitute the turbulent kinetic energy, one finally gets

$$\overline{\left(\frac{\partial u'}{\partial x}\right)^2} = \frac{C_\mu \tau_w^2}{15\nu_w^2 \kappa y^+ \rho_w^2 C_\mu} = \frac{\tau_w^2}{15\kappa y^+ \mu_w^2}. \tag{28}$$

With the HIT assumption, Taylor also demonstrated that

$$\overline{\left(\frac{\partial u'}{\partial x}\right)^2} = \frac{1}{2}\overline{\left(\frac{\partial u'}{\partial y}\right)^2} = \frac{1}{2}\overline{\left(\frac{\partial u'}{\partial z}\right)^2}, \tag{29}$$

$$\overline{\left(\frac{\partial u'}{\partial x}\right)^2} = \overline{\left(\frac{\partial v'}{\partial y}\right)^2} = \overline{\left(\frac{\partial w'}{\partial z}\right)^2}, \tag{30}$$

which leads to the root mean square quantities,

$$\sqrt{\overline{\left(\frac{\partial u_i'}{\partial x_j}\right)^2}} = \frac{\tau_w}{\sqrt{15\kappa y^+}\mu_w} \quad \text{for i = j}, \tag{31}$$

and

$$\sqrt{\overline{\left(\frac{\partial u_i'}{\partial x_j}\right)^2}} = \sqrt{2}\frac{\tau_w}{\sqrt{15\kappa y^+}\mu_w} \quad \text{for i} \neq j. \tag{32}$$

Finally, to reconstruct LES-filtered values, a random variable is introduced that is arbitrary chosen to follow a normal distribution to represent these fluctuations. The quantile function (also known as the inverse cumulative distribution function) of a normal distribution writes

$$f(\zeta) = \gamma + \sigma\sqrt{2}erf^{-1}(2\zeta - 1), \tag{33}$$

γ being the mean, considered here as the initial prediction of the LES code, and σ is the standard deviation. ζ is a random variable with $0 \leq \zeta \leq 1$. σ being computed from Eqs. (31) and (32), this leads to

$$\left(\frac{\partial u_i'}{\partial x_j}\right)(\zeta) = \frac{\tau_w}{\sqrt{15\kappa y^+}\mu_w}\sqrt{2}erf^{-1}(2\zeta - 1) \quad \text{for i = j}, \tag{34}$$

and

$$\left(\frac{\partial u_i'}{\partial x_j}\right)(\zeta) = \frac{\tau_w}{\sqrt{15\kappa y^+}\mu_w}2erf^{-1}(2\zeta - 1) \quad \text{for i} \neq j. \tag{35}$$

Ultimately, the velocity gradient tensor used in the turbulent viscosity operator of WALE or Sigma models is corrected as

$$\left(\frac{\partial \tilde{u}_i}{\partial x_j}\right)_{corr} = \left(\frac{\partial \tilde{u}_i}{\partial x_j}\right)_{LES} + \left(\frac{\partial u_i'}{\partial x_j}\right)(\zeta). \tag{36}$$

In the specific cell-vertex context of AVBP, the correction is applied at the cell center of the wall cells as described in Fig. 4. Note that ζ is

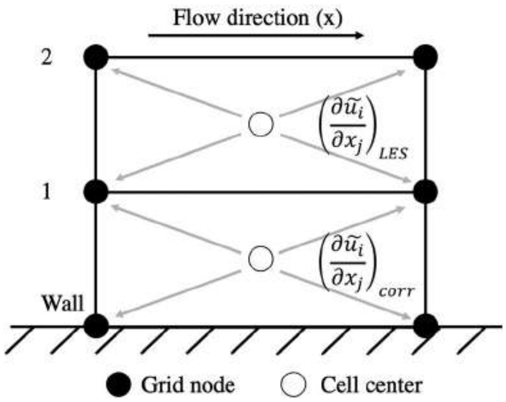

FIG. 4. Velocity gradient modification at the wall: artificial fluctuations are generated at the wall cell center. The corrected velocity gradient then feeds the SGS operator also computed at the cell center. The resulting turbulent viscosity is then scattered at the wall and off-wall nodes. The rest of the domain is not modified.

randomly generated for each gradient component at each node and at each integration time step. For each concerned wall cell, nine gradients (in 3 D) are therefore perturbed as described above. Finally, a particular emphasis is put on this point: the fluctuations are only used to build the turbulent viscosity value and are not used elsewhere in the code (*i.e.,* the velocity field is not changed directly, and its modification is only induced by the modified μ_t value).

The resulting WMLES framework, coupling the law of the wall, the SGS model, and the proposed stochastic forcing method, is summarized in Fig. 5.

B. Results with stochastic forcing

In the following, the proposed coupling formalism is applied to the previous test cases using WALE and Sigma, respectively, denoted by the "_sf" tag (for "*stochastic forcing*") to distinguish them with the non-perturbed wall velocity gradient cases. Note that with the use of the proposed strategy, the computational speed of the simulations has been decreased by about 2%.

Wall shear stress issued by the new proposed coupling for the $Re_\tau = 547$ and $Re_\tau = 934$ cases are presented in Tables IV and V. They evidence a significant improvement in τ_w predictions for WALE and Sigma with the proposed stochastic forcing. The prediction errors are reduced from $\simeq$25% to about 4% for WALE, and from $\simeq$20% to about 1% for Sigma.

Figures 6(a) and 6(b) illustrate velocity profiles for Sigma and WALE with the proposed stochastic forcing that are found in close agreement with the one obtained with the Smagorinsky model, without the gradient perturbations. The first off-wall velocity value is found to be exactly on the DNS prediction. This is confirmed by the profiles plotted in wall units, Figs. 6(c) and 6(d), evidencing that the proposed correction has significantly reduced the previously obtained log-layer mismatch. As pointed out in Sec. II B, this specific point is at the origin of the observed improvement since this velocity is related to u_τ and therefore τ_w.

The impact of the proposed correction on the turbulent viscosity profiles is observed on Figs. 6(e) and 6(f). Trends are now reversed, Sigma and WALE providing more turbulent viscosity in the near-wall region as expected in a WMLES context. This is also highlighted on Fig. 7 depicting instantaneous fields of wall turbulent viscosity for Smagorinsky, Sigma, and corrected Sigma models, where the effect of added fluctuations is clearly visible at the wall. The direct consequence of the proposed forcing is to increase dissipation at the wall, as shown by Fig. 8. As anticipated, the added fluctuations fulfill their role although the limit of the proposed approach can be a too dissipative/diffusive process. Although dissipation is usually considered as a drawback for LES, it allows here to enhance the wall shear stress prediction, to provide a better modeling of the turbulent structures enclosed within the first cell in the WMLES context. Therefore, a better

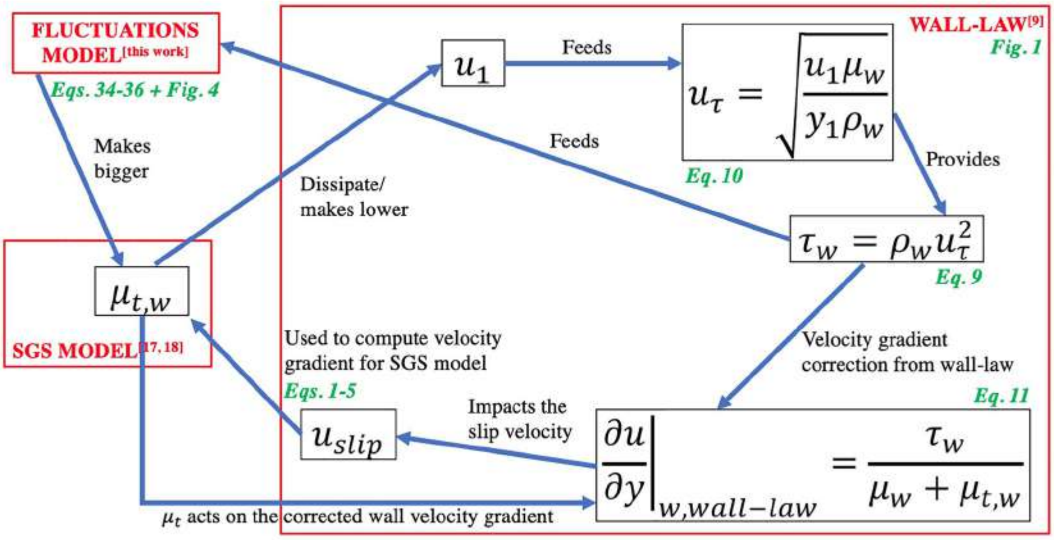

FIG. 5. Sum up of the coupling strategy between the wall law, SGS model, and the proposed fluctuations model/stochastic forcing.

TABLE IV. Comparison of the wall shear stress in the turbulent channel flow $Re_\tau = 547$ with stochastic forcing. Errors are relative to the KNc.

	KNc	Sigma_sf		WALE_sf	
	Value	Value	Error	Value	Error
τ_w	2.59	2.58	−0.48%	2.51	−3.18%

TABLE V. Comparison of the wall shear stress in the turbulent channel flow $Re_\tau = 934$ with stochastic forcing. Errors are relative to the KNc.

	KNc	Sigma_sf		WALE_sf	
	Value	Value	Error	Value	Error
τ_w	7.57	7.44	−1.69%	7.17	−5.26%

turbulent kinetic energy profile is found when compared to the DNS, Fig. 9: again, Smagorinsky seems to better fit the DNS due to its better original prediction of the wall shear stress, and thanks to the fluctuations WALE and Sigma tend also to match better the DNS results.

The detail of the turbulent kinetic energy can be found in the second-order moment of the statistics, namely, the root mean square ("rms") of the velocity components, which are presented in Fig. 10. They highlight a strong impact of the proposed model on the velocity fluctuations that are found closer to the Smagorinsky case and way more in accordance with the DNS for the streamwise direction [Figs. 10(a) and 10(b)]. For the other directions [wall-normal and spanwise, Figs. 10(c)–10(f)], the comparison with the DNS is not as straightforward: the near-wall zone (until $y^+ = 200$) seems in favor of the non-model cases for both Sigma and WALE, but in the channel bulk flow ($y^+ > 200$), the agreement is overall better with the model. Note a particular behavior due to the coupling effect of the strategy: even if

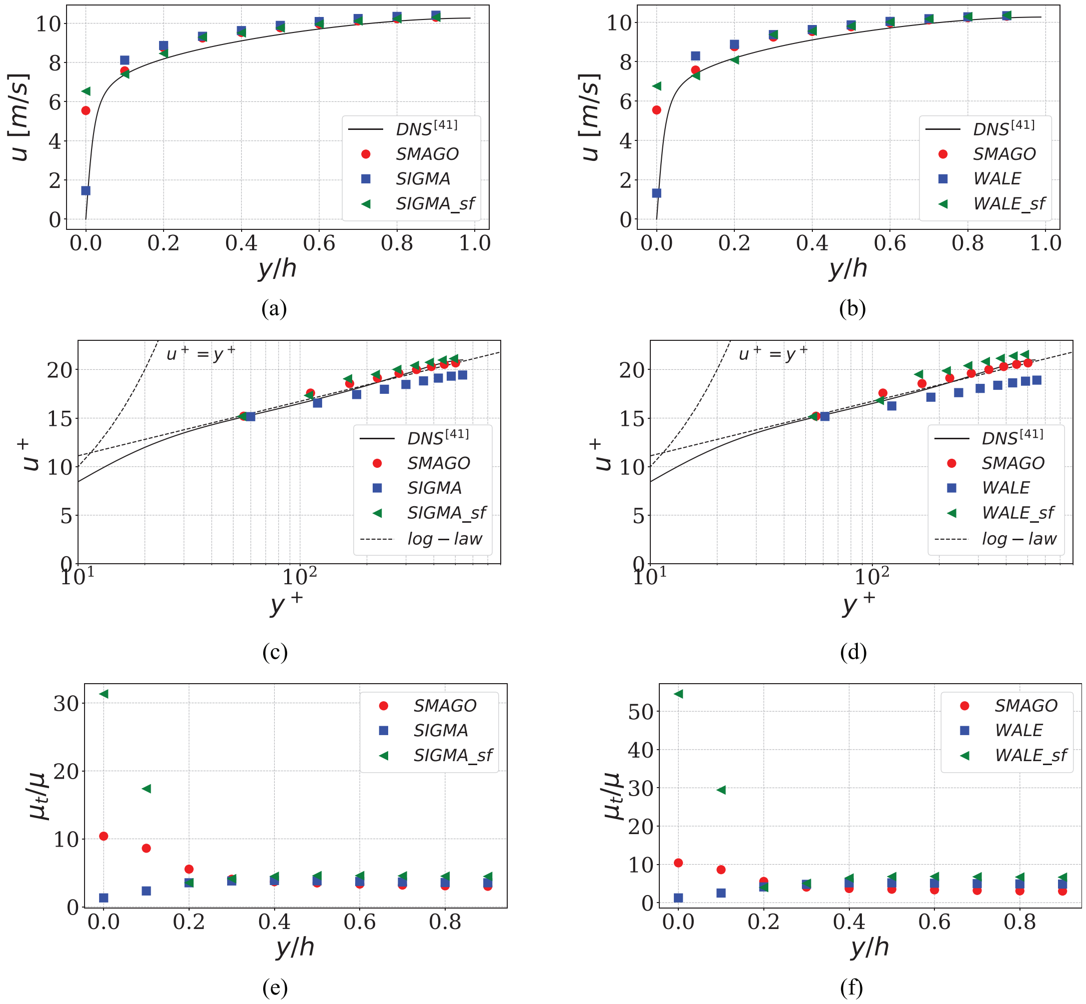

(a) (b) (c) (d) (e) (f)

FIG. 6. Comparison between the SGS models with adding of the gradients of velocity fluctuations for channel flow $Re_\tau = 547$. (a) Streamwise velocity, Sigma. (b) Streamwise velocity, WALE. (c) Streamwise velocity in wall units, Sigma. (d) Streamwise velocity in wall units, WALE. (e) Dynamic viscosity ratio, Sigma. (f) Dynamic viscosity ratio, WALE.

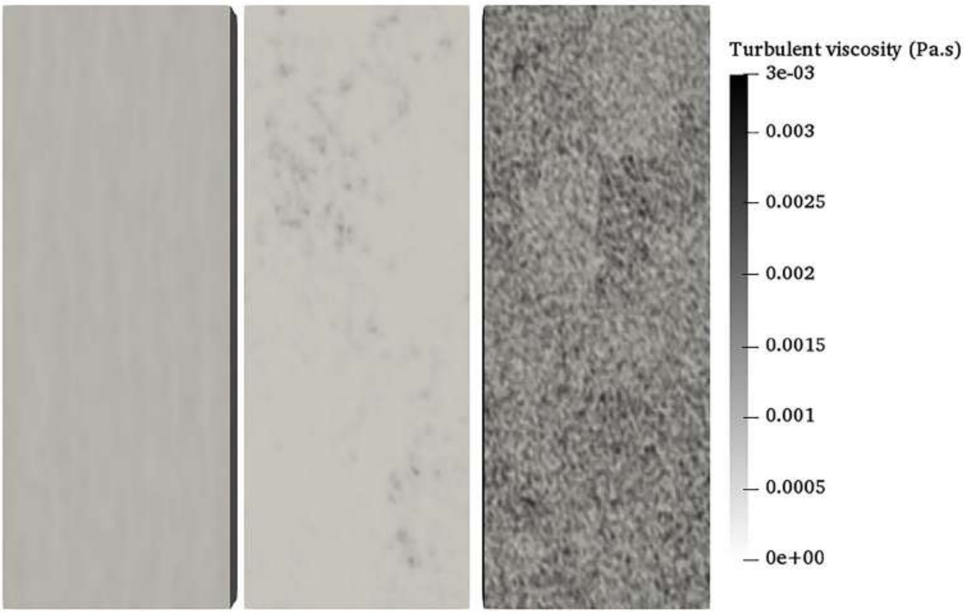

FIG. 7. Instantaneous fields of the wall turbulent viscosity ($\mu_{t,w}$), in the case $Re_\tau = 934$. From left to the right: Smagorinsky, Sigma, and Sigma with fluctuations.

fluctuations of velocity gradients are added, as their effect is to increase the wall turbulent viscosity, which leads to a better estimation of the wall friction flux that was initially over-estimated, the rms are actually lower with the use of the model than without.

Note that the proposed method relies on the generation of random fluctuations of velocity gradients, but one could also choose to directly act on the fluctuating velocity (therefore at a node level instead of the cell level for the specific cell-vertex context of AVBP). Following

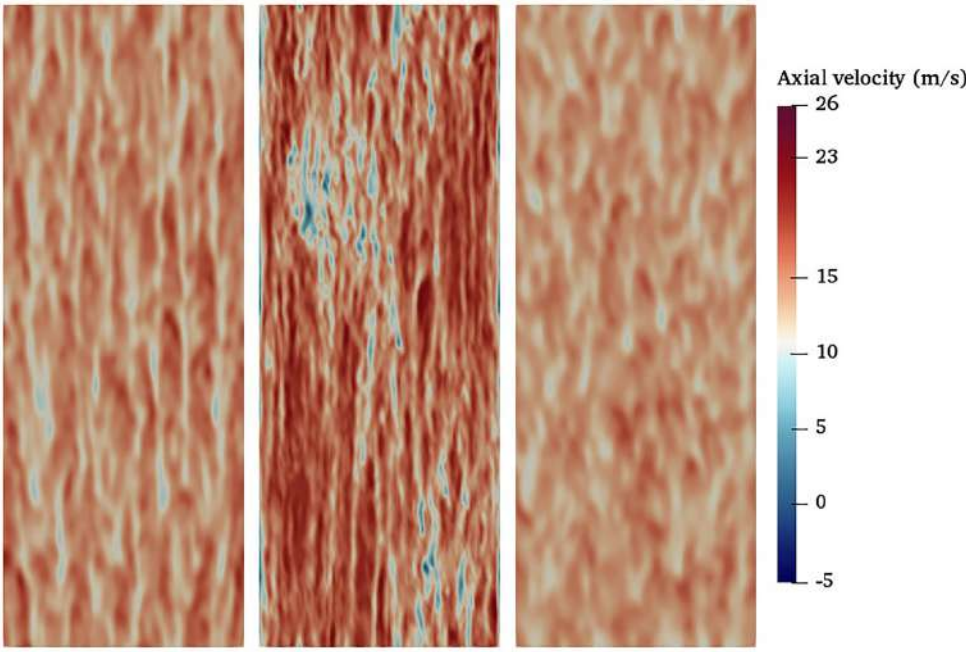

FIG. 8. Instantaneous fields of the first off-wall axial velocity (u_1), in the case $Re_\tau = 934$. From left to the right: Smagorinsky, Sigma, and Sigma with fluctuations.

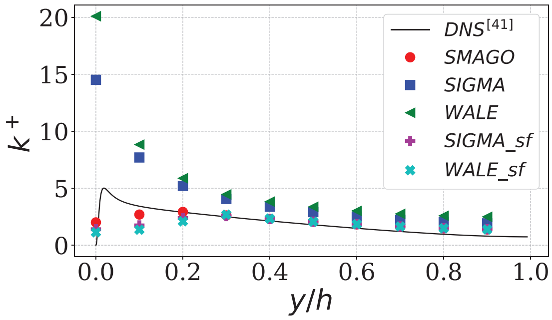

FIG. 9. Turbulent kinetic energy (in wall units) for all the models for the case $Re_\tau = 934$.

similar developments as the one presented in Sec. III A, a relation between the turbulent kinetic energy and velocity fluctuations can be established using a correlation coefficient of the form $u_i'^2/k = C_i$ within the log-layer, C_i being constants provided in Pope[45] for example. Although not detailed here, similar results were obtained for both the velocity profiles and the wall shear stress predictions with this second approach. However, a tuning process of the velocity fluctuating intensity at the wall nodes was found necessary, which is therefore case-dependent and not relevant for general consideration.

IV. CONCLUSION

A stochastic forcing method is proposed in this paper to address the log-layer mismatch experienced through the use of WALE and Sigma subgrid scale models in a wall-modeled LES context (WMLES).

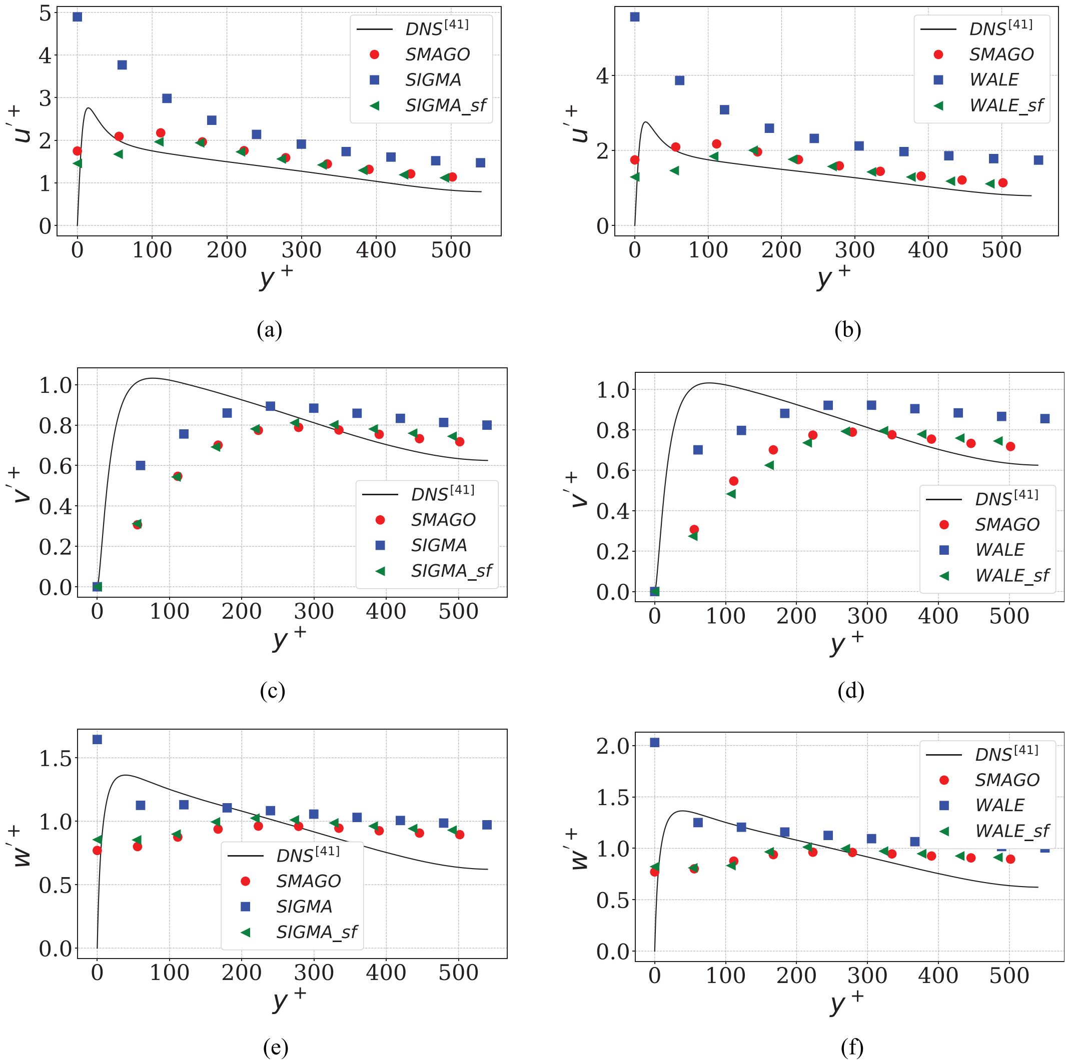

FIG. 10. Comparison between the SGS models of the root mean square of the velocity components with adding of the gradients of velocity fluctuations for channel flow $Re_\tau = 547$, in wall units. (a) Streamwise rms velocity, Sigma. (b) Streamwise rms velocity, WALE. (c) Wall-normal rms velocity, Sigma. (d) Wall-normal rms velocity, WALE. (e) Spanwise rms velocity, Sigma. (f) Spanwise rms velocity, WALE.

Results with a classical use of Smagorinky, WALE, and Sigma on a WMLES turbulent channel configuration are first investigated, and evidence accurate wall predictions with Smagorinsky (known to be too dissipative in the bulk flow), while the WALE and Sigma models predict an overestimated wall shear stress with about 25% of error. It is shown that this behavior results from the inherent turbulent viscosity damping at the wall with the WALE and Sigma models, that is, an accurate behavior in a wall-resolved context, but not in a wall-modeled one where the first off-wall node lies in the logarithmic region. Such turbulent viscosity damping does not allow one to model the turbulent structures within the first cell.

To address this indirect weakness, a combination of the mixing-length algebraic model and the turbulent kinetic energy model is considered to provide the expected kinetic energy within the log region on the basis of the available LES quantities at the wall and first off-wall node. This evaluated turbulent kinetic energy is then recast in terms of unsteady LES quantities through a stochastic forcing that provides a gradient of fluctuating velocity within the first cell. This stochastic forcing allows to correct the gradient predicted by the law of the wall and accurately feeds the WALE and Sigma operators thus accounting for turbulent activity within the first cell.

Results show that this stochastic forcing procedure allows to reduce the log-layer mismatch with WALE and Sigma SGS models in a WMLES context, and error predictions for the wall shear stress are reduced from $\simeq$25% to about 4% for WALE and from $\simeq$20% to about 1% for Sigma.

Future work will be devoted to anisothermal channels with high temperature gradients between the wall and the bulk flow, which suffer from similar issues in WMLES, and focus will be put on the wall heat flux prediction.

ACKNOWLEDGMENTS

This work has been funded by CNES and ArianeGroup and was performed using HPC resources from GENCI-[TTGC] (Grant No. 2021-A0092B10157).

The authors have no conflicts to disclose.

DATA AVAILABILITY

The data that support the findings of this study are available within the article.

REFERENCES

[1] M. Germano, "Turbulence—The filtering approach," J. Fluid Mech. **238**, 325–336 (1992).

[2] A. Kolmogorov, "The local structure of turbulence in incompressible viscous fluid for very large Reynolds numbers," Proc. R. Soc. London Ser. A **434**, 9–13 (1941); available at https://www.jstor.org/stable/51980?origin=JSTOR-pdf.

[3] P. Sagaut, *Large Eddy Simulation for Incompressible Flows* (Springer, 2006).

[4] M. Lesieur, *Turbulence in Fluids*, 4th ed. (Springer, 2008).

[5] D. R. Chapman, "Computational aerodynamics development and outlook," AIAA J. **17**, 1293–1313 (1979).

[6] H. Choi and P. Moin, "Grid-point requirements for large eddy simulation: Chapman's estimates revisited," Phys. Fluids **24**, 011702 (2012).

[7] J. Larsson, S. Kawai, J. Bodart, and I. Bermejo-Moreno, "Large eddy simulation with modeled wall-stress: Recent progress and future directions," Mech. Eng. Rev. **3**, 15-00418 (2016).

[8] S. T. Bose and G. I. Park, "Wall-modeled large-eddy simulation for complex turbulent flows," Annu. Rev. Fluid Mech. **50**, 535–561 (2018).

[9] B. E. Launder and D. B. Spalding, "The numerical computation of turbulent flows," Comput. Methods Appl. Mech. Eng. **3**, 269–289 (1974).

[10] F. Nicoud, J. S. Baggett, P. Moin, and W. Cabot, "Large eddy simulation wall-modeling based on suboptimal control theory and linear stochastic estimation," Phys. Fluids **13**, 2968 (2001).

[11] S. Rezaeiravesh, T. Mukha, and M. Liefvendahl, "Systematic study of accuracy of wall-modeled large eddy simulation using uncertainty quantification techniques," Comput. Fluids **185**, 34–58 (2019), arXiv:1810.05213.

[12] H. J. Bae, A. Lozano-Durán, S. T. Bose, and P. Moin, "Dynamic slip wall model for large-eddy simulation," J. Fluid Mech. **859**, 400–432 (2019).

[13] F. De Vanna, M. Cogo, M. Bernardini, F. Picano, and E. Benini, "Unified wall-resolved and wall-modeled method for large-eddy simulations of compressible wall-bounded flows," Phys. Rev. Fluids **6**, 034614 (2021).

[14] X. I. Yang, G. I. Park, and P. Moin, "Log-layer mismatch and modeling of the fluctuating wall stress in wall-modeled large-eddy simulations," Phys. Rev. Fluids **2**, 104601 (2017).

[15] R. Deleon and I. Senocak, "The role of forcing and eddy viscosity variation on the log-layer mismatch observed in wall-modeled large-eddy simulations," J. Fluids Eng., Trans. ASME **141**, 054501 (2019).

[16] X. I. Yang and Y. Lv, "A semi-locally scaled eddy viscosity formulation for LES wall models and flows at high speeds," Theor. Comput. Fluid Dyn. **32**, 617–627 (2018).

[17] B. Giacomini and M. Giometto, "On the suitability of second-order accurate finite-volume solvers for the simulation of atmospheric boundary layer flow," Geosci. Model Dev. **14**(3), 1409–1426 (2021).

[18] H. J. Bae and A. Lozano-Durán, "Effect of wall boundary conditions on a wall-modeled large-eddy simulation in a finite-difference framework," Fluids **6**, 112–112 (2021).

[19] J. Smagorinsky, "General circulation experiments with the primitive equations," Mon. Weather Rev. **91**, 99–164 (1963).

[20] F. Nicoud and F. Ducros, "Subgrid-scale stress modelling based on the square of the velocity gradient tensor," Flow, Turbul. Combust. **62**, 183–200 (1999).

[21] F. Nicoud, H. B. Toda, O. Cabrit, S. Bose, and J. Lee, "Using singular values to build a subgrid-scale model for large eddy simulations," Phys. Fluids **23**, 085106 (2011).

[22] F. Jaegle, O. Cabrit, S. Mendez, and T. Poinsot, "Implementation methods of wall functions in cell-vertex numerical solvers," Flow, Turbul. Combust. **85**, 245–272 (2010).

[23] L. Temmerman, M. A. Leschziner, C. P. Mellen, and J. Fröhlich, "Investigation of wall-function approximations and subgrid-scale models in large eddy simulation of separated flow in a channel with streamwise periodic constrictions," Int. J. Heat Fluid Flow **24**, 157–180 (2003).

[24] P. Wu and J. Meyers, "A constraint for the subgrid-scale stresses in the logarithmic region of high Reynolds number turbulent boundary layers: A solution to the log-layer mismatch problem," Phys. Fluids **25**, 015104 (2013).

[25] S. Feng, X. Zheng, R. Hu, and P. Wang, "Large Eddy Simulation of high-reynolds-number atmospheric boundary layer flow with improved near-wall correction," Appl. Math, Mech. **41**, 33–50 (2020).

[26] S. Hickel, N. A. Adams, and N. N. Mansour, "Implicit subgrid-scale modeling for large-eddy simulation of passive-scalar mixing," Phys. Fluids **19**, 095102 (2007).

[27] C. Marchioli, "Large-eddy simulation of turbulent dispersed flows: A review of modelling approaches," Acta Mech. **228**, 741–771 (2017).

[28] M. Bassenne, M. Esmaily, D. Livescu, P. Moin, and J. Urzay, "A dynamic spectrally enriched subgrid-scale model for preferential concentration in particle-laden turbulence," Int. J. Multiphase Flow **116**, 270–280 (2019).

[29] P. L. Johnson, M. Bassenne, and P. Moin, "Turbophoresis of small inertial particles: Theoretical considerations and application to wall-modelled large-eddy simulations," J. Fluid Mech. **883**, A27 (2020).

[30] P. Mason and D. Thomson, "Stochastic backscatter in large-eddy simulation of boundary layers," J. Fluid Mech. **242**, 51–78 (1992).

[31] U. Piomelli *et al.*, "The inner–outer layer interface in large-eddy simulations with wall-layer models," Int. J. Heat Fluid Flow **24**, 538–550 (2003).

[32] A. Keating and U. Piomelli, "A dynamic stochastic forcing method as a wall-layer model for large-eddy simulation," J. Turbul. **7**, N12–N41 (2006).

[33] T. Schönfeld and M. Rudgyard, "Steady and unsteady flow simulations using the hybrid flow solver avbp," AIAA J. **37**, 1378–1385 (1999).

[34] N. Gourdain, L. Gicquel, M. Montagnac, O. Vermorel, M. Gazaix, G. Staffelbach, M. Garcia, J.-F. Boussuge, and T. Poinsot, "High performance parallel computing of flows in complex geometries: I. methods," Comput. Sci. Discovery **2**, 015003 (2009).

[35] L. Y. Gicquel, N. Gourdain, J. F. Boussuge, H. Deniau, G. Staffelbach, P. Wolf, and T. Poinsot, "High performance parallel computing of flows in complex geometries," C. R. Mecan. **339**, 104–124 (2011).

[36] E. Riber, V. Moureau, M. García, T. Poinsot, and O. Simonin, "Evaluation of numerical strategies for large eddy simulation of particulate two-phase recirculating flows," J. Comput. Phys. **228**, 539–564 (2009).

[37] J.-M. Senoner, M. Sanjose, T. Lederlin, F. Jaegle, M. Garcia, E. Riber, B. Cuenot, L. Gicquel, H. Pitsch, and T. Poinsot, "Eulerian and Lagrangian Large-Eddy simulations of an evaporating two-phase flow," Comptes Rendus Mécanique. **337**(6) 458–468 (2009).

[38] P. Lax and B. Wendroff, "Systems of conservation laws," Commun. Pure Appl. Math. **13**, 217–237 (1960).

[39] J. Kim, P. Moin, and R. Moser, "Turbulence statistics in fully developed channel flow at low Reynolds number," J. Fluid Mech. **177**, 133–166 (1987).

[40] J. Nikuradse, "Strömungsgesetze in rauhen rohren," Forsch. Geb. Ing. **361**, 1 (1933); available at https://citeseerx.ist.psu.edu/viewdoc/download?doi=10.1.1.467.2980&rep=rep1&type=pdf.

[41] S. Hoyas and J. Jiménez, "Reynolds number effects on the Reynolds-stress budgets in turbulent channels," Phys. Fluids **20**, 101511 (2008).

[42] G. Coleman, J. Kim, and R. D. Moser, "A numerical study of turbulent supersonic isothermal-wall channel flow," J. Fluid Mech. **305**, 159–183 (1995).

[43] R. M. So, T. B. Gatski, and T. P. Sommer, "Morkovin hypothesis and the modeling of wall-bounded compressible turbulent flows," AIAA J. **36**, 1583–1592 (1998).

[44] D. R. Chapman and G. D. Kuhn, "The limiting behaviour of turbulence near a wall," J. Fluid Mech. **170**, 265–292 (1986).

[45] S. B. Pope, *Turbulent Flows* (Cambridge University Press, 2000).

[46] L. Prandtl, "Uber die ausgebildete turbulenz," in *Proceedings of 2d International Congress of Applied Mechanics* (Zürich, 1925), pp. 62–74.

[47] T. V. Kármán, "Turbulence and Skin Friction," J. Aeronaut. Sci. **1**, 1–20 (1934).

[48] H. Schlichting and K. Gersten, *Boundary-Layer Theory* (Springer Berlin Heidelberg, 1979).

[49] G. Taylor, *Statistical Theory of Turbulence* (Royal Society, 1935).

5.2.2 Non-isothermal cases

The method described in the paper is now tested for non-isothermal cases, in order to come closer to LRE conditions. In a bi-periodic channel flow, the energy equation takes the form:

$$\frac{\partial}{\partial y}\left(\overline{\lambda\frac{\partial T}{\partial y}} - \bar{\rho}\widetilde{v''h''_s} + \lambda_t\overline{\frac{\partial T}{\partial y}}\right) = -Q_x \tag{5.13}$$

where Q_x denotes the energy source term, which compensates the heat losses and maintain the bulk temperature $T_b = 1660K$, while the wall temperature is fixed at $T_w = 320K$. The Kármán-Nikuradse correlation for the heat transfer takes the form [Nikuradse, 1933]:

$$\mathrm{Nu}_{KNc} = \frac{0.023\,\mathrm{Re}_{f,D_h}^{0.8}\,\mathrm{Pr}}{0.88 + 2.03\left(\mathrm{Pr}^{2/3} - 0.78\right)\mathrm{Re}_{f,D_h}^{-0.1}} \tag{5.14}$$

$$q_{w,KNc} = \lambda_{film}\ (T_b - T_w)\ Nu_{KNc}/D_h \tag{5.15}$$

where film values (subscript "f") are used:

$$\begin{aligned}
T_f &= (T_w + T_b)/2 && (5.16)\\
\mu_f &= 2(1/\mu_w + 1/\mu_b)^{-1} && (5.17)\\
\rho_f &= P/(rT_f) && (5.18)\\
\lambda_f &= \mu_f Cp_f/\,\mathrm{Pr} && (5.19)\\
\mathrm{Re}_{f,D_h} &= uD_h\rho_f/\mu_f && (5.20)
\end{aligned}$$

In [Kays and Crawford, 1993] are introduced corrections to take into account the variability of fluid properties, both for the friction coefficient and the Nusselt number. These corrections are therefore used as the reference values for friction ($C_{f,KNc}$ has been defined Eq. 13 of the paper) and heat transfer (denoted as "KNc,corr" in the following):

$$C_{f,KNc,corr} = C_{f,KNc}\left(\frac{T_w}{T_b}\right)^{-0.1} = 0.046\,\mathrm{Re}_{b,Dh}^{-0.2}\left(\frac{T_w}{T_b}\right)^{-0.1} \tag{5.21}$$

$$\mathrm{Nu}_{KNc,corr} = \mathrm{Nu}_{KNc}\left(\frac{T_w}{T_b}\right)^{n} \text{ with } \begin{cases} n = 0 & \text{if } T_w/T_b < 1\\ n = -\left[\log_{10}\left(\frac{T_w}{T_b}\right)\right]^{1/4} + 0.3 & \text{if } 1 < T_w/T_b < 5\\ n = -0.5 & \text{if } T_w/T_b > 5 \end{cases} \tag{5.22}$$

Likewise the momentum source term, the dynamic energy source term is computed as:

$$Q_x^{t+\Delta t} = \bar{\rho}\overline{Cv}\frac{T_\mathrm{b} - \frac{1}{V}\iiint_\Omega T^t dV}{\tau_\mathrm{relax}} \tag{5.23}$$

This setup results in a ratio $T_b/T_w \approx 5.2$, meaning that the use of the coupled wall-law is here mandatory. The friction Reynolds number is therefore higher, $Re_\tau = 2001$, and $y^+ \approx 100$. Results obtained with the standard method, *i.e.*, without the influence of the SGS model, are presented in Table 5.1.

	KNc,corr	Smagorinsky		Sigma		WALE	
	Value	Value	Error	Value	Error	Value	Error
$\tau_w[Pa]$	34.73	36.36	+4.70%	43.48	+25.20%	44.35	+27.71%
$q_w[MW/m^2]$	1.01	1.02	+1.37%	1.09	+8.23%	1.10	+9.83%

Table 5.1: Comparison of friction and heat fluxes in the non-isothermal turbulent channel flow for $Re_\tau = 2001$.

The same comments as for the isothermal cases can be made here. Again, the Sigma and WALE models fail to predict both the wall shear stress and the heat flux, overestimating both quantities. The Smagorinsky model on the other hand gives good results with an error lower than 5%.

The same simulations now performed with the addition of fluctuations in the velocity gradients used to determine μ_t as described in the paper, give the results reported in Table 5.2.

	KNc,corr	Sigma_sf		WALE_sf	
	Value	Value	Error	Value	Error
τ_w	34.73	31.91	-8.11%	29.16	-16.03%
q_w	1.01	0.91	-9.83%	0.83	-17.29%

Table 5.2: Comparison of friction and heat fluxes in the non-isothermal turbulent channel flow $Re_\tau = 2001$ with stochastic forcing.

If the friction is well improved, the error on wall heat fluxes stays high, and is even higher for the WALE model. For both SGS models the wall heat flux is now underestimated, surely because of the over-dissipating effect induced by the extra turbulent viscosity at the wall. The results are therefore quite similar to the isothermal cases of the paper for the wall friction, with better results with Sigma than WALE, but it seems that the addition of velocity gradient fluctuations tends to under-predict the wall heat flux. The increase of the turbulent viscosity at the wall may induce other phenomena affecting the heat flux. Future work is needed to understand these phenomena and extend the method to the prediction of wall heat fluxes.

5.3 Influence of chemical reactions on wall fluxes

Using the developed ARC schemes, it is now possible to investigate the possible influence of chemical activity on the wall fluxes. Due to the cooled wall at a lower temperature than the burnt gas, the near-wall area is colder than the bulk flow, which can change the chemical equilibrium. In the context of Liquid Rocket Engines, the study of this effect remains quite rare. Using RANS of combustion chambers up to 100 bar, [Betti et al., 2016] studied several chemical models (equilibrium, frozen, simplified kinetics) for H2/O2 and CH4/O2 mixtures, and highlighted the fact that recombination reactions could increase up to 30% the wall heat flux in the case of methane, and up to 14% in the case of hydrogen. This behaviour was as well observed in [Perakis et al., 2020] in the cold boundary layer of LES of a CH4/O2 configuration studied at TUM [Silvestri et al., 2016, Silvestry et al., 2018]. Such recombination reactions are only present in sufficiently detailed chemistry models such as ARC.

This raises the question of the possible need to develop wall models that take into account this chemical activity. This was for example made in [Muto et al., 2018, Muto et al., 2019] in the case of hydrogen/oxygen combustion, where a chemical equilibrium condition in the first wall cell, allowing to compute the momentum and enthalpy flux in the boundary layer equations thanks to a table look-up procedure to estimate chemical factors. Another idea developed and applied in CH4/O2 cases by [Perakis et al., 2020] is to pre-compute non-adiabatic flamelet library used as model to predict heat transfer.

For a 1D stationary flow, the total wall heat flux is recalled here and is actually divided into four contributions:

$$\overline{q_{tot}} \approx \underbrace{\bar{\rho}\widetilde{v''h''_s}}_{1} + \underbrace{\bar{\rho}\sum_k \widetilde{v''Y''_k}\Delta h^0_{f,k}}_{2} - \underbrace{\overline{\lambda\frac{dT}{dy}}}_{3} + \underbrace{\bar{\rho}\sum_k \overline{h_k Y_k V_{k,y}}}_{4} \tag{5.24}$$

- 1: Turbulent flux of sensible enthalpy, modeled by: $-\lambda_t \frac{d\bar{T}}{dy}$.
- 2: Turbulent flux of chemical enthalpy, which is the term of interest here.
- 3: Laminar (or Fourier) flux, negligible in the turbulent region.
- 4: Species diffusion effect, also negligible in the turbulent region as shown in [Cabrit and Nicoud, 2009].

The viscous effect and pressure forces are also neglected, as recalled in [Potier, 2018]. As already introduced in Section 5.1, the turbulent flux of chemical enthalpy is not implemented in the current version of AVBP. The objective is then to evaluate the chemical activity in the boundary layer and its impact on wall fluxes. More precisely, the following questions are addressed in this section:

- Is there a strong chemical activity in the boundary layer?
- If yes, does it have an influence on the wall fluxes?
- If yes, from which quantity change does it come from: thermal conductivity, heat capacity, heat release, temperature gradient...?
- Knowing these information, is the current coupled wall-law enough to take into account these changes?

To answer these questions, simulations of reacting turbulent channel flows are performed with both WRLES and WMLES.

5.3.1 Numerical setup

Simulating stationary bi-periodic channel flows requires to add a source term to the momentum equation in order to compensate the wall-friction (as in Section 5.2.1) and, in the case of non-isothermal flows (typically hot bulk flow, cold wall), to add an energy source term to the energy equation (as in Section 5.2.2). However, activating chemical reactions which are highly sensitive to temperature, that they also modify through their heat release, raises a coupling

problem: reactions modify the temperature, then the energy source term tries to correct this temperature to go back to the target bulk temperature; the corrected temperature in turn modifies the reaction rates, and so on. This coupling makes it very difficult and even impossible to reach a target operation point.
Therefore it was preferred to use a non-periodic channel with inlet and outlet boundary conditions, and leading to a spatially developing turbulence and boundary layer. To obtain a sufficiently developed turbulent boundary layer, synthetic turbulence is superimposed to the bulk flow at the inlet, and statistics are computed only in a relevant part of the channel. Results are presented in two transverse planes A and B as indicated on Fig. 5.3, located at X=25mm and X=49.5mm, respectively.

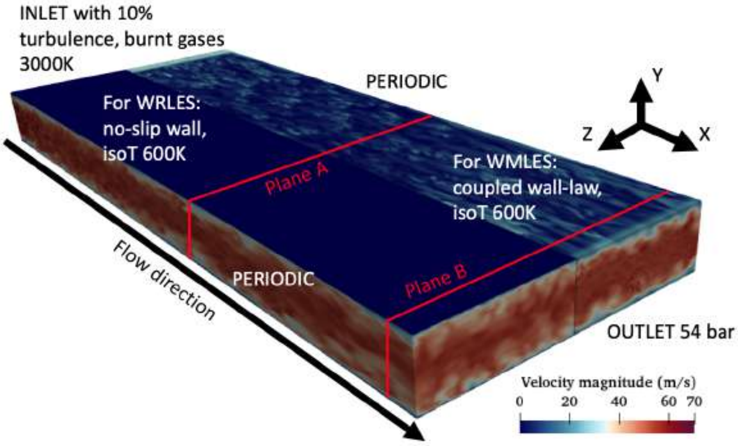

Figure 5.3: Turbulent channel flow configuration, with associated boundary conditions. Instantaneous velocity fields of the WRLES (foreground) and WMLES (background) are shown. Plane A (X=25mm) and Plane B (X=49.5mm) where results are collected and spatially and temporally averaged are also shown.

For all simulations presented below, the inlet condition is a burnt gases mixture resulting from a CANTERA CH4/O2 equilibrium with the ARC derived in Section 4.3.1 for 54 bar, 3000K, RM=3. The detailed composition of the inlet is detailed in Table 5.3. It is expected for the reacting cases that the mixture at equilibrium should not evolve much in the bulk flow at the same temperature of 3000K, but may change in the near-wall region under the heat loss through the walls at a temperature of 600K. As the ratio $T_{bulk}/T_{wall} = 5$, it represents a high temperature gradient, and the coupled wall-law from Cabrit [Cabrit and Nicoud, 2009] is used. The outlet is imposed at 54 bar since the ARC scheme has been derived for this pressure.

The numerical methods are exactly the same as for the channel flows computed in Section 5.2.1. The Lax-Wendroff convection scheme is applied to a hexaedral element mesh. Note that the SGS model used here is Sigma. From the conclusions of Section 5.2 about coupling between the wall-law and the SGS model, it may seem not the best choice as the Sigma model was found to over-predict wall fluxes. However this choice will not impact the conclusions about chemical activity in the boundary layer.

T (K)	3000
H2	0.0116504
H	0.000360494
O	0.000310369
O2	0.00106129
OH	0.0087071
H2O	0.449527
CO	0.275636
CO2	0.252742

Table 5.3: Channel inlet boundary condition: temperature and major species mass fractions (other ARC species in minor proportion are not shown).

5.3.2 Laminar cases

Firstly, laminar Poiseuille flows are considered to give a first insight on the chemical activity without any notion of turbulence modelling.
Two cases are simulated, with and without chemical reactions, denoted respectively LAM_F ("Frozen") and LAM_R ("Reactive"). Temporal averaging was performed over two convective times, which is here $\tau_{conv} \approx 10ms$. The boundary layer is resolved for both cases with $y^+ \approx 0.5$.

Quantity	Unit	LAM_F	LAM_R	Relative difference
τ_w	Pa	0.347	0.350	-0.9%
ρ_w	kg/m^3	22.70	23.25	-2.4%
μ_w	$Pa.s$	3.22E-05	3.22E-05	0.0%
$(\partial u/\partial y)_w$	s^{-1}	1.067E+04	1.073E+04	-0.6%
q_w	MW/m^2	0.551	0.627	-10.4%
Cp_w	$J/kg/K$	1696	1688	0.5%
λ_w	$W/m.K$	0.094	0.094	0.0%
$(\partial T/\partial y)_w$	K/m	5.83E+06	6.50E+06	-10.4%

Table 5.4: Comparison of main wall quantities in the two cases of Poiseuille flow (the relative difference is computed with the reactive case as the reference), computed in Plane A (X=25mm)

Table 5.4 indicates that the wall fluxes differ between the two cases, the reacting case exhibiting a slightly higher friction flux, but a much higher heat flux. The physical properties (ρ_w, μ_w, Cp_w, λ_w) at the wall are however very similar in both cases, meaning that the flux differences come from the gradients of flow quantities (velocity for friction, temperature for heat fluxes) at the wall: indeed their relative difference are of the same order than the respective flux relative difference.
Figure 5.4 shows the details of these differences: an exothermic heat release is found (Fig. 5.4c) in the near-wall region (between $10 < y^+ < 100$), which explains the slightly higher temperature in the reacting case (Fig. 5.4a). The impact of the temperature is found on the heat capacity, Fig. 5.4d, for which the value is globally slightly higher in the reacting case. Finally the temperature gradient difference at the wall is clearly observable in Fig. 5.4b and grows towards the wall, resulting in higher heat flux in the reacting case. Theses differences have therefore a chemical origin that is explained in the next section.

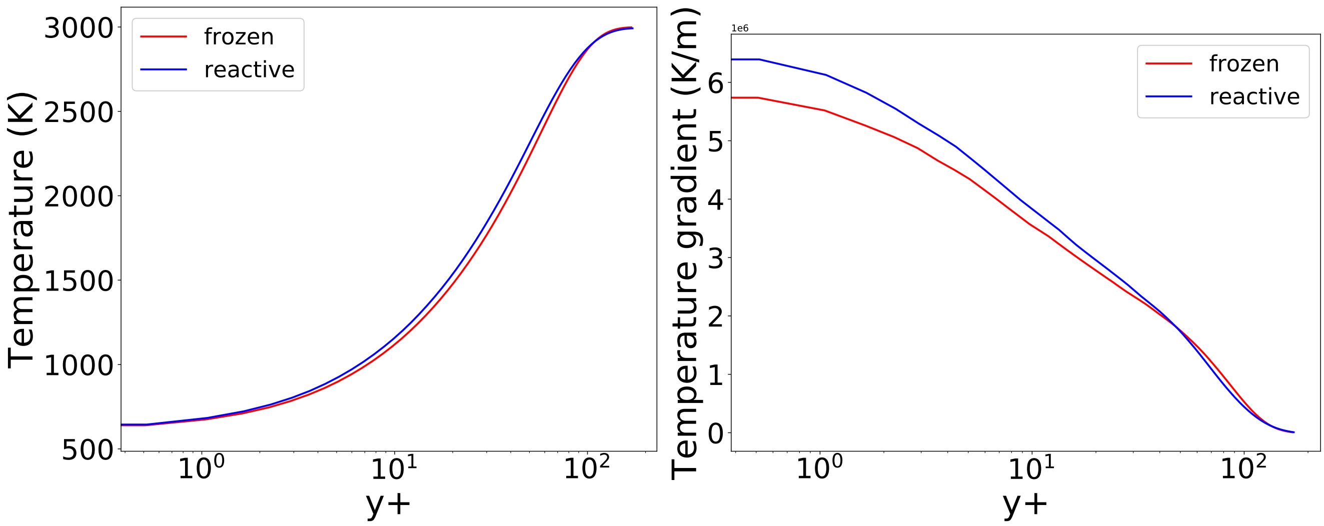

(a) Temperature

(b) Temperature gradient

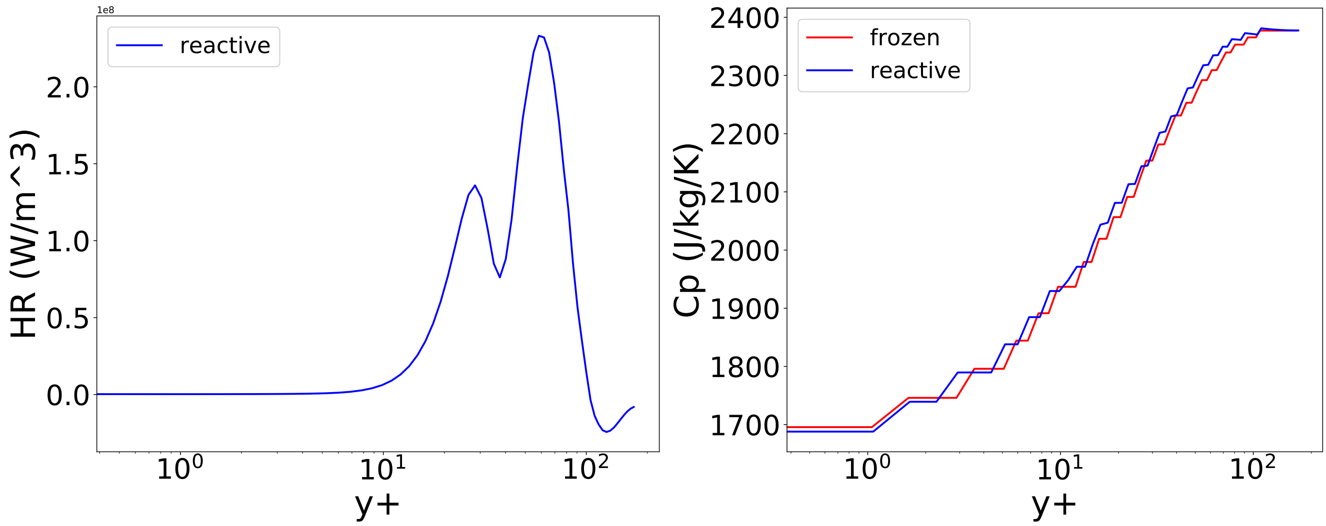

(c) Heat release

(d) Heat capacity

Figure 5.4: Comparison between the frozen and boundary layer on the case of Poiseuille laminar flow, located at plane A (X=25mm).

5.3.3 Turbulent cases

Using turbulent reactive channels raises the question about the behaviour of a wall law when chemical reactions occur in the boundary layer. To study this, the test matrix shown in Table 5.5 containing the name of 4 cases is proposed. These tests will allow to evaluate the importance of including chemistry in wall-laws.

	Resolved BL	Modeled BL
Frozen BL	WRLES_F	WMLES_F
Reacting BL	WRLES_R	WMLES_R

Table 5.5: Test matrix for turbulent channel flows.

The point is here to compare the differences between the frozen and reacting conditions found in the WRLES and in the WMLES, by looking at the relative differences indicated in Table 5.6 and 5.7. Note that because of computational cost, the WRLES are not exactly resolved at the wall but are constructed to target $y^+ \approx 5$. This is however considered generally sufficient to consider the boundary layer as almost resolved: $y^+ \approx 5$ lies in the viscous sub-layer, where no turbulent activity is expected (see Fig. 5.1). The WMLES are then designed to reach a resolution of $y^+ \approx 80$. With a convective time of the channel of about $\tau_{conv} \approx 1ms$, the WRLES have been averaged over at least 3ms, and 30ms have been calculated for the WMLES. Note that in the following graphs presented with y^+ as abscissa, the wall point, normally at $y/h = y^+ = 0$, has been artificially moved to $y^+ = 1$ for better clarity.

		Plane A			Plane B		
Quantity	Unit	WRLES_F	WRLES_R	RD	WRLES_F	WRLES_R	RD
τ_w	Pa	22.55	23.95	-5.8%	22.96	24.51	-6.3%
ρ_w	kg/m^3	22.72	23.12	-1.7%	22.76	23.14	-1.6%
μ_w	$Pa.s$	3.21E-05	3.21E-05	0.0%	3.21E-05	3.21E-05	0.0%
$(\partial u/\partial y)_w$	s^{-1}	6.33E+05	6.66E+05	-5.0%	6.35E+05	6.73E+05	-5.7%
q_w	MW/m^2	3.647	4.061	-10.2%	3.581	3.945	-9.2%
Cp_w	$J/kg/K$	1695.7	1691.1	0.3%	1695.7	1692	0.2%
λ_w	$W/m.K$	0.094	0.094	0.0%	0.094	0.094	0.0%
$(\partial T/\partial y)_w$	K/m	3.37E+07	3.70E+07	-9.2%	3.28E+07	3.58E+07	-8.4%

Table 5.6: Comparison of main wall quantities in the case of turbulent WRLES (relative difference ("RD" in the table) computed with the reactive simulation as the reference).

		Plane A			Plane B		
Quantity	Unit	WMLES_F	WMLES_R	RD	WMLES_F	WMLES_R	RD
τ_w	Pa	28.57	27.92	2.3%	32	32.45	-1.4%
ρ_w	kg/m^3	24.16	24.44	-1.1%	23.28	23.6	-1.4%
μ_w	$Pa.s$	3.20E-05	3.20E-05	0.0%	3.20E-05	3.20E-05	0.0%
q_w	MW/m^2	4.211	4.384	-3.9%	4.33	4.628	-6.4%
Cp_w	$J/kg/K$	1895.2	1900.0	-0.3%	1897.6	1915.5	-0.9%
λ_w	$W/m.K$	0.105	0.105	0.0%	0.105	0.106	-0.9%

Table 5.7: Comparison of main wall quantities in the case of turbulent WMLES (relative difference ("RD" in the table) computed with the reactive simulation as the reference).

It seems that the differences between the frozen and the reacting cases are lower in the WMLES than in the WRLES. It means that a contribution to the wall fluxes due to chemical reactions is missed in the case of WMLES.

As for the Poiseuille flow, the WRLES indicate that the wall flux differences mainly come from velocity and temperature gradients at the wall (visible between the two first grid points of Fig. 5.9b), the other physical properties remaining almost the same in all cases. However in the case of WMLES, the resolved velocity and temperature gradients, as well as λ_w, are not used by the wall-law to compute the fluxes (as recalled by Eqs. 5.8 and 5.9), so that the flux prediction difference has another origin.

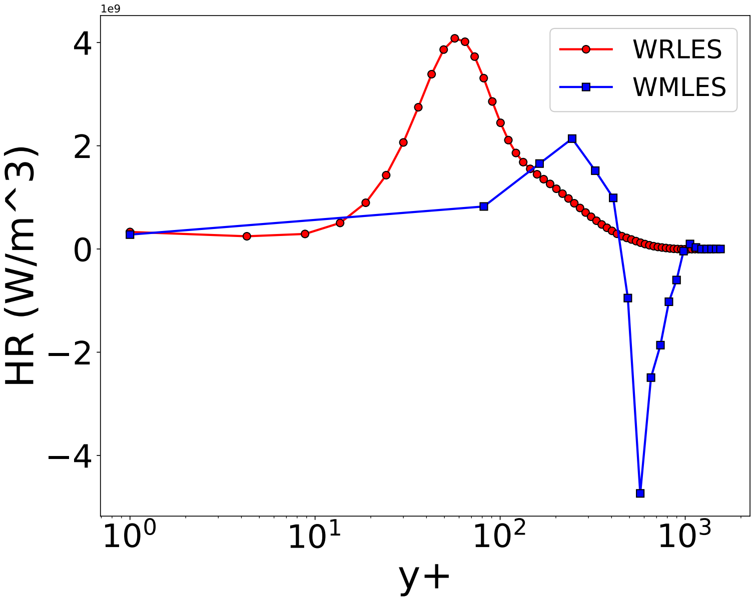

Figure 5.5: Averaged heat release rate profiles normal to the wall in plane A.

The averaged heat release rate profiles normal to the wall of the reacting cases presented Fig. 5.5 show important differences between WRLES and WMLES. In WRLES a single exothermic peak is observed between roughly $10 < y^+ < 120$, including therefore the buffer layer and the beginning of the turbulent boundary layer zones. The maximum value is reached at $y^+ = 60$. In the WMLES however, the first grid point being located at $y^+ = 80$, the simulation cannot describe this behaviour. The coarse mesh produces also an exothermic zone but around $y^+ = 200$, endothermic reactions appear and take over, something that does not exist in the WRLES.

Details of this heat release rate are in Fig. 5.6, where fields of the heat release rate and the source terms of the main contributing species to the chemical activity in the near wall region in Plane A are presented. Exothermic activity is indeed found (top-left image) and is related to the consumption of OH and O2 to produce H2O. Meanwhile, the CO/CO2 equilibrium characteristic of post-flame zones which is exothermic, is found to move as the two species exhibit quite high source terms next to the wall. Interestingly the averaged species profiles of Fig. 5.7 show that despite a lower near-wall resolution, the WMLES follows the same trend than WRLES. However it can be seen again that species CO, CO2 and H2O reach different values at the wall, meaning that some reactions of CO/CO2 equilibrium and H2O production are not correctly described in WMLES.
The contribution of the main species to the heat release rate is shown in Fig. 5.8. Note that these plots have been normalized by the mean heat release rate in plane A to easily compare the WR- and WMLES cases. The plots confirm the above findings: the chemical activity in the WMLES *qualitatively* follows the same trends as in the WRLES. the species CO2 and H2O are found to be the main responsibles for the heat release in both simulations, with an exothermic for CO2, endothermic for H2O contribution in the temperature range 1200 - 2200K, and conversely an endothermic for CO2, exothermic for H2O contribution for higher temperature

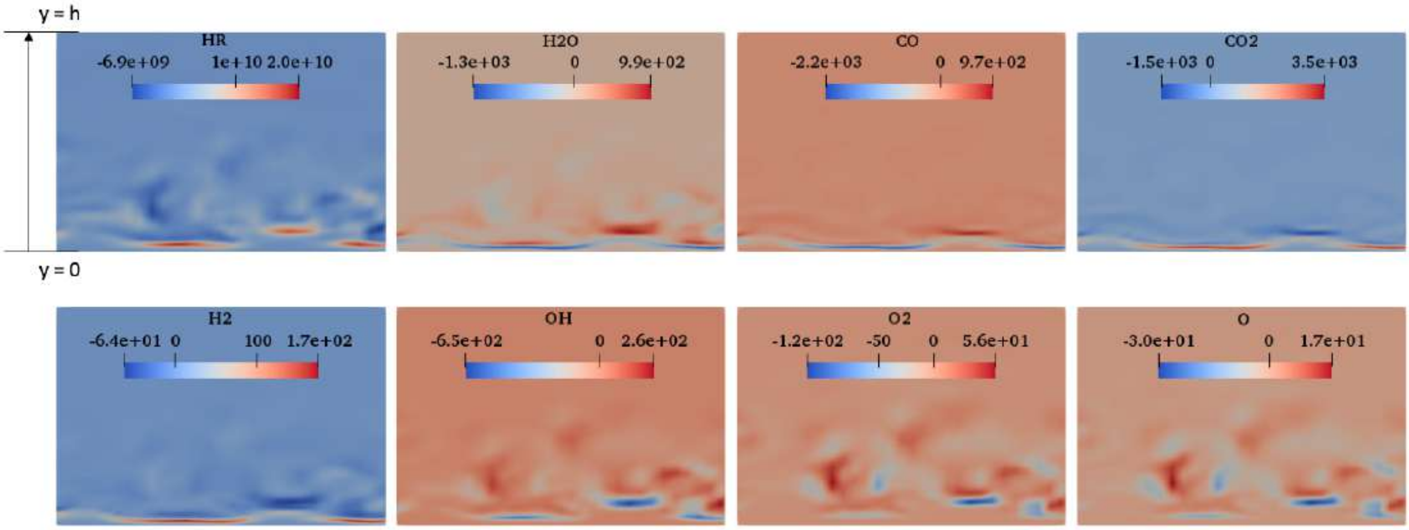

Figure 5.6: Instantaneous fields in Plane A (case WRLES_R) over the channel half-height h of the heat release rate (top-left corner, in W/m^3) and the main species source terms (in $kg/m^3/s$).

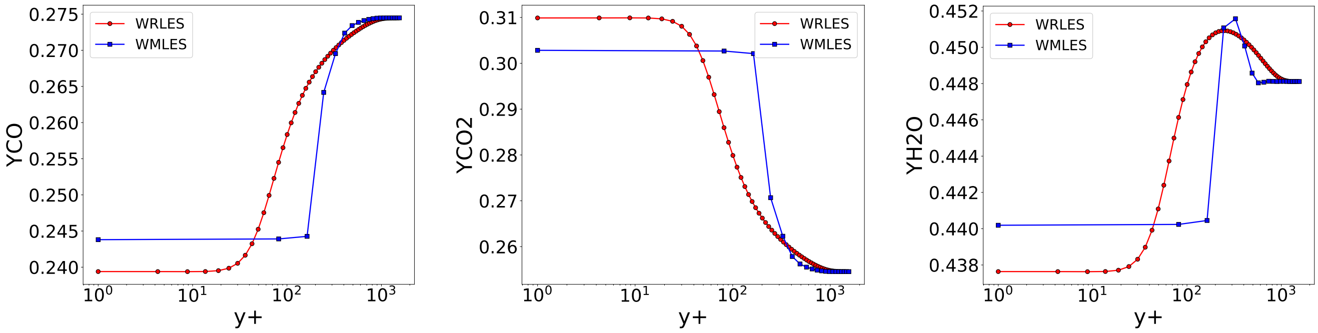

(a) CO (b) CO2 (c) H2O

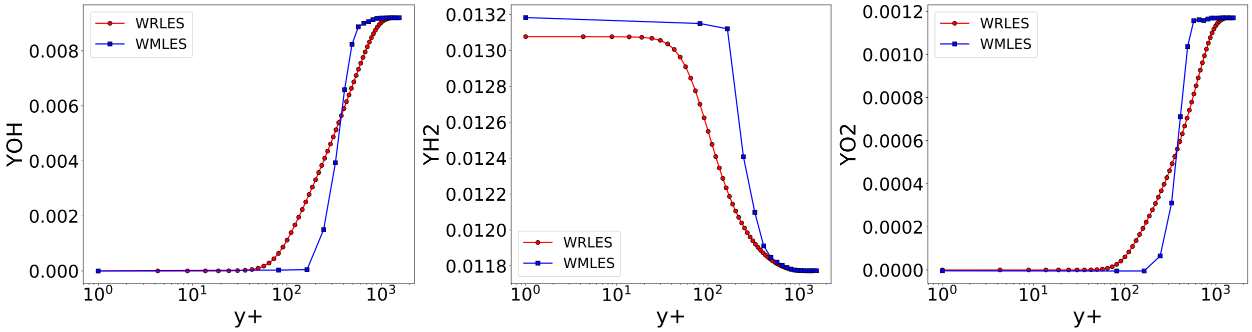

(d) OH (e) H2 (f) O2

Figure 5.7: Average profiles of the main species mass fraction as function of y^+ in WRLES and WMLES of the reacting cases, located in plane A.

up to ≈ 2700K. However, Fig. 5.9 also recalls that these large temperature intervals are poorly represented in the WMLES, covered with no more than 2 grid points in the temperature profile. Therefore, the active reactions in these temperature ranges cannot be properly represented *quantitatively* by the WMLES. Their intensity seems actually under-estimated, as shown in the scale difference in Fig. 5.8 of one order of magnitude, which explains the lower wall heat flux difference between the frozen and reacting cases in WMLES compared to WRLES. This low resolution effect may also explain the weird point at $y/h = 0.1$ in the temperature profile in Fig. 5.9a.

Another striking difference in Fig. 5.8 is the heat release contributions at T=3000K, where almost no reactivity is seen in the WRLES, while it is maximum in the WMLES, corresponding to the endothermic peak of Fig. 5.5. This again may be attributed to the filtering induced by the coarse mesh in this region.

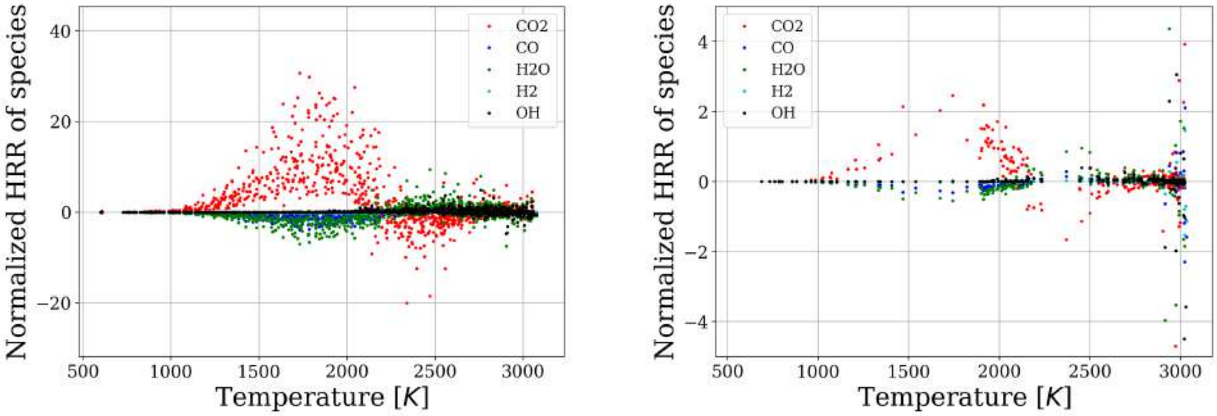

(a) WRLES

(b) WMLES

Figure 5.8: Instantaneous scatter plots of WRLES (a) and WMLES (b) of the contribution of the main species to the heat release rate, normalized by the mean HRR in plane A, as function of the temperature.

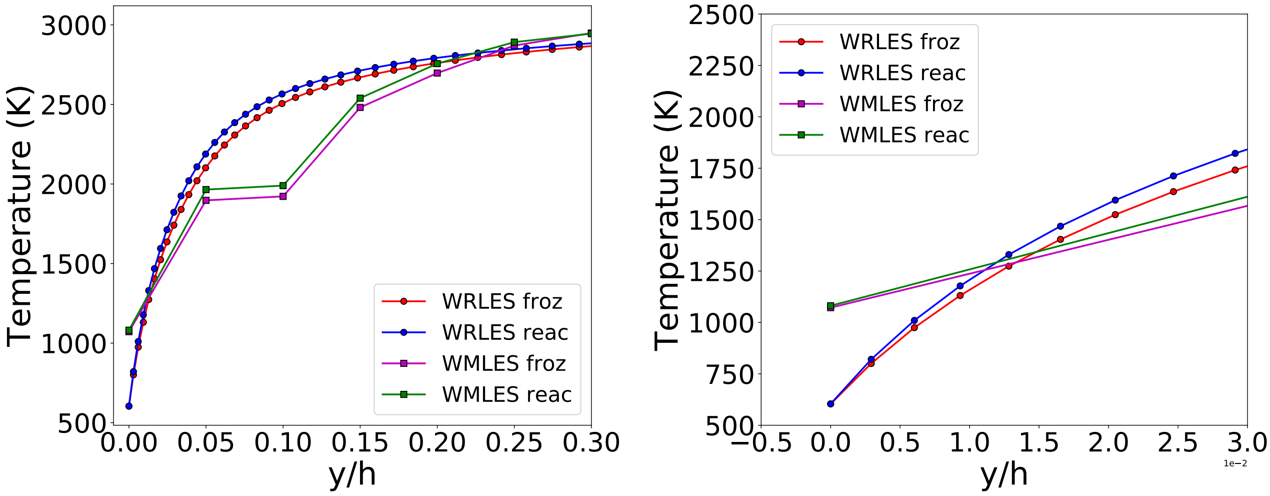

(a)

(b)

Figure 5.9: Average temperature profiles as functions of y/h in WRLES and WMLES for the frozen and reacting cases, located in plane A. Figure (b) is a zoom on the viscous sub-layer.

Remarks:

- *Note that the same behaviours about coupling wall-law and SGS model, as investigated in Section 5.2, are observed here. Considering the WRLES as the reference, the WMLES run as well with the Sigma model overall over-predicts the fluxes by the same order of magnitude, about +10 to +20%, respectively for the frozen and reacting flows.*
- *In Table 5.7 (WMLES cases), the physical properties* ρ_w *and* μ_w *are computed with the wall temperature imposed by the boundary condition (i.e., 600K), as is done in the wall-law. The heat capacity* Cp_w *is computed differently, taken as the cell value therefore using the cell temperature, about 1075K in this case (first grid point of Fig. 5.9b). In the WRLES, the wall temperature value is indeed 600K, explaining the lower* Cp_w *than in WMLES. This effect also contributes to the wall heat flux over-prediction in WMLES. Note that* λ_w *is also taken at the cell temperature, leading to a higher value in WMLES than in WRLES, but as this quantity is not used in the wall-law it is difficult to conclude about its effect.*
- *Results in Plane B show the same trends. However problematic pressure waves near the outlet make them less converged so that only Plane A results were presented.*

5.3.4 Conclusions

Both wall-resolved laminar and turbulent cases show that chemical activity in the boundary layer has a non-negligible impact on the prediction of the wall heat flux with a difference about +8-10% compared to the non-reacting case, which is consistent with the literature [Perakis et al., 2020, Betti et al., 2016]. A difference is also observed for the wall friction prediction, but to a lesser extent. The origin of the difference is identified to be the wall gradients of temperature and velocity, which are significantly impacted by chemical activity. In particular the CO-CO2 equilibrium seems to play a key role, also previously highlighted by the same authors [Perakis et al., 2020, Betti et al., 2016].

This behaviour is qualitatively retrieved in WMLES, however the poorer resolution tends to decrease the difference between the reacting and non-reacting boundary layers. This means that in order to get closer to a reference resolved boundary layer, the effect of chemistry on the temperature and velocity gradients should be introduced in the wall model. Without this effect, the current coupled wall-law as implemented in AVBP is not able to recover the correct wall fluxes in case of reacting boundary layers.

In order to model the impact of chemistry on wall fluxes in WMLES, a first possibility would be to implement the full formulation of the coupled wall-law, as originally developed by Cabrit [Cabrit and Nicoud, 2009], and taking into account chemical enthalpy fluxes. However, this may not be sufficient considering the results of this section, as it seems that the chemical reactions in WMLES are not at the right level of intensity. This calls for a sub-grid scale chemical reaction model suited to near-wall flows. To go in this direction, [Muto et al., 2019] considered to evaluate chemical equilibrium at the wall. This was applied for H2/O2 combustion, *i.e.*, a highly reactive mixture close to equilibrium in most locations. In the case of CH4/O2 combustion however the CO/CO2 equilibrium is a much slower process and the assumption of equilibrium may not hold.

Part IV

Applications

Chapter 6

The CONFORTH configuration

The CONFORTH configuration is a lab-scale Liquid Rocket Engine owned by ONERA (Palaiseau), and is a modification of the Mascotte test bench [Palerm et al., 2015]. It allowed to study many aspects of cryogenic rocket engines both experimentally and numerically, like flame dynamics [Candel et al., 2006, Habiballah et al., 2006], heat transfer [Ordonneau et al., 2016, Pichillou et al., 2017, Grenard et al., 2019], and more recently, soot emission [Vingert et al., 2019], however particularly focusing on wall heat transfer in conditions close to a real LRE. CONFORTH can be run at pressure from 20 to 70 bar and with oxy-combustion of hydrogen or methane at various mixture ratios. Two versions exist: a "thermal" version used to measure temperature and heat fluxes at the wall and a "visualization" version with a glass window to see the flame shape and atomization process. The development of this test bench is part of the CNES strategy in support of future LRE programs [Palerm et al., 2015].

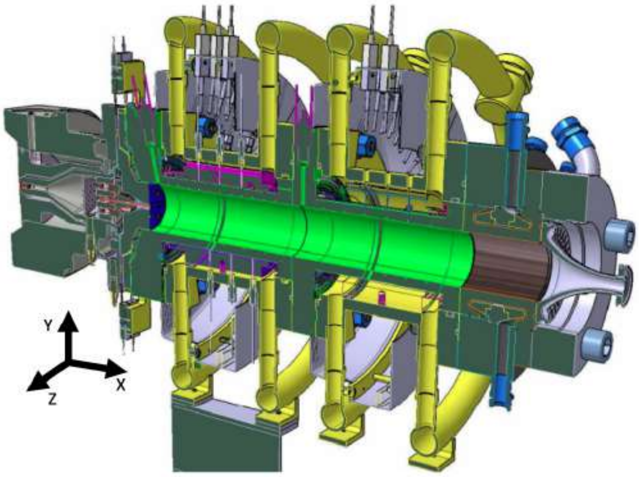

Figure 6.1: CAD of the CONFORTH test bench from ONERA [Pichillou et al., 2017].

The objectives of this section is twofold. First the high pressure ARC methane-oxygen scheme and the exponential time integration of chemistry presented in the Section 4.4.1 are evaluated, this time in the LES of a real system; also the ability of LES to predict wall heat transfers and temperature is studied, taking into account the conclusions of Section 5.3. With these objectives the LES have been run in the "thermal" configuration of the test bench (see Fig. 6.1).

Note that some parts reported below are directly taken from [Blanchard et al., 2022], and enhanced with some information complements.

6.1 Experimental setup

The experimental setup is detailed in [Ordonneau et al., 2016]. The CONFORTH test bench consists of five coaxial injectors: one central and four others placed all around on an external ring, as shown in Fig. 6.2. The chamber has a circular section and ends with a nozzle. The chamber walls, made of copper, are cooled by a water circuit. The injection head (faceplate) is not cooled. The chosen operating point for the present work, summarized in Table 6.1, is methane oxy-combustion at a pressure of 54 bar with a rich global equivalence ratio $\phi_g = 1.262$. Details about the geometry are not given for confidentiality reasons. For all the following, "X" denotes the axial direction (flow direction), and Y and Z the transverse coordinates: see Fig. 6.1.

Pressure	[bar]	54
GO_2 mass flow rate	[g/s]	124.78
GCH_4 mass flow rate	[g/s]	39.38
Global equivalence ratio	[-]	1.262
Mixture ratio	[-]	3.17
GO_2 temperature	[K]	279.7
GCH_4 temperature	[K]	283.8

Table 6.1: Operating point for the LES of the CONFORTH test bench.

The instrumentation of the bench is composed of thermocouples aligned along 3 so-called generating lines ("lignes génératrices"), shown in Fig. 6.2, in order to get the heat flux information at 3 locations:

- line A: is lined up with an external injector
- line B: is in-between the line aligned with an external injector and the line between two external injectors
- line C: is between two external injectors

Due to the axi-periodicity of the test bench the generating lines can also be considered to be at position 0°, 22.5°and 45°.

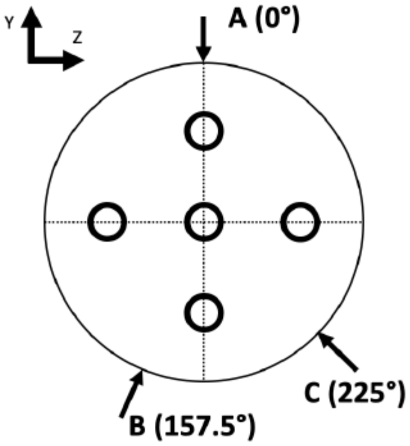

Figure 6.2: Generating line positions (cut normal to the X-axis).

Along each line pairs of thermocouples are regularly placed at several positions along the 400mm-long chamber: one thermocouple gives the temperature T_{PG} on the hot side (or gas side), the other one gives the temperature T_{PE} on the cold side (or cooling water side): see Fig. 6.5. The heat flux is then derived from these two temperatures at each point and from the known thermal conductivity λ_w of the solid material that separates them.
Two measurements of pressure were also made at the chamber wall at positions x=14mm and x=215.9mm.

6.2 Modelling

The AVBP solver is used, with the Lax-Wendroff convection scheme [Lax and Wendroff, 1960] and simplified transport rules: Prandtl and Schmidt numbers are constant. Furthermore, the subgrid-scale turbulence model is the Sigma model [Nicoud et al., 2011] and constant turbulent Schmidt and Prandtl numbers (fixed at 0.6 for both) are used for sub-grid species and thermal turbulent diffusion. The Soave-Redlich-Kwong cubic equation of state is used [Soave, 1972], and local filtering is applied to the density and pressure fields following the LAD approach [Schmitt, 2020] to avoid spurious numerical perturbations.
Two simulations are performed: one with the classic time integration scheme (referred to as LES-CLASS), the other with the exponential time integration presented in Section 4.4.1 (referred to as LES-EXPO). Similarly to the 2D flame computations shown in Sections 4.4.1 and 4.5, the diffusion flames which develop in the chamber are artificially thickened by the mesh and do not require further thickening to be resolved. Subgrid-scale flame-turbulence interactions however are not explicitly taken into account, and in principle should be modeled. In the present case subgrid-scale effects are assumed small in comparison to the resolved turbulence thanks to the refined mesh in the flame zone and are omitted. It will be checked *a posteriori* that the flames are indeed purely non-premixed and that subgrid-scale turbulence is weak.

6.2.1 Numerical setup

Geometry and mesh

The whole 3D combustion chamber (with the five injectors) is simulated except the nozzle. The mesh about 33M cells is fully made of tetrahedral elements, which size from $\Delta x_0 = 40\mu m$ at the injector lips to $\Delta x_M = 3000\mu m$ in the domain. At the walls, tetrahedra are also used and y^+ values scale from 40 to 60 along the chamber. There are about 10 points to solve the flame thermal thickness. Fig. 6.3 shows an overview of the mesh.

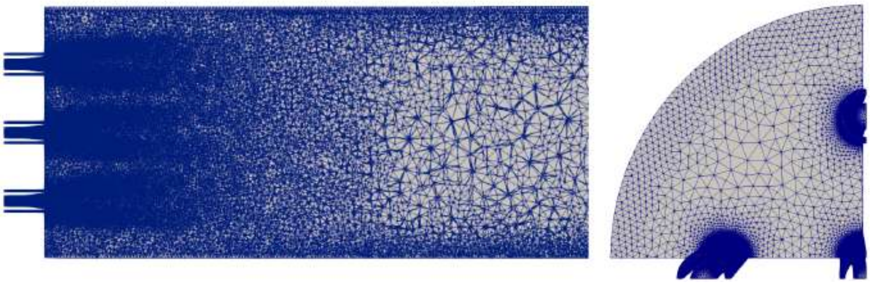

Figure 6.3: CONFORTH test bench mesh overview. Left: cut normal to Z-axis. Right: quarter of injection head normal to the X-axis.

Boundary conditions

The boundary conditions are formulated with the Navier-Stokes Characteristic Boundary Condition (NSCBC) approach [Poinsot and Lele, 1992]. Inlets are set with the recently published Non-Reflective Inlets (NRI) method [Daviller et al., 2019] which allows to absorb acoustics while maintaining the injection fluxes. As the nozzle is not computed, the outlet pressure is set at 54 bar. At the GCH_4 and GO_2 inlets, turbulent velocity profiles (of shape 1/7) are imposed. The injector (including lips) walls are treated with adiabatic slip conditions with the use of the standard wall-law. The injector head wall is treated as an isothermal wall with T=500K. The chamber walls receive a particular treatment which is described hereafter.
All boundary conditions are summarized in Fig. 6.4.

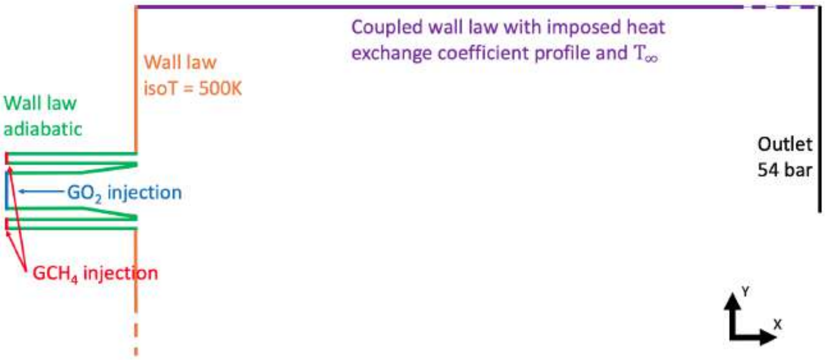

Figure 6.4: Boundary conditions: zoom on the top injector (cut normal to the Z-axis).

Wall modelling

The chamber walls make use of the coupled wall law derived by Cabrit [Cabrit and Nicoud, 2009], which takes into account the high temperature gradients expected between the burnt gases and the walls. The heat transfer through the wall is taken into account by imposing a heat exchange coefficient profile based on experimental results with a reference temperature set at $T_\infty = 280.15$K. The heat exchange coefficient was computed as explained in the following.

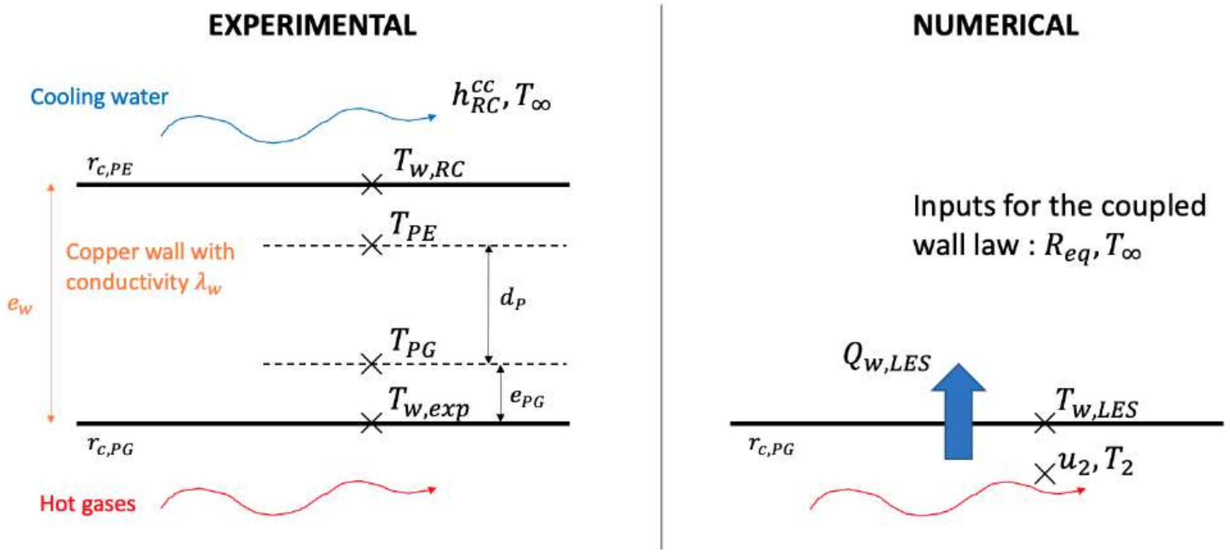

Figure 6.5: Thermal boundary condition (proposed by CNES). $Q_{w,LES}$ is the LES output, from which $T_{w,LES}$ is then retrieved.

The heat exchange coefficient in the cooling water was provided by ONERA for the 3 generating lines (not provided here for confidentiality reasons). They were averaged to get one single longitudinal profile h_{RC}^{cc}. Then the equivalent heat exchange coefficient h_{eq} is calculated following Eq. 6.1 (the details are given in Annex A., as proposed by CNES in [Martin-Benito, 2019]), which takes into account convection from the cooling water h_{RC}^{cc} and conduction through the wall material with λ_w. $r_{c,PG}$ is the chamber radius, $r_{c,PE}$ is the chamber radius plus the wall thickness, e_w is the wall thickness, e_{PG} is the distance between the wall and the thermocouple located on the hot side, and d_P is the distance between the two thermocouples. Figure 6.5 sums up the modelling, from the experimental data to the simulation inputs.

$$h_{eq} = \frac{1}{r_{c,PG}\left(\frac{\ln\left(\frac{r_{c,PE}}{r_{c,PG}}\right)}{\lambda_w} + \frac{1}{r_{c,PE}h_{RC}^{cc}}\right)} \tag{6.1}$$

In AVBP, the coupled wall boundary condition with heat loss (WALL_LAW_COUPLED_LOSS) requires as input a heat resistance R_{eq}, which is here simply the inverse of h_{eq}. The experimental values have therefore been fitted into a 7-order polynomial, as indicated in Fig. 6.6, to be easily implemented.

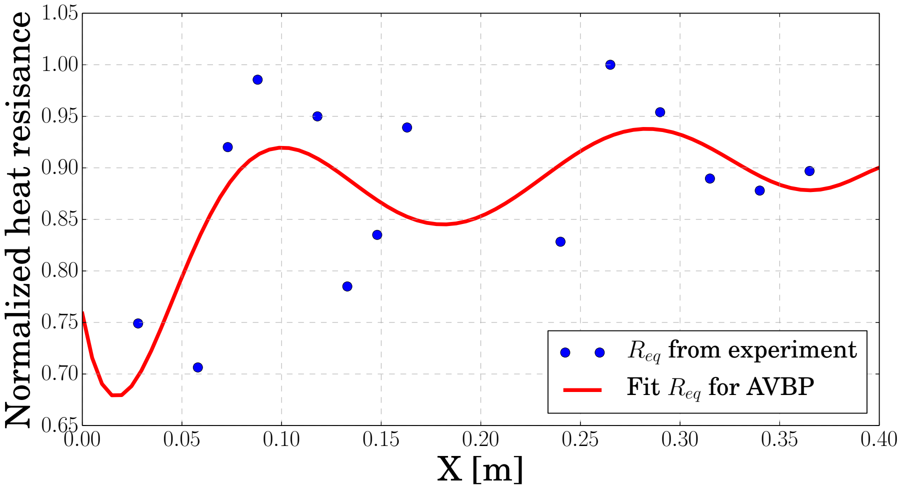

Figure 6.6: Longitudinal heat resistance profile R_{eq} used in AVBP as wall boundary condition.

6.3 Results

Two simulations are performed: one with the classic Arrhenius form time integration (referred to as LES-CLASS), the other with the exponential time integration of chemistry presented in Section 4.4.1 (referred to as LES-EXPO). The simulations were run for about two convective times, estimated to be 8.5ms. This represents in terms of CPU cost about 1100 kh for the LES-CLASS and about 800 kh for the LES-EXPO, meaning a reduction of about 27% with the exponential integration. Computations were run on the TGCC cluster IRENE, both on Skylake and KNL processors.
Some parts of the next section (the flame analysis) are directly taken from [Blanchard et al., 2022] published in *Acta Astronautica.*

6.3.1 Computational cost gain

The CFL time step is $\Delta t_{CFL} = 7.3ns$ while Eq. 4.7 gives a chemical time step $\Delta t_{chem} = 0.23ns$, i.e., about 32 times smaller. In practice, the case LES-CLASS runs with $\kappa_{CLASS} = 20$ while the case LES-EXPO runs with $\kappa_{EXP} = 10$, i.e., a 2 times higher chemical integration time step.

6.3.2 Flame analysis

Flame shape

All views presented in this Section are cuts across the Z-normal axis. Note that for confidentiality reasons, axes have been non-dimensionalized to new units X', Y', Z', the length $X' = 1$ corresponding to the mean flame length found (see Fig. 6.7).
Fig. 6.7 contains various averaged fields to compare the two integration methods, where a typical diffusion flame shape anchored at the lip is easily recognizable. The fields exhibit differences between the central and the side flames because of flame-flame and flame-wall interactions. The central flame is shorter, and it seems that the side flames are slightly bended towards the walls. Also, the main exothermic zone of the side flames is shorter next to the walls, due to the colder area near the walls. Both time integration methods give very similar results, also concerning the flame length.

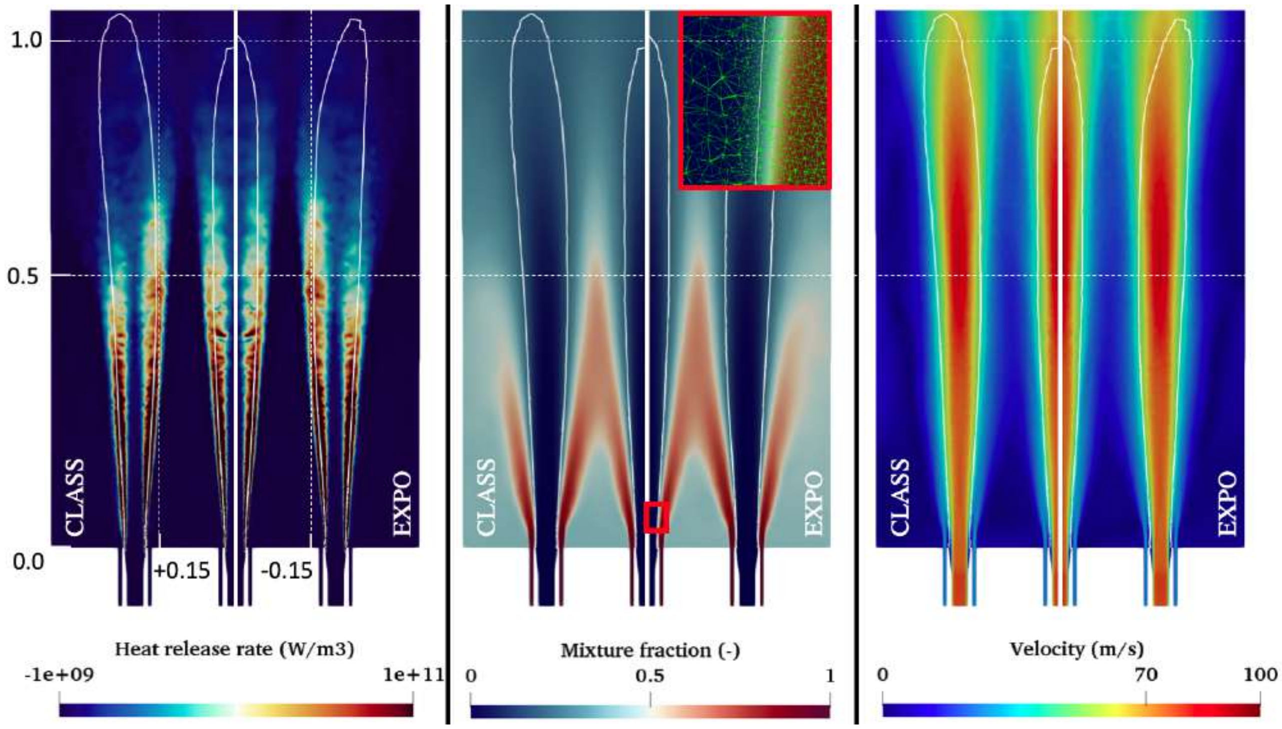

Figure 6.7: CONFORTH test bench. Cuts of averaged fields of heat release rate, mixture fraction and velocity obtained with the classic (left half) and the exponential (right half) methods, with the stoichiometric line in white ($Z_{st} = 0.2$). The red box indicates where the scatter plots are realized (see next Section).

Fig. 6.8 and 6.9 shows instantaneous fields of the temperature with superimposed streamlines. Corner and inter-injector recirculation zones appear with different sizes, extending to about $X' = 0.6$ and $X' = 0.15$ respectively in the axial direction. Short flames and fast thermal expansion lead to a thermally homogeneous flow of hot gases above 3500K from $X' = 0.9$ and downwards. However looking at Fig. 6.9, the burnt gases composition is less homogeneous: due to the different relative positions of the flames, CO is trapped in the corner recirculation zone, but entrained downstream by the accelerated flow between the flames.

It is also worth noting that the use of a cubic equation of state was indeed necessary to take into account the real gas conditions of the simulation in the flame zone due to the supercritical regime: Fig. 6.10 shows that the high intensity of heat release rate is located within the zone of compressibility factor $\mathcal{Z} = P/\rho r T = 0.95$, so that real gas effects is happening here. Note that as previously mentioned in Section 4.3.2, the ARC used in this simulation was reduced by using the perfect gas assumption for practicality reasons, however this does not impact its use for a cubic EoS.

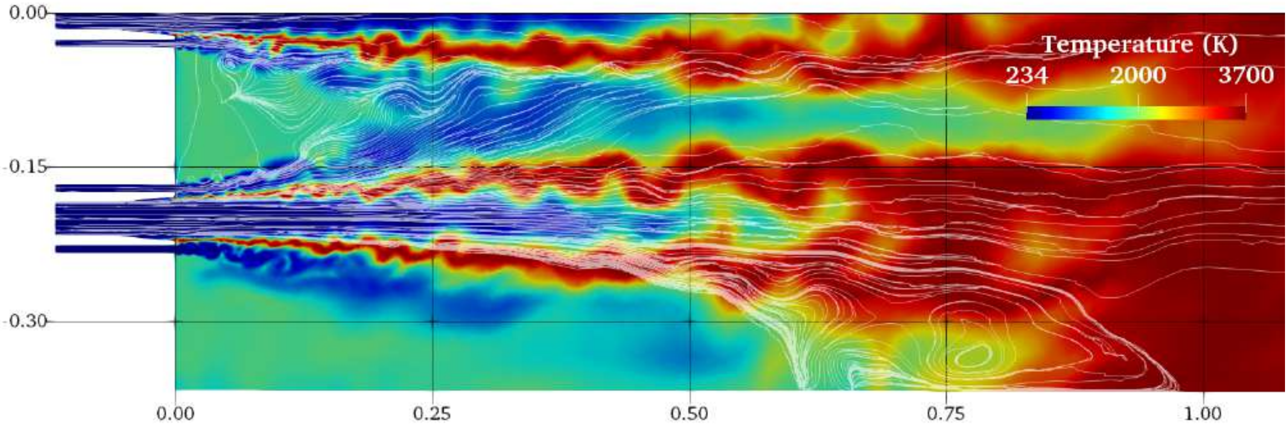

Figure 6.8: CONFORTH test bench. Instantaneous temperature field of the classical integration case with streamlines.

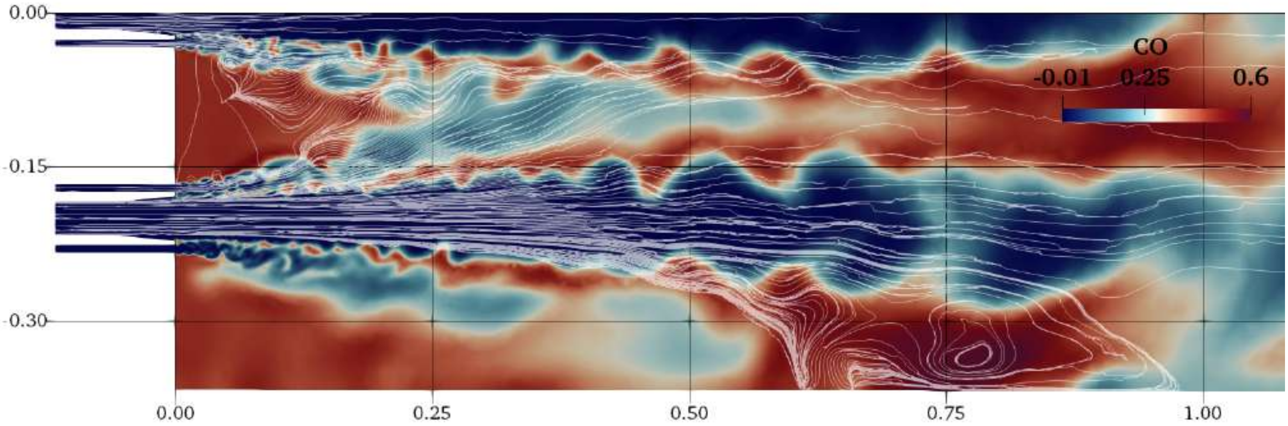

Figure 6.9: CONFORTH test bench. Instantaneous CO mass fraction field of the classical integration case with streamlines.

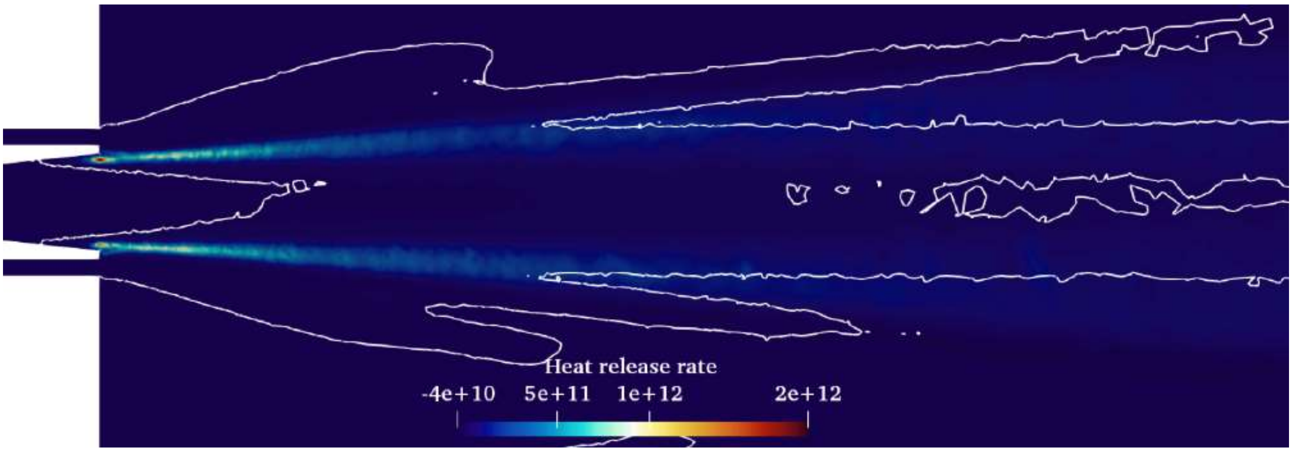

Figure 6.10: Averaged heat release rate field focusing on the central flame. The white isoline indicates the compressibility factor $\mathcal{Z} = 0.95$: inside this zone, $\mathcal{Z} < 0.95$.

Flame structure

It is first verified that the flame is purely non-premixed, using the Takeno index [Yamashita et al., 1996] ζ weighted by the heat release rate $\dot{\omega}_T$, computed and integrated through the whole domain V, as:

$$\zeta_{HR} = \int_V \zeta \times \dot{\omega}_T \tag{6.2}$$

It is found that about 73% of the heat is produced in non-premixed conditions. The remaining 27%, therefore burning as premixed, are identified to be at either far from the stoichiometric line, either at the tip of the flame where the resolution is poorer or either located in-between the flames, where the mixture is mainly composed of burnt gas products H_2O, CO and CO_2 but not yet at equilibrium: the mixture continues to react in a premixed mode to establish the correct CO-CO_2 equilibrium.

The flame structure is studied through scatter plots realized in the red box shown in Fig. 6.7 on the time-averaged solution. As a major control parameter of diffusion flames, strain rate statistics are first shown in Fig. 6.11. In the LES simulations, the resolved strain rate along the flame is computed as:

$$a_t = (\delta_{ij} - n_i n_j) S_{ij} \tag{6.3}$$

where n_i, n_j are the components of the flame normal, S_{ij} is the resolved fluid strain rate tensor, and δ_{ij} is the Kronecker symbol.

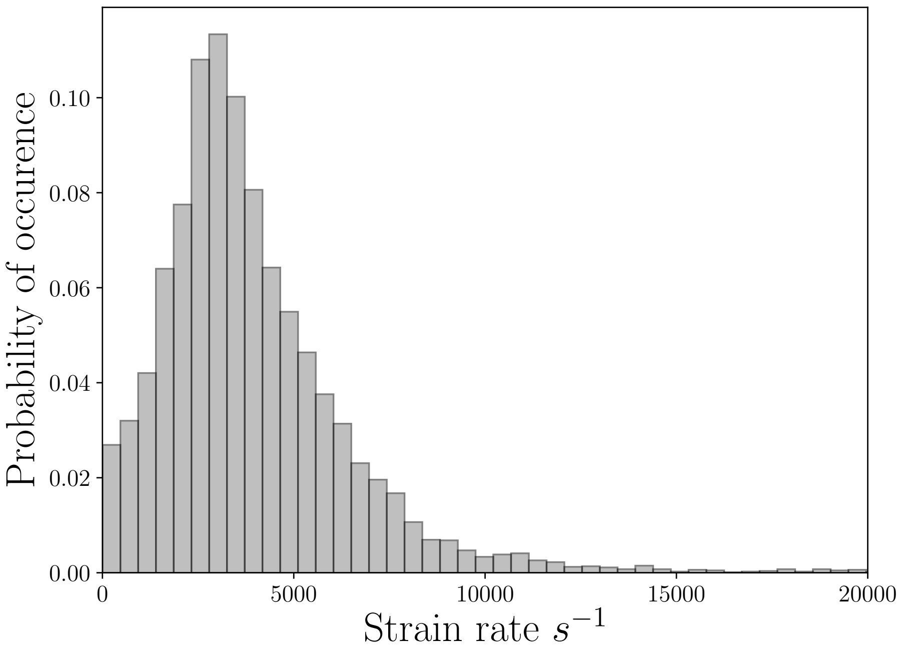

Figure 6.11: CONFORTH test bench. Strain rate distribution in the classical integration case.

In the considered area, 75% of the turbulent flame see a strain rate below 5000 s^{-1}, with a peak of the probability around 3000 s^{-1}. At this pressure, the extinction strain rate of a methane-oxygen flame is of the order of $3 \times 10^6 s^{-1}$, far above the maximum strain rate observed (of the order of $1.5 \times 10^5 s^{-1}$) which means that the present turbulent flame never quenches in the studied zone.

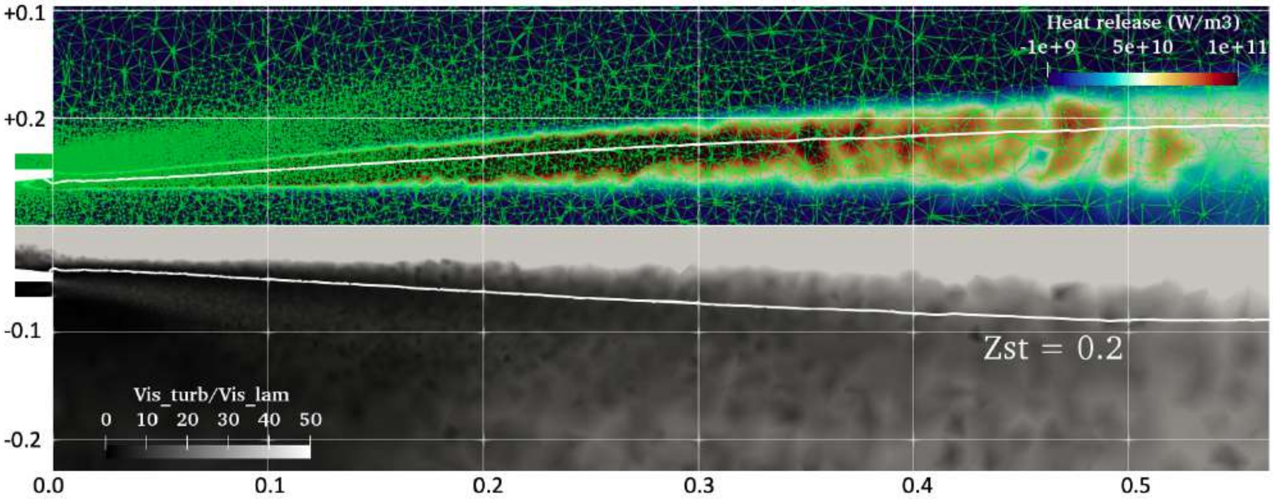

Figure 6.12: CONFORTH test bench. Details of the mesh in the central flame (top) and ratio of turbulent over laminar viscosities (bottom) for the averaged solution of the classical integration case. White isoline shows the stoichiometric mixture fraction.

As announced in the model description, the subgrid-scale flame-turbulence interaction is evaluated. To do this the ratio of the turbulent viscosity over the laminar viscosity is shown on Fig. 6.12. One can see that this ratio is quite low (below 10) in most part of the flame. This is explained by the fine mesh at the flame location, as shown in the top-half of the figure. Towards the flame tip, the mesh coarsens quite rapidly which results in higher values for the viscosity ratio, but at this location most of the heat release has already been produced. This low turbulent viscosity indicates a small flame-turbulence sub-grid intensity, which can be therefore neglected, following the same idea as in [Breda et al., 2020].
The maximum temperature gradient in the flame controls the thermal flame thickness which is calculated with Eq. 4.18 and is found to be between $220 < \delta_{th} < 49 \mu m$ for strain rates of $3000 < a < 30000 s^{-1}$. With a cell size going from 40 to 80 μm in this area, the mesh refinement is considered sufficiently fine to solve correctly this gradient.
To complete these statements about simulation quality, as the computations were long to converge and required many integration time steps, an error accumulation study is performed following the technique described in [Smirnov et al., 2015]. An average cell size is considered and compared to the domain lengths in each direction, providing a 3D relative integration error. Taking into account the total number of iterations performed, in the case of the LES-CLASS case the accumulation error estimate due to computation duration is found to be less than 2%, which is acceptable.

Scatter plots of temperature with mixture fraction are shown in Fig. 6.13 for the two cases and compared to the CANTERA solution at strain rate 4000 s^{-1}, which corresponds to the mean value in the zone defined by the red box of Fig. 6.7. They confirm that the flame is substantially stretched but stays far from quenching. Note that ARC remains valid for strain rates largely exceeding its range of derivation presented in Section 4.3.1: this is a known advantage of ARC as demonstrated in [Felden et al., 2019]. The two AVBP simulations give very same results, which are however different from the laminar CANTERA solution. The maximum temperature is lower in AVBP with about 400K gap, which can be explained by the fact that the LES flames are simply not adiabatic. It can be noticed that in the rich side of the flame, a group of points seems slightly out of the curves: they are found in the premixed zone, in between the flames.

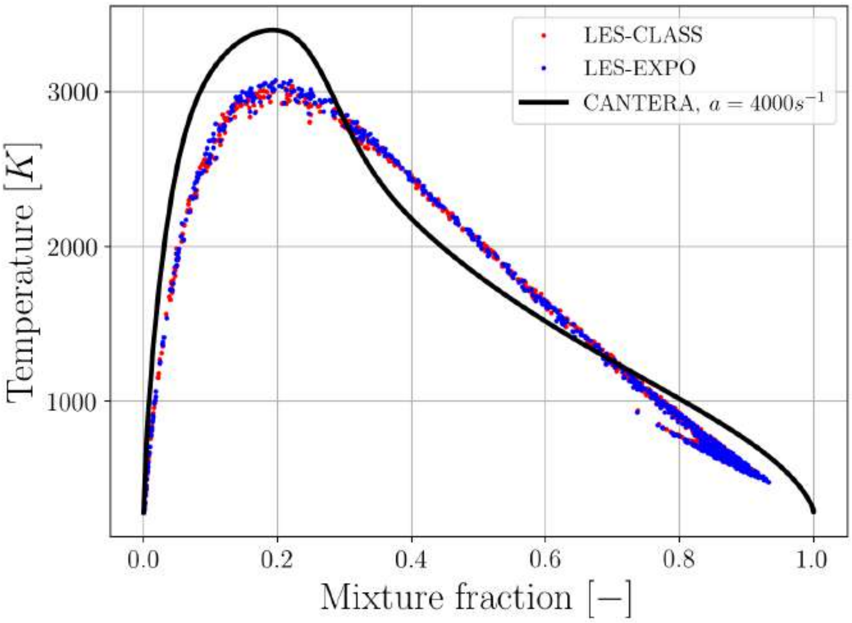

Figure 6.13: CONFORTH test bench. Scatter plots of temperature in the zone defined by the red box of Fig.6.7 for cases with classical and exponential integration, compared to the temperature profile of a laminar flame at equivalent mean strain rate.

To go further in the flame structure analysis, statistics of the time-averaged heat release rate in the mixture fraction space are shown in Fig. 6.14. In the figure, both the time-averaged and the standard deviation in the zone defined by the red box of Fig. 6.7 are plotted. The two AVBP computations are again very similar. However, due to the time-averaging operation, the complex shape with two exothermic and one endothermic peaks, as observed in the laminar flame solution at the representative strain rate of $a_{mean} = 4000s^{-1}$, is not recovered.

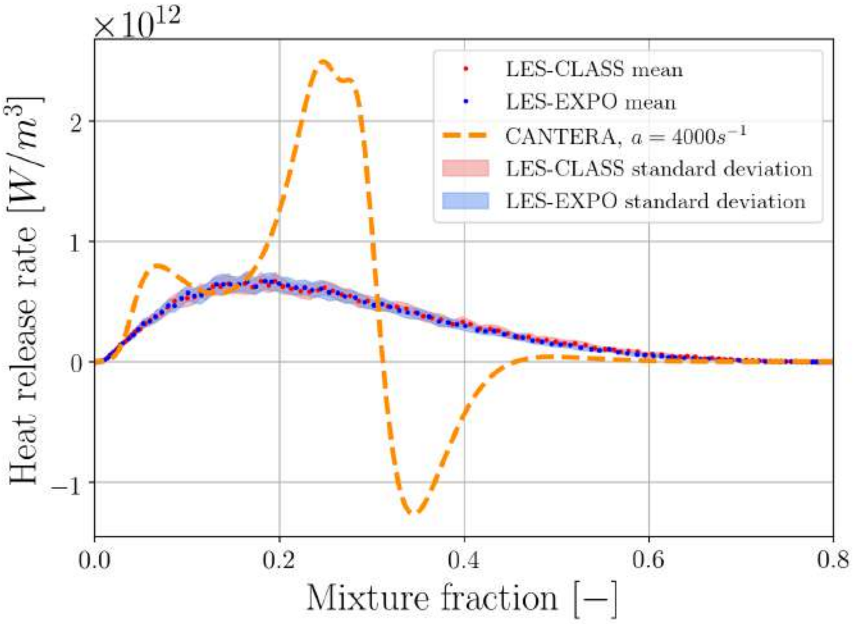

Figure 6.14: CONFORTH test bench. Time-averaged heat release rate: mean of the points located in the red box of Fig. 6.7 and their standard deviation, for cases with classical and exponential integration, compared to heat release rate profile of a laminar flame at equivalent mean strain rate.

To better elucidate the LES flame structure, the instantaneous heat release rate (together with the main species contributions) is plotted against the mixture fraction in Fig. 6.15. To obtain a typical curve, a reduced number of instantaneous solutions have been used to build scatter plots in the red box of Fig. 6.7 from which a fitted curve was extracted. Only the LES-CLASS case is shown, as same results were obtained for the LES-EXPO case. The instantaneous LES results clearly recover the whole complex, three-peaks flame structure, which confirms that time-averaging is responsible for the smooth heat release rate profile of Fig. 6.14. The species contributions explain the origin of the endothermic peak due to the species C_2H_2 and H_2 and, to a less extent, CO_2, while the main exothermic zone is due to C_2H_2 and CH_3. This highlights the importance of some species which are usually not found in simpler chemical schemes.

The flame can also be described in Fig. 6.16 where instantaneous chemical source terms are plotted (curves fitted on scatter plots). The first exothermic peak in the lean side around $Z = 0.1$ is due to the oxidation of CO in CO_2. The main exothermic peak between $0.2 < Z < 0.3$ corresponds to the consumption of the reactants O_2 and CH_4, the production of H_2O and CO, and the oxidation of radicals such as OH, CH_3 and C_2H_2. Finally the endothermic zone on the rich side is associated to the production of C_2H_2 and H_2 and the consumption of CO_2.

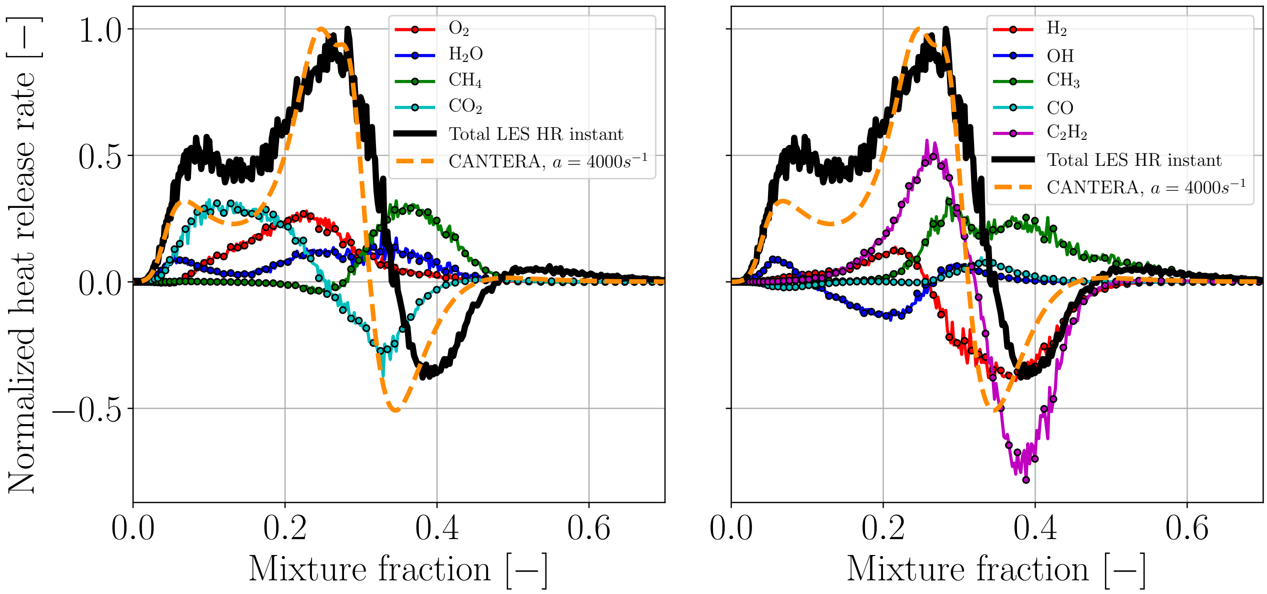

Figure 6.15: CONFORTH test bench. Instantaneous heat release rate and species contributions to the heat release (curves fitted on scatter plots in the red box of Fig. 6.7) for the classical integration case.

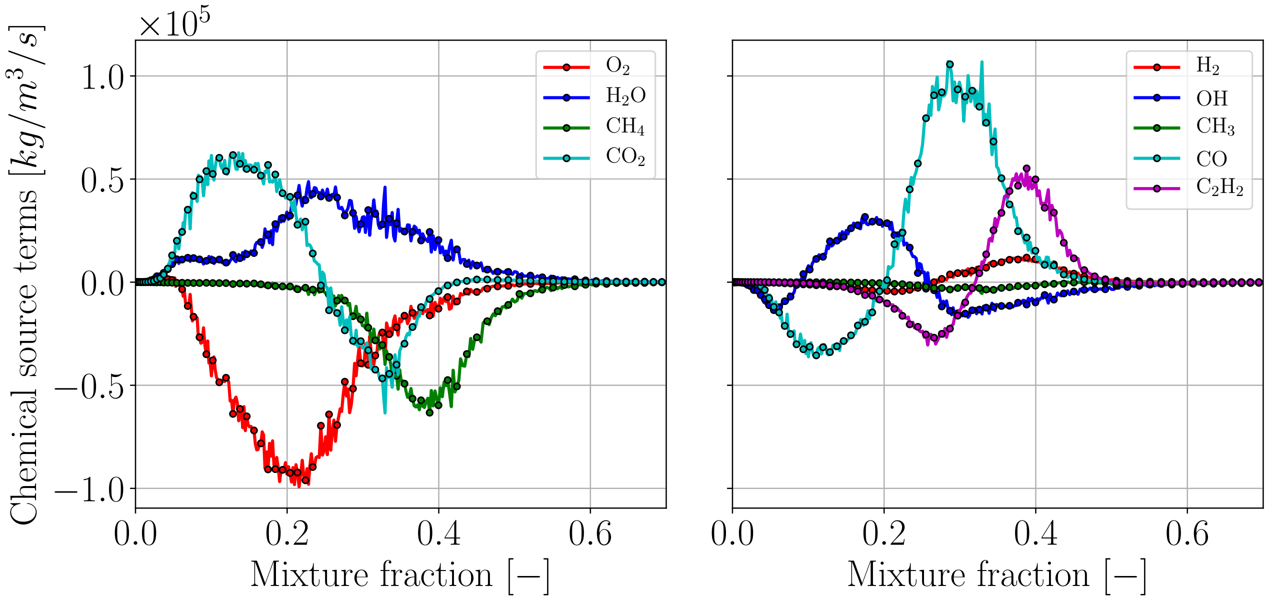

Figure 6.16: CONFORTH test bench. Instantaneous chemical source terms (curves fitted on scatter plots in the red box of Fig. 6.7) for the classical integration case.

Time-averaged species profiles are plotted in Fig. 6.17 to 6.19. For the propellants CH_4 and O_2, AVBP results fit correctly the CANTERA laminar flame solution, with little dispersion. The main products H_2O, CO and CO_2 show more discrepancies, in particular the CO-CO_2 equilibrium is slightly moved. Smallest species like CH_3 and OH exhibit larger differences compared to the laminar flame. In all those figures, note however the perfect match between the LES-CLASS and LES-EXPO case, demonstrating the validity of the exponential time integration method.

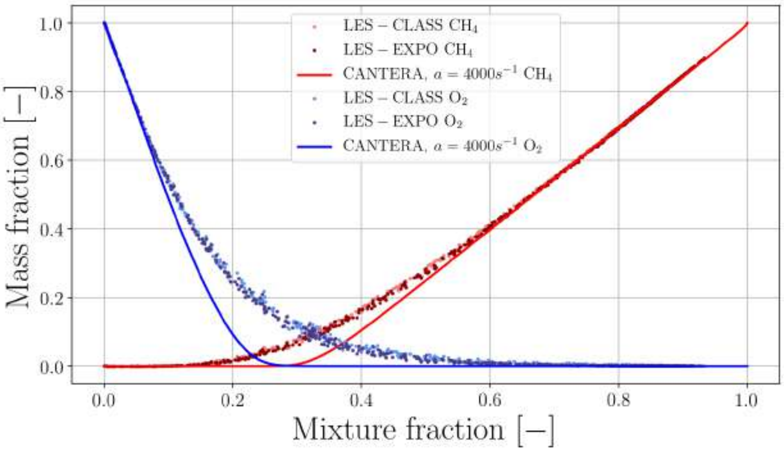

Figure 6.17: CONFORTH test bench. Scatter plots of CH_4 and O_2 from the time-averaged solution in the red box of Fig. 6.7.

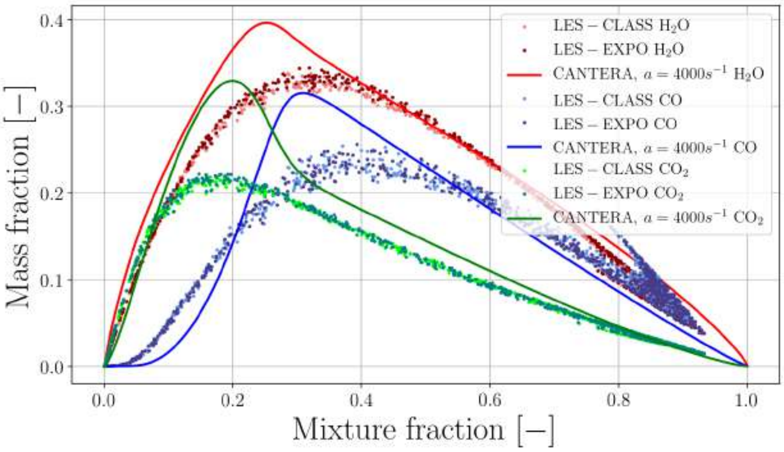

Figure 6.18: CONFORTH test bench. Scatter plots of H_2O, CO and CO_2 from the time-averaged solution in the red box of Fig. 6.7.

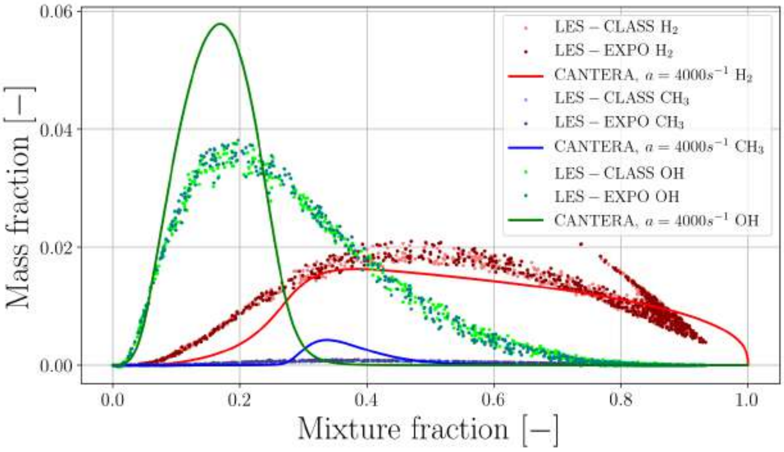

Figure 6.19: CONFORTH test bench. Scatter plots of H_2, CH_3 and OH from the time-averaged solution in the red box of Fig. 6.7.

6.3.3 Power budget

Here a global analysis of the combustion chamber power is performed. Note that in the experiment this power was not measured. The theoretical power released by a flame $\mathcal{P}_{th}$, in adiabatic conditions and assuming complete combustion, can be evaluated from the burnt fuel mass flow rate $\dot{m}_f$, multiplied by its lower heating value LHV_f (computed with CANTERA for these particular operating conditions). As the CONFORTH test bench operates in rich conditions ($\phi_g > 1$), the amount of burnt fuel is the total fuel mass divided by the equivalence ratio, so that:

$$\mathcal{P}_{th} = \dot{m}_f LHV_f/\phi_g = 0.03938[kg/s] \times 50.04[MJ/kg]/1.262 = 1.56MW \tag{6.4}$$

This is a crude estimation of the flame power which is in fact the maximum possible value corresponding to a fully adiabatic combustion chamber and no reversible chemical reactions.

Therefore the theoretical power of the test bench is better evaluated by taking the burnt gas at equilibrium. The solver CANTERA is used to compute the equilibrium (at constant enthalpy and pressure) with the ARC scheme species and in the conditions of CONFORTH, and starting from the initial composition defined as:

$Y_{O2,i}$	[-]	0.76
$Y_{CH4,i}$	[-]	0.24
Pressure	[bar]	54
T_i	[K]	280

Table 6.2: Initial conditions to compute the CANTERA equilibrium.

The sensible enthalpy difference between the initial state (index "i") and the final state (index "f") gives the flame power as:

$$\mathcal{P}_{th,CANT} = \dot{m}_{tot} \int_{T_i}^{T_f} C_p(T)dT = 1.34MW \tag{6.5}$$

where $\dot{m}_{tot} = 0.165kg/s$ is the total mass flow rate. The value $\mathcal{P}_{th,CANT}$ can be directly compared to the power found in the simulation. Figure 6.20 shows the two contributions to the total power computed from the LES: the heat release rate $\dot{\omega}_T$ (abbreviated as "HRR" and defined in Eq. 2.33) and the wall heat losses Q_w. Both quantities are first integrated in the cross section of the chamber S, and then presented as cumulative integrals. Starting from the location $x_0 = 0mm$ at the injection head plane, they are successively integrated along the x-axis until the end of the domain at $x_{max} = 390mm$:

$$C_{\dot{\omega}_T}(x') = \int_{x_0}^{x'} \int_S \dot{\omega}_T dS dx' \tag{6.6}$$

$$C_{Q_w}(x') = \int_{x_0}^{x'} \int_S Q_w dS dx' \tag{6.7}$$

The cumulative HRR exhibits a rapid growth from $x = 0$ to $x = 100mm$, giving therefore an indication on the flame length in the LES of about 100 mm, consistent with the flame analysis presented in Section 6.3.2. The cumulative HRR continues to grow, but more slowly until the

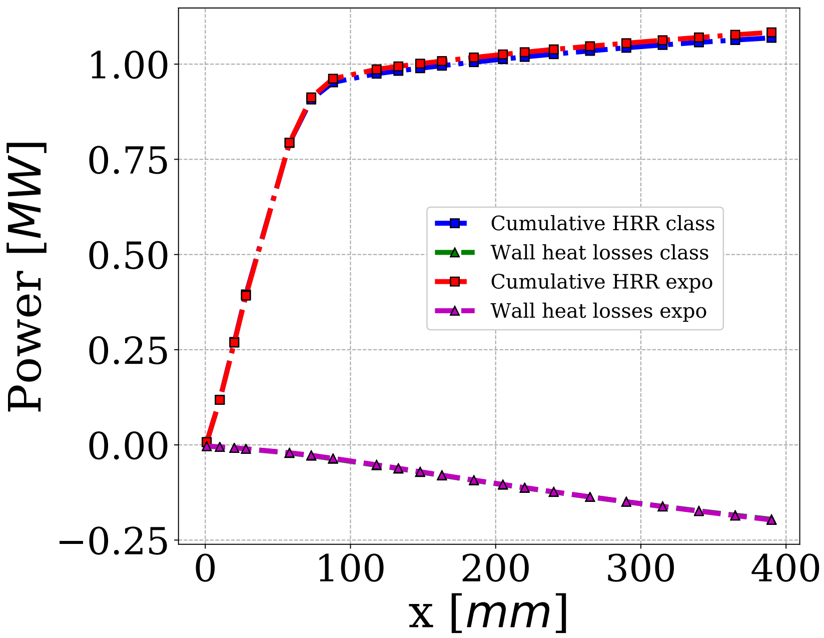

Figure 6.20: Axial power evolution.

end of the chamber, indicating that there are still exothermic chemical reactions in the post-flame zone and that equilibrium is not reached at the chamber exit. This behaviour mainly comes from chemical activity at the walls and is discussed further. Meanwhile wall heat losses increase almost linearly. Note that both classical and exponential integration methods show again an excellent agreement.

The final value of the cumulative HRR at x_{max} is the total power generated by the flame in the whole domain and equivalently, the final cumulative wall heat loss is the total power loss:

$$\mathcal{P}_{HRR} = C_{\dot{\omega}_T}(x_{max}) \tag{6.8}$$

$$\mathcal{P}_{Q_w} = C_{Q_w}(x_{max}) \tag{6.9}$$

In fact wall heat losses have an impact on the sensible enthalpy of the mixture throughout the domain, which is taken from $\mathcal{P}_{HRR}$. Therefore to compare to the theoretical power in adiabatic conditions, $\mathcal{P}_{HRR}$ and $\mathcal{P}_{Q_w}$ are simply added. Note that the heat losses at the injection head are taken into account: they represent about 1.6% of the total wall heat flux $\mathcal{P}_{Q_w}$.

$$\mathcal{P}_{tot,LES} = \mathcal{P}_{HRR} + \mathcal{P}_{Q_w} \approx 1.07 + 0.20 = 1.27MW \tag{6.10}$$

It is found that the total power of the LES is about 5.2% lower than the theoretical power of Eq. 6.5, obtained with the CANTERA equilibrium. This is not a surprise because as explained above, the mixture does not reach equilibrium at the end of the domain, and therefore more heat could be still released if the chamber was longer. To evaluate this missing enthalpy, another equilibrium calculation is performed with CANTERA, starting with the burnt gases mean composition and temperature at the outlet plane (*i.e.*, the composition of LES-CLASS shown in Table 6.3). The sensible enthalpy difference between the obtained equilibrium and the initial state is found to be $\Delta h_{equil} = 0.27MJ/kg$, here per kg of mixture (here in adiabatic conditions). Multiplying by $\dot{m}_{tot}$, the power P_{equil} which would be released by the mixture at the outlet plane when reaching equilibrium is:

$$\mathcal{P}_{equil} = \Delta h_{equil} \dot{m}_{tot} = 0.045 MW \tag{6.11}$$

Note that $\mathcal{P}_{equil}$ is computed without heat losses and therefore is only an estimation of the missing enthalpy. Finally, if the equilibrium was reached in the LES, the total power would be:

$$\mathcal{P}_{tot,LES,eq} = \mathcal{P}_{HRR} + \mathcal{P}_{Q_w} + \mathcal{P}_{equil} \approx 1.07 + 0.20 + 0.045 = 1.315 MW \tag{6.12}$$

With this estimation the theoretical power $\mathcal{P}_{th,CANT} = 1.34MW$ is almost recovered, and considered satisfactory in view of the approximations made. This energy budget shows that wall heat losses impact significantly the enthalpy and the temperature of the burnt gases in two ways: directly through the loss of sensible enthalpy, and indirectly through the modification of the chemical composition and final equilibrium.

6.3.4 Burnt gases composition

The burnt gases composition is analysed at $x = 390mm$, slightly before the outlet. As the mixture is stratified due the temperature change from the bulk flow to the walls, only the bulk zone is considered here, as shown in Fig. 6.21. Table 6.3 presents averaged values in this inner zone, obtained both from the LES cases and a CANTERA reactor case that has been computed with the temperature and pressure found in the LES-CLASS: $T_{bulk,out} = 3427K, P_{bulk,out} = 54.07bar$.

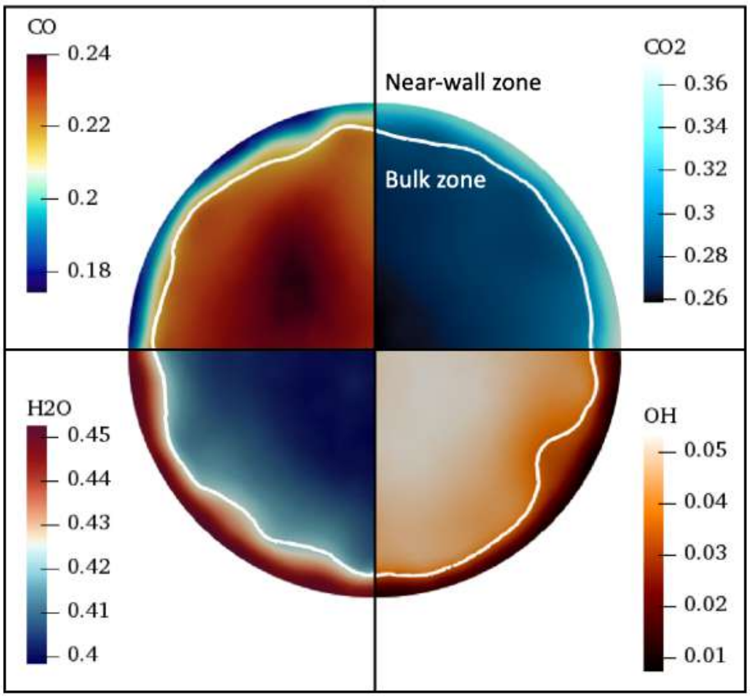

Figure 6.21: Outlet plane of the LES-CLASS where the burnt gases composition is analysed. The white isocontour corresponds to $T = 3300K$, the arbitrary delimitation between the bulk and the near-wall region.

	CANTERA	LES-CLASS	LES-EXPO
$T(K)$	3427	3427	3432
$\rho(kg/m^3)$	4.17	4.13	4.17
H2O	0.417	0.405	0.400
CO	0.219	0.224	0.211
CO2	0.278	0.270	0.277
OH	0.043	0.047	0.050
O2	0.030	0.038	0.048
H2	0.007	0.008	0.007
O	0.006	0.007	0.008
H	0.0009	0.001	0.001
HO2	0.0001	0.0001	0.0002

Table 6.3: Burnt gases composition comparison of the bulk flow at $x = 390mm$ (species below 1e-5 in mass fraction are omitted).

The burnt gases composition is in good agreement between the two LES cases, and also with the CANTERA equilibrium. The differences mainly originate from the O2 and OH mass fractions, two quite reactive species which are found at higher level in the LES cases. The CO/CO2 equilibrium seems reached in Table 6.3, however this is true for the bulk flow only: as indicated by Fig. 6.22a, the main mass fractions are still evolving in the axial direction, but this is mainly due to near-wall reactions: this is investigated further. This is in agreement with the fact that the cumulative heat release rate continues to grow slowly in the axial direction, as presented in Fig. 6.20. It is also interesting to note that despite the rich equivalence ratio, no methane remains in the burnt gases (this is consistent with the CANTERA result). It means that the methane excess has been consumed in intermediate reactions and transformed in other carbonated species.

Thus, note that the direct comparison between the LES and CANTERA suffers from the arbitrary delimitation between the bulk flow and the near-wall zone, and also that CANTERA was run with a perfect gas assumption, different from AVBP run with the SRK EoS.

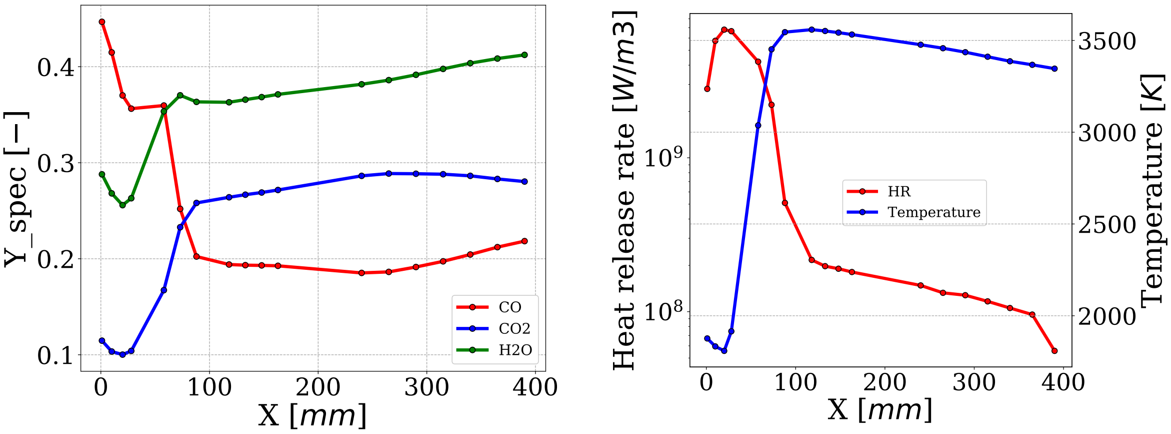

(a)

(b)

Figure 6.22: Time-averaged axial evolution of main combustion products (a) and temperature and heat release rate (b), integrated over cross section normal to the flow direction.

So far the analysis focused on the bulk flow. The radial evolution of the composition, *i.e.*, from the center line to the wall at different axial locations is now studied. This is presented in Fig. 6.23. As expected, the burnt gases composition is modified by the local temperature, which decreases when approaching the wall under the effect of heat losses. The position $x = 58mm$ is in the flame zone so that a homogeneous burnt gases mixture is not yet established. Going downstream, from $x = 118mm$ and further, the radial evolution is clear: close to the chamber walls (R=28mm) the lower temperature modifies the burnt gases composition significantly in a relatively small distance. This is particularly true for the CO-CO2 equilibrium, which moves toward more CO conversion into CO2 for colder temperature.

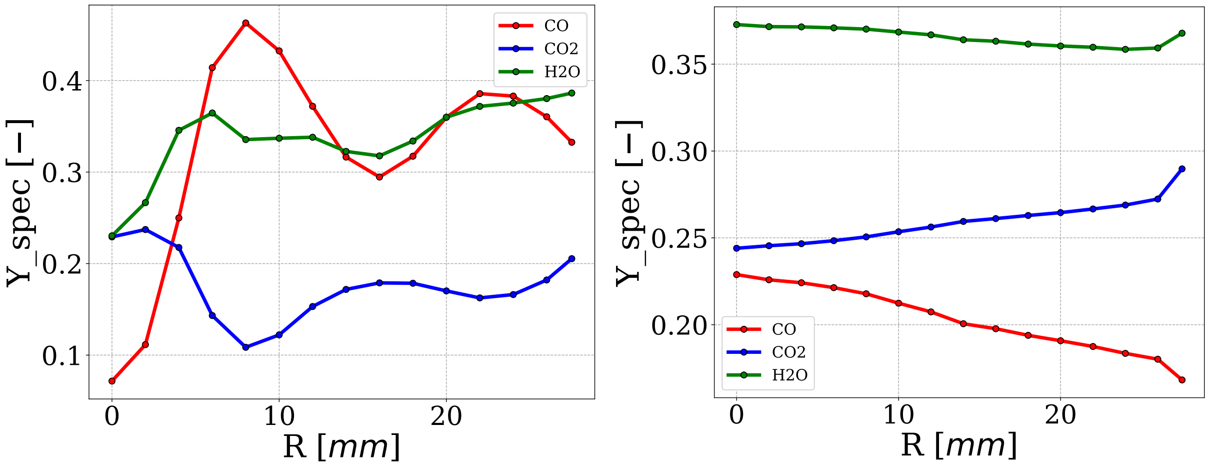

(a) x=58mm (b) x=118mm

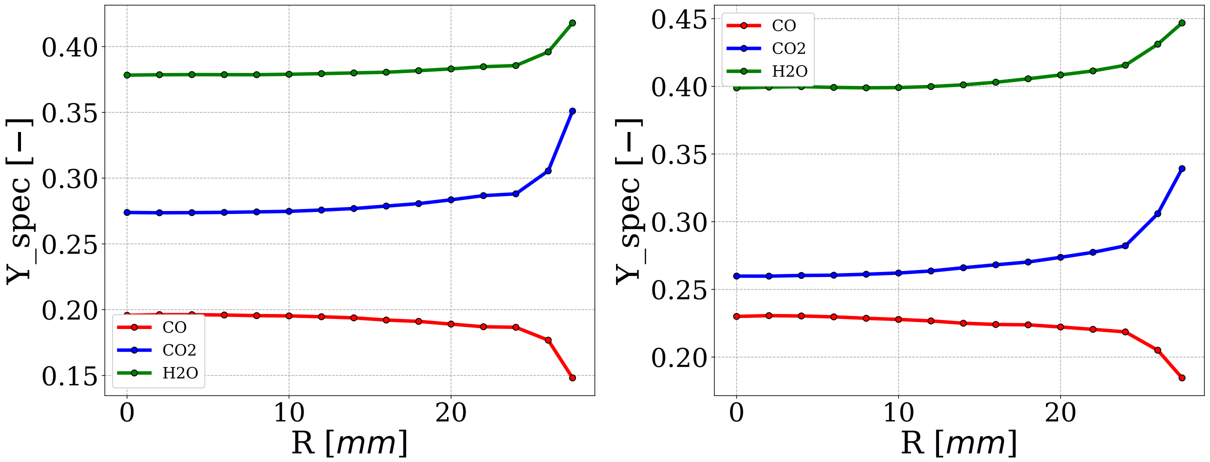

(c) x=265mm (d) x=390mm

Figure 6.23: Time-averaged radial evolution of the main combustion product mass fractions at several axial positions along the chamber. The profiles are spatially-averaged in azimuthal direction.

Thanks to the use of an ARC scheme, it is possible to go further in the analysis of the chemical activity at the wall. Radial profiles of the chemical source terms of the main species are plotted in Fig. 6.24 at two axial positions. One can see that downstream the flame zone (x>100mm) the chemical activity in the bulk flow (from r=0 to r=24mm) is very limited compared to the near wall-region (from r=24 to r=28mm). In this zone the source terms are consistent with the previous analysis on the species: H2O and CO2 are produced while other species as CO, O, OH are consumed. Typically, reactions such as [CO + O2 <=> CO2 + O], [CO + OH <=> CO2 + H], or [CO + O + M <=> CO2 + M], "M" being a third-body, contribute majorly to this strong chemical activity. It is interesting to note that O2 is among the main consumed species, despite the fact that the test bench operates in global rich conditions.

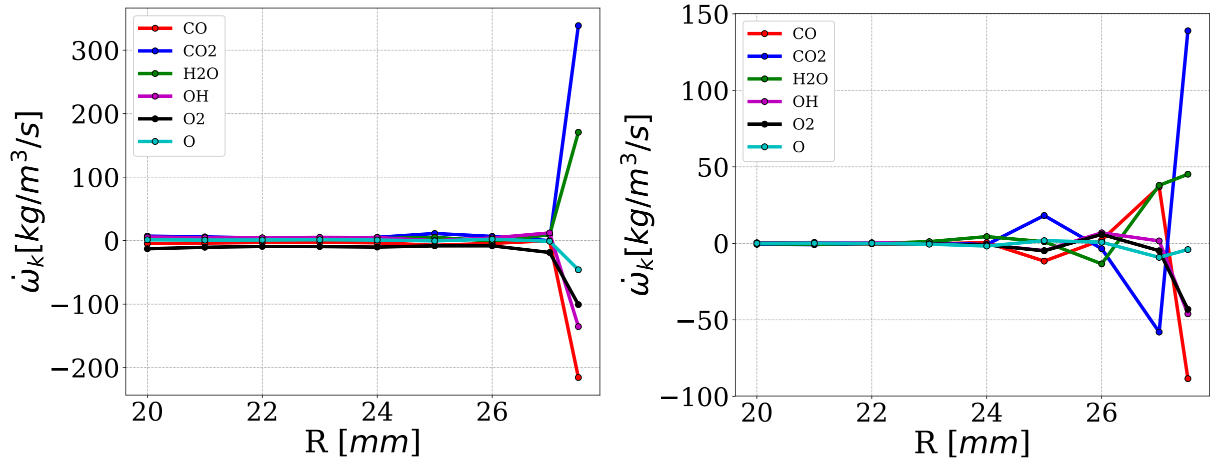

(a) x=118mm (b) x=315mm

Figure 6.24: Time-averaged radial profiles of the main species chemical source terms at two axial positions downstream the flame. The profiles are spatially-averaged in azimuthal direction.

6.3.5 Prediction of the wall heat flux and comparison with experiment

Note : due to confidentiality reasons, the numerical values of this section are normalized.

Assuming steady state in the experiment, the wall temperature has been reconstructed from the two measured temperatures T_{PG} and T_{PE}, the distance between the two probes d_P and the thermal conductivity of copper λ_w (see Fig. 6.5). First the experimental heat flux is computed as:

$$Q_{w,exp} = \lambda_w (T_{PE} - T_{PG})/d_P \tag{6.13}$$

Then the wall temperature is calculated as:

$$T_{w,exp} = Q_{w,exp} \times (d_P + e_{PG})/\lambda_w + T_{PG} \tag{6.14}$$

In the LES using a wall model, the wall temperature is not predicted (as only the heat flux is needed and computed by the wall law) and it must be therefore reconstructed from the wall heat flux and the imposed temperature boundary condition as in Eq. 6.15. The wall temperature reconstruction in both experiment and LES is made along the 3 generating lines and the comparison is presented in Fig. 6.25.

$$T_{w,LES} = Q_{w,LES} \times R_{eq} + T_{\infty} \tag{6.15}$$

where R_{eq} is calculated as in $1/h_{eq}$ (see Section 6.2.1).

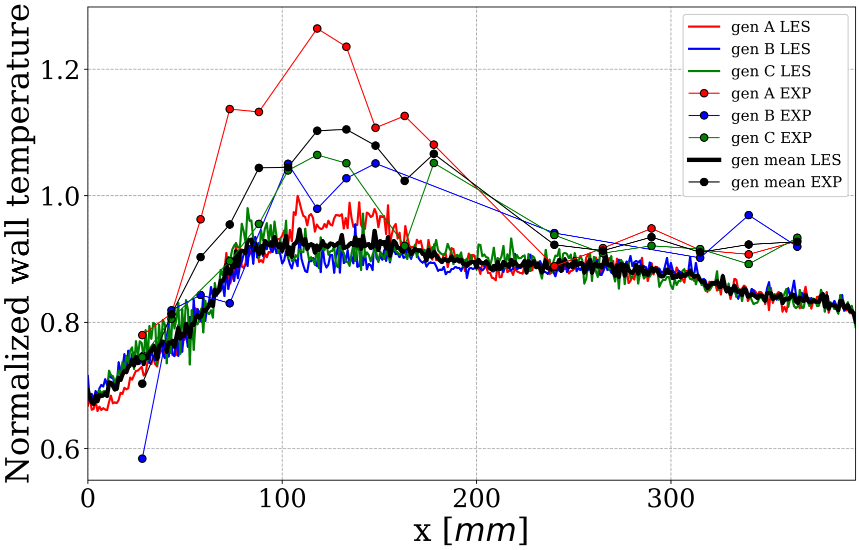

Figure 6.25: Comparison between the experimental and the LES wall temperatures along the three generating lines (all normalized by the same value). The average of the three lines is also plotted.

The first thing to remark is that the three generating lines are way more similar in the LES than in the experiment. This is consistent with the fact that the equivalent thermal resistance R_{eq} was built from an average of all generating lines. This behaviour is visible on the averaged temperature fields shown in Fig. 6.26, which shows quite similar temperature levels in the different planes and same order of magnitude of the wall temperature.

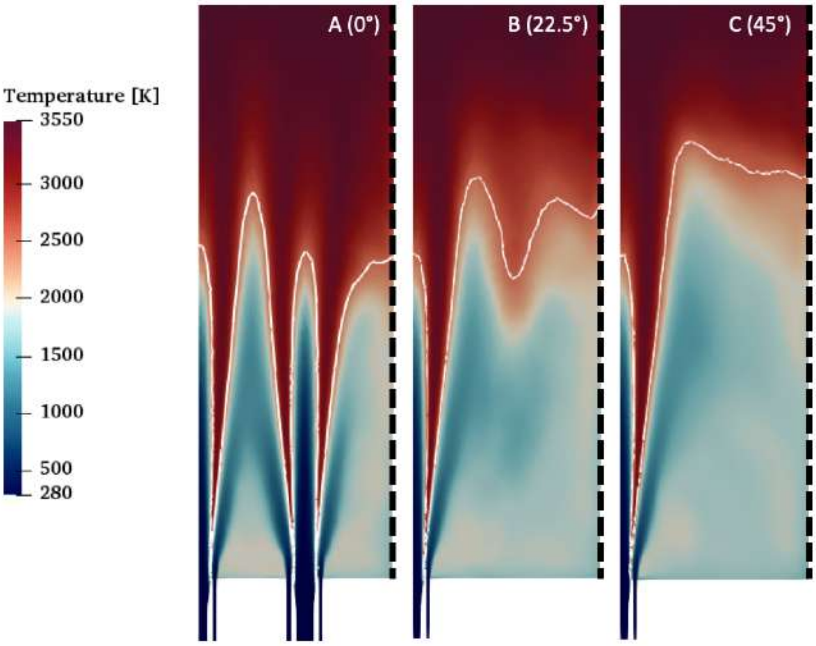

Figure 6.26: Averaged temperature fields at 3 azimuthal positions corresponding to the 3 generating lines. The white line is a temperature isocontour at T=2500K. The black dashed lines show the wall position.

In comparison to the experiment the LES shows a similar shape of the temperature profiles with a maximum around x=120mm, coinciding with the flame tips. However the LES overall founds a lower wall temperature, especially around x=120mm, where a difference with the experiment of about 15% is observed on the mean profiles. However more downstream, a better agreement is recovered with a deviation between 2% and 10%.

The LES and experimental wall heat fluxes are now compared in Fig. 6.27 along the three generating lines, as well as their mean. As for the wall temperatures, the profile shapes are correct and maximum around x=120mm, but the fluxes of the LES are globally underestimated compared to the experiment, mainly at the same peak location around x=120mm.

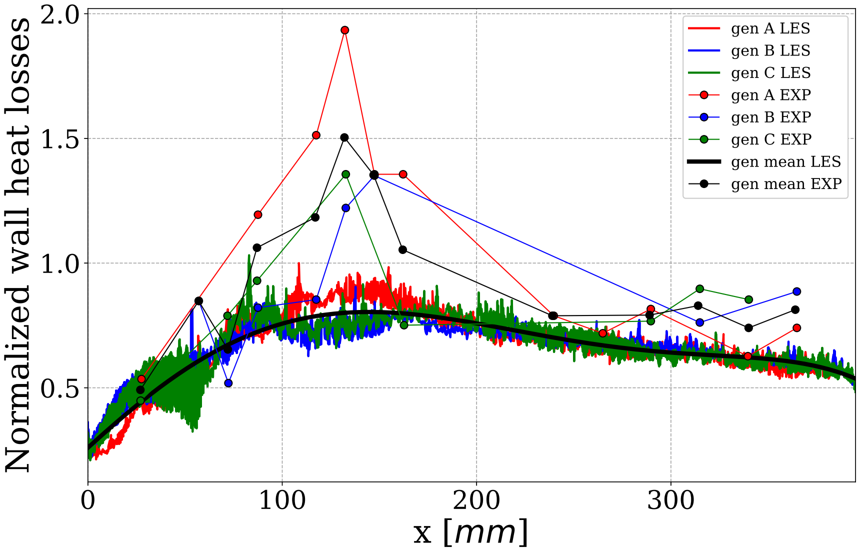

Figure 6.27: Comparison between the experimental and the LES wall heat flux along the three generating lines (all normalized by the same value). The average of the three lines is also plotted.

The differences between numerical and experimental results may be attributed to several reasons listed below.

- As introduced in Section 5.1.2, the coupled wall-law is very sensitive to the molecular Prandtl number, which is constant in AVBP (here $Pr = 0.578$). It is important to recall that this Prandtl number has been optimized during the ARC derivation to obtain the correct consumption speed. However this burnt gas mixture is not reached until x=200mm, meaning that the true Prandtl number of the mixture in the upstream zone of the chamber may be different and lead to a different wall heat flux.

- The wall-law makes use of the first off-wall node information (velocity u_2, temperature T_2 as indicated in Fig. 6.5), *i.e.*, quantities on which the combustion process inside the chamber has a first order impact. The underestimation of the wall temperature and heat flux in the LES is therefore a sign that the burnt gases are not hot enough at the near-wall area, so that the flame is too far from the wall.

- As seen in Section 5.3, the chemical reactions occurring close to the wall in this context of WMLES (with y^+ values between 40 and 60), may contribute to the predicted temperature and wall heat flux. The ARC scheme used here is the one derived in Section 5.3, also used in the reacting channels study of Section 5.3, in almost the same thermodynamic conditions (pressure and burnt gases temperature). From the results of Section 5.3, it may be deduced that the wall heat flux is under-evaluated by about 5 to 10% due to the omission of the chemical activity in the wall model.

- The Sigma SGS model was used, and as shown in Section 5.2.2 (Tab. 5.1 to overestimate the heat flux due to the coupling between this SGS model and the wall-law.

- All along the chamber wall, the LES indicates a strong exothermic heat release at the wall nodes, whereas a moderate endothermic heat release slightly off-wall as shown in Fig. 6.28). The final impact on T_2 is difficult to predict as it depends on the relative importance of the exothermic and endothermic peaks, which are also balanced by heat diffusion.

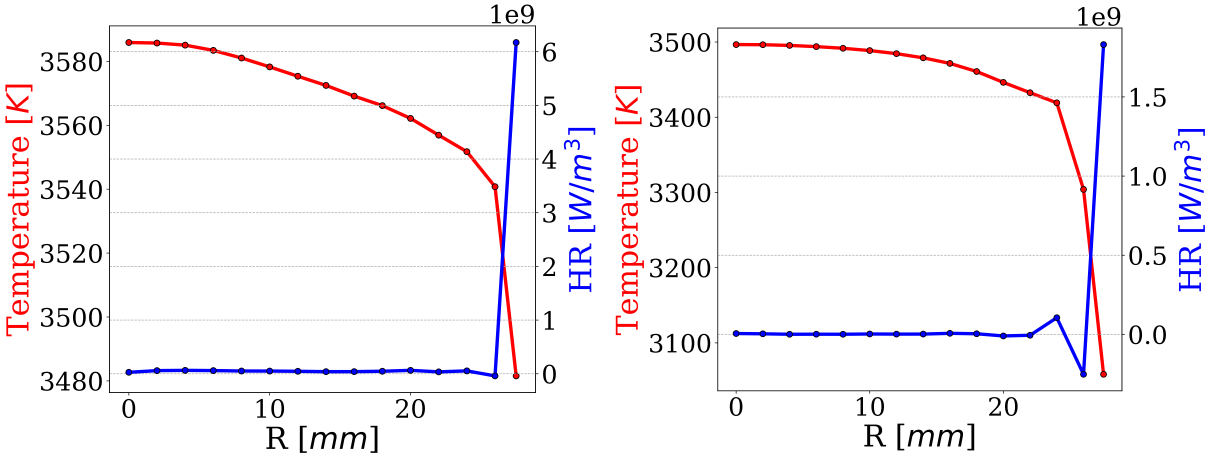

(a) x=118mm

(b) x=315mm

Figure 6.28: Time-averaged radial profiles of the temperature and heat release rate at two axial positions downstream the flame. The profiles are spatially-averaged in azimuthal direction.

- There is no model for radiative heat transfer in the simulation. Due to presence of carbon, so potentially soots, this may increase overall the heat transfers in the chamber. Experimental work is going on to quantify this aspect [Vingert et al., 2019].

- Finally, the provided experimental data may be quite biased, as many thermocouples returned non-physical cold values $T = 280K$ downstream the flame and had be deleted from the database. The resulting uncertainty of the experimental data which were used to set the boundary conditions for LES may have introduced some bias in the LES.

Finally pressure measurements were also provided at two locations (at the wall): $x_1 = 14mm$ and $x_2 = 215.9mm$. As shown in Table 6.4, the pressure is found almost constant along the axis through the chamber in both the experiment and the LES. Both LES cases find exactly the same chamber pressure as the experiment at position x_2, while the pressure at x_1 is slightly under-estimated but the difference is so small that it could be attributed to numerical errors.

Position	x_1	x_2
Normalized pressure, EXP	1.002 ± 0.002	0.999 ± 0.002
Normalized pressure, LES-CLASS	0.998	0.998

Table 6.4: Pressure probes comparison between the experiment and the LES-CLASS (LES-EXPO has the same result).

6.4 Conclusions on the CONFORTH test bench

A numerical study of the CONFORTH thrust chamber has been successfully conducted with LES . The simulation is multi-physics, using complex ARC chemistry and wall flux modelling in super-critical conditions. The validity and interest of using the exponential time-integration of chemistry in a realistic case is demonstrated. The comparison with experiment has been made for the wall heat flux, showing overall a good behaviour of the LES but differences in peak levels which may be attributed to a number of uncertainties both the in the experiment and in the LES.

The results obtained in the CONFORTH configuration show that AVBP is able to perform LES of methane oxy-combustion with accurate chemistry in realistic LRE configurations.

Chapter 7

The TUM configuration

In the general context of future space propulsion already introduced in Chapter 1, the Technische Universität of München (TUM) has developed several methane-fed sub-scale rocket combustors. So far many GOx/GCH4 firing tests were performed with different configurations (single-, five- and seven-injectors in square or circular sections [Silvestri et al., 2014, Silvestri et al., 2016, Perakis et al., 2017]). In order to come closer to real rocket engine conditions, the gaseous single-injector test bench has been modified to allow LOx/GCH4 firing tests [Von Sethe et al., 2019]. The objective is to provide experimental data to the scientific community, for better understanding and assessment of models and numerical codes.

The study of this configuration started with the participation to the Summer Program 2019 organized in Munich within the project SFB TRR40 about *"Technological Foundations for the Design of Thermally and Mechanically Highly Loaded Components of Future Space Transportation Systems"*. It resulted into a proceeding paper [Blanchard and Cuenot, 2019]. The results presented below are also part of a joint paper (in preparation) with some of the other participating organizations to the Summer Program: TUM, Japan Aerospace Exploration Agency (JAXA), Moscow Aviation Institute (MAI) and ArianeGroup.

The objective of this chapter is to assess, on another methane oxy-combustion test case the usefulness and validity of ARC for both the flame behaviour and the wall heat transfer prediction. The main difference with the CONFORTH configuration presented above is that the TUM configuration was tested in the subcritical regime (cryogenic oxygen), implying modelling techniques for the dense phase. Furthermore, as the residence time is much lower in the TUM than in CONFORTH cases, with shorter simulation times, it was possible to study the influence of the chemical modelling. In particular a new approach to establish global mechanisms (GLOMEC) is presented and compared to ARC. Note that the exponential time integration, validated in the previous chapters, is used for the ARC simulation, allowing to slightly accelerate it by a factor 1.15. The GLOMEC case uses classic integration of the chemical source terms.

7.1 Experimental setup

The experimental configuration is here briefly introduced, but more details can be found in [Von Sethe et al., 2019]. It consists of a single coaxial injector combustion chamber fed by gaseous methane and liquid oxygen. It is 290mm long, has a square cross section of 12x12mm and is equipped with convergent-divergent nozzle with a trapezoidal shape. The chamber is designed for a 20-25bar pressure range. The combustion chamber is capacitively cooled making use of the copper high thermal conductivity (19mm thick walls). The summary of the geometry can be found in Table 7.1 and the visual of the configuration is shown Fig. 7.1.

Chamber length	[mm]	290
Chamber width	[mm]	12
Chamber height	[mm]	12
LOx diameter	[mm]	3
Lip thickness	[mm]	1
GCH4 inner diameter	[mm]	5
GCH4 outer diameter	[mm]	6

Table 7.1: Main geometrical parameters, without the nozzle.

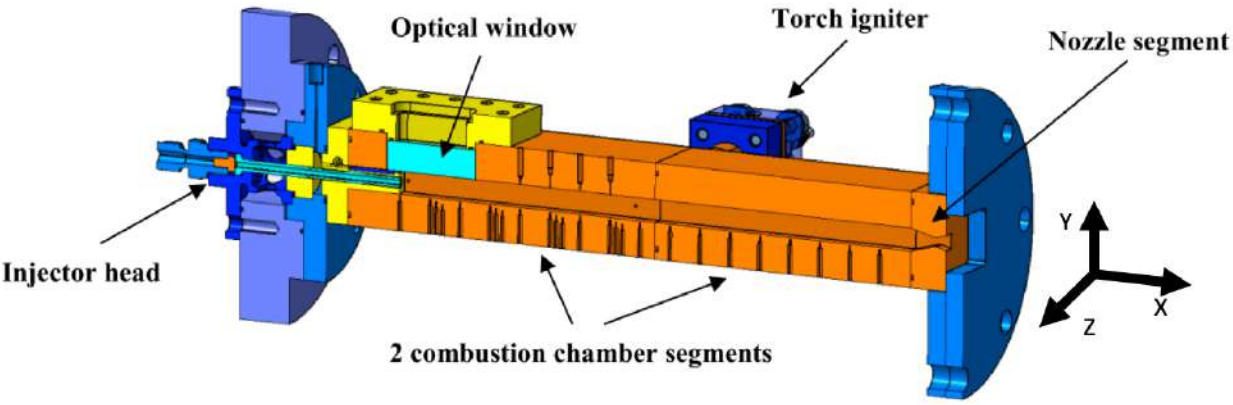

Figure 7.1: Combustion chamber with cryogenic injector head and optical access window [Von Sethe et al., 2019]. Note than in the present simulation, the optical window is replaced by copper.

The simulated operating point is sum up in Table 7.2. For oxygen, both pressure and temperature are below the critical values, so that oxygen is liquid at injection. The methane is injected near ambient temperature.

Pressure	[bar]	18.5
LOx mass flow rate	[g/s]	44.63
GCH4 mass flow rate	[g/s]	14.9
Mixture ratio	[-]	3.0
Global equivalence ratio	[-]	1.33
LOx temperature	[K]	103.04
GCH4 temperature	[K]	270.76

Table 7.2: Operating point for the LES.

The instrumentation allows to obtain longitudinal temperature profiles, thanks to 17 thermocouples separated by a distance of 17mm and placed all along the top wall of the combustion chamber. The static pressure is taken at 9 positions with a spacing of 34mm, starting 0.5mm downstream the face plate. The provided experimental data consist of a longitudinal pressure profile (varying from 18.5 bar at the injection head to 17 bar right upstream the nozzle) and wall heat loss measurements all along the top wall and averaged over the chamber circumference. The measurement uncertainties lie around 8%.

7.2 Modelling

The simulation is run with the LES solver AVBP. For convection, the second order in time and space Lax-Wendroff scheme is used [Lax and Wendroff, 1960]. The turbulent closure is made thanks to the Sigma model [Nicoud et al., 2011]. The Soave-Redlich-Kwong equation of state is used [Soave, 1972] because of the cold oxygen injection. Constant turbulent Schmidt and Prandtl numbers (fixed at 0.6 for both) are used for the sub-grid species and heat diffusion terms. The power-law function is utilized for the molecular viscosity, and constant Schmidt and Prandtl numbers are used for species molecular diffusion and thermal conductivity. The LAD model for artificial viscosity is used in zones where high density and pressure gradients occur [Schmitt, 2020].

Combustion chemistry is described with the ARC scheme derived in Annex C., following the same reduction procedure than for CONFORTH. In the context of the Thickened Flame Model [Colin et al., 2000], diffusion flames which are already artificially thickened by the mesh are not thickened further [Shum-Kivan, 2017], but subgrid-scale flame-turbulence interactions however remain and should be modeled (Section 4.5). As for CONFORTH these effects are assumed small in comparison to the resolved turbulence thanks to the refined mesh in the zones of interest and are omitted. It will be checked *a posteriori* that the flame is indeed a purely non-premixed flame and that subgrid-scale turbulence is weak.

The oxygen droplets are described with a Lagrangian approach and the Abramzon-Sirignano evaporation model, coupled to the gaseous flow solver via mass, momentum and enthalpy exchange terms as detailed in Chapter 3.

7.2.1 Numerical setup

Geometry and mesh

The full 3D combustion chamber is computed without the nozzle. Only a small part of the coaxial injector is modeled (2mm length). The injection and atomization of LOx are not resolved, but modeled as explained in detail in Section 7.2.2. In this model, the liquid jet formed by the LOx injection is replaced by a solid cone as shown Fig. 7.2 and 7.5.
The mesh about 20 million cells is fully tetrahedral. The post-lip and flame zone are particularly refined with a characteristic mesh size at the lip of $\Delta_0 = 30\mu m$, progressively coarsened to $\Delta_c = 800\mu m$ at $x = 110mm$ (x being the longitudinal axial coordinate). At the walls, the boundary layer is also made of tetrahedra and the mesh results in y^+ values from 95 to 130 along the chamber. Indeed the resolution of the turbulent boundary layer is too expensive in

LES and is replaced by wall models. An overview of the mesh is presented Fig. 7.2.

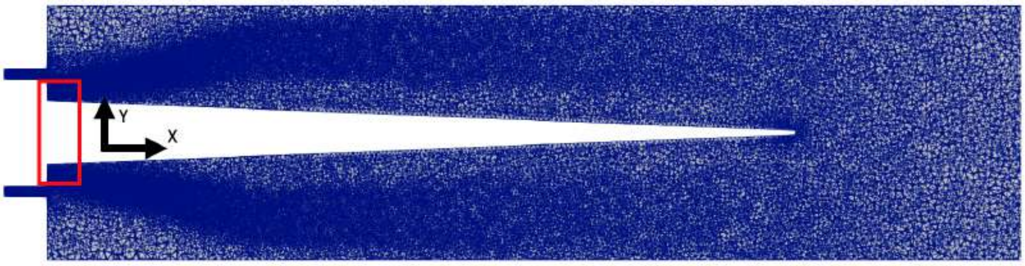

Figure 7.2: Mesh cut (normal to Z-axis): zoom at the liquid oxygen cone (the rest of the domain is about 7 times longer). The red box indicates where the scalar dissipation rate has been measured to derive the ARC (Annex C.), and also where the scatter plots of the flame have been extracted (Section 7.3.4).

Boundary conditions

The boundary conditions are formulated with the NSCBC approach [Poinsot and Lele, 1992]. Inlets are set with the recent Non-Reflective Inlets (NRI) method [Daviller et al., 2019] which allows to absorb acoustics while maintaining the target fluxes. As the nozzle is not computed, the outlet is set at 17 bar, which is around the value of the last pressure sensor from the experiment, just upstream the nozzle. At the GCH_4 inlets, turbulent velocity profiles are imposed. The inlet walls and the lip walls use adiabatic wall-law conditions, while an isothermal wall at 500K is imposed on the rest of the face plate. The chamber walls make use of the coupled wall-law derived by Cabrit [Cabrit and Nicoud, 2009], which takes into account the high temperature gradients expected between the burnt gases and the walls in a combustion chamber. The heat transfers through the wall is taken into account by imposing the temperature profile from the experiment interpolated as an order-3 polynomial, presented in Fig. 7.3. The boundary conditions are sum up Fig. 7.4.

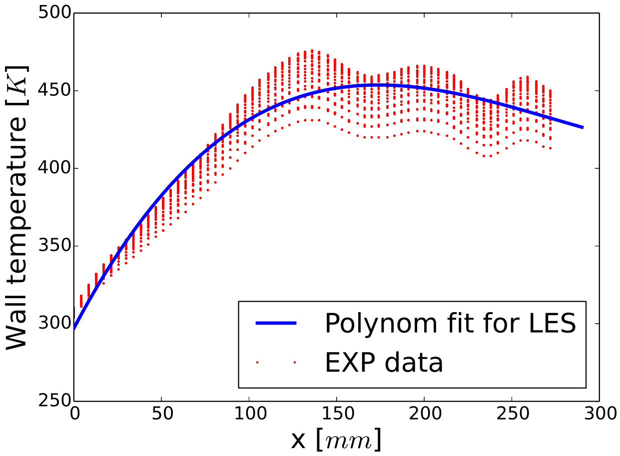

Figure 7.3: Imposed wall temperature profile: 3rd-order polynomial interpolated from experimental data.

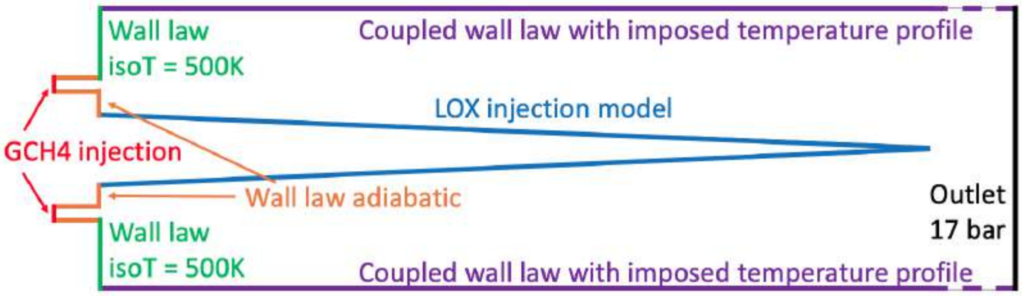

Figure 7.4: Boundary conditions scheme.

All inlets/outlets are considered as exits for the LOx droplets. Their interaction with walls are limited to rebound: no splash (separation of particles in several smaller particles) or liquid film are considered here, as they are not important phenomena in the studied case. Note that the LOx injection boundary condition is considered as a wall for the droplets and the gaseous phase (with slip condition). It may seem counter-intuitive, but the Lagrangian formulation used for the LOx droplets allows to inject droplets from a wall. This choice was made after observing injected droplets rapidly leaving the domain through the injection surface if treated as an exit: due to the flow motion generated by acoustics following combustion start, about a third of the LOx particles were ejected from the domain right after being injected.

7.2.2 Liquid oxygen injection

The LOx atomization is modelled following the work of Potier [Potier, 2018] and is briefly summarized here. The idea is to avoid describing the liquid dense phase and its atomization, which require specific modelling of which the development is out of scope of the present work. Instead the liquid oxygen is injected in the form of spherical droplets, at the surface of the liquid jet represented by a conical surface. The determination of the droplet size and velocity is detailed below.

The model of Potier used in this work is called "focal point". The principle is to consider that the angle of injection of a droplet θ_p depends on its location of injection x_p along the cone length L. This is sketched in Fig. 7.5.

First, it is needed to estimate the liquid core length. This is done thanks to empirical correlations of the literature, using the Weber number:

$$\mathrm{We}_g = \frac{\rho_g (u_g - u_l)^2 D_l}{\sigma} \tag{7.1}$$

with D_l the diameter of the LOx injector, and σ the surface tension, calculated (in dynes/cm) for O2 as in [Lemmon and Penoncello, 1994]:

$$\sigma = 38.612652 (1 - \frac{T}{T_c})^{1.228} \tag{7.2}$$

The mean liquid velocity u_l is estimated thanks to the liquid mass flow rate $\dot{m}_l$ and the section of the liquid injector $A_l = \pi D_l^2/4$:

$$u_l = \frac{\dot{m}_l}{\rho_l A_l} \tag{7.3}$$

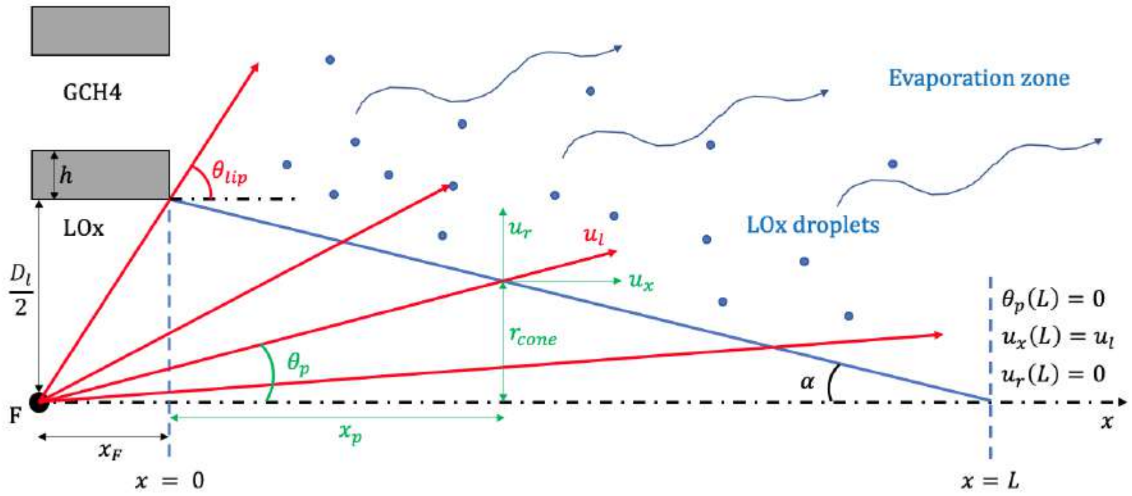

Figure 7.5: LOx atomization model overview.

Following the conclusions of [Potier et al., 2018] who tested several correlations, the Weber number allows to use the Woodward correlation [Woodward et al., 2006] to estimate the liquid cone length L:

$$\frac{L}{D_l} = 0.0025 \frac{\rho_g}{\rho_l}^{-0.44} \mathrm{Re}_l^{0.76} \, \mathrm{We}_g^{-0.22} \tag{7.4}$$

Note that this expression has been established from experiments and in cold conditions. From the cone length, one can estimate the injection angle at the cone base ([Hopfinger, 2001]):

$$\theta_{lip} \approx \frac{\pi}{4} - tan^{-1}(\frac{\sqrt{J}}{12}) \tag{7.5}$$

Again, this estimation is based on cold flow results, at atmospheric pressure. J is the momentum flux ratio between the gas and the liquid phase, computed as:

$$J = \frac{\rho_g u_g^2}{\rho_l u_l^2} \tag{7.6}$$

Then the focal point model makes use of θ_{lip} with trigonometric relations in order to change the velocity components of the injected particles along the cone. The focal point position x_F is computed as:

$$x_F = \frac{D_l/2}{tan(\theta_{lip})} \tag{7.7}$$

The injection angle θ_p of a particle changes with its injection position x_p along the axis and is computed as $tan(\theta_p) = r_{cone}/(x_p + x_F)$, with $r_{cone} = D_l/2 \times (1 - x_p/L)$. From this the axial and radial contributions u_x and u_r are computed as:

$$u_x = u_l cos(\theta_p), u_r = u_l sin(\theta_p) \tag{7.8}$$

Finally the mean droplet diameter d_{10} is estimated from [Hopfinger, 2001], Eq. 6 (valid for $We \approx 10^3$ or above):

$$d_{10} = 5\sqrt{\frac{\nu_g}{u_g} 2\delta_g \sqrt{\frac{\rho_l}{\rho_g}}} \tag{7.9}$$

with δ_g the vorticity thickness. Its definition is taken from [Marmottant and Villermaux, 2004], Eq. 2.2:

$$\frac{\delta_g}{h} = 5.6\,\mathrm{Re}_g^{-1/2} \tag{7.10}$$

h being in this case the lip thickness.

From the above, the liquid fraction α_l at droplet injection on the lateral cone surface $S_{cone} = \pi\frac{D_l}{2}\sqrt{(D_l/2)^2 + L^2}$ is expressed as:

$$\alpha_l = \frac{\dot{m}_l}{u_l \rho_l S_{cone}} \tag{7.11}$$

Numerical values of all simulation parameters are summarized in Table 7.3.

Momentum flux ratio (J)	[-]	5.83
Weber	[-]	58584
Droplets diameter (d_{10})	[μm]	6.135
Cone length (L)	[mm]	35.305
Injection angle at lip (θ_{lip})	[deg]	33.47
Mean liquid velocity (u_l)	[m/s]	5.85
Liquid fraction (α_l)	[-]	0.03977

Table 7.3: LOx particle injection parameters.

The droplet size diameter is fixed at injection for all droplets at a value given by the above correlations of about 6 μm. This value is quite small and will result in rapid evaporation. Actually this parameter is quite critical for any subcritical two-phase flow simulation, as the droplet size might change the flame shape, with eventually big droplets crossing the flame. However in the absence of information about the droplet size distribution at injection, this choice is made by default.

Note finally that α_l is quite high compared to the initial assumption of the Lagrangian model ($\alpha_l < 0.01$). This is however only the case at the injection boundary condition, where the liquid core is quite dense. It is then observed that the liquid fraction diminishes rapidly after injection, reaching $\alpha_l \approx 0.1$ or below.

7.2.3 The GLOMEC mechanism

In order to reduce the computational cost, and because many tests do not require a detailed description of chemistry, an alternative to ARC is presented here which consists in a 4-steps global scheme called GLOMEC. The main difficulty in deriving global chemistry is to ensure a correct burnt gas state in rich conditions. Indeed the burnt gas state results from chemical equilibrium, which does not depend on the chemical kinetics but only on the species present in the scheme. In other words, whatever the number of reactions and their rate constants, the correct burnt gas state can not be recovered if the necessary species are not included.

To overcome this difficulty, an original idea was proposed at CERFACS and developed during the internship of Julian Strauss, a student from TUM, under my co-supervision [Strauss, 2020]. The concept of GLOMEC is to recover the correct equilibrium temperature whatever the number of species, by artificially moving the equilibrium conditions. This is simply achieved by acting on the species standard entropy. The detail of the creation of the process can be found in Annex D., which is an extract from the master thesis of J. Strauss.

The target operating point corresponds to the conditions of the TUM configuration, namely $P = 18.5bar$, $\phi_g = 1.33$, $T_{GCH4} = 270.76K$ and $T_{LOx} = 103.04K$. The objective is to guarantee a correct prediction of the equilibrium temperature with only few species and a correct flame speed with only few reactions. These two quantities are chosen since they are the most important when reducing a chemical scheme with premixed flames as test cases. The reference scheme is the RAMEC [Petersen et al., 1999] which was also used to derive the ARC. The chosen species and reactions are largely inspired from Lindstedt [Jones and Lindstedt, 1988].

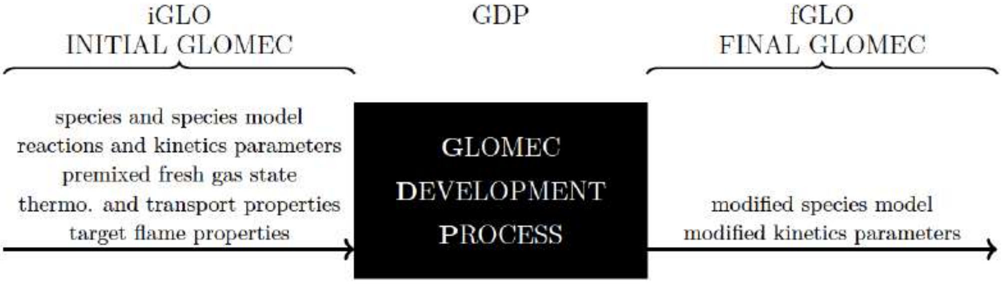

Figure 7.6: Black box model of GLOMEC development procedure.

As described in Annex D., the reduction can be expressed as an optimisation problem. The procedure is summarized in the block diagrams of Figs. 7.6 and 7.7. In the following, "initial GLOMEC" is the original RAMEC mechanism keeping only 6 species (CH4, O2, CO, CO2, H2O, H2) and 4 reactions as done in [Jones and Lindstedt, 1988]. The "final GLOMEC" corresponds to the same scheme after the optimization process. Note that the 6 retained species are normally not enough to reach the correct equilibrium as it was early presented in Section 4.2.2, explaining why such optimization is needed.

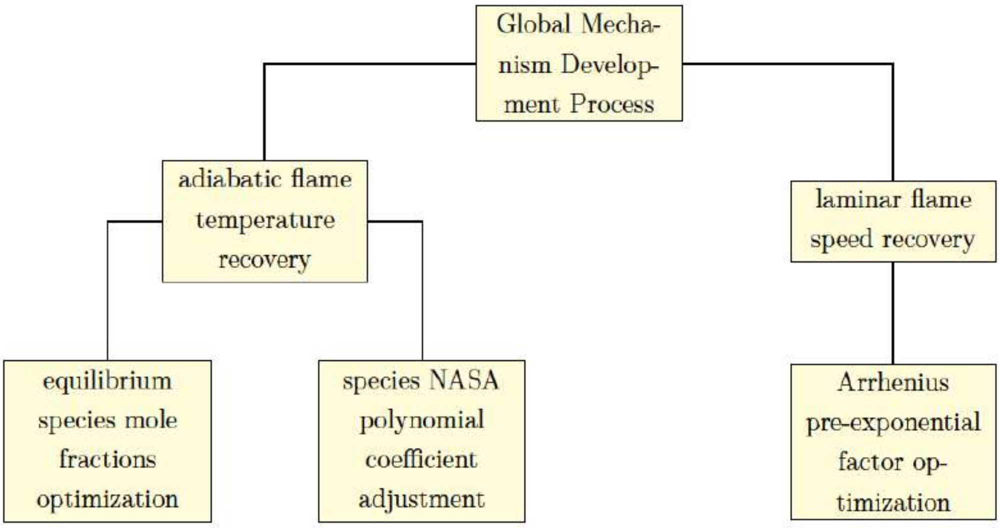

Figure 7.7: Block definition diagram of the GLOMEC development procedure.

To sum up, the optimization procedure mainly consists in modifying (i) the 7^{th} coefficient of the NASA polynomials for entropy of the 6 selected species in order to reach the target equilibrium temperature and (ii) the pre-exponential factors of the 4 reaction rate constants to reach the target flame speed. Target quantities are reference ones computed with the RAMEC. Note that only the entropy tables of the species are modified, which is not used for any other calculation in a LES and then has a minor impact. All other thermodynamic properties, in particular enthalpy, remain unchanged. This slight changes on entropy affects only a little the modified equilibrium in terms of composition, as described by Fig. 7.8. The noticeable changes are the presence of CH4 in the final equilibrium, and also about twice the amount of O2 (it however remains at a low level).

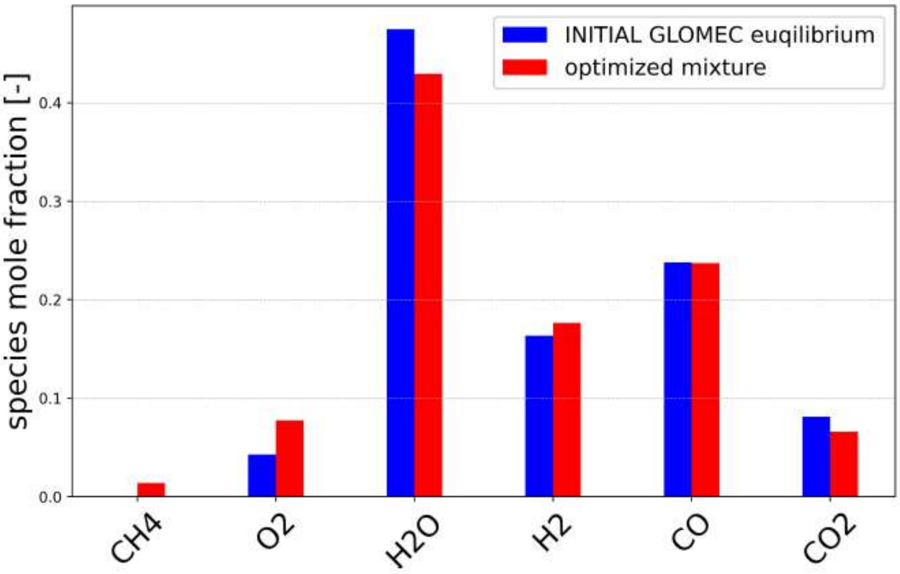

Figure 7.8: Change of composition of the GLOMEC equilibrium, before and after optimization of the 7^{th} coefficient of the NASA polynomials to reach the target temperature.

The results concerning the equilibrium temperature and the laminar flame speed can be seen on Figs. 7.9 and 7.10 showing that the optimization gives an excellent recovery of the two quantities of interest for the target operating point. It is also observable that the GLOMEC is slightly off for other equivalence ratio than the target operating point, and that this difference becomes larger in the rich zone of Fig. 7.9. This was expected considering that only one operating point was targeted in the optimization. In the future, it is foreseen to add the possibility to optimize a global scheme on a wider range of conditions.

The final GLOMEC consists in 4 chemical reactions, two of them irreversible ("$\Longrightarrow$"), and the two others reversible ("$\Longleftrightarrow$"):

$$\begin{aligned} CH4 + 0.5O2 &\Longrightarrow CO + 2H2 \quad (7.12)\\ CH4 + H2O &\Longrightarrow CO + 3H2 \quad (7.13)\\ H2 + 0.5O2 &\Longleftrightarrow H2O \quad (7.14)\\ CO + H2O &\Longleftrightarrow CO2 + H2 \quad (7.15) \end{aligned}$$

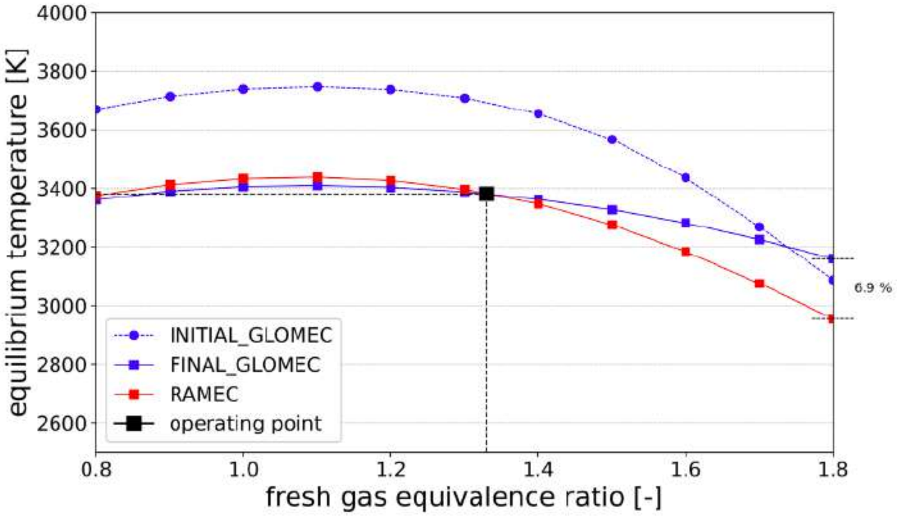

Figure 7.9: Equilibrium temperature of RAMEC, INITIAL GLOMEC and FINAL GLOMEC plotted against equivalence ratio.

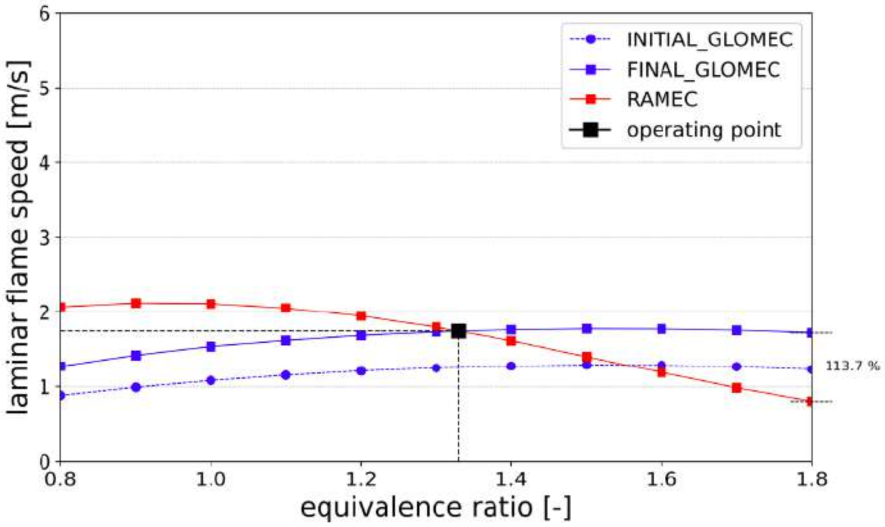

Figure 7.10: Laminar flame speed of RAMEC, INITIAL GLOMEC and FINAL GLOMEC plotted against equivalence ratio.

Their Arrhenius parameters, after the optimization process (that are still close to the ones provided by Lindstedt [Jones and Lindstedt, 1988]), can be found in Annex E.. Figure 7.11 shows that a correct flame structure is retrieved by the GLOMEC compared to the RAMEC reference, the only difference being that the main endothermic peak (around $Z = 0.35$) is not well represented by the GLOMEC. The simplified set of chemical reactions could be the reason behind this.

Finally, note that the reduction targets of the GLOMEC differ from the ones chosen for the ARC used for this simulation. The ARC is derived on diffusion flames, and a range of pressure, strain rate etc (see Annex C.), whereas the GLOMEC targets a single operating point and for equilibriums and a premixed flame. In fact, the optimization procedure described above was found much easier to proceed on premixed flames and 0D equilibriums than diffusion flames.

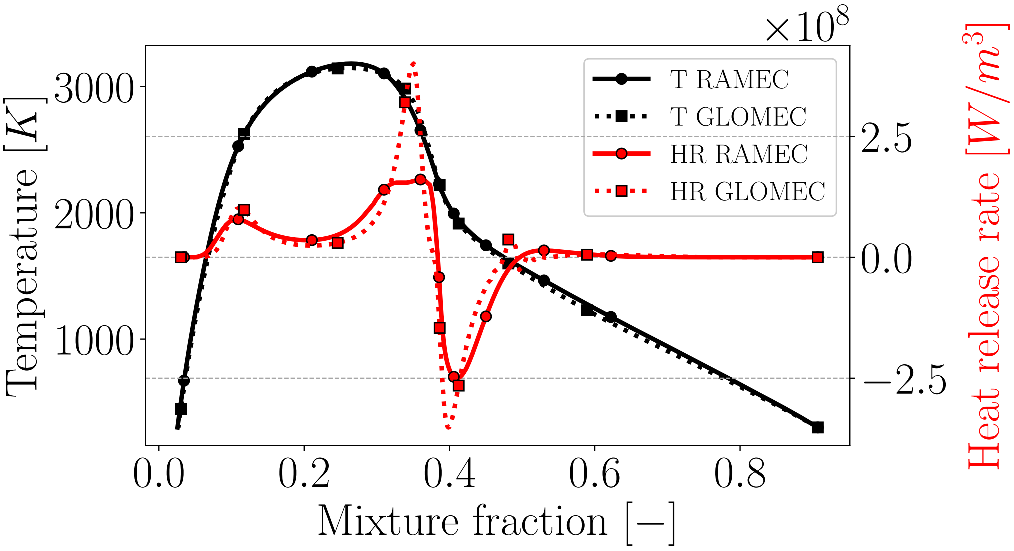

Figure 7.11: Counterflow diffusion flame (in mixture fraction space) showing the temperature and heat release rate profiles with the RAMEC and final GLOMEC schemes, for $P = 18.5bar$, $\chi_{st} = 1s^{-1}$ and $T_{init} = 236K$.

However the GLOMEC still gives good results for diffusion flame as presented in Fig. 7.11. To build such global scheme, it would be better of course to target a larger range of operating points, but the GLOMEC, at this stage of development, has to be considered as a first step to develop more accurate global schemes with this method in the future.

7.3 Results

The results of the two LES (one with the ARC, one with the GLOMEC, abbreviated as "GLO" in the following graphs and field) are presented below, and compared when possible to the experiment. In terms of computational cost, the LES with GLOMEC, with only 6 transported species, runs about 2.25 faster than the LES with ARC which includes 18 transported species. The ARC run has been averaged over 3.7ms, while the GLOMEC run only over 1.2ms due to greater numerical instability. This was found however sufficient to converge the burnt gases (gaseous) part ($\tau_{conv,g} \approx 1ms$), while to converge the dense part, due to the low velocities, at least 5ms would have been required. This time was evaluted by taking the mean velocity value a particule *a posteriori*, found to be $u_{p,mean} \approx 10m/s$, compared to the typical distance crossed by a particle, also determined *a posteriori* and about 50mm: see Fig 7.12 for an overview of an instantaneous particle field.

7.3.1 Averaged fields and profiles

Figure 7.13 shows time-averaged fields of temperature and O2 mass fraction of the two cases. Overall the two chemistry models show a similar result concerning the flame shape and length, even if the GLOMEC case exhibits a slightly shorter flame, as shown by the stoichiometric line which touches the wall sooner in the GLOMEC case. Note that the flame does not have a

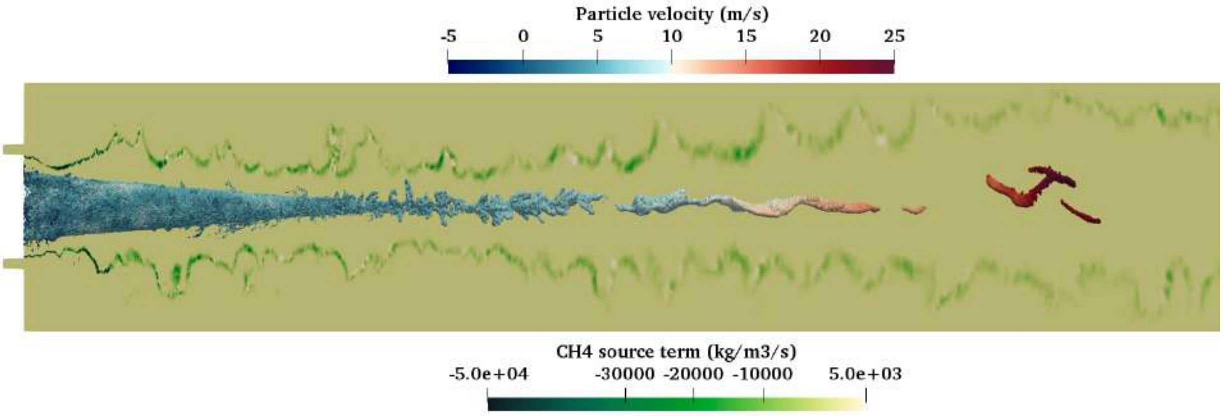

Figure 7.12: Instantaneous field of CH4 source term with a particle set highlighted by their velocity (zoom on the O2 injection cone). The images are scaled by a factor 0.5 in the axial direction for better clarity. The last particles on the right side (with maximum velocity) are found around x=50mm.

closed shape and simply vanishes when O2 has been fully consumed.

The shape of the oxygen core follows logically the cone shape imposed by the injection modelling, except near the chamber inlet where the oxygen field expands rapidly in the radial direction before shrinking again close to the cone surface. Downstream the tip of the cone ($L \approx 35mm$), the oxygen fields expands again rapidly, which has the effect to push the flame towards the wall. Actually it seems that the high turbulent viscosity in this zone, which adds a diffusion effect, contributes to this phenomenon, as suggested by Fig. 7.14. In the same figure, re-circulation zones are highlighted in red, showing small recirculation zones at the walls and at the basis of the oxygen cone that help stabilizing the methane injection and the flame burning (Fig. 7.15), and a larger one around the oxygen cone with significant negative axial velocities.

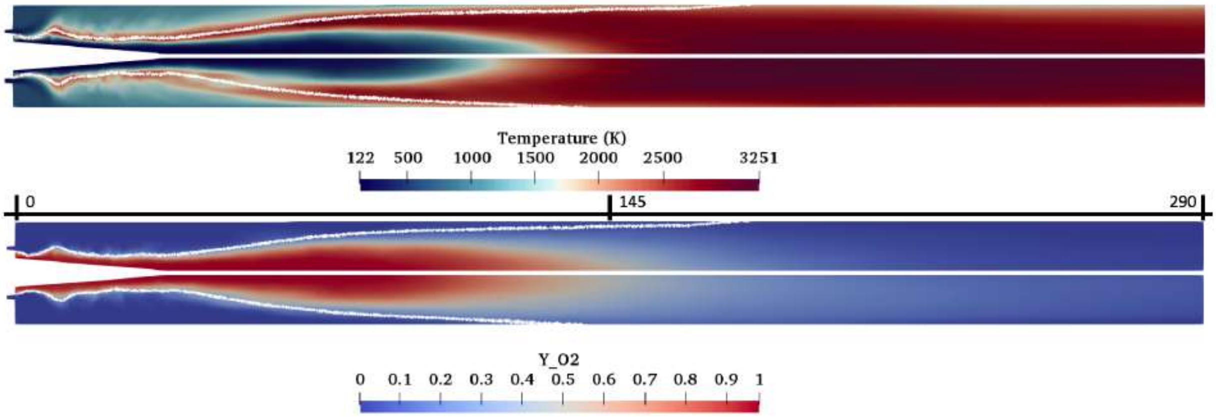

Figure 7.13: Temperature (top) and O2 mass fraction (bottom) of the ARC case (top half) and GLOMEC case (bottom half). The images are scaled by a factor 0.5 in the axial direction for better clarity (dimensions in millimeter). The white line is the stoichiometric mixture fraction isocontour $Z_{st} = 0.2$.

The flame is attached to the injector (Fig. 7.15) thanks to the high reactivity of methane with oxygen. Following the stoichiometric line, it rapidly opens under the effect of the recirculation

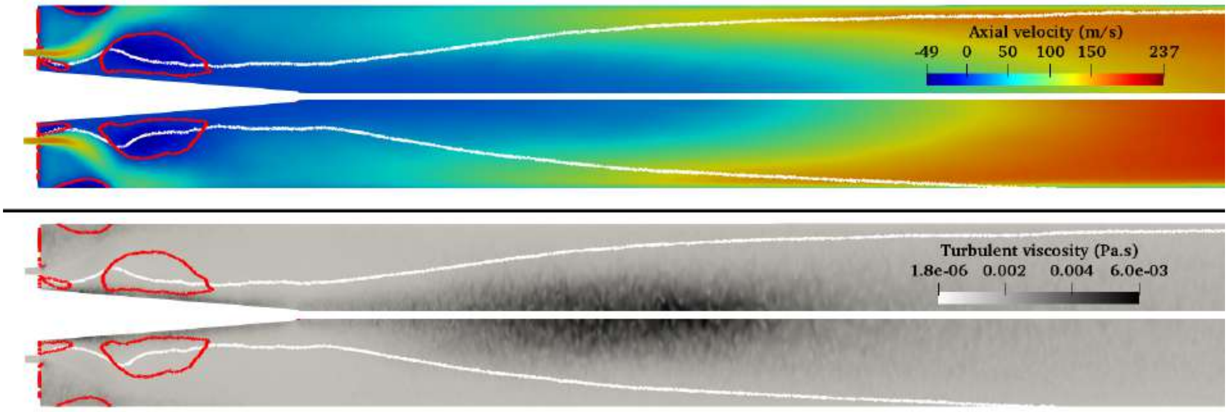

Figure 7.14: Axial velocity (top) and turbulent viscosity (bottom) of the ARC case (top half) and GLOMEC case (bottom half). The images are scaled by a factor 0.5 in the axial direction for better clarity. The white line is the stoichiometric mixture fraction isocontour $Z_{st} = 0.2$. Red isocontours of zero-axial velocity indicate the recirculation zones.

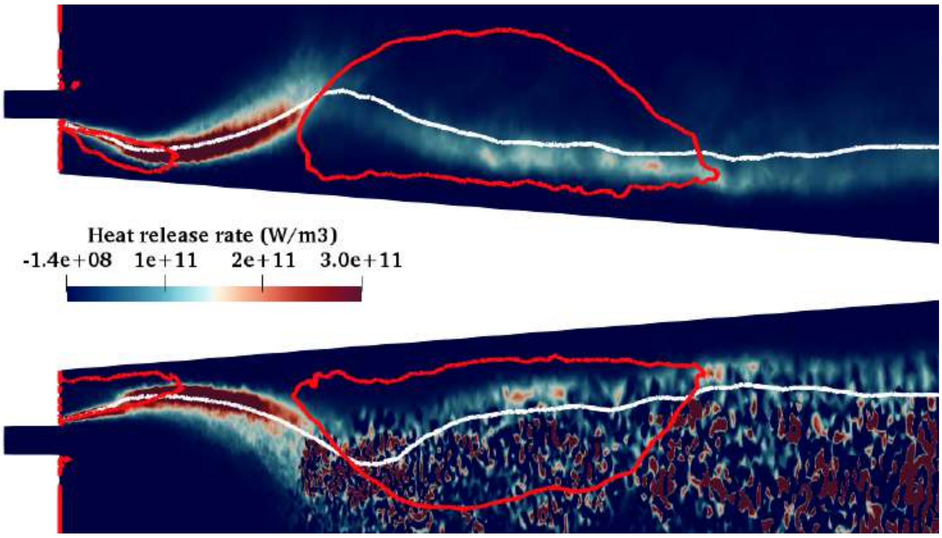

Figure 7.15: Heat release rate of the ARC case (top half) and GLOMEC case (bottom half). The images are scaled by a factor 0.5 in the axial direction for better clarity. The white line is the stoichiometric mixture fraction isocontour $Z_{st} = 0.2$. Red isocontours of zero-axial velocity indicate the recirculation zones.

zones, before coming back closer to the liquid oxygen cone and later expanding again toward the walls where it vanishes after the full consumption of oxygen. The flame is fed by the oxygen evaporation, illustrated in Figs. 7.12 and 7.16 for both ARC and GLOMEC cases, which appear very similar. The evaporation process is limited to the flame zone, as expected and verifying the assumption made in 3.1.1 that particles do not reach any wall, and even do not cross the flame front. Along the liquid oxygen cone, evaporation is enhanced by the proximity of the flame with strong heat transfer due to the important temperature difference between the droplets and the gas. Downstream the injection cone, droplets heat up gradually and evaporate further away from the flame front, with a maximum mass transfer rate at a location where the combination of droplet density and temperature levels is most favorable. In this zone the evaporation transfer rate stays moderate due to the droplet pre-heating.

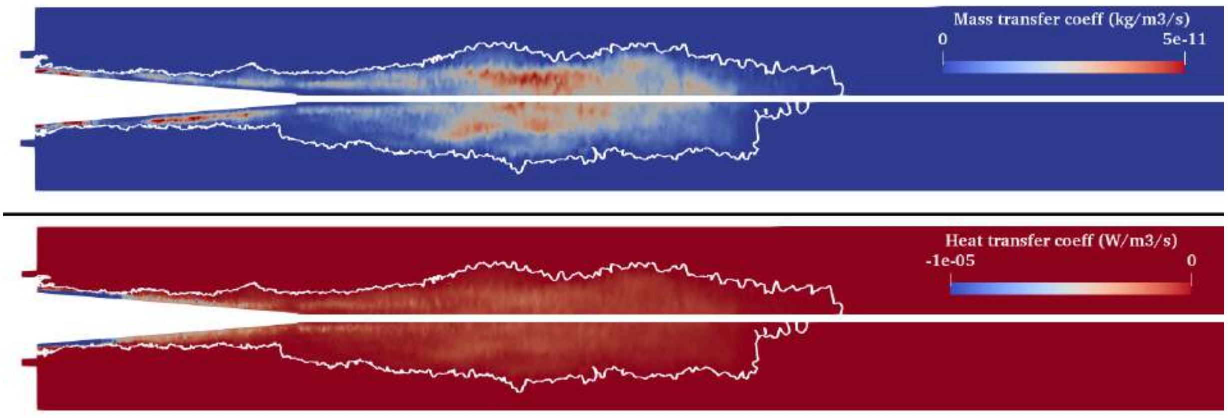

Figure 7.16: Instantaneous evaporation mass (top) and heat (bottom) transfer rates to the gas of the ARC case (top half) and GLOMEC case (bottom half). The images are scaled by a factor 0.5 in the axial direction for better clarity. The white line corresponds to the isocontour of evaporation heat transfer $\dot{Q}_p = 0$.

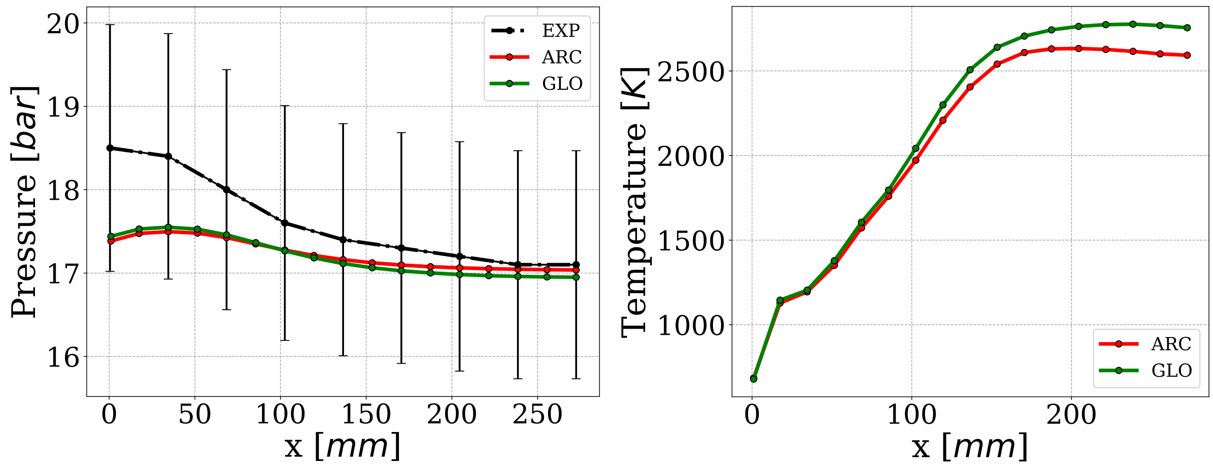

(a) Pressure (b) Temperature

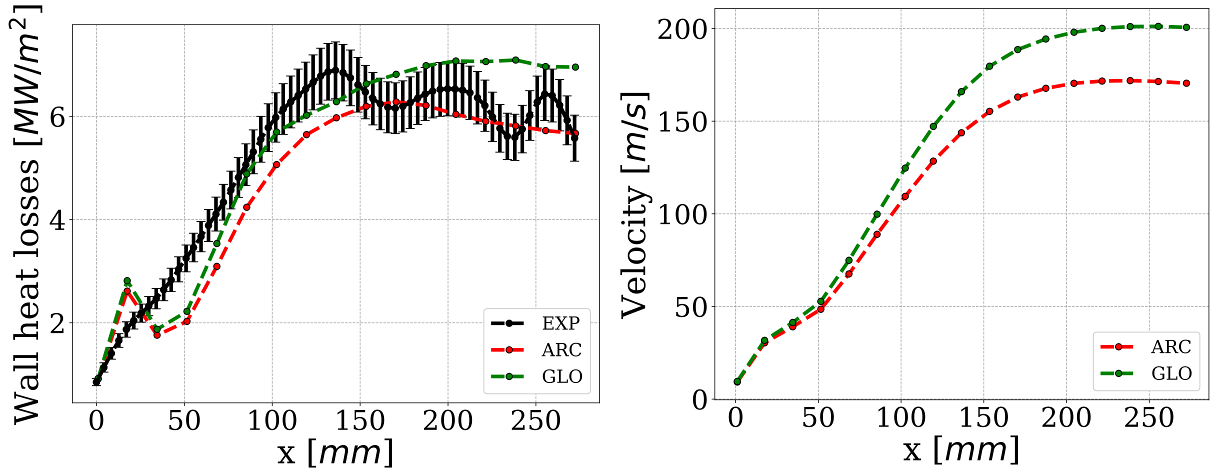

(c) Wall heat losses (d) Velocity

Figure 7.17: Averaged axial profiles of pressure, temperature, wall heat losses and velocity obtained in the LES of the TUM configuration with ARC and GLOMEC, compared to the experiment (with 8% error bars).

Axial profiles (averaged over the cross section) are presented Fig. 7.17. Both LES simulations are in agreement concerning pressure (Fig. 7.17a), and are close to the experiment, in the 8% uncertainty, even if the exact value of 18.5bar at the inlet is not retrieved, suggesting missing sub-grid scale burning rate. In the upstream part, which is therefore most of the flame zone, both simulations show quite similar results, and also a good agreement with the experimental wall heat flux (averaged over the section), in Fig 7.17c. In the first half of the channel, both chemical models slightly under-estimate fluxes, but the slope is close to the experiment. The maximum heat flux is reached at $x = 170mm$ in the LES, which is slightly further downstream than in the experiment where the maximum is reached at about $x = 140mm$. This indicates a longer flame in the LES. Downstream the flame in the homogeneous burnt gases part, the LES with ARC is in good agreement with the experiment, while the GLOMEC case slightly over-estimates the heat flux. This is linked to the higher temperature of the burnt gases found with the global scheme (Fig. 7.17b), which also induces a higher velocity in the burnt gases (Fig. 7.17d). The temperature difference between the two LES cases may be related to the different chemical compositions between the two cases, which was unavoidable due to the different number of species. This is reported in Table 7.4.

7.3.2 Burnt gases

	CANTERA-ARC	LES-ARC	CANTERA-GLO	LES-GLO
$T(K)$	2585	2585	2749	2749
$\rho(kg/m^3)$	1.61	1.59	1.58	1.53
H2O	0.43	0.39	0.45	0.41
CO	0.33	0.34	0.27	0.33
CO2	0.23	0.21	0.25	0.19
OH	0.002	0.02	N/A	N/A
CH4	0	0	0.01	0.001
O2	0	0.02	0.006	0.06
H2	0.02	0.02	N/A	0.02
O	0.00003	0.003	N/A	N/A
H	0.0002	0.001	N/A	N/A
HO2	0	0.0001	N/A	N/A

Table 7.4: Burnt gases composition comparison at $x = 289mm$ (species below $1e^{-5}$ in mass fraction are not reported).

The reference burnt gases composition "CANTERA-ARC" is basically the mixture of the case LES-ARC put at equilibrium at the same temperature, and equivalently for the GLOMEC. The LES-ARC composition is quite close from its equilibrium computed with CANTERA, but this is not the case for the GLOMEC, typically the CO/CO2 equilibrium are not the same: this is consistent with Fig. 7.19 presented further, where the exothermic heat release continues to grow for the GLOMEC but much less for the ARC. The LES-ARC and -GLOMEC common species levels are close except for oxygen: the GLOMEC simulation contains 3 times more oxygen than the ARC simulation. Note also, as already remarked in CONFORTH, that no CH4 remains despite the rich global equivalence ratio: the fuel excess is also found in other carbonated species such as CO, present in large quantity.

With a similar evaporation process (see Fig. 7.16), the difference between the two cases is attributed solely to the different chemical modelling. Indeed it has to be recalled that the GLOMEC scheme was built for one particular point and in adiabatic conditions, which does not guarantee exact results in non-adiabatic cases leading to lower burnt gas temperature and therefore a different equilibrium. To overcome this difficulty, the GLOMEC scheme should be extended to a wider temperature range, by including this range in the optimisation procedure. Also, it is to be noticed that in the modified equilibrium after the optimization process of the GLOMEC, about twice more oxygen is found in the optimized mixture (see Fig. 7.8). This outcome is clearly the result of the optimization choices that were made (different equilibriums could have been found) and maybe that some degrees of freedom could be constrained in the future while building a global scheme.

Furthermore, the presence of oxygen in the burnt gases observed in the LES is somewhat surprising as oxygen is fully consumed in the globally rich flame, as shown in Fig. 7.12. This means that O2 is produced in the post-flame zone. In the GLOMEC which exhibits the highest level of oxygen in the burnt gases, among the 4 reactions written in Eqs. 7.12-7.15, the only reaction that produces O2 is the reversible $H2 + 0.5O2 \iff H2O$. The 4 reaction rate fields are presented in Fig. 7.18.

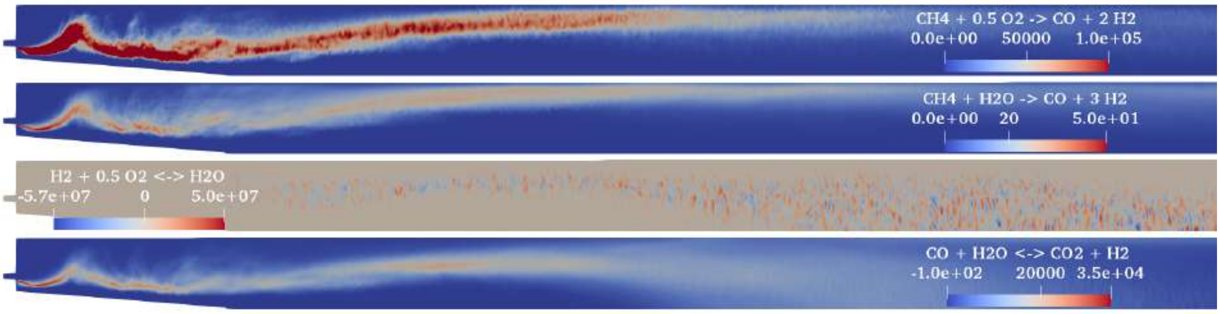

Figure 7.18: Averaged reaction rates (in $kg/m^3/s$) of the 4 GLOMEC reactions. The images are scaled by a factor 0.5 in the axial direction for better clarity.

It appears that the reaction $H2 + 0.5O2 \iff H2O$, having the highest pre-exponential Arrhenius factor is the fastest, with peak levels 2 orders of magnitude higher than the second fastest reaction of methane combustion with oxygen (see Annex E.). As a consequence it introduces numerical stiffness in the system, leading to the strongly perturbed field visible in the figure, even on an averaged solution. Note that the 2 reversible reactions are the only ones active in the post-flame zone, the second one being the CO-CO2 equilibrium. This finally means that the LES with GLOMEC was run with a too large timestep, and that the over-prediction of O2 in the burnt gas may, in complement of the equilibrium optimization process outcome on the O2 quantity, be the result of this numerical under-resolution. Maybe that to use the exponential integration in the GLOMEC would have helped, as it was observed that it enhanced numerical stability.

7.3.3 Power budget

As for CONFORTH, the maximum theoretical power of the TUM configuration, corresponding to complete combustion, is computed as:

$$\mathcal{P}_{th} = \dot{m}_f LHV_f/\phi_g = 0.0149[kg/s] \times 50.04[MJ/kg]/1.33 = 561kW \tag{7.16}$$

A more accurate evaluation is to use equilibrium as the final state. As CANTERA does not allow initial temperatures below 200K, the initial mixture temperature is slightly increased compared to the TUM conditions (as a mix of the two propellants). Assuming that this change has a negligible impact on the enthalpy difference between the initial and final states, the equilibrium is calculated with the following initial mixture :

Pressure	[bar]	18.5
$Y_{O2,i}$	[-]	0.75
$Y_{CH4,i}$	[-]	0.25
T_i	[K]	236

Table 7.5: Initial conditions used for the CANTERA equilibrium calculation.

The sensible enthalpy difference between the initial state (index "i") and the final state (index "f") is:

$$\mathcal{P}_{th,CANT} = \dot{m}_{tot} \int_{T_0}^{T_f} C_p dT = 469kW \tag{7.17}$$

An important difference with CONFORTH is the liquid state of the injected oxygen, adding latent heat evaporation L_{O2} to the power budget. As it corresponds to the energy brought to the liquid to allow evaporation, it must be removed from the gaseous power. The latent heat of evaporation depends on pressure, as recalled in Table 7.6.

Pressure (bar)	L_{O2} (kJ/kg)
1	213.2
18.5	150.4

Table 7.6: Latent heat of evaporation of oxygen (from NIST Chemistry WebBook).

As oxygen is fully evaporated in the domain (Fig. 7.12), the corresponding power to be removed is:

$$\mathcal{P}_{evap} = \dot{m}_o L_{O2} = 0.04463[kg/s] \times 150.4[kJ/kg] = 6.7kW \tag{7.18}$$

which finally gives $\mathcal{P}_{th,CANT} \approx 462kW$.

The contributions to the power budget in the chamber is shown in Fig. 7.19 with cumulative integrals as explained in 6.3.3. In both cases ARC and GLOMEC, the cumulative HRR first grows almost linearly through the chamber, and almost stabilises after x=250mm. Heat losses are similar in both cases. The following total values are found:

$$\mathcal{P}_{HRR,ARC} = 255kW, \quad \mathcal{P}_{HRR,GLO} = 332kW \tag{7.19}$$

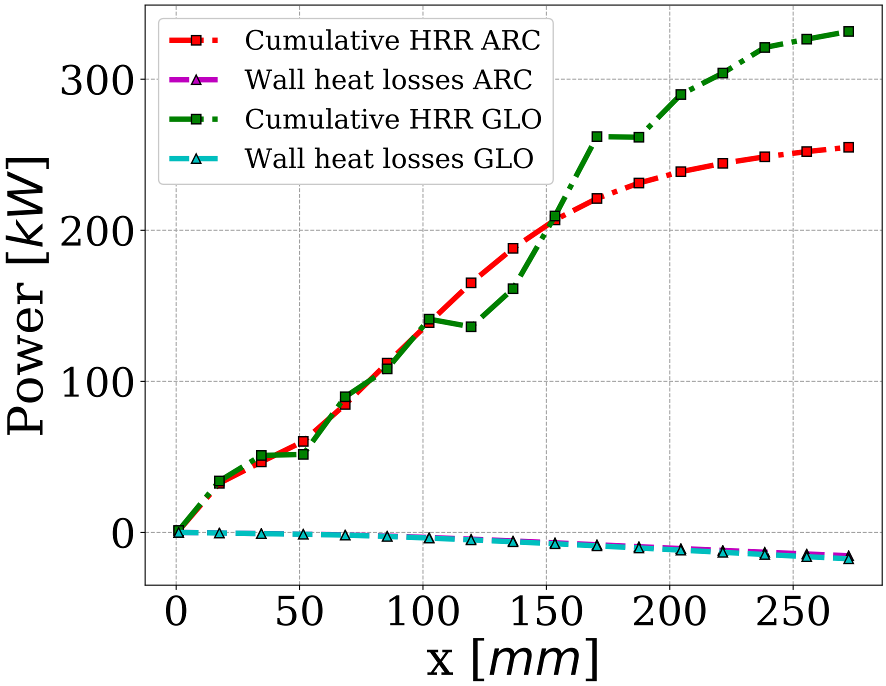

Figure 7.19: Power budget in the TUM configuration.

$$\mathcal{P}_{Q_w,ARC} = 15.4kW, \;\; \mathcal{P}_{Q_w,GLO} = 17.5kW \tag{7.20}$$

And by adding them (and not forgetting the latent heat of evaporation), the total power is found as:

$$\mathcal{P}_{LES,ARC} = 277kW, \;\; \mathcal{P}_{LES,GLO} = 356kW \tag{7.21}$$

In both cases the total power is found quite below the theoretical power of 462kW corresponding to the burnt gas at equilibrium in adiabatic conditions. Not only it means that equilibrium is not reached, as indicated by the growing cumulative heat release rate in both cases near outlet, but it may also point out a lack of convergence of the solutions due to numerical difficulties. Thus, it is believed that the previous budget might be biased. However the following comments about the modelling and numerical approach can be made:

- The pressure curve of Fig. 7.17a indicates that the flame power is probably to small in the upstream half of the chamber. This may be due to the lack of subgrid-scale flame-turbulence interaction, which would enhance the burning rate of the flame, although this effect is evaluated to be small (see next section).
- The simulations lack of convergence due to lack of time, meaning that the analysed solutions are still transient solutions toward equilibrium.
- As already explained, GLOMEC was integrated with a too large timestep, possibly impacting the burnt gas evolution.
- The flame front comes into contact with the walls at the middle of the combustion chamber, which calls for specific modeling of flame-wall interaction, not included in the present work.

7.3.4 Flame structure analysis

The inner flame structure is here analysed with species and temperature scatter plots extracted from time-averaged solutions in the near injection region, as indicated in Fig. 7.2. Both LES results are again compared to CANTERA as reference and are shown in Fig. 7.20. The CANTERA strained flame was computed *a posteriori* using a strain rate in the range of the observed values in the LES, more precisely at the mean value in the scatter plot zone found to be $a_{mean} \approx 18000 s^{-1}$.

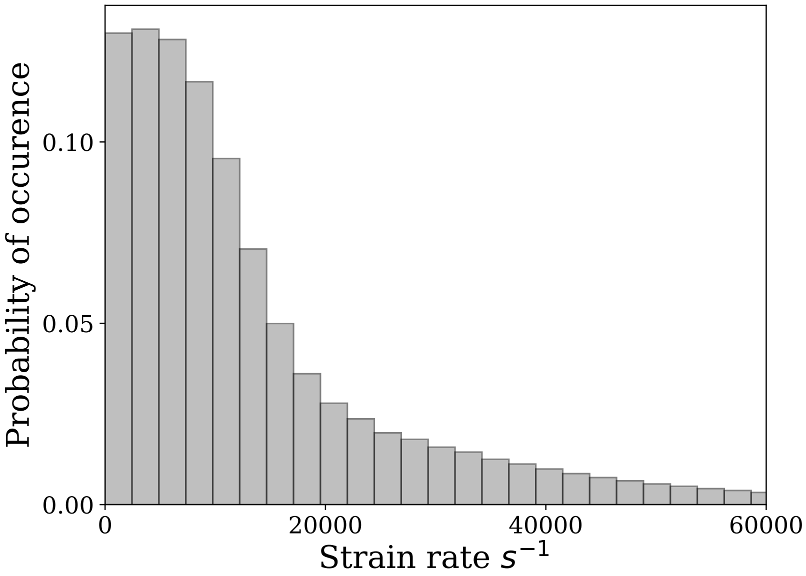

Figure 7.20: Strain rate probability distribution in the red box indicated in Fig. 7.2, for the case LES-ARC (similar result is observed for GLOMEC).

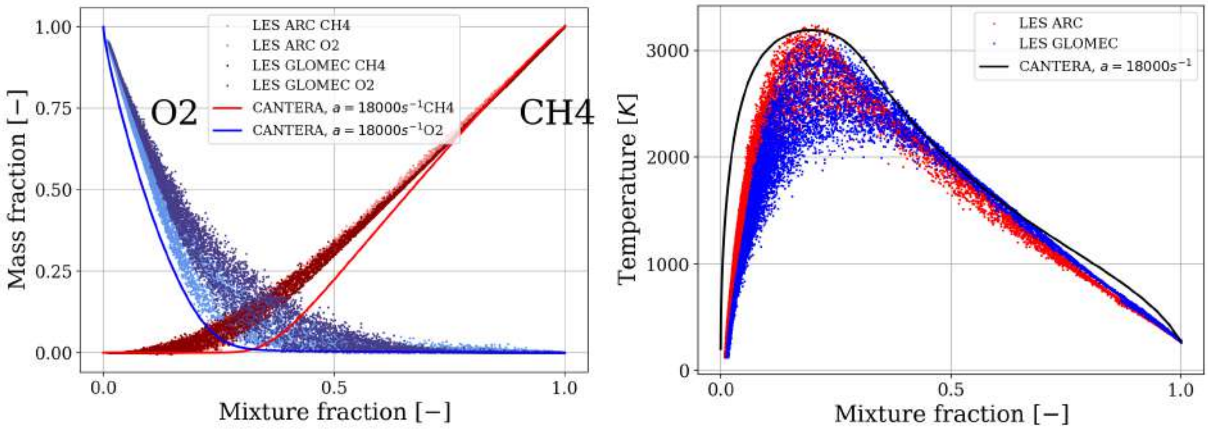

(a) Reactants

(b) Temperature

Figure 7.21: Scatter plots in the mixture fraction space, from LES-ARC (light dots) and LES-GLOMEC (dark dots) compared to a reference CANTERA flame at $a_{mean} = 18000 s^{-1}$. Left: reactants (Fig. 7.21a). Right: temperature (Fig. 7.21b).

The scatter plots are typical of purely diffusion flames, as was observed in the solution fields. Turbulence, non-adiabaticity and strain induce significant scattering in the reacting zone, where the fluctuating strain rate leads to fluctuations in the flame structure. The propellant profiles of Fig. 7.21a show overall a good agreement between the two simulations, with however some discrepancies in the lean zone (oxygen side), where the ARC simulation is closer to the CANTERA curve. The temperature profiles in Fig. 7.21b exhibit overall colder temperatures in the LES with most scatter points located below the temperature curve of CANTERA, and peak values below the maximum CANTERA value of 3191K. This is due first to the non-adiabaticity of the LES cases, with important heat loss in this zone as the injection head was set with an isothermal boundary condition at 500K. Also, oxygen is injected as a gas and at a higher temperature in the CANTERA flame ($T_{O2} = 201K$), ignoring gas cooling by evaporation.

As announced in the modelling section, it is checked that the flame mainly burns in a diffusion regime. This is made the same way as for the CONFORTH, by using a Takeno index [Yamashita et al., 1996] ζ weighted by the heat release rate $\dot{\omega}_T$ as in Eq. 6.2: 98.5% of the heat release flame located in the flame area defined by the Takeno index is found to be in a diffusion regime, the rest being in premixed regime.

The impact of the LES filter on the flame is now checked. The viscosity ratio $\psi = \mu_t/\mu_{lam}$ is used to evaluate the level of subgrid-scale turbulence and is shown in Fig. 7.22 along with the averaged heat release rate.

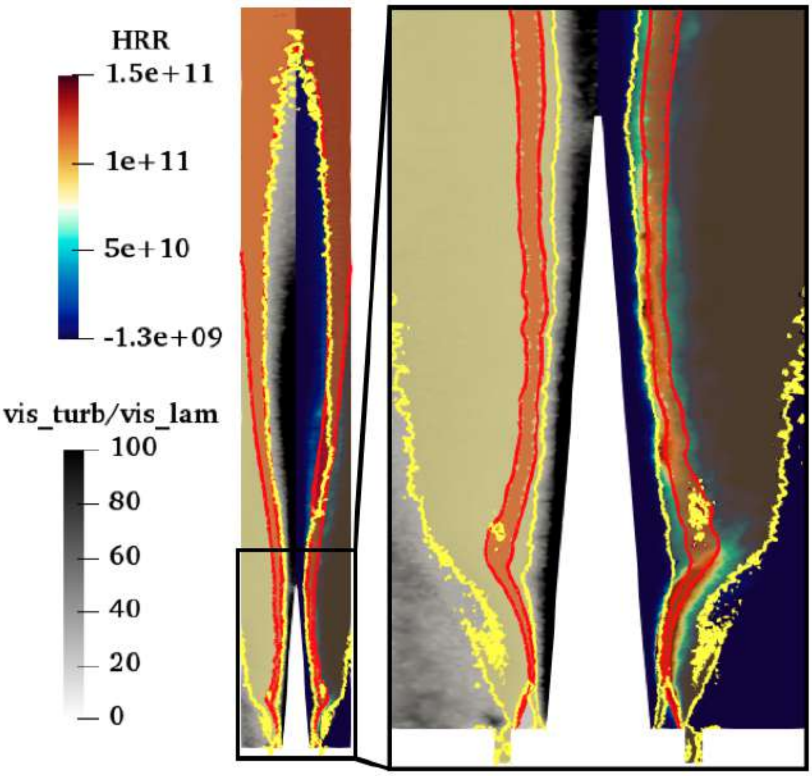

Figure 7.22: Viscosity ratio ψ (left half cut) and heat release rate (right half cut) of the ARC case with a zoom on the oxygen cone region (right). The images are scaled by a factor 0.5 in the axial direction for better clarity. The yellow zone indicates $1 < \psi < 10$ and the red zone indicates $0.1 < Z < 0.3$.

The red zone highlights the mixture fraction field in the range $0.1 < Z < 0.3$, therefore indicating the area where the HRR is maximum (both for exo- and endothermic zones of the flame structure), meaning the zone where most of the combustion process happens. This zone is well contained in the yellow area corresponding to $1 < \psi < 10$, *i.e*, well refined LES. This suggests that the subgrid-scale phenomena are relatively weak in the flame zone compared to the resolved scales.

Similarly to the CONFORTH test bench, the use of the SRK equation of state is checked looking at the compressibility factor. Figure 7.23 indicates, contrarily to the CONFORTH, that most of the intense heat release rate is found outside the isocontour $\mathcal{Z} = 0.95$, meaning that the combustion process happens near to perfect gas conditions. However and as expected by the cryogenic injection of oxygen, all the cold zone is marked by a compressibility factor $\mathcal{Z} < 0.95$, showing the necessity of the SRK EoS here.

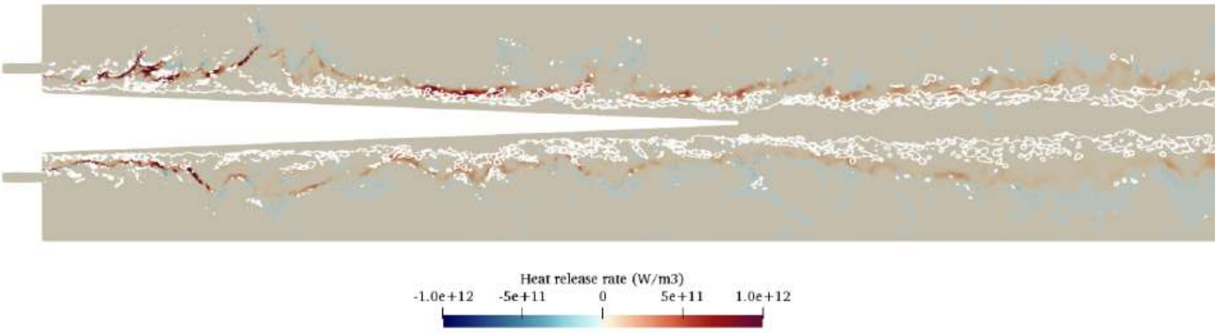

Figure 7.23: Instantaneous heat release rate field zoomed on the oxygen region. The white isoline indicates the compressibility factor $\mathcal{Z} = 0.95$: inside this zone, $\mathcal{Z} < 0.95$.

Finally the flame resolution is checked by evaluating the thermal flame thickness $\delta_{th} = [\pi D_{th}/(2a)]^{0.5}$. In the scatter plots zone where the mean strain rate has been evaluated to be $a \approx 18000 s^{-1}$, this means $\delta_{th} \approx 68\mu m$. In this area where the mesh has been particularly refined, the cell size is about $30\mu m$. Thus, two grid points is the minimum but still enough to describe the temperature gradient in the flame. Of course, the mesh is coarsened progressively in the axial direction (see Fig. 7.2), but the strain rate of the flame diminishes as well, therefore meaning a larger thermal flame thickness.

7.3.5 Influence of the liquid fraction parameter at injection

The simulation of the TUM case was particularly difficult to set up and stabilize mainly due to the injection cone model used for liquid oxygen. Most parameters (like angle of injection, cone length...) used in the model come from empirical correlations, and many tests led to the conclusion that the result is quite sensitive to these parameter values. To illustrate this behaviour, a parametric study is here conducted on one parameter, the liquid fraction α_l as it was found to be a particularly critical parameter. As shown in Eq. 7.11, its value directly controls the velocity of the injected particles. In the simulations of the TUM case (both ARC and GLOMEC), the liquid fraction was chosen under the hypothesis that the particles are injected with the mean liquid velocity at the cone surface (*i.e.*, using the liquid mass flow rate, the cone surface area and a liquid volume fraction of 1) $u_l = 5.85 m/s$. It is actually a

strong hypothesis because it means that the surrounding gaseous phase has no influence on the particles when they detach from the cone.
In the following test cases, the value of α_l has been decreased by a factor 2, 5 and 10, which therefore multiplies the injection velocity by the same factors (the cone length and surface is kept constant, even though it should be changed as described in the model). The GLOMEC mechanism has been used for this parametric study, as it allows faster computations. As expected, α_l has a direct influence on the size of the oxygen field, as shown in Fig. 7.24.

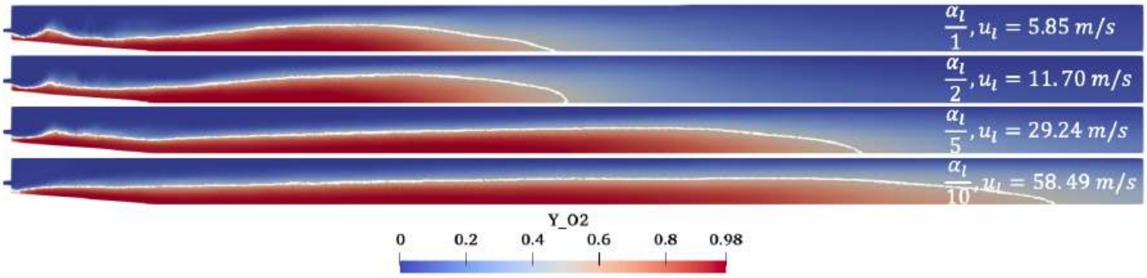

Figure 7.24: Comparison of the oxygen vapor fields obtained with different values of α_l. The white isocontour highlights $Y_{O2} = 0.5$.

For $\alpha_l/2$ the difference is not significant, but for the cases $\alpha_l/5$ and $\alpha_l/10$, the oxygen field is clearly longer, by almost a factor 2 in the latter case due to the increased droplet injection velocity. Of course, this has an impact on the burnt gases composition and temperature, as shown in Tab. 7.7.

	$\alpha_l/1$	$\alpha_l/5$	$\alpha_l/10$
$T(K)$	2749	2950	3030
$\rho(kg/m^3)$	1.53	1.42	1.59
H2O	0.41	0.38	0.35
CO	0.33	0.33	0.25
CO2	0.19	0.17	0.17
O2	0.06	0.1	0.21
H2	0.02	0.02	0.01
CH4	0.001	0.003	0

Table 7.7: Burnt gases composition at $x = 289mm$ with GLOMEC depending on the liquid fraction value at injection.

As it may be expected the burnt gas at the chamber exit are further away from equilibrium as the flame zone is extended. This strong impact of the liquid injection model calls for a more accurate approach.

7.4 Conclusions on the TUM test bench

The single injector LOx/GCH4 configuration from TUM has been simulated with AVBP using the LES methodology developed in the previous chapter, and two chemical models: an ARC and a global scheme (GLOMEC), both specifically derived for the operating point at 18.5 bar. Both models are in good agreement in the flame zone, but show some discrepancies in terms of composition, temperature and wall heat flux, in the burnt gases. It was shown that these differences were solely due to the chemical models, proving again the interest of using ARCs in LES of rocket engine combustion chambers. Nonetheless the GLOMEC approach is found very useful to accelerate the computations and has the capability to give accurate solutions provided that a larger temperature range is included in the optimization procedure. These ideas are currently debated at CERFACS to enhance the GLOMEC and globally its derivation technique.

The LES gave a correct prediction of wall heat flux, which is a critical design parameter. Nonetheless, a number of limitations have been highlighted and are summarized below.

- Turbulent combustion model:
  Because the flame is under-resolved, higher integral heat release rate due to increased numerical diffusion may be obtained as explained in Section 4.5. In the same time, neglecting the sub-grid turbulent activity (strain rate and wrinkling) may lead to an under-estimation of the total heat release rate. Finally, the net effect of not applying any turbulent combustion model remains uncertain.

- Artificial viscosity:
  To ensure numerical stability, the use of LAD viscosity was necessary at a substantial level. The drawback is again the numerical over-diffusion which plays a critical role in diffusion flames (as investigated in the case of the CONFORTH in Annex B.).

- Chemical reactions in the unresolved boundary layer and flame-wall interaction:
  Same remark as for CONFORTH, the chemical reactions in case of WMLES are not modeled in the present simulations, so that a part of the heat flux is missed and could be under-estimated by 5-10%, as highlighted in Section 4.5.

Next to chemistry influence, this simulation also highlighted the importance of the liquid phase modelling which is still challenging. The technique retained for this work, initially developed in the thesis of Potier [Potier, 2018], is extremely sensitive to the inputs given to the model. The cone length and the injection angle come from empirical correlations, and drive directly the oxygen injection zone which is assumed constant. The unique droplet diameter at injection is also a strong hypothesis that is difficult to verify as no experimental data is available. Finally another strong hypothesis is the particle injection velocity which was demonstrated to drastically impact the result.
The technique is obviously limited to stationary cases, as the cone length is fixed by the mesh. In a more practical way, the Lagrangian framework also leads to repeated numerical problems, difficult to deal with. Therefore the next step, also currently a topic of research at CERFACS, is to include the simulation of the liquid core ant its atomization with a diffuse interface method, where a liquid-gas interface is introduced.

Part V

General conclusion and perspectives

This thesis brings several new contents in the field of Large-Eddy Simulation of Liquid Rocket Engines. A particular emphasis has been put in this work on the oxy-combustion of methane in the conditions met in thrust chambers since, as recalled in Section 1.3.3, it is foreseen to be used in future rocket engines thanks to its global lower cost.

The growth of computational power allows now to use finite-rate reduced kinetic schemes in CFD codes, in particular in the form of reduced schemes such as ARCs. The recently developed tool ARCANE [Cazères et al., 2021], developed at CERFACS, allows today to build such schemes for any operating point, including the extreme conditions found in rocket thrust chambers. This was performed for the two test rigs simulated in this work: the CONFORTH and the TUM cases, in Section 4.3.1 and Annex C. respectively. This reduction allowed to reduce the computational cost to a moderate level keeping a good description of the kinetics in the LES, despite the complex flame structure found in CH4/O2 flames, as demonstrated in Section 6.3.2. However ARCs can still be costly to use in LES simulations, due to the possible large difference between the flow and the chemical time step. This statement led to the creation of a new integration method, called exponential integration, presented in Section 4.4.1, which can be seen as an implicitation technique for an explicit code, here AVBP (however it is easy to implement it in other CFD codes and was actually performed during this thesis in a DNS code). Depending on the test case, the exponential integration allows to run faster reacting LES, as it was made in the CONFORTH study (Section 6.3.2). The method is already operational at CERFACS and was tested on other configurations, showing even better computation acceleration [Pestre et al., 2021]. However the method could be further enhanced, for example about the mass conservation enforcing method, and such work is already undergoing.

A study about diffusion flames has also been conducted in laminar flames, in order to highlight the problem of being under-resolved when computing such flames on LES grids. The filtering and numerical diffusion produce an increase of the heat release rate, *i.e.*, a faster flame. It was shown in Section 4.5.2 that modifying the diffusion coefficients allows to counteract this effect, allowing to retrieve the correct heat release overall in laminar flames. However in LES code like AVBP, it appeared that artificial/numerical diffusion effects can take over the physical diffusion, limiting in principle the efficiency of the model (Section 4.5.3). Turbulent flames with subgrid-scale contribution (strain rate, wrinkling) may solve this problem as they tend to increase the flame consumption speed. It is expected that the final model including both mesh and subgrid-scale effects will be efficient in a numerical environment such as the one of AVBP.

The progress in chemistry made with the development of ARCs and the exponential integration allowed to investigate the effect of chemical reactions in boundary layers, in Section 5.3. This was performed in laminar and turbulent channel flows. By comparing the wall fluxes between the non-reacting and reacting cases, with a non-resolved and resolved boundary layer, it was found that the influence of chemical reactions on the wall heat flux is not negligible (about 8-10%) and should be taken into account.

Another topic that was previously highlighted at CERFACS by Potier [Potier, 2018] and Maestro [Maestro, 2018] was the strong influence of the SGS model coupled with the standard wall-law to predict wall fluxes. This question was addressed in this work in Section 5.2, showing that the coupling between the SGS model (like WALE and Sigma) with the standard wall-law resulted in errors due to insufficient turbulent viscosity at the wall. From this observation a stochastic model was created in order to generate velocity gradient fluctuations (Section 5.2.1), allowing to rise turbulent viscosity values at the wall. The model was demonstrated to improve the results so far in isothermal flows, but is however not yet ready for anisothermal flows as presented in Section 5.2.2. The extension to anisothermal flows requires more work but it should be feasible by including temperature in the developments.

The oxy-combustion of methane was finally studied in two real test benches: the supercritical 5-injectors GCH4/GOX CONFORTH from ONERA (Chapter 6) and the subcritical single-injector LOx/GCH4 from TUM (Chapter 7). Both make use of ARCs, and showed their usefulness concerning the accurate description of the flame as well as the burnt gases composition.
The exponential integration was validated again, this time in a typical 3D LES simulation that is the CONFORTH simulation, demonstrating its applicability and interest not only in 1D flame calculations but also for industrial configurations. The use of accurate chemistry also allowed in the CONFORTH test bench to retrieve the complex flame structure of CH4/O2 flames, as well as to analyse in detail the near-wall behaviour of the chemistry in a modeled boundary layer. The comparison with experiment provided satisfactory results, however with slightly under-estimated wall heat flux and temperature, that may come from different sources. Finally the TUM test rig was also the occasion to compute a cryogenic case, more realistic of a real LRE. The LOx injection was modelled following the methodology developed by Potier 7.2.2 since no proper atomization model is yet ready in AVBP. It however showed its limits due to some uncertainties linked to the models, mainly the injection velocity of the O2 droplets or the evaporation model, not entirely valid for this dense oxygen cone. Another chemical modeling taking the form of a global scheme, the GLOMEC, was also tested on this configuration in order to reduce the computational cost. It gave similar results compared to the ARC simulation in the flame zone, but however seemed to show difficulties in the burnt gases part due to its simplicity and the non-adiabatic conditions of the test rig.

Research on combustion modeling in rocket engine combustion chambers is continuing at CERFACS, now mainly focusing on the two-phase flow aspects. This will allow to leverage the limitations observed in this work of the cone injection model. To this purpose the diffuse interfaces approach is currently under investigation and could allow to better describe the complex atomization process.

Part VI

Appendices

A. Calculation of the equivalent heat transfer coefficient for the CONFORTH walls boundary condition

The computation of h_{eq} is extracted from [Martin-Benito, 2019] and was used in the LES simulation in order to keep the same methodology than CNES. Notations used below are the same than Fig. 6.5, presented again below for clarity. Radial coordinates (r, x) are used for the following.

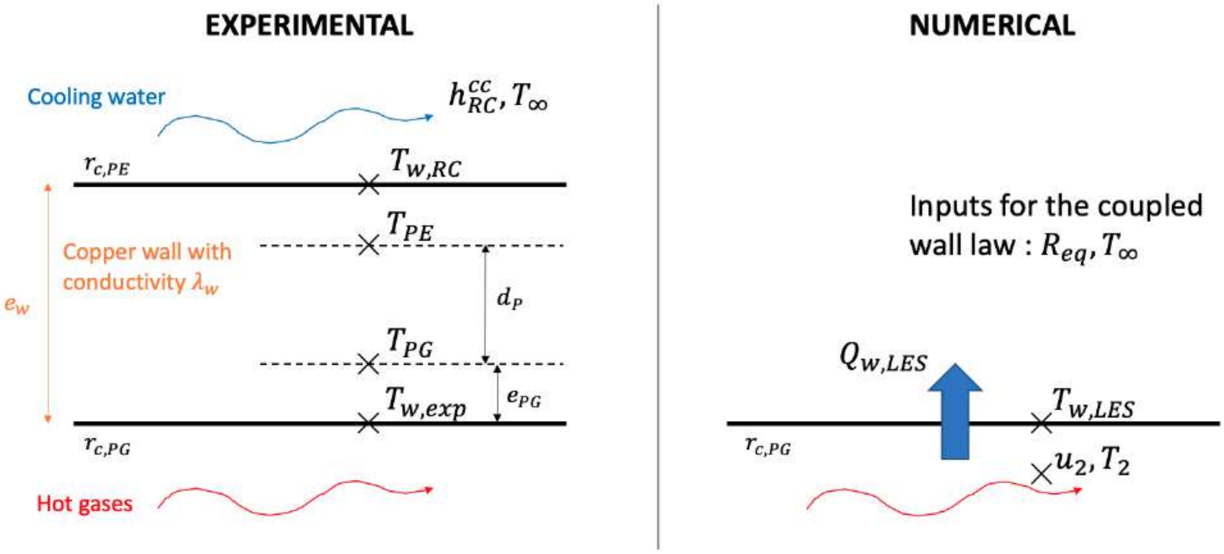

Figure 1: Thermal boundary condition (proposed by CNES). $Q_{w,LES}$ is the LES output, from which $T_{w,LES}$ is then retrieved.

The experimental heat flux ϕ through the cooling water circuit writes:

$$\phi = h_{RC}^{cc}(T_{w,RC} - T_\infty) \tag{22}$$

The conduction part of the heat flux through the solid of thickness e_w must be taken into account. Supposing the run in a stationary state, where the axial heat transfer is negligible compared to the radial heat transfer ($\partial\phi/\partial x = 0$):

$$\begin{aligned} 0 &= \frac{\partial}{\partial r}[r\lambda(T,r)\frac{\partial T}{\partial r}] && (23) \\ \phi(r) &= -\lambda(T,r)\frac{dT}{dr} && (24) \end{aligned}$$

Integrating these equations:

$$r\phi(r) = cste \tag{25}$$

The thermal heat flux between the cold ("PE") and hot ("PG") sides of the material gives:

$$\phi(r)r = \lambda\left(\frac{T_{w,exp} + T_{w,RC}}{2}\right)\frac{T_{w,exp} - T_{w,RC}}{\ln\left(\frac{r_{c,PE}}{r_{c,PG}}\right)} \tag{26}$$

The thermal conductivity is supposed constant for this development ($\lambda(T,r) = \lambda_w$) so that the previous equation is recast as:

$$T_{w,exp} - T_{w,RC} = \phi(r) r \frac{\ln\left(\frac{r_{c,PE}}{r_{c,PG}}\right)}{\lambda_w} \tag{27}$$

Then:

$$T_{w,exp} - T_{w,RC} = T_{w,exp} - T_{w,RC} + T_\infty - T_\infty \tag{28}$$

By definition:

$$\phi = h^{cc}_{RC}(T_{w,RC} - T_\infty) = \phi(w, PE) = \frac{r\phi(r)}{r_{c,PE}} \tag{29}$$

So:

$$T_{w,RC} - T_\infty = \frac{r\phi(r)}{r_{c,PE} h^{cc}_{RC}} \tag{30}$$

We obtain finally:

$$T_{w,exp} - T_\infty = r\phi(r)\left(\frac{\ln\left(\frac{r_{c,PE}}{r_{c,PG}}\right)}{\lambda_w} + \frac{1}{r_{c,PE} h^{cc}_{RC}}\right) \tag{31}$$

Which gives the heat flux between the hot side position and the cooling circuit:

$$\phi(r_{c,PG}) = \frac{T_{w,exp} - T_\infty}{r_{c,PG}\left(\frac{\ln\left(\frac{r_{c,PE}}{r_{c,PG}}\right)}{\lambda_w} + \frac{1}{r_{c,PE} h^{cc}_{RC}}\right)} \tag{32}$$

Since:

$$\phi(r_{c,PG}) = h_{eq}(T_{w,exp} - T_\infty) \tag{33}$$

Therefore the equivalent heat transfer coefficient h_{eq}, used as boundary condition in the CONFORTH LES simulation (Chapter 6) is deduced:

$$h_{eq} = \frac{1}{r_{c,PG}\left(\frac{\ln\left(\frac{r_{c,PE}}{r_{c,PG}}\right)}{\lambda_w} + \frac{1}{r_{c,PE} h^{cc}_{RC}}\right)} \tag{34}$$

B. Influence of the LAD parameter in CONFORTH

Prior to the presented simulation of the CONFORTH configuration (Chapter 6), another one has been performed with exactly the same numerical settings, except for the LAD parameter. Figure 2 shows a comparison of the flame length between the reference case ("low LAD") and the previous simulation run with stronger LAD coefficients ("high LAD"). The parameters of the LAD used in the AVBP computations are given in Table 1.

It is clear that the "high LAD" case exhibits a really smaller flame length, about a factor 2. The LAD is responsible and this is here a demonstration of the influence of an over-diffusion effect in such rocket engine flames. This enhances the diffusion velocities of the species, which is a driving factor for diffusion flames: they burn faster (until extinction). The shorter length

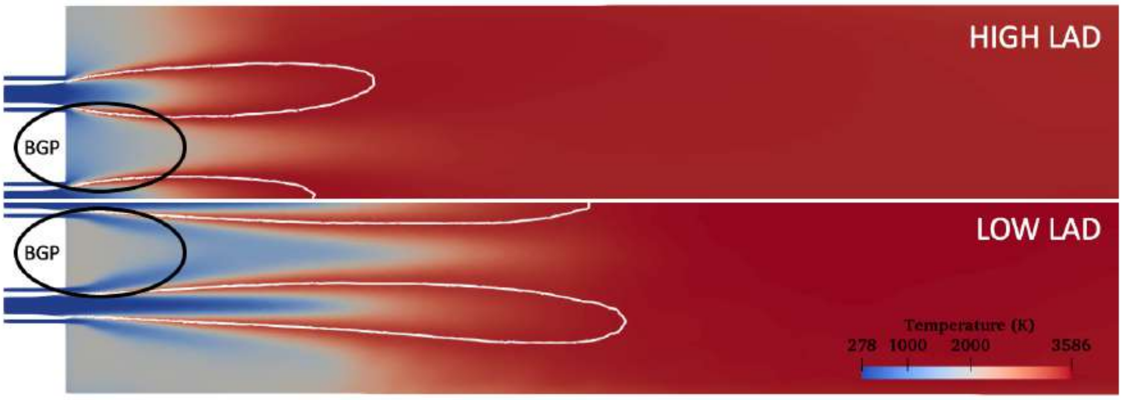

Figure 2: Comparison between the "high LAD" (top half) and the "low LAD" (bottom half) cases. The white isocontour shows the stoichiometric line $Z_{st} = 0.2$, and the black circled area the burnt gases pockets in-between the flames.

	high LAD	low LAD
Coeff on pressure gradients	3.0	2.0
Coeff on density gradients	3.0	2.0
Threshold	0.0	1.0

Table 1: LAD parameters used in the simulation. The higher the coefficients, the more the stiff gradients (of P and ρ respectively) are diffused. The lower the threshold, the more the LAD activates in the domain.

of the "high LAD" flame is the consequence of this higher consumption speed. Even not shown here, the influence on the wall fluxes is quite important at the flame location, but is almost invisible more downstream, in the burnt gases.

The LAD parameters influences therefore the temperature at the stoichiometric line, which is much higher in the "high LAD" case, and also the zones in-between the flames and next to the walls. The burnt gases pockets (indicated as "BGP " in the circled area of Fig. 2) are much hotter in the "low LAD" case.

Thus, the LAD model as artificial viscosity model was found to have a strong impact on the simulations. Even if acting a lot on the flame behaviour, it is nevertheless necessary to avoid spurious oscillations: therefore its values must be chosen with care.

C. Analytical reduced chemistry for the TUM configuration

Reduction process

Like for the CONFORTH test bench, ARCANE [Cazères et al., 2021] is used to derive an ARC that will be used specifically for the simulation of the TUM's LOx/GCH$_4$ test bench. The RAMEC mechanism [Petersen et al., 1999] (38 species, 190 reactions, coming from GRI1.2) is again chosen as the reference scheme for the same reason: it was specifically made for the methane oxycombustion at high pressures. The chemistry reduction is performed this time for the same scalar dissipation range ($100 < \chi_{st} < 1500 s^{-1}$) but with a different pressure range fitting to the test bench operating point: $17 < P < 23 bar$.

Execpt the target operating point (pressure, temperature), the same methodology (chosen species, error limits, etc...) than for the CONFORTH test bench is used: report to Sections 4.3.1 and 4.3.2. After the reduction process, a 18 transported species (17 reactive + N_2), 4 QSS and 89 reactions mechanism is obtained: about half of the species and reactions are removed from the RAMEC. The new reduced mechanism, detailed in Table 2, is now tested in CANTERA against the reference scheme to verify its good behaviour on the targeted operating point.

Transported	QSS
H2 H O O2 OH H2O HO2 CH3 CH4 CO CO2	C2H3 CH2CO
HCO CH2O C2H2 C2H4 C2H5 C2H6 N2	CH3O2 CH3O

Table 2: Species contained in the derived ARC.

Validation

Table 3 shows the error induced by the reduction on the range of the chosen parameters, and is found to be very low both on temperature and the integral of heat release rate.

Case	Conditions	T_{max}	$\int \dot{\omega}_T$
A	17 bar, $\chi_{st} = 100s^{-1}$	-0.66%	+0.99%
B	17 bar, $\chi_{st} = 1500s^{-1}$	-0.64%	+1.00%
C	20 bar, $\chi_{st} = 1000s^{-1}$	-0.66%	+0.96%
D	23 bar, $\chi_{st} = 100s^{-1}$	-0.68%	+1.06%
E	23 bar, $\chi_{st} = 1500s^{-1}$	-0.67%	+0.97%

Table 3: Validation cases: relative errors of the ARC compared to the RAMEC detailed mechanism.

Details about the flame structure is presented for the case C in Fig. 3 (other cases show really similar shapes and are not presented here). One can observe and excellent agreement both temperature and heat release profiles. Actually both kinetic schemes match perfectly, except on the heat release rate profile around $Z = 0.28$, where the ARC fails to represent the slight curve pit. However it does not have a strong impact as the integral of heat release rate is only higher by 0.96%.

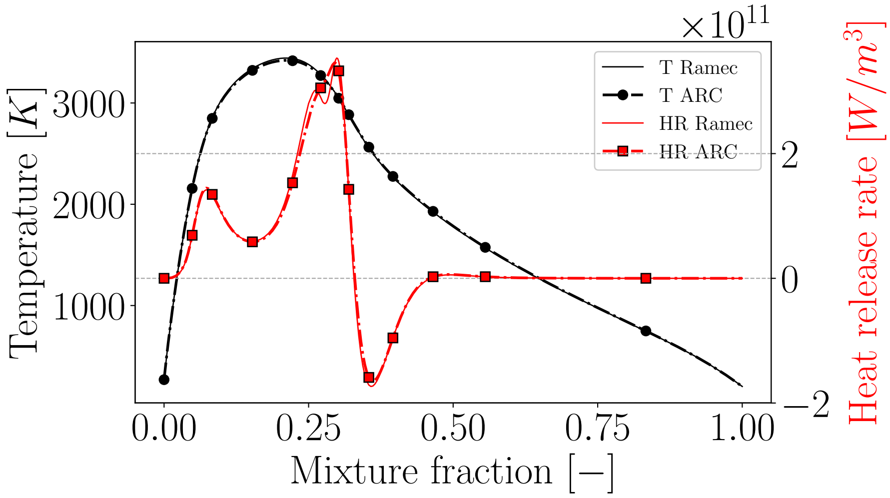

Figure 3: 1D profile of strained diffusion flame: evolution with mixture fraction of the temperature (black) and the heat release rate (red). Thick lines: RAMEC. Lines with markers: ARC. Case C: $P = 20bar$, $\chi_{st} = 1000s^{-1}$.

The validation continues by checking the main species profiles on Fig. 4. Again the ARC shows a very good agreement with the RAMEC. The biggest deviation is observed on CO, and this could be then the main responsible of the deviations presented in Table 3.

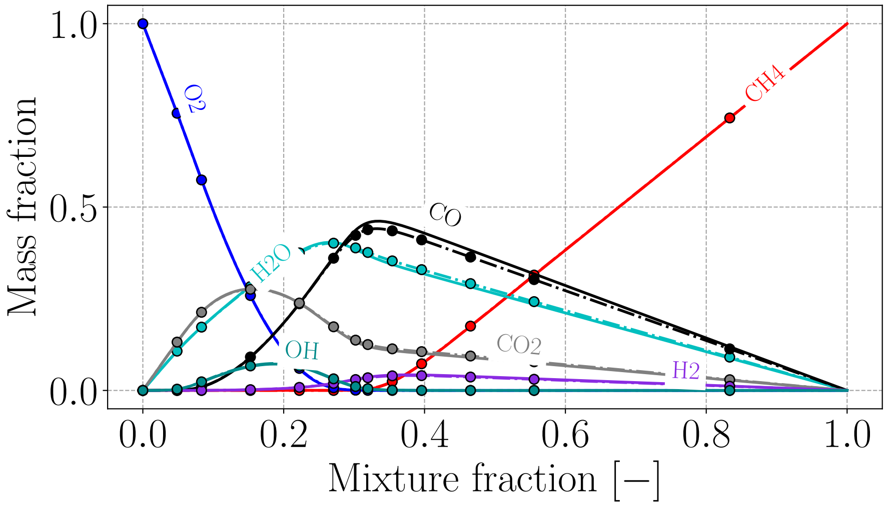

Figure 4: 1D profile of strained diffusion flame: evolution with mixture fraction of the main species. Case C: $P = 20bar$, $\chi_{st} = 1000s^{-1}$.

Finally, the influences of scalar dissipation rate and pressure on temperature and integral of heat release are tested and presented Fig. 5 and 6.

Both mechanisms have a very similar reaction to the scalar dissipation rate growth, even far beyond the range of derivation: the temperature never exceeds 1% error, and 5% for the integral of heat release rate. The differences are found the largest for the high values of χ_{st}.

The response to pressure growth is again similar for both chemical schemes, with an error on temperature remaining about 0.7% all along the range, and less than 1% for integral of heat release rate.

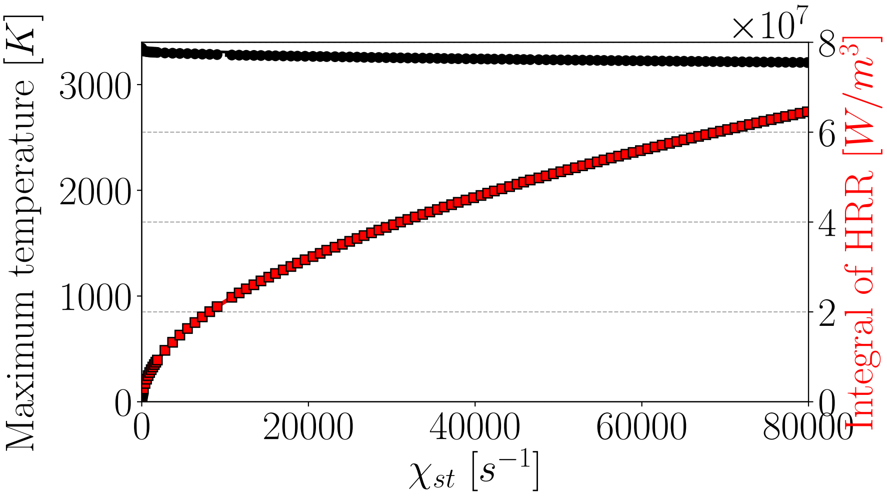

Figure 5: Evolution with scalar dissipation rate of the maximum temperature (black) and the integral of heat release rate (red) at $P = 20bar$. Thick lines: RAMEC. Lines with markers: ARC.

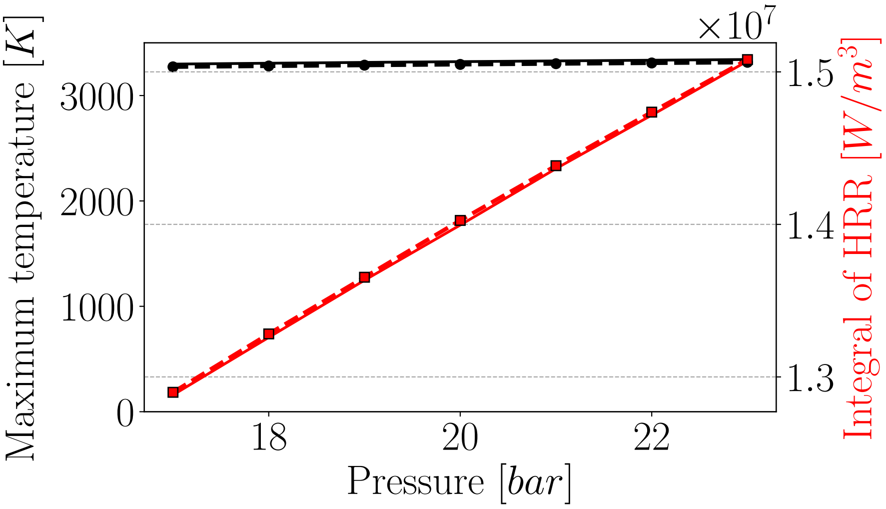

Figure 6: Evolution with pressure of the maximum temperature (black) and the integral of heat release rate (red) at $\chi_{st} = 1000s^{-1}$. Thick lines: RAMEC. Lines with markers: ARC.

All these elements show that the specific chemistry derived for the TUM LOx/GCH$_4$ test case will represent with a good fidelity the complex chemical processes involved. It is then used in the LES simulation.

D. GLOMEC development methodology

Extracted from [Strauss, 2020], on courtesy of Julian Strauss.

Chapter 3

Global Reaction Mechanism Development Methodology

This chapter is concerned with the methodology behind the development of the global oxidation reaction mechanism. Basically, it is to be noted that the methodology is not restricted to methane oxygen combustion (also called $methaneoxy - combustion$). From the beginning it was the purpose to propose a general method to be used by CERFACS, also applicable to other reactants.
Hence, for better illustration and comprehension, the methodology explained in general and simultaneously directly applied to the combustion of methane and oxygen at the operating point of the test case described in the previous chapter. The name of this mechanism in particular is introduced as **GLOMEC** which stands for **GLO**bal **O**xygen **ME**thane **MEC**hanism.

This chapter is subdivided into four sections. At first, it is dealt with notation conventions and the naming of the employed software tools. Afterwards the methodology is decomposed by providing different views of it to clearify and explain the required information and procedures.

3.1 Notation Conventions

Quantities are denoted using a syntax that allows for distinguishing between scalars, vectors, states (e.g. chemical equilibrium or fresh gas) and the reaction mechanism from which the quantity is obtained. See the logic below (as examples, the scalar mole fraction of the k_{th} species at the chemical equilibrium computed by GLOMEC and the vector of all N species mole fractions at the chemical equilibrium computed by GLOMEC are given):

$$\left(\boxed{1}_{\boxed{2}}^{\boxed{3}}\right)^{\boxed{4}}, e.g.\ \left(X_k^{eq}\right)^{GLO} \quad or \quad \left(\mathbf{X}_N^{eq}\right)^{GLO} \tag{3.1}$$

$\boxed{1}$ symbol of the quantity (scalar or vector), e.g. X for a scalar mole fraction or $\mathbf{X}$ for a vector of mole fractions

$\boxed{2}$ supplement to 1 and/or index addressing an element of a vector for scalar quantities respectively the number of elements for vector quantities, e.g. k for the k_{th} species, or N for the number of species

$\boxed{3}$ specification of the state of the system, e.g. *eq* for equilibrium

$\boxed{4}$ specification of the reaction mechanism from which the quantity is obtained (for general validity it is omitted), e.g. *GLO* for GLOMEC

Computing the difference between two quantities the above notation is using the Δ symbol as well as stating the second mechanism from which the quantity is obtained and the kind of comparison:

$$\left(\Delta\boxed{1}_{\boxed{2}}^{\boxed{3}}\right)_{\boxed{6}}^{\boxed{4},\boxed{5}}, e.g.\ \left(\Delta T^{eq}\right)_{abs}^{iGLO,GLO} \tag{3.2}$$

$\boxed{5}$ specification of the reaction mechanism from which the the quantity is obtained, which is compared with the quantity obtained from the other reaction mechanism $\boxed{4}$

$\boxed{6}$ specification of the kind of comparison, e.g. *abs* for *absolute*

3.2 Tools and Computations

The method is implemented in a generic way leveraging PYTHON 3 [45] to coordinate and launch executions of all subprocesses. The scripts underly version control in GITLAB [43].
Flame properties are computed using the software CANTERA [15] which is an open-source tool to solve chemical kinetics, thermodynamics, and transport process problems. The files used as inputs in this work are given in Appendices A.1, A.2 and A.3.

Computing laminar premixed flames is commonly done during the validation of a chemical reaction mechanism [34]. Thus, the global reaction mechanism methodology incorporates steady one-dimensional laminar premixed flame computations to obtain the laminar flame speed s_L on the one hand. Note that the flame in the TUM rocket combustor is a diffusion flame. However, in this work it is preferred to use premixed flames, as diffusion flames would lead to other to other considerations such as the strain rate which would substantially complicate the problem.
On the other hand, the adiabatic flame temperature is obtained through chemical equilibrium (henceforth just called *equilibrium*) computations at constant pressure and enthalpy. Note that all equilibrium computations are performed at constant pressure and enthalpy in this work, since this a validated assumption with respect to deflagrations [34].
Furthermore, the CERFACS in-house tool ARCANE (Analytical Reduction of Chemistry: Automatic, Nice and Efficient) [7] is employed to optimize thermodynamic and transport properties for the specified operating point.

All in all, the methodology does not demand for special or hardly accessible tools and the CPU cost is cheap.

3.3 Black Box Model

A very global view of the methodology can be given by a black box model [16]. It focusses on the inputs and the outputs, while the detailed relations between those remain undisclosed.

In general, the development of a chemical reaction mechanism means to establish a system comprising thermodynamics, fluid dynamics and chemistry models as well as initial and boundary conditions. Therefore, the inputs of the black box model comprise:

- species and species model
- reactions and kinetics parameters
- premixed fresh gas state
- thermodynamic and transport properties
- target flame properties

GLOMEC is not obtained directly. It evolves throughout a development process being called **GLOMEC DEVELOPMENT PROCESS** or, in short, GDP. Thus, for the purpose of unambiguity, the reaction mechanism inputted to the GDP is henceforth being called **INITIAL GLOMEC** (iGLO) and the the one which is the output of GDP is called **FINAL GLOMEC** (fGLO).

A black box model of the GDP is given in Figure 3.1. The inputs are used to construct INITIAL GLOBAL. Yet, INITIAL GLOMEC is required to be modified in order to recover a set of certain flame properties correctly. The modifications are performed by the GDP. In the end, modifications of the species model and the reaction kinetics parameters are used to construct FINAL GLOMEC.

Figure 3.1: Black box model of GLOMEC development process.

3.4 GDP Inputs

This section serves to introduce the thermodynamics, fluid dynamics and chemistry models as well as the initial and boundary conditions employed to construct the system INITIAL GLOMEC. Moreover, the INITIAL GLOMEC and the RAMEC target flame properties are given to complete the gathering of all information required by the GDP.

3.4.1 Species and Species Model

The set of considered species $(\mathbb{N})^{iGLO}$ contains the $N = 6$ (index k) species methane, oxygen, water, hydrogen, carbonmonoxide and carbondioxide respectively CH_4, O_2, H_2O, H_2, CO, CO_2. The species are not varied throughout the GDP:

$$N = (N)^{iGLO} = (N)^{fGLO} = 6 \tag{3.3}$$

$$\mathbb{N} = (\mathbb{N})^{iGLO} = (\mathbb{N})^{fGLO} = \{CH_4, O_2, H_2O, H_2, CO, CO_2\} \tag{3.4}$$

These comprise $L = 3$ (index i) chemical elements hydrogen, oxygen, and carbon respectively H, O and C given as set $\mathbb{L}$:

$$L = (L)^{iGLO} = (L)^{fGLO} = 3 \tag{3.5}$$

$$\mathbb{L} = (\mathbb{L})^{iGLO} = (\mathbb{L})^{fGLO} = \{H, O, C\} \tag{3.6}$$

Properties such as the species molecular weight, critical temperature, critical pressure and formation enthalpy are given in Table 3.1.
Moreover, the reference-state thermodynamic properties of the species are obtained via the NASA 7-coefficient polynomial parametrization [1]:

$$\frac{C^{\circ}_{p,k}}{R}(T) = a_{0,k} + a_{1,k}T + a_{2,k}T^2 + a_{3,k}T^3 + a_{4,k}T^4 \quad , \tag{3.7}$$

$$\frac{H^{\circ}_{k}}{R}(T) = a_{0,k} + \frac{a_{1,k}}{2}T + \frac{a_{2,k}}{3}T^2 + \frac{a_{3,k}}{4}T^3 + \frac{a_{4,k}}{5}T^4 + \frac{a_{5,k}}{T} \quad , \tag{3.8}$$

$$\frac{S^{\circ}_{k}}{R}(T) = a_{1,k}ln(T) + a_{2,k}T + \frac{a_{3,k}}{2}T^2 + \frac{a_{4,k}}{3}T^3 + \frac{a_{5,k}}{4}T^4 + a_{7,k} \quad , \tag{3.9}$$

where the superscript 0 symbolizes the reference state, $C^{\circ}_{p,k}$ is the reference-state species heat capacity at constant pressure, H_k° is the reference-state species enthalpy and S_k° is reference-state the species entropy.

The GDP performs a modification of the coefficients $a_{7,k}$, thus:

$$a_{j,k} = \left(a_{j,k}\right)^{iGLO} = \left(a_{j,k}\right)^{fGLO} \quad for\ j = 1, \ldots, 6 \tag{3.10}$$

The values for the coefficients $a_{k,i}$ of INITIAL GLOMEC for two temperature ranges ([200 K;1000 K] and [1000 K;3000 K]) can be read on the CANTERA ⋆.cti file in Appendix A.2.

	molecular weight	**critical temperature**	**critical pressure**	**formation enthalpy**
	W_k	T_{crit}	P_{crit}	Δh_f°
	[kg/kmol]	[K]	[bar]	[kJ/kg]
O_2	31.10	154.6	50.4	0.0
CH_4	16.04	190.6	46.0	-4650.0
H_2	2.02	32.94	12.8	0.0
H_2O	18.02	647.3	220.9	-13423.3
CO	28.01	132.91	35.0	-3946.0
CO_2	44.01	304.2	73.8	-8941.4

Table 3.1: Collection of species properties (formation enthalpies at $T = 298.15$ K).

3.4.2 Chemical Reactions and Kinetics Parameters

$M = (M)^{iGLO} = (M)^{fGLO} = 4$ reactions (index j) are taken into account in the GDP, namely two irreversible fuel breakdown reactions (3.11, 3.12) and two reversible equilibrium reactions (3.13, 3.14):

$$\mathrm{CH_4} + 0.5\,\mathrm{O_2} \longrightarrow \mathrm{CO} + 2\,\mathrm{H_2} \tag{3.11}$$

$$\mathrm{CH_4} + \mathrm{H_2O} \longrightarrow \mathrm{CO} + 3\,\mathrm{H_2} \tag{3.12}$$

$$\mathrm{H_2} + 0.5\,\mathrm{O_2} \rightleftharpoons \mathrm{H_2O} \tag{3.13}$$

$$\mathrm{CO} + \mathrm{H_2O} \rightleftharpoons \mathrm{CO_2} + \mathrm{H_2} \tag{3.14}$$

This set of reactions was proposed by Jones and Lindstedt [19] back in 1988 and is derived from considerations coming along with the two-reaction-zone flame model. The primary reaction zone is characterized by the conversion of fuel into hydrogen and carbon monoxide, while the oxidation to water and carbon dioxide takes place in the secondary reaction zone. The basic idea of how to form the above reactions is to analyse the fundamental reaction steps in the different zones and then to eradicate the presence of radicals through certain techniques (e.g. linear combinations of reaction equations) and assumptions. This can be further studied in works by Mitchell et al. [28], Peeters et al. [30], Warnartz [48], Peters [32] or Biordi [2].

The kinetics parameters of the reactions are described using the empirical Arrhenius law which has been introduced in chapter 1. The selected values in Table 3.2 are taken from an analysis and experiment comparisons performed by Jones and Lindstedt [19]. Yet, only some of these values are only used in the INITIAL GLOMEC.

	A_f [cgs]	β [-]	E_a [kcal/mol]
reaction 3.11	0.44×10^{12}	0.0	30.0
reaction 3.12	0.3×10^{9}	0.0	30.0
reaction 3.13	0.25×10^{17}	-1.0	40.0
reaction 3.14	0.275×10^{10}	0.0	20.0

Table 3.2: INITIAL GLOMEC Arrhenius kinetics parameters.

Temperature exponents β_j and activation energies $E_{a,j}$ remain constant in the GDP.

$$\beta_j = \left(\beta_j\right)^{iGLO} = \left(\beta_j\right)^{fGLO}, \;\; E_{a,j} = \left(E_{a,j}\right)^{iGLO} = \left(E_{a,j}\right)^{fGLO} \tag{3.15}$$

3.4.3 Premixed Fresh Gas State

Relevant information concerning the premixed fresh gas state has already been given in the previous chapter. It is compactly given by Tables 3.3 (devoted to the mixture) and 3.5 (devoted to the fresh gas species). The index f denotes $fresh$.

	unit	mixture
fresh gas temperature T^f	[K]	250.0
fresh gas pressure P^f	[bar]	18.5
fresh gas equivalence ratio ϕ^f	[-]	1.33

Table 3.3: Premixed fresh gas state.

3.4.4 Thermodynamic and Transport Properties

Via ARCANE, thermodynamic and transport properties have been optimized for premixed flames obtained from RAMEC valid at pressures between 17 bar and 23 bar in order to take pressure fluctuations into account. The obtained values are also used for INITIAL GLOMEC and FINAL GLOMEC.

First, the molecular viscosity is computed with the Power Law:

$$\mu(T) = \mu^\circ \left(\frac{T}{T^\circ} \right)^b \tag{3.16}$$

with the reference-state viscosity $\mu^\circ = 0.9514 \times 10^{-5}$ pa·s, the reference-state temperature $T^\circ = 3303.4\,\mathrm{K}$ and the viscosity law coefficient $b = 0.65$.

Second, species Schmidt numbers Sc_k are written in Table 3.4 and, third, the mixture Prandtl number Pr is set to the value of 0.5735. The CANTERA input file containing the transport properties is given in Appendix A.3.

	O_2	CH_4	H_2	H_2O	CO	CO_2
Sc_k	8.51×10^{-1}	8.03×10^{-1}	2.35×10^{-1}	6.24×10^{-1}	9.13×10^{-1}	1.11×10^{0}

Table 3.4: Species Schmitt numbers Sc_k.

3.4.5 Target Flame Properties

The reference reaction mechanism used to define the values of the target premixed flame properties is a detailed reaction mechanism referred to as **RAMEC** (**RAM** accelerator **MEC**hanism) [33]. RAMEC will be abbreviated with *RAM* in this work. RAMEC is based on the Gas Research Institute (GRI) mechanism GRI-Mech 1.2 [13]. Comprising 38 species in 190 reactions, the mechanism is capable of modeling shock tube ignition delay times for CH_4/O_2 mixtures. It is valid for pressures between 40 and 260 atm, intermediate temperatures ranging from 1040 to 1500 K and fuel-rich stoichiometry ($\phi \geq 3.0$).

RAMEC delivers the values of the target premixed flame properties which are the adiabatic flame temperature $T_{ad,target}$ and the laminar flame speed $s_{L,target}$. They have been computed for both RAMEC and INITIAL GLOMEC.
A comparison of the values obtained from RAMEC respectively INITIAL GLOMEC yields that INITIAL GLOMEC overestimates the adiabatic flame temperature, whereas it underestimates the laminar flame speed:

	unit	RAMEC	INITIAL GLOMEC
equilibrium temperature T_{ad}	[K]	3381.12	3690.95
laminar flame speed s_L	[m/s]	1.7421	1.2574

Table 3.5: RAMEC and INITIAL GLOMEC adiabatic temperature and flame speed.

3.5 Global Mechanism Development Process

After the collection of all necessary inputs, the global mechanism development process can be launched. The goals of the GDP are recapped:

$$\boxed{\left.\left(\left(T_{ad}\right)^{fGLO} \overset{!}{=} \left(T_{ad}\right)^{RAM}\right)\right|_{T^f,P^f,\phi^f}} \tag{3.17}$$

$$\boxed{\left.\left(\left(s_L\right)^{fGLO} \overset{!}{=} \left(s_L\right)^{RAM}\right)\right|_{T^f,P^f,\phi^f}} \tag{3.18}$$

Note these definitions, as the adiabatic flame temperature is obtained from equilibrium computations in CANTERA:

$$T_{ad,target} \equiv \left(T_{ad}\right)^{RAM} \equiv \left(T^{eq}\right)^{RAM}, \;\; s_{L,target} \equiv \left(s_L\right)^{RAM} \tag{3.19}$$

$$\left(T_{ad}\right)^{iGLO} \equiv \left(T^{eq}\right)^{iGLO} \tag{3.20}$$

The differences (absolute and relative) of the target flame properties obtained from INITIAL GLOMEC and RAMEC are:

$$\left(\Delta T^{eq}\right)_{abs}^{iGLO,RAM} = \left|\left|\left(T^{eq}\right)^{iGLO} - \left(T^{eq}\right)^{RAM}\right|\right| = ||3690.95\,\mathrm{K} - 3381.12\,\mathrm{K}|| = 309.83\,\mathrm{K} \tag{3.21}$$

$$\left(\Delta T^{eq}\right)_{rel}^{iGLO,RAM} = \frac{\left(\Delta T^{eq}\right)_{abs}^{iGLO,RAM}}{\left(T^{eq}\right)^{RAM}} = \boxed{9.163\,\%} \tag{3.22}$$

$$\left(\Delta s_L\right)_{abs}^{iGLO,RAM} = \left|\left|\left(s_L\right)^{iGLO} - \left(s_L\right)^{RAM}\right|\right| = ||1.2574\,\mathrm{m/s} - 1.7421\,\mathrm{m/s}|| = 0.4847\,\mathrm{m/s} \tag{3.23}$$

$$\left(\Delta s_L\right)_{rel}^{iGLO,RAM} = \frac{\left(\Delta s_L\right)_{abs}^{iGLO,RAM}}{\left(s_L\right)^{RAM}} = \boxed{27.82\,\%} \tag{3.24}$$

Now, while continuing to deal with th GDP, the black box given by Figure 3.1 will be gradually decomposed to disclose the methodology in detail.

First, a structural breakdown of the GDP is carried out. That is to say, the process can be divided into two separate subprocesses:

- adiabatic flame temperature recovery
- laminar flame speed recovery

The adiabatic flame temperature recovery originates from the idea of imposing the target temperature to the INITIAL GLOMEC equilibrium mixture and then to optimize the equilibrium species mole fractions such that the conservation of mass and fresh gas total enthalpy is not violated in a first step. In a second step, species NASA polynomial coefficients are adjusted such that an equilibrium can be computed by FINAL GLOMEC which features the species mole fractions and temperature of the optimized mixture from the first step.

The laminar flame speed is recovered by an optimization of an as low as possible number of the reaction's pre-exponential factors.

An static view of the structure of the GDP [16] is given as a block definition diagram in Figure 3.2:

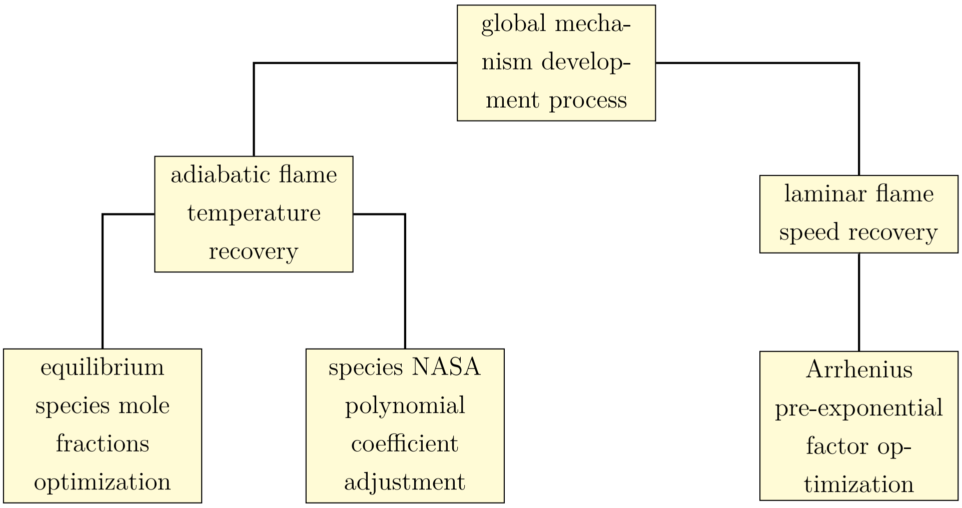

Figure 3.2: Block definition diagram of the GLOMEC DEVELOPMENT PROCESS.

3.5.1 Adiabatic Flame Temperature Recovery

3.5.1.1 Equilibrium Species Mole Fractions Optimization

Preliminary Considerations

A chemical reaction mechanism must naturally conserve mass and total enthalpy. Mass conservation can be expressed by the conservation of atoms:

$$\sum_{k=1}^{N} \psi_{ik} \cdot \delta X_k = 0 \quad , i = 1, \ldots, L \tag{3.25}$$

where ψ_{ik} denotes the number of atoms of the i_{th} element in the k_{th} species and δX_k is the deviation of the k_{th} species mole fraction in the mixture.

With regard to the total enthalpy, the total enthalpy of the fresh gas equals the total enthalpy of the gas in equilibrium. Yet, temperature and species mole fractions are significantly different. As expressed by Equation 1.18, the enthalpy of a species in a mixture at a certain temperature $h_k(T)$ comprises two fractions, namely the specific sensible enthalpy $h_{s,k}$ and the specific standard enthalpy of formation $\Delta h^0_{f,k}$. Consequently, the total specific enthalpy of a mixture is calculated as follows:

$$h_{tot}(T) = \sum_{k=1}^{N} h_{s,k} + \sum_{k=1}^{N} \Delta h^0_{f,k} = \sum_{k=1}^{N} \int_{T_{ref}}^{T} c_{p,k} dT + \sum_{k=1}^{N} \Delta h^0_{f,k} \tag{3.26}$$

To be precise, this equation reveals, that the total enthalpy of a mixture is also a function of the species mole fractions:

$$h_{tot} = f(X_k, T) \tag{3.27}$$

Introducing the species mole fractions as a new parameter to compute the total enthalpy enables the development of a method to impose an arbitrary temperature deviation on a gas mixture while preserving mass and enthalpy conservation by means of an optimal species mole fraction variation.

During the GDP, this method can be applied to impose the target adiabatic flame temperature $(T_{ad,target})^{RAM}$ on the INITIAL GLOMEC equilibrium mixture. A moderate shift of the species mole fractions is estimated to be reasonable due to the fact that global reaction mechanisms show imprecise burnt gas species mole fraction predictions in general.

Stating the Problem in General

The method, which can be deduced from the preliminary considerations, is now being stated mathematically as an optimization problem [21], [3].

> *For a given gas mixture with N species, L chemical elements, initial temperature T^0 and initial species mole fractions $\mathbf{X}_N^0$, which temperature is deviated by ΔT, find a modification of the species mole fractions $\mathbf{dX}_N^\star$ such that the total specific enthalpy of the initial gas mixture $h_{tot}(\mathbf{X}_N^0,T^0)$ best matches the total specific enthalpy of the modified gas mixture $h_{tot}(\mathbf{X}_N^0+\mathbf{dX}_N^\star,T^0+\Delta T)$, while conserving the mass of the mixture.*

$$\textit{design variable vector}: \quad \mathbf{dX}_N = \Big(\delta X_1, \quad \delta X_2, \quad \ldots, \quad \delta X_N\Big)^T \tag{3.28}$$

$$\textit{objective function}: \quad f(\mathbf{dX}_N) = \Big|\Big|h_{tot}(\mathbf{X}_N^0 + \mathbf{dX}_N,T^0 + \Delta T) - h_{tot}(\mathbf{X}_N^0,T^0)\Big|\Big| \tag{3.29}$$

$$\textit{constraints}: \quad \sum_{k=1}^{N} \psi_{ik} \cdot \delta X_k = 0 \quad , i = 1, \ldots, L \tag{3.30}$$

$$\textit{design space}: \quad \mathbf{dX}_{N,l} \leq 0 \leq \mathbf{dX}_{N,u} \tag{3.31}$$

where the subscripts l and u denote the lower respectively the upper boundaries.
In this set of equation the objective function must be minimized,

$$\underset{\mathbf{dX}_N}{min}\, f(\mathbf{dX}_N) \quad , \tag{3.32}$$

in order to compute the optimum solution $\mathbf{dX}^\star$ which writes:

$$\mathbf{dX}_N^\star = \left(\delta X_1^\star, \delta X_2^\star, \ldots, \delta X_N^\star\right)^T \tag{3.33}$$

Special attention is paid to the mass conservation constraint given by Equation 3.42. A closer examination of these equations (conservation of atoms) reveals that the N species mole fractions of a mixture cannot be varied independently. This is due to the fact, that in a chemical system with L elements and N species, certain species mole fraction deviations δX_k can be freely fixed, whereas the other deviations are computed as a function of the fixed ones. The numbers $\tilde{N}$ (index $\tilde{k}$) of freely fixable and $\hat{N}$ (index $\hat{k}$) of computed species mole freaction is defined:

$$\hat{N} = N - \tilde{N} \Leftrightarrow \tilde{N} = N - L \tag{3.34}$$

The vectors to note down the mole fraction deviations of the $\tilde{k}_{th}$ respectively the $\hat{k}_{th}$ species in the sets $\tilde{\mathbb{N}}$ respectively $\hat{\mathbb{N}}$ are defined:

$$\mathbf{d}\tilde{\mathbf{X}}_{\tilde{N}} = \left(\delta\tilde{X}_1, \ldots, \delta\tilde{X}_{\tilde{N}}\right)^T, \; \mathbf{d}\hat{\mathbf{X}}_{\hat{N}} = \left(\delta\tilde{X}_1, \ldots, \delta\tilde{X}_{\hat{N}}\right)^T \tag{3.35}$$

where $\mathbf{d}\tilde{\mathbf{X}}_{\tilde{N}}$ is introduced as *reduced design variable vector*. As a result the *actual design variable vector* $\mathbf{dX}_N$ can be formed through concatenation of $\mathbf{d}\tilde{\mathbf{X}}_{\tilde{N}}$ and $\mathbf{d}\hat{\mathbf{X}}_{\hat{N}}$:

$$\mathbf{dX}_N = \left(\mathbf{d}\tilde{\mathbf{X}}_{\tilde{N}}^T, \mathbf{d}\hat{\mathbf{X}}_{\hat{N}}^T\right)^T \tag{3.36}$$

while $\mathbf{d}\hat{\mathbf{X}}_{\hat{N}}$ and $\mathbf{d}\tilde{\mathbf{X}}_{\tilde{N}}$ are related as follows:

$$\underbrace{\begin{pmatrix} \psi_{1,1} & \psi_{1,2} & \cdots & \psi_{1,\hat{N}} \\ \psi_{2,1} & \psi_{2,2} & \cdots & \psi_{2,\hat{N}} \\ \vdots & \vdots & \ddots & \vdots \\ \psi_{L,1} & \psi_{L,2} & \cdots & \psi_{L,\hat{N}} \end{pmatrix}}_{\substack{coefficient \\ matrix \\ \mathbf{A}}} \underbrace{\begin{pmatrix} \delta\hat{X}_1 \\ \delta\hat{X}_2 \\ \vdots \\ \delta\hat{X}_{\hat{N}} \end{pmatrix}}_{\substack{computed \\ deviations \\ \mathbf{x}=\mathbf{d}\hat{\mathbf{X}}_{\tilde{N}}}} = \underbrace{\begin{pmatrix} \psi_{1,1} & \psi_{1,2} & \cdots & \psi_{1,\tilde{N}} \\ \psi_{2,1} & \psi_{2,2} & \cdots & \psi_{2,\hat{N}} \\ \vdots & \vdots & \ddots & \vdots \\ \psi_{L,1} & \psi_{L,2} & \cdots & \psi_{L,\tilde{N}} \end{pmatrix}}_{\substack{input \\ matrix \\ \mathbf{B}}} \underbrace{\begin{pmatrix} \delta\tilde{X}_1 \\ \delta\tilde{X}_2 \\ \vdots \\ \delta\tilde{X}_{\tilde{N}} \end{pmatrix}}_{\substack{fixed \\ deviations \\ \mathbf{b}=\mathbf{d}\tilde{\mathbf{X}}_{\tilde{N}}}} \tag{3.37}$$

Finally, the species mole fractions $\mathbf{X}_N^\star$ of the optimized mixture is obtained through adding the optimized species mole fration deviations $\mathbf{dX}_N^\star$ to the initial mixture species mole fractions $\mathbf{X}_N^0$, followed by normalization so that the sum of all vector elements is equal to one:

$$\boxed{\mathbf{X}_N^\star = \frac{\mathbf{X}_N^0 + \mathbf{dX}_N^\star}{\sum_{k=1}^N \left(X_k^0 + dX_k^\star\right)} \Leftrightarrow X_k^\star > 0 \; \forall \; k = 1, \ldots, N} \tag{3.38}$$

Stating the Problem for INITIAL GLOMEC
With regard to the development of FINAL GLOMEC, the equilibrium species mole fractions of INITIAL GLOMEC are intended to be modified, as the equilibrium temperature difference between INITIAL GLOMEC and RAMEC is added to the temperature of the INITIAL GLOMEC equilibrium mixture. Thus, Equations 3.28, 3.29, 3.42 become:

$$\mathbf{dX}_N = \Big(\delta X_{CH_4},\;\; \delta X_{O_2},\;\; \delta X_{H_2O},\;\; \delta X_{H_2},\;\; \delta X_{CO},\;\; \delta X_{CO_2}\Big)^T \tag{3.39}$$

$$f\Big(\mathbf{dX}_N\Big) = \\ \left\| h_{tot}\Big(\Big(\mathbf{X}_N^{eq}\Big)^{iGLO} + \mathbf{dX}_N, \Big(T^{eq}\Big)^{iGLO} + \Delta T\Big) - h_{tot}\Big(\Big(\mathbf{X}_N^{eq}\Big)^{iGLO}, \Big(T^{eq}\Big)^{iGLO}\Big) \right\| \tag{3.40}$$

where:

$$\Delta T = \Big(\Delta T^{eq}\Big)_{abs}^{RAM,iGLO} = \Big(T^{eq}\Big)^{RAM} - \Big(T^{eq}\Big)^{iGLO} \tag{3.41}$$

$$\sum_{k=1}^{N} \psi_{ik} \cdot \delta X_k = 0 \quad , i = 1, \ldots, L \tag{3.42}$$

which fully written becomes:

$$H: \;\; 4 \cdot \delta X_{CH_4} + \cancelto{0}{0 \cdot \delta X_{O_2}} + 2 \cdot \delta X_{H_2} + 2 \cdot \delta X_{H_2O} + \cancelto{0}{0 \cdot \delta X_{CO}} + \cancelto{0}{0 \cdot \delta X_{CO_2}} = 0 \tag{3.43}$$

$$H: \;\; \delta X_{CH_4} + 2 \cdot \delta X_{H_2} + 2 \cdot \delta X_{H_2O} = 0 \tag{3.44}$$

$$O: \;\; \cancelto{0}{0 \cdot \delta X_{CH_4}} + 2 \cdot \delta X_{O_2} + \cancelto{0}{o \cdot \delta X_{H_2}} + 1 \cdot \delta X_{H_2O} + 1 \cdot \delta X_{CO} + 2 \cdot \delta X_{CO_2} = 0 \tag{3.45}$$

$$O: \;\; 2 \cdot \delta X_{O_2} + 1 \cdot \delta X_{H_2O} + 1 \cdot \delta X_{CO} + 2 \cdot \delta X_{CO_2} = 0 \tag{3.46}$$

$$C: \;\; 1 \cdot \delta X_{CH_4} + \cancelto{0}{0 \cdot \delta X_{O_2}} + \cancelto{0}{2 \cdot \delta X_{H_2}} + \cancelto{0}{0 \cdot \delta X_{H_2O}} + 1 \cdot \delta X_{CO} + 1 \cdot \delta X_{CO_2} = 0 \tag{3.47}$$

$$C: \;\; 1 \cdot \delta X_{CH_4} + 1 \cdot \delta X_{CO} + 1 \cdot \delta X_{CO_2} = 0 \tag{3.48}$$

The number of species with freely fixable and computed mole fraction deviations are defined as follows:

$$\tilde{N} = N - L = 6 - 3 = 3 \tag{3.49}$$

$$\hat{N} = N - \tilde{N} = 6 - 3 = 3 \tag{3.50}$$

These $\tilde{N}$ (index $\tilde{k}$) and $\hat{N}$ (index $\hat{k}$) species are written as sets of species $\tilde{\mathbb{N}}$ respectively $\hat{\mathbb{N}}$:

$$\tilde{\mathbb{N}} = \{H_2, CO, CO_2\},\ \hat{\mathbb{N}} = \{CH_4, O_2, H_2O\} \tag{3.51}$$

Correspondingly, the vectors to note down the mole fraction deviations of the $\tilde{k}_{th}$ respectively the $\hat{k}_{th}$ species in the sets $\tilde{\mathbb{N}}$ respectively $\hat{\mathbb{N}}$ are defined as:

$$\mathbf{d\tilde{X}}_{\tilde{N}} = \left(\delta\tilde{X}_{H_2}, \delta\tilde{X}_{CO}, \delta\tilde{X}_{CO_2}\right)^T,\ \mathbf{d\hat{X}}_{\hat{N}} = \left(\delta\hat{X}_{CH_4}, \delta\hat{X}_{O_2}, \delta\hat{X}_{H_2O}\right)^T \tag{3.52}$$

In order to obtain the still unknown computed species mole fraction deviations $\mathbf{d\hat{X}}_{\hat{\mathbb{N}}}$ from the fixed ones $\mathbf{d\tilde{X}}_{\tilde{\mathbb{N}}}$, Equations 3.44, 3.46 and 3.48 are transformed into the subsequent matrix notation according to Equation 3.37:

$$\begin{pmatrix} 4 & 0 & 2 \\ 0 & 2 & 1 \\ 1 & 0 & 0 \end{pmatrix} \begin{pmatrix} \delta\hat{X}_{CH_4} \\ \delta\hat{X}_{O_2} \\ \delta\hat{X}_{H_2O} \end{pmatrix} = \begin{pmatrix} -2 & 0 & 0 \\ 0 & -1 & -2 \\ 0 & -1 & -1 \end{pmatrix} \begin{pmatrix} \delta\tilde{X}_{H_2} \\ \delta\tilde{X}_{CO} \\ \delta\tilde{X}_{CO_2} \end{pmatrix} \tag{3.53}$$

Developing a Technique to Solve the Problem

The statement of the optimization problem is succeeded by the choice of a technique to solve it. In this work it is numerically solved leveraging an algorithm which can be classified as an enumerative and full-factorial one from a methodical point of view [3]. In this approach, all possible combinations of the reduced design variables in the design space are analyzed. The technique to discretize the design space is illustrated hereafter.

As a repetition, the reduced design variable vector $\mathbf{d\tilde{X}}$ describes the deviation of the mole fraction of the species contained by the set $\tilde{\mathbb{N}}$ from the corresponding initial mole fractions $\mathbf{X}^0$. In order to avoid a solution suggesting a very strong deviation from the initial mole fractions the design space is required to be limited by lower and upper boundaries $\mathbf{d\tilde{X}}_l$ and $\mathbf{d\tilde{X}}_u$ on the one hand:

$$\mathbf{d\tilde{X}}_{\tilde{N},l} = \begin{pmatrix} \delta\tilde{X}_{1,l} \\ \delta\tilde{X}_{2,l} \\ \cdots \\ \delta\tilde{X}_{\tilde{N},l} \end{pmatrix} = \begin{pmatrix} -\xi_1 \cdot \tilde{X}_1^0 \\ -\xi_2 \cdot \tilde{X}_2^0 \\ \cdots \\ -\xi_{\tilde{N}} \cdot \tilde{X}_{\tilde{N}}^0 \end{pmatrix}, \; \mathbf{d\tilde{X}}_{\tilde{N},u} = \begin{pmatrix} \delta\tilde{X}_{1,u} \\ \delta X_{2,u} \\ \cdots \\ \delta\tilde{X}_{\tilde{N},u} \end{pmatrix} = \begin{pmatrix} \xi_1 \cdot \tilde{X}_1^0 \\ \xi_2 \cdot \tilde{X}_2^0 \\ \cdots \\ \xi_{\tilde{N}} \cdot \tilde{X}_{\tilde{N}}^0 \end{pmatrix} \tag{3.54}$$

where $\xi_{\tilde{k}}$ is a factor to dimension the elements of the vectors $\mathbf{d\tilde{X}}_{\tilde{N},l}$ and $\mathbf{d\tilde{X}}_{\tilde{N},u}$.
On the other hand, a discretisation of the allowed range has to be performed with the goals to both prohibit an explosion of the computational and to make sure that a solution is found. Equistant points are defined in the ranges limited by the boundaries $\mathbf{d\tilde{X}}_l$ and $\mathbf{d\tilde{X}}_u$. The step size is defined as follows:

$$w_{step} = \zeta_{\tilde{k}} \tilde{X}_{\tilde{k}}^0 \tag{3.55}$$

where $\zeta_{\tilde{k}}$ is again a dimensiong factor. Note that $\xi_{\tilde{k}}$ must be an integer multiple of $\zeta_{\tilde{k}}$. The total number of points $O_{\tilde{k}}$ for each $\tilde{k}_{th}$ species can be computed like this:

$$O_{\tilde{k}} = \frac{\xi_{\tilde{k}} \cdot 2}{\zeta_{\tilde{k}}} + 1 \tag{3.56}$$

To better comprehend the above descriptions, also see the Figure 3.3 below:

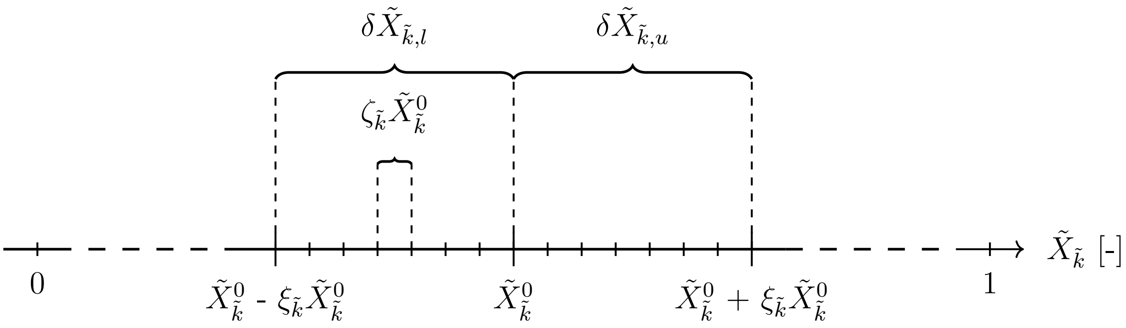

Figure 3.3: Sketch of design space discretization.

In the end, the discretized design space allows for the construction of a set of reduced design variable combinations $\mathbb{Z}_{\mathbf{d\tilde{X}}}$ counting $O_{\mathbb{Z}}$ combinations (index m):

$$\mathbb{Z}_{\mathbf{d\tilde{X}}} = \{\mathbf{d\tilde{X}}^1_{\tilde{N}}, \ldots, \mathbf{d\tilde{X}}^O_{\tilde{N}}\} \tag{3.57}$$

$$O_{\mathbb{Z}} = \prod_{\tilde{k}=1}^{\tilde{N}} O_{\tilde{k}} \tag{3.58}$$

The m_{th} element of $\mathbb{Z}$ is written:

$$\mathbf{d\tilde{X}}^m_{\tilde{N}} = \left(\delta\tilde{X}^m_1, \ldots, \delta\tilde{X}^m_{\tilde{N}}\right)^T \tag{3.59}$$

The algorithm performs $O_{\mathbb{Z}}$ iterations. In the m_{th} iteration the combination $\mathbf{d\tilde{X}}^m_{\tilde{N}}$ is selected from $\mathbb{Z}$ and used to compute $\mathbf{d\hat{X}}^m_{\hat{N}}$ and $\mathbf{dX}^m_N$ consecutively. For this computation (solving Equation 3.37), a unique solution is obtained via the Gaussian elimination method [21]. Then, the objective function $f(\mathbf{dX}^m_N)$ can be evaluated. The species mole fraction deviation $\mathbf{dX}^m_N$ is the optimum one $\mathbf{dX}^\star_N$ if the following criterion is fulfilled, that is to say when it is identified to produce the minimum value of the objective function:

$$\mathbf{dX}^m_N = \mathbf{dX}^\star_N \iff ||f(\mathbf{dX}^m_N)|| < ||f(\mathbf{dX}^r_N)|| \;\; \forall\, r = 1, \ldots, m-1, m+1, \ldots, O_{\mathbb{Z}} \tag{3.60}$$

Conclusion

To conclude, it has been shown how the species mole fraction optimization problem is stated in general as well as for INITIAL GLOMEC and which methods/strategies/criteria are chosen to solve it in this work. The resulting algorithm is depicted in Figure 3.4.

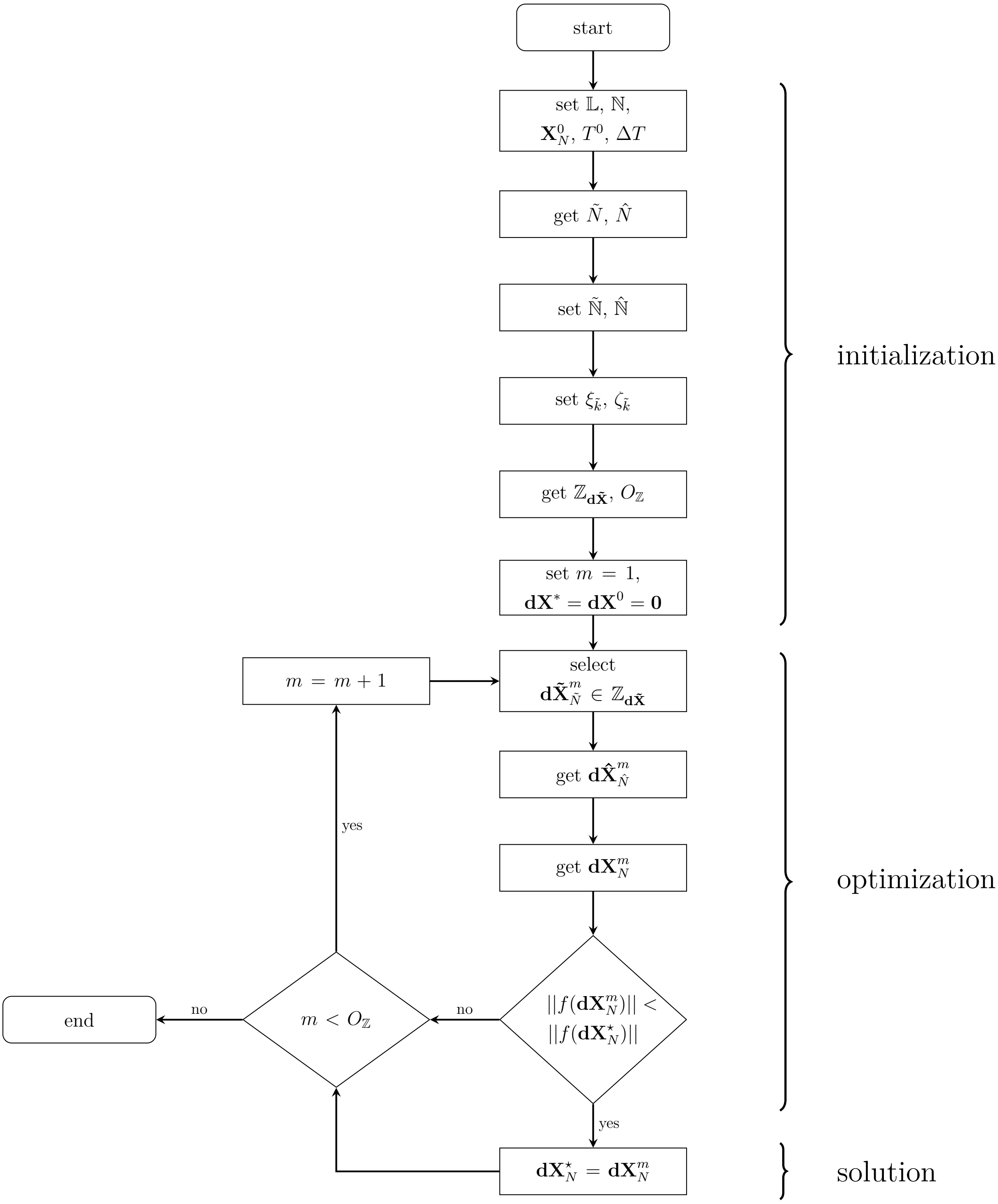

Figure 3.4: Species mole fraction optimization algorithm.

Applying the Technique to INITIAL GLOMEC

This very last section of chapter 3.3.1.1 is a full and compact description of the practical application of this algorithm to INITIAL GLOMEC:

1. **Initialisation**

Problem Initialization	**specification**	**Unit**
Elements $\mathbb{L}$	H, C, O	[-]
Species $\mathbb{N}$	CH_4, O_2, H_2O, H_2, CO, CO_2	[-]
Free Species $\tilde{\mathbb{N}}$	H_2, CO, CO_2	[-]
Computed Species $\hat{\mathbb{N}}$	CH_4, O_2, H_2O	[-]
Initial Temperature T^0	3690.95	[K]
Temperature Deviation $\left(\Delta T^{eq}\right)^{RAM,iGLO}_{abs}$	-309.83	[K]
$X^0_{CH_4}$	1.22×10^{-10}	[-]
$X^0_{O_2}$	4.27×10^{-2}	[-]
$X^0_{H_2O}$	4.75×10^{-1}	[-]
$X^0_{H_2}$	1.63×10^{-1}	[-]
X^0_{CO}	2.38×10^{-1}	[-]
$X^0_{CO_2}$	8.11×10^{-2}	[-]
Solver Configuration	**Specification**	**Unit**
ξ_{H_2}	15.0	[%]
ξ_{CO}	15.0	[%]
ξ_{CO_2}	15.0	[%]
ζ_{H_2}	1.25	[%]
ζ_{CO}	1.25	[%]
ζ_{CO_2}	1.25	[%]
$O_{\mathbb{Z}}$	15624	[-]

Table 3.6: Initialization of GDP species mole fraction optimization.

2. **Optimization**

The optimization comprises the solving of Equation System 3.53 for each $\mathbf{d\tilde{X}}^m_{\tilde{N}}$ to obtain $\mathbf{d\hat{X}}^m_{\hat{N}}$ and then $\mathbf{dX}^m_N$. As a consequence, the objective function can be evaluted and the result is checked against the criterion (Equation 3.60) deciding whether $\mathbf{dX}^m_{N_{iGLO}}$ is better than $\mathbf{dX}^{m-1}_N$ of the prior iteration at minimizing the objective function. As an example, the evaluation of the objective function with $\mathbf{dX}^0_{GLO} = \mathbf{0}$ is demonstrated (note that the obtained value is the initial absolute enthalpy error due to the deviation of the temperature ΔT):

$$f(\mathbf{dX}^0) = || -1.973 \times 10^6 J/kg - (-1.221 \times 10^6 J/kg)|| = 0.752 \times 10^6 J/kg \tag{3.61}$$

Thus, the initial relative enthalpy error $\Delta h^0_{tot,rel}$ is as follows:

$$\left(\Delta h^o_{tot}\right)_{rel} = \left\| \frac{f\left(\mathbf{dX}^0\right)}{h_{tot}\left(\left(\mathbf{X}^{eq}\right)^{iGLO}, \left(T^{eq}\right)^{iGLO}\right)} \right\| = 61.59\,\% \tag{3.62}$$

3. Solution

The algorithm finds the solution with the minimum total enthalpy error in the specified and discretized design space. The subsequent table sums up the total enthalpy error, the temperature and the species mole fractions of the solution mixture:

Solution Properties	**Specification**	**Unit**
enthalpy $h^{\star}_{tot}$	-1.221 × 10^{6}	[J/kg]
rel. enthalpy error $\left(\Delta h^{\star}_{tot}\right)_{rel}$	6.1344 × 10^{-5}	[-]
Solution Temperature $T^{\star}$	3381.12	[K]
$dX^{\star}_{H_2}$	8.75	[%]
$dX^{\star}_{CO}$	-6.25	[%]
$dX^{\star}_{CO_2}$	1.25	[%]
$X^{\star}_{CH_4}$	1.38 × 10^{-2}	[-]
$X^{\star}_{O_2}$	7.75 × 10^{-2}	[-]
$X^{\star}_{H_2O}$	4.30 × 10^{-1}	[-]
$X^{\star}_{H_2}$	1.76 × 10^{-1}	[-]
$X^{\star}_{CO}$	2.37 × 10^{-1}	[-]
$X^{\star}_{CO_2}$	6.58 × 10^{-2}	[-]

Table 3.7: Solution of GDP species mole fraction optimization.

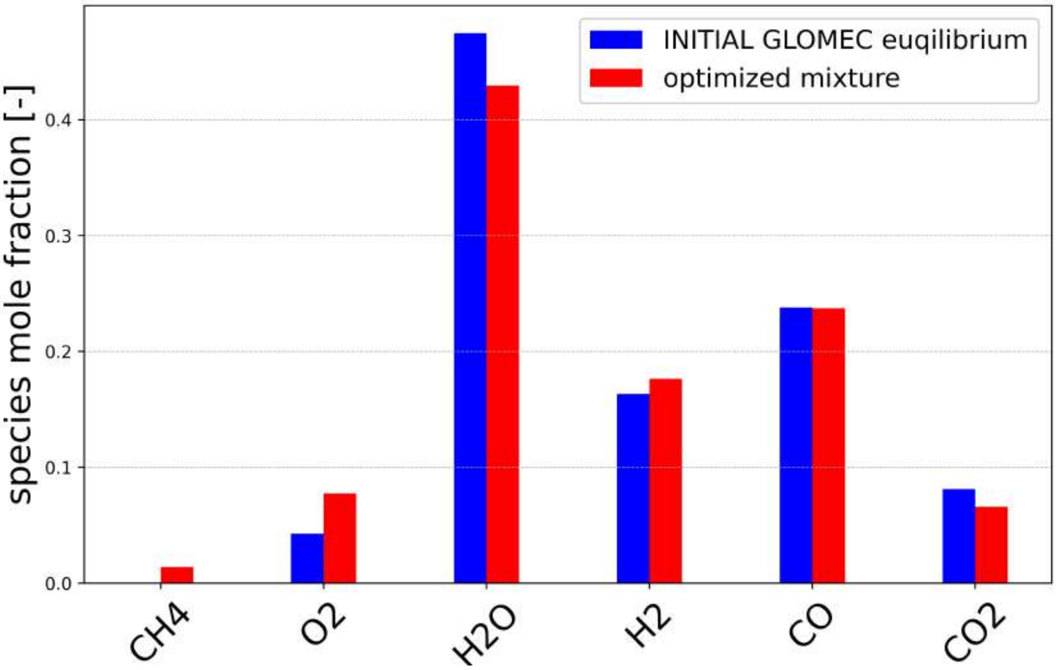

Figure 3.5: Bar plot to compare INITIAL GLOMEC equilibrium and optimized mixture species mole fractions.

3.5.1.2 Species NASA Polynomial Coefficient Adjustment

Preliminary Considerations

So far, temperature, pressure, mole fractions and enthalpy have been the only quantities to describe the thermodynamic states in this work. Now, another quantity, namely the Gibbs free energy G, is introduced as a thermodynamic potential, which is suitable to describe systems with fixed temperature and pressure [41]. For a system with N species it writes:

$$G(T,P,n_k) = H - TS \tag{3.63}$$

$$G(T,P,n_k) = \sum_{k=1}^{N} n_k \mu_k = \sum_{k=1}^{N} n_k G_{m,k} \tag{3.64}$$

where H is the enthalpy, T is the temperature, S is the entropy, n_k is the number of particles of species k and μ_k is the chemical potential respectively the partial molar Gibbs free energy of species k. The Gibbs free energy can also be expressed as molar Gibbs free energy:

$$G_m(T,P,X_k) = H_m - TS_m \tag{3.65}$$

$$G_m(T,P,X_k) = \sum_{k=1}^{N} X_k \mu_k = \sum_{k=1}^{N} X_k G_{m,k} \tag{3.66}$$

Furthermore, the Gibbs free energy is used as a criterion indicating whether a thermodynamic system has reached equilibrium. In equilibrium, the total differential of the Gibbs free energy must be equal to zero (here formulations for the molar Gibbs free energy are given):

$$dG_m^{eq} = \left(\frac{\partial G_m}{\partial T}\right) dT + \left(\frac{\partial G_m}{\partial P}\right) dP + \left(\frac{\partial G_m}{\partial X_k}\right) dX_k \overset{!}{=} 0 \tag{3.67}$$

$$dG_m^{eq} = \sum_{k=1}^{N} X_k d\mu_k + \sum_{k=1}^{N} \mu_k dX_k \overset{!}{=} 0 \tag{3.68}$$

Moving an Equilibrium in General

In the following, the known equilibrium computed by reaction mechanism I featuring $(T^{eq})^I$ and $(X_k^{eq})^I$ is intended to be moved such that a target temperature $T^\star$ and target species mole fractions $X_k^\star$ are reached (constant pressure and total enthalpy). Achieving this results in a modification of the reaction mechanism I so that a modified one, namely reaction mechanism II is obtained. Thus is it is demanded:

$$\boxed{\left(\left(T^{eq}\right)^{II} \overset{!}{=} T^\star \neq \left(T^{eq}\right)^{I}\right)\Bigg|_{HP}} \tag{3.69}$$

$$\boxed{\left(\left(X_k^{eq}\right)^{II} \overset{!}{=} X_k^\star \neq \left(X_k^{eq}\right)^{I}\right)\Bigg|_{HP}} \tag{3.70}$$

The technique proposed in this work, is based on the idea to modify the computation of the reference-state species entropies S_k° through linking them with the species chemical potentials μ_k. The chemical potential can be directly linked to the chemical equilibrium [36].

On the one hand, for a perfect gas, the chemical potential μ_k of species k is calculated as follows:

$$\mu_k(T,P,X_k) = \mu_k^\circ(T,P) + RTln(a_k) \tag{3.71}$$

where a_k is the activity of species k and $\mu_k^\circ(T,P)$ is the standard chemical potential of species k being dependent on temperature and pressure, but not on the species mole fractions. Yet, due to the fact that CANTERA is capable of computing the species chemical potentials directly, no further examination of the species chemical potentials is necessary. The only thing which is worth being memorized is, that they are a function of temperature, pressure and species mole fractions.

On the other hand, assuming an ideal, constant partial molar volume solution mixture and pure species phases, the molar entropy S_m becomes:

$$S_m(T,P,X_k) = \sum_{k=1}^{N} X_k S_k^\circ(T) - R\sum_{k=1}^{N} X_k ln(X_k) \tag{3.72}$$

where the reference-state species entropies s_k° can be computeted with the NASA 7-coefficient polynomial given by Equation 3.9:

$$S_k^\circ(T) = R\Bigg(\underbrace{a_{1,k}ln(T) + a_{2,k}T + \frac{a_{3,k}}{2}T^2 + \frac{a_{4,k}}{3}T^3 + \frac{a_{5,k}}{4}T^4}_{\equiv C_k(T)} + a_{7,k}\Bigg) \tag{3.73}$$

A comparison of this NASA polynomial with the two other ones given by Equations 3.8 and 3.7 yields, that the coefficient $a_{7,k}$ is solely existent in the polynomial dedicated to the entropy. Thus, this coefficient is the only one which is appropriate for a modification of the entropy without having an impact on other system quantities. Note, that the Nasa polynomial coefficients are easily modifyable, as they are explicitly listed in the GDP inputs.

Therefore, merging all terms related to the coefficients $a_{1,k}, \dots, a_{5,k}$ (calling it $C_k(T)$ from now) and simultaneously freeing the coefficient $a_{7,k}$ as another variable parameter, Equation 3.73 can be turned into:

$$s_k^\circ(T,a_{7,k}) = R\Big(C_k(T) + a_{7,k}\Big) \tag{3.74}$$

In a next step, a substituion of S_m in Equation 3.65 with Equations 3.72 and 3.74 yields:

$$G_m(T,P,X_k,a_{7,k}) = H_m - T\left[\sum_{k=1}^{N} X_k R\Big(C_k(T) + a_{7,k}\Big) - R\sum_{k=1}^{N} X_k ln(X_k)\right] \tag{3.75}$$

Writing it out, the molar Gibbs free energy G_m becomes finally:

$$G_m(T,P,X_k,a_{7,k}) = H_m - RT\sum_{k=1}^{N} X_k C_k(T) - RT\sum_{k=1}^{N} X_k a_{7,k} + RT\sum_{k=1}^{N} X_k ln(X_k) \tag{3.76}$$

The examination of equilibria additionally allows for the assumption, that temperature, pressure and species mole fractions are fixed. Hence, extending the total differential (Equation 3.67) of the molar Gibbs free energy by a term devoted to the coefficients $a_{7,k}$ and simplifications yields:

$$dG_m^{eq} = \cancelto{T fixed}{\left(\frac{\partial G_m}{\partial T}\right)} dT + \cancelto{P fixed}{\left(\frac{\partial G_m}{\partial P}\right)} dP + \cancelto{X_k fixed}{\left(\frac{\partial G_m}{\partial X_k}\right)} dX_k + \left(\frac{\partial G_m}{\partial a_{7,k}}\right) da_{7,k} \overset{!}{=} 0 \tag{3.77}$$

$$dG_m^{eq} = \left(\frac{\partial G_m}{\partial a_{7,k}}\right) da_{7,k} \overset{!}{=} 0 \tag{3.78}$$

Moreover, Equation 3.68 can be simplified:

$$dG_m^{eq} = \sum_{k=1}^{N} X_k d\mu_k + \cancelto{X_k fixed}{\sum_{k=1}^{N} \mu_k} dX_k \overset{!}{=} 0 \tag{3.79}$$

$$dG_m^{eq} = \sum_{k=1}^{N} X_k d\mu_k \overset{!}{=} 0 \tag{3.80}$$

Afterwards Equations 3.78 and 3.80 can be set equal:

$$\left(\frac{\partial G_m}{\partial a_{7,k}}\right) da_{7,k} = \sum_{k=1}^{N} X_k d\mu_k \tag{3.81}$$

For an ideal, constant partial molar volume solution mixture and pure species phases Equation 3.81 becomes (by creating the partial derivate of G_m with respect to $a_{7,k}$):

$$-RT \sum_{k=1}^{N} X_k da_{7,k} = \sum_{k=1}^{N} X_k d\mu_k \tag{3.82}$$

Equation 3.82 is now written for only one species k and subsequently simplified as well as rearranged:

$$-RT \cancelto{}{X_k} da_{7,k} = \cancelto{}{X_k} d\mu_k \tag{3.83}$$

$$da_{7,k} = -\frac{1}{RT} d\mu_k \tag{3.84}$$

Finally, the integration of Equation 3.84 delivers an equation to compute which value needs to be added to the species coefficients $(a_{7,k})^I$ in order to obtain $(a_{7,k})^{II}$. The equilibrium inherent to this modified mechanism features the target temperature $T^\star$ and the target species mole fractions $X_k^\star$, thus fulfilling the demands stated by Equations 3.69 and 3.70.

$$\left(\Delta a_{7,k}\right)_{abs}^{I,II} = -\frac{1}{R} \int_{(eq)^I}^{(\star)^I} \frac{1}{T} d\mu_k = -\frac{1}{R} \left[\frac{1}{T}\mu_k\right]_{(eq)^I}^{(\star)^I} = -\frac{1}{R} \left(\frac{\left(\mu_k^\star\right)^I}{T^\star} - \frac{\left(\mu_k^{eq}\right)^I}{\left(T^{eq}\right)^I} \right) \tag{3.85}$$

$$\boxed{\left(\Delta a_{7,k}\right)_{abs}^{I,II} = \left(a_{7,k}\right)^I - \left(a_{7,k}\right)^{II} = \left(\frac{\left(\mu_k^{eq}\right)^I}{R\left(T^{eq}\right)^I} - \frac{\left(\mu_k^\star\right)^I}{RT^\star} \right)} \tag{3.86}$$

To finish up these theoretical explanations, the transitions from different thermodynamic states to other ones on account of equilibrium computations using mechanisms I and II are illustrated in a state diagram (cf. Figure 3.6):

- using mechanism I, the computation of an equilibrium starting from the fresh gas, the state featuring the target properties or the mechanism I equilibrium always leads to a transition to the mechanism I equilibrium
- using mechanism II, the computation of an equilibrium starting from the fresh gas, the state featuring the target properties or the mechanism I equilibrium always leads to a transition to the state featuring the target properties

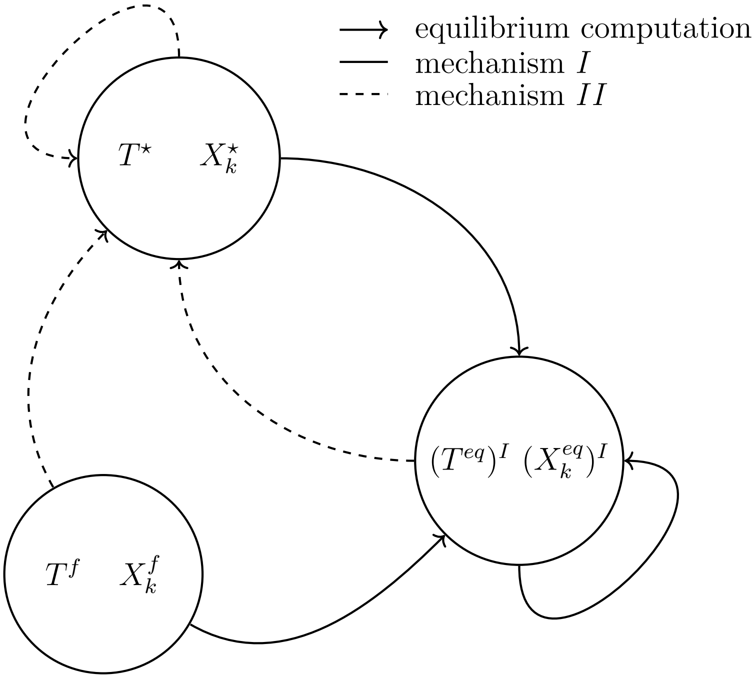

Figure 3.6: Equilibrium computations using mechanisms I and II.

Moving the Equilibrium of INITIAL GLOMEC

Due to the fact that the optimized mixture has a certain total enthalpy error coming from the species mole fraction optimization process, the computation of $(\Delta a_{7,k})^{iGLO,fGLO}_{abs}$ becomes:

$$\boxed{\left(\Delta a_{7,k}\right)^{iGLO,fGLO}_{abs,prac} = \left(\frac{\left(\mu_k^{eq}\right)^{iGLO}}{R\left(T^{eq}\right)^{iGLO}} - \frac{\left(\mu_k^{\star}\right)^{iGLO}}{RT^{\star}} \right) \Bigg|_{h_{tot}=h^{\star}_{tot}}} \tag{3.87}$$

Applying Equation 3.87 to all N species yields the following differences of the coefficients $a_{7,k}$ when comparing INITIAL GLOMEC and FINAL GLOMEC.

	Value	**Unit**
$(\Delta a_{7,CH_4})^{iGLO,fGLO}_{abs,prac}$	19.2875	[-]
$(\Delta a_{7,O_2})^{iGLO,fGLO}_{abs,prac}$	0.9692	[-]
$(\Delta a_{7,H_2O})^{iGLO,fGLO}_{abs,prac}$	-0.3549	[-]
$(\Delta a_{7,H2})^{iGLO,fGLO}_{abs,prac}$	0.4099	[-]
$(\Delta a_{7,CO})^{iGLO,fGLO}_{abs,prac}$	0.0589	[-]
$(\Delta a_{7,CO2})^{iGLO,fGLO}_{abs,prac}$	-0.8409	[-]

Table 3.8: $a_{7,k}$ modifications based on equilibriua computed from fresh gas or the optimized $X_k^{\star}$ and $T^{\star}$.

Finally, an equilibrium computation starting from the fresh gas and using both the updated coefficients $(a_{7,k})^{fGLO}$ delivers:

$$\left(T^{eq}\right)^{fGLO} = 3380.92\,\mathrm{K} \tag{3.88}$$

Thus, the absolute and relative errors of the adiabatic flame temperature computed by FINAL GLOMEC can be determined:

$$\left(\Delta T^{eq}\right)^{fGLO,RAM}_{abs,prac} = \left|\left|\left(T^{eq}\right)^{fGLO}_{prac} - \left(T^{eq}\right)^{RAM}\right|\right| = ||3380.92\,\mathrm{K} - 3381.12\,\mathrm{K}|| = \boxed{0.2\,\mathrm{K}} \tag{3.89}$$

$$\left(\Delta T^{eq}\right)^{fGLO,RAM}_{rel} = \frac{\left(\Delta T^{eq}\right)^{fGLO,RAM}_{abs,prac}}{\left(T^{eq}\right)^{RAM}} = \boxed{5.915 \times 10^{-5}} \tag{3.90}$$

It can be concluded, that the recovery of the adiabatic flame temperature is very accurate using the demonstrated technique.

3.5.2 Laminar Flame Speed Recovery

The second target quantitiy, namely the laminar flame speed, is rovered by a modification of the Arrhenius pre-exponential factors $A_{f,j}$ (reactions 3.11 and 3.13) aka block "Arrhenius pre-exponential factor optimization" in the block definition diagram.

3.5.2.1 Arrhenius Pre-Exponential Factor Optimization

In this work no special algorithm is employed to find the optimized values for the pre-exponential factors. Instead, via trial and error, the following modifications of the INITIAL GLOMEC pre-exponential factors have been found in order to make the laminar flame speed computed with FINAL GLOMEC match with the ones computed by RAMEC:

$$\left(A_{f,1}\right)^{fGLO} = 0.947 \cdot \left(A_{f,1}\right)^{iGLO} \tag{3.91}$$

$$\left(A_{f,3}\right)^{fGLO} = 0.99 \cdot \left(A_{f,3}\right)^{iGLO} \tag{3.92}$$

With these modifications, the absolute and relative errors of the laminar flame speed obtained from FINAL GLOMEC can be computed:

$$\left(\Delta s_L\right)_{abs}^{iGLO,RAM} = \left|\left|\left(s_L\right)^{fGLO} - \left(s_L\right)^{RAM}\right|\right| = ||1.7423\,\mathrm{m/s} - 1.7421\,\mathrm{m/s}|| = \boxed{0.0002\,\mathrm{m/s}} \tag{3.93}$$

$$\left(\Delta s_L\right)_{rel}^{iGLO,RAM} = \frac{\left(\Delta s_L\right)_{abs}^{iGLO,RAM}}{\left(s_L\right)^{RAM}} = \boxed{1.148 \times 10^{-4}} \tag{3.94}$$

To put it in a nutshell, very sligth modifications of the Arrhenius pre-exponential factors of two reactions lead to recovery of the laminar flame speed at the operating point. See the $\star.cti$ files of INITIAL GLOMEC and FINAL GLOMEC in the appendix to see the absolute numbers of the kinetics parameters.

E. GLOMEC Arrhenius parameters

Extracted from [Strauss, 2020], on courtesy of Julian Strauss.

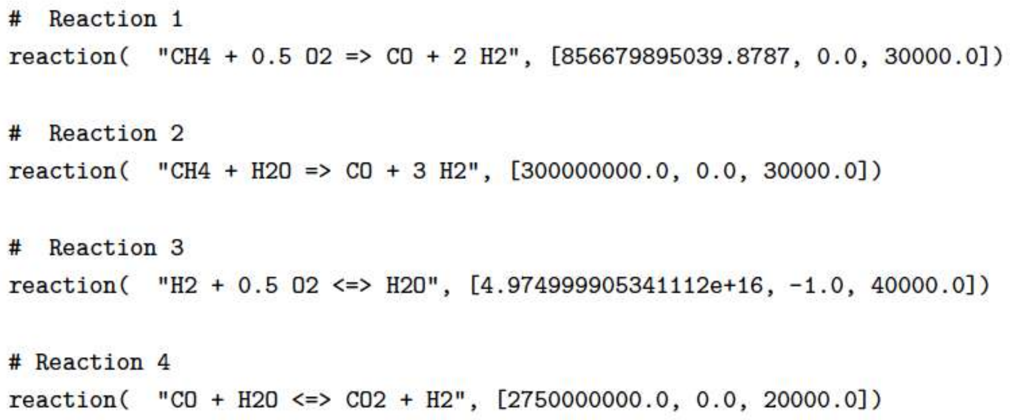

```
#  Reaction 1
reaction(  "CH4 + 0.5 O2 => CO + 2 H2", [856679895039.8787, 0.0, 30000.0])

#  Reaction 2
reaction(  "CH4 + H2O => CO + 3 H2", [300000000.0, 0.0, 30000.0])

#  Reaction 3
reaction(  "H2 + 0.5 O2 <=> H2O", [4.974999905341112e+16, -1.0, 40000.0])

# Reaction 4
reaction(  "CO + H2O <=> CO2 + H2", [2750000000.0, 0.0, 20000.0])
```

Figure 7: Chemical reactions in the GLOMEC mechanism and their Arrhenius parameters, from left to right in the brackets and following notation of Eq. 2.27: A_j, β_j, E_j.

F. Paper published in *Acta Astronautica*

As the paper was split in three parts along the manuscript (Sections 4.3.1, 4.4.1 and 6.3.2), the full paper is found below.

Acta Astronautica 190 (2022) 98–111

Contents lists available at ScienceDirect

Acta Astronautica

journal homepage: www.elsevier.com/locate/actaastro

Research Paper

Chemical modeling for methane oxy-combustion in Liquid Rocket Engines

Simon Blanchard [a,b,*,1], Quentin Cazères [b,2], Bénédicte Cuenot [b,3]

[a] National Centre for Space Studies (CNES), 52 rue Jacques Hillairet, Paris Cedex 75612, France
[b] European Center for Research and Advanced Training in Scientific Computation (CERFACS), 42 avenue Gaspard Coriolis, Toulouse Cedex 01 31057, France

ARTICLE INFO

Keywords:
Large Eddy Simulation
Methane oxy-combustion
Chemical kinetics
Implicitation
Liquid Rocket Engine

ABSTRACT

Methane–oxygen burning is considered for many future rocket engines for practicality and cost reasons. As this combustion is slower than hydrogen–oxygen, flame ignition and stability may be more difficult to obtain. To address these questions, numerical simulation with realistic chemistry is appropriate. However the high pressure and turbulence intensity encountered in rocket engines enhance drastically the stiffness of methane oxy-combustion. In this work, Analytically Reduced Chemistry (ARC) is proposed for accurate chemistry description at a reasonable computational cost. An ARC scheme is specifically derived for typical rocket engine conditions. It is validated by comparison with its parent skeletal mechanism on a series of laminar flames. Then the numerical stiffness of chemistry is overcome with an original approach for time integration, allowing to run simulations close to the acoustic time step whatever the chemical stiffness. It is demonstrated on laminar cases that the flame structure is well preserved, and that numerical stability is ensured while decreasing significantly the computational cost. The performance of ARC with the fast time integration method is finally demonstrated in a 3D Large-Eddy Simulation of a lab-scale Liquid Rocket Engine combustion chamber, where a detailed flame analysis is conducted.

1. Introduction

The space launchers sector currently knows a noticeable evolution towards a competitive commercial market, with a price race initiated by new private actors. The cost of access to space decreases, and the historical actors, mainly governmental space agencies, are challenged to propose cheaper but still reliable solutions for commercial launches. This impacts propulsion systems, for which the concept of reusability [1] is pushed forward. For Liquid Rocket Engines (LRE), hydrogen is replaced by methane, which brings the advantages of high density, good specific impulse and lower cost for production and storage, largely compensating for a lower mass energy [2,3]. Several projects of methane/oxygen LRE for commercial launches as well as for deep space missions have appeared throughout the world, e.g., Prometheus (CNES/ArianeGroup), Raptor (SpaceX), or the Liquid Natural Gas (LNG) family (JAXA/IHI). Nevertheless, except for some early research in the 1970s–1990s [4], most studies of methane oxy-combustion in rocket engine conditions are quite recent and many questions require further investigation [5].

In the past decade, Large Eddy Simulation (LES) has been successfully applied to LRE to predict the flame, its ignition, wall heat transfer or thermo-acoustic instabilities [6–8]. Most studies considered hydrogen oxy-combustion, which is close to the infinitely fast chemistry limit and may be treated as such without critical loss of accuracy [9]. The situation is different with methane oxy-combustion, whose slower chemistry impacts combustion phenomena [10]. It is therefore necessary to include in LES an accurate, but still cost-effective description of the combustion kinetics. There exists a wide range of kinetic schemes, from fully detailed mechanisms, containing hundreds to thousands species and reactions, to global schemes which only contain few species and one to four reactions. As each chemical species requires to solve one additional transport equation in the LES code, the direct integration of detailed mechanisms is computationally unaffordable in 3D simulations. Even the so-called skeletal mechanisms which are much reduced compared to detailed ones, stay too large for LES. On the contrary, one- or two-steps kinetic schemes are very fast but their lack of precision is critical for many aspects of the flame.

As an alternative, the concept of Analytically Reduced Chemistry (ARC) introduced some decades ago [11], may be viewed as a good

---

[*] Corresponding author at: European Center for Research and Advanced Training in Scientific Computation (CERFACS), 42 avenue Gaspard Coriolis, Toulouse Cedex 01 31057, France.

E-mail address: blanchard@cerfacs.fr (S. Blanchard).

[1] Researcher, Launchers Directorate (CNES)/CFD team (CERFACS).
[2] Researcher, CFD team, CERFACS.
[3] Senior researcher, head of CFD team, CERFACS.

https://doi.org/10.1016/j.actaastro.2021.09.039
Received 29 June 2021; Received in revised form 20 September 2021; Accepted 25 September 2021

Nomenclature

Latin characters

A	sum of destruction source terms (scaled by c), s^{-1}
a	strain rate, s^{-1}
B	sum of creation source terms, kg/m^3/s
c	mass concentration, kg/m^3
D	diffusion coefficient m^2/s
D_{th}	thermal diffusion coefficient m^2/s
dm	mass excess/loss, kg
H	length of the counterflow laminar diffusion flame domain, m
J	diffusive flux, kg/m^2/s
N_e	number of elements
N_s	number of species
P	pressure, *bar*
$\dot{r}$	mass reaction rate, kg/m^3/s
S	strain rate tensor, s^{-1}
T	temperature, K
u	flow velocity, m/s
u_a	acoustic velocity, m/s
Y	mass fraction
y^+	normalized wall distance
Z	Bilger mixture fraction

Greek characters

Δx	characteristic mesh size, *m*
Δt	simulation time step, *s*
Δt_{chem}	explicit integration chemical time step, *s*
Δt_{CFL}	CFL time step, *s*
δ_{ij}	Kronecker symbol
δ_{th}	thermal flame thickness, *m*
ζ	Takeno index
κ	ratio between the CFL and the simulation time step
ν', ν''	reactants and products stoichiometric coefficients
ρ	density, kg/m^3
τ	viscous stress tensor, N/m^2
τ_{chem}	characteristic chemical time scale, *s*
χ	scalar dissipation rate, s^{-1}
$\dot{\omega}$	mass chemical source term, kg/m^3/s
$\dot{\omega}_T$	total (integral) of heat release rate, W/m^3

Subscripts

$CLASS$	quantity computed with classical integration method
$EXPO$	quantity computed with exponential integration method
e	element (atom)
F	fuel
j	reaction index
k	species index
$mean$	mean quantity
O	oxidizer
st	stoichiometric quantity
V	integration volume

Superscripts

$corr$	corrected quantity
n	current iteration
$n+1$	next iteration

Abbreviations

ARC	Analytical Reduced Chemistry
ARCANE	Analytical Reduced Chemistry: Automatic, Nice and Efficient
AVBP	A Very Big Project
CERFACS	Centre Européen de Recherche et de Formation Avancée en Calcul Scientifique
CFD	Computational Fluid Dynamics
CFL	Courant–Friedrichs–Lewy
CNES	Centre National d'Études Spatiales
CONFORTH	CONception et Fabrication d'un bOîtier Refroidi et d'une Tuyère – Haut rapport de mélange
DRGEP	Direct Relation Graph with Error Propagation
HPC	High Performance Computing
JAXA	Japan Aerospace Exploration Agency
LES	Large Eddy Simulation
LOI	Level Of Importance
LRE	Liquid Rocket Engine
NRI	Non-Reflective Inlets
NSCBC	Navier–Stokes Characteristic Boundary Conditions
ONERA	Office National d'Études et de Recherches Aérospatiales
QSSA	Quasi Steady State Assumption
RAMEC	RAM accelerator MEChanism

compromise between complexity and accuracy. An ARC scheme derives from a skeletal mechanism, in which only the species and reactions required to correctly predict flame quantities, such as total heat release rate, adiabatic flame temperature, or flame speed, are kept. ARC then introduces the Quasi Steady State Assumption (QSSA) [12] for the fastest species that are immediately consumed after production, and introduce strong numerical stiffness due to their very short timescale. These QSS species are kept in the chemical scheme but they are not computed with a transport equation: their concentration is calculated from algebraic relations issuing from the condition of zero net chemical source term. The ARC approach has already shown promising results on diverse applications [13]. Also, compared to other chemistry reduction approaches such as neural networks [14,15] or virtual chemistry concept [16,17], ARC has the advantage to keep true reaction pathways. Thus, ARCs are known to keep a realistic description of the true chemistry [13,18,19], even if it usually means a higher cost compared to the other mentioned techniques.

ARC schemes already exist in the literature for methane–air combustion [19,20]. They may not be valid for methane oxy-combustion in LRE conditions, i.e., at very high pressure and in highly strained non-premixed combustion regime. Deriving an ARC scheme valid for future LRE technologies is a first objective of this paper.

As already mentioned, methane oxy-combustion at very high pressure leads to extremely small chemical time scales. By construction the QSSA only reduces the stiffness of the fastest radicals, but does not help for the main oxidation paths which still introduce time scales typically 10 times smaller than the flow time scale. Implicit time integration is a standard way to tackle such problem but it increases the complexity of the code [21] and remains computationally expensive, especially for large chemical systems because of the cost of inversion of the Jacobian matrix [18]. Thus, a second objective of this work is to propose an original and fast time-integration method of chemistry for LES solvers.

This paper is organized as follows. In Section 2, the derivation of an ARC mechanism for methane oxy-combustion is derived for high pressure and high strain rate diffusion flames. Then in Section 3, a new time integration method for the chemical source terms is proposed and validated on laminar flames. Then the developed methods are applied in the LES of a lab-scale LRE combustion chamber in Section 4. Conclusions and perspectives are finally given in Section 5.

2. Derivation of Analytical Reduced Chemistry for methane oxy-combustion

2.1. Methodology

Measurements of chemical kinetics in CH_4/O_2 flames at high pressure induce complexity and safety issues which make them rare, if not inexistant and there is no reference detailed scheme available for these conditions. Among the chemical schemes found in the literature, GRI3.0 [22], RAMEC [23] and Slavinskaya [24] are good candidates. As RAMEC (38 species, 190 reactions), initially coming from the GRI1.2, was specifically made for methane oxy-combustion at high pressure by adding several reactions specific of such condition, and was validated against low-diluted CH_4/O_2 shock tubes experiments, it seems the most appropriate for the present study.

To target LRE conditions, the reduction is performed for pressure in the range $49 < P < 59$ bar, i.e., above the critical pressure of both propellants and sufficient to reach the supercritical combustion regime with injection temperatures of $280K$. Using diffusion flames as target flames, the range of strain rate a_{st} (or equivalently scalar dissipation rate χ_{st}, recalled in Eq. (1) [25]) must be defined. It is here taken quite large, representative of conditions met in lab-scale LRE [3,26]: $100 < \chi_{st} < 1500$ s^{-1}. This corresponds to strain rates in the range $650 < a_{st} < 9500$ s^{-1}, of the same order of magnitude as in [8].

$$\chi_{st} = 2D\left(\frac{\partial Z}{\partial x}\right)^2_{st} \tag{1}$$

In Eq. (1), D is the diffusion coefficient of methane and Z the mixture fraction with Bilger's definition [27].

The chemistry reduction process goes through several steps which are realized within an automatic algorithm implemented in the numerical platform ARCANE [28]. First, Direct Relation Graph with Error Propagation (DRGEP) is performed several times on the detailed mechanism to keep only the most relevant species and reactions. Chemical lumping is then applied to remove the isomeric molecules. Finally, a Level Of Importance (LOI) criterion is applied on the remaining species to select the ones to be treated with the QSSA. An overview of these methods are described in [28,29].

The primary target flame property used to control the reduction process is the total heat release rate, with a maximum tolerance of 5%. This quantity, linked to the consumption speed, is indeed the first property to preserve as, similarly to premixed flames, it controls the flame stabilization and flame length which are used for engine design.

With these constraints, a reduced mechanism with 14 transported species, 4 QSS species (listed in Table 1) and 68 reactions was obtained with ARCANE.

2.2. Validation

The ARC scheme is validated on laminar diffusion flames (computed with CANTERA [30]) in the target conditions that are solved following the steady flamelet equations for mass and temperature, recalled here [25]:

$$\dot{\omega}_k = -\frac{1}{2}\rho\chi\frac{\partial^2 Y_k}{\partial Z^2} \text{ and } \dot{\omega}_T = -\frac{1}{2}\rho\chi\frac{\partial^2 T}{\partial Z^2} \tag{2}$$

where $\dot{\omega}_k$ is the chemical source term of species k and $\dot{\omega}_T$ is the energy source term. Overall five test cases are considered to cover all the range of values of P and χ_{st}. The obtained relative errors, shown in Table 2, never exceed 0.83% for the maximum temperature and 1.62% for the total (integral) heat release rate, indicating a very good agreement with the RAMEC detailed mechanism.

Cases A and E are illustrated on Figs. 1 and 2 respectively. In both cases an excellent agreement is observed for the temperature and heat release profiles. With a limited number of species and reactions, even the complex flame structure typical of the LRE conditions is

Table 1
Species contained in the derived ARC mechanism for high pressure methane oxy-combustion.

Transported	QSS
H_2 H O O_2 OH H_2O HO_2 CH_3 CH_4 CO CO_2 C_2H_2 C_2H_4 C_2H_6	HCO CH_2O C_2H_3 C_2H_5

Table 2
Validation cases: relative errors of the ARC scheme compared to the RAMEC detailed mechanism, on the maximum temperature (T_{max}) and the total heat release rate ($\int \dot{\omega}_T$).

Case	Conditions	T_{max}	$\int \dot{\omega}_T$
A	49 bar, χ_{st} = 100 s^{-1}	−0.75%	+1.29%
B	49 bar, χ_{st} = 1500 s^{-1}	−0.83%	+1.62%
C	54 bar, χ_{st} = 1000 s^{-1}	−0.80%	+1.36%
D	59 bar, χ_{st} = 100 s^{-1}	−0.77%	+1.55%
E	59 bar, χ_{st} = 1500 s^{-1}	−0.83%	+1.50%

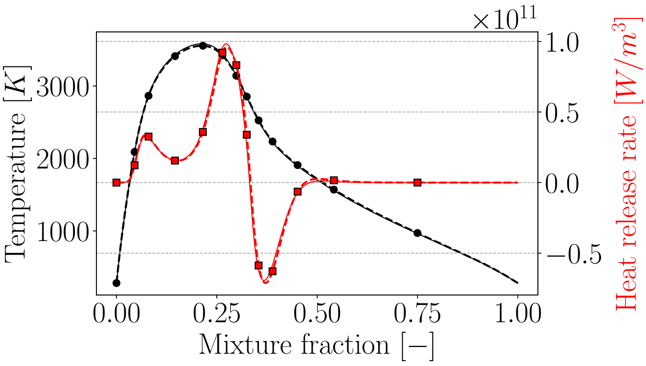

Fig. 1. 1D strained diffusion flame: evolution with mixture fraction of the temperature (black) and the heat release rate (red). Thick lines: RAMEC. Dashed lines with markers: ARC. Case A: $P = 49bar$, $\chi_{st} = 100$ s^{-1}. (For interpretation of the references to color in this figure legend, the reader is referred to the web version of this article.)

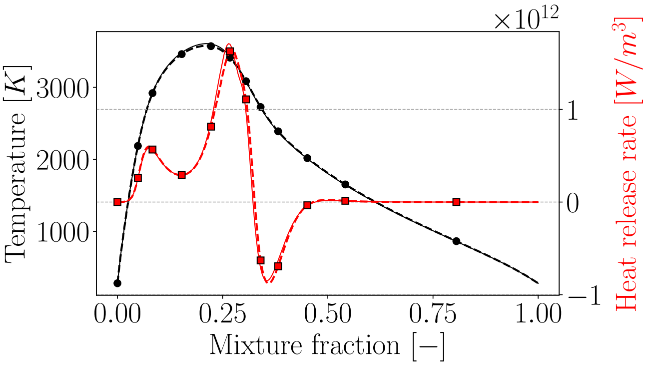

Fig. 2. 1D strained diffusion flame: evolution with mixture fraction of the temperature (black) and the heat release rate (red). Thick lines: RAMEC. Dashed lines with markers: ARC. Case E: $P = 59bar$, $\chi_{st} = 1500$ s^{-1}. (For interpretation of the references to color in this figure legend, the reader is referred to the web version of this article.)

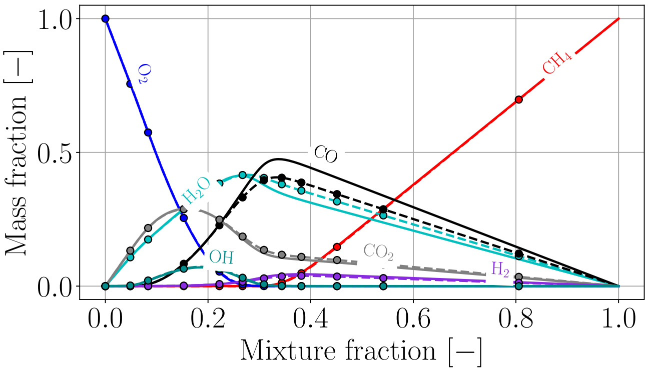

Fig. 3. 1D strained diffusion flame: evolution with mixture fraction of the main species. Thick lines: RAMEC. Dashed lines with markers: ARC. Case C: $P = 54bar$, $\chi_{st} = 1000\ \mathrm{s}^{-1}$.

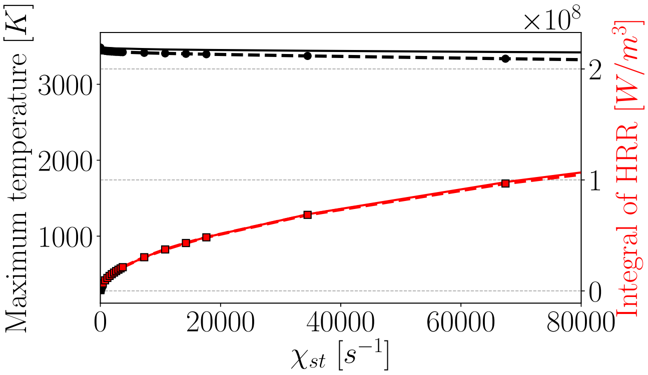

Fig. 4. Evolution with scalar dissipation rate of the maximum temperature (black) and the total heat release rate (red) at $P = 54bar$. Thick lines: RAMEC. Dashed lines with markers: ARC. (For interpretation of the references to color in this figure legend, the reader is referred to the web version of this article.)

retrieved. This also means that the intermediate species profiles are globally well retrieved, as shown Fig. 3. Slight deviation is observed on the heat release rate profile for case E but without significant impact on the integral of heat release rate.

Fig. 4 shows the response of ARC flames to strain. Even if derived over a limited range of χ_{st}, the ARC exhibits a very good agreement with the RAMEC over a larger range: below $\chi_{st} = 20000\ \mathrm{s}^{-1}$, the error keeps lower than 2.5% on maximum temperature, and lower than 2% on the total heat release rate. It never exceeds 5% on the latter quantity until extinction.

Finally Fig. 5 shows the evolution with P of the same quantities over the whole pressure range for which it was derived. The ARC mechanism reproduces well the increase with P of both quantities in excellent agreement with the RAMEC detailed scheme. Only a slightly lower maximum temperature ($\approx -1.0\%$) and very similar total heat release rate ($\approx -2.0\%$) are observed for all pressures.

The reduced chemistry has been validated in the case of laminar flames, although its final use is for turbulent flows (Section 4). Note that turbulence modifies combustion processes via mixing only, and does not affect chemistry. Of course it could happen that this reduction procedure ignores some chemical phenomena which may occur due to turbulent mixing, leading to reacting mixtures of fresh gas with burnt gas and intermediate species that are not encountered in the 0D and 1D cases. These chemical processes are however assumed negligible and are indeed not represented in most turbulent combustion models, such as flamelet-based approaches for example. Moreover, these processes are much sensitive to the turbulent flow and ensuring to describe them in all cases with the same ARC scheme would be impossible.

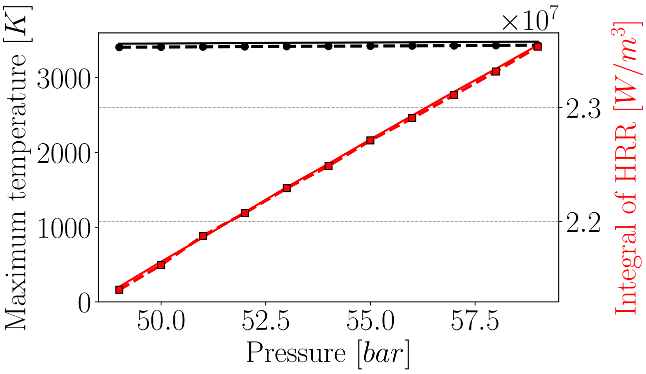

Fig. 5. Evolution with pressure of the maximum temperature (black) and the total heat release rate (red) at $\chi_{st} = 1000\ \mathrm{s}^{-1}$. Thick lines: RAMEC. Dashed lines with markers: ARC. (For interpretation of the references to color in this figure legend, the reader is referred to the web version of this article.)

3. Time integration of stiff chemistry

Although the strongest stiffness has been removed thanks to the QSSA applied to the fastest radicals, very small chemical time scales remain as methane oxy-combustion at high pressure is a very fast oxidation process. Explicit time integration then requires a time step at least of the order of the shortest chemical time step Δt_{chem}, calculated in the simulations as:

$$\Delta t_{chem} = min\left(\frac{\rho Y_k}{\dot{\omega}_k}\right), \tag{3}$$

with $\dot{\omega}_k$ the source term of the species k and ρ the mixture density. The ARC scheme presented in the previous sections leads to a integration time step of the order of 1×10^{-10}s due mainly to the radicals (detailed in Fig. 7), which may therefore considerably increase the computing time. This time step is to be compared to the flow time step Δt_{CFL}, imposed by the CFL number (fixed at 0.7) as:

$$\Delta t_{CFL} = \frac{\Delta x\ CFL}{u + u_a}, \tag{4}$$

with u the flow velocity, u_a the acoustic velocity and Δx the characteristic mesh size. With typical mesh sizes used in 3D LES of LRE, Δt_{CFL} is found of the order of 5×10^{-9}s. As a consequence, the use of ARC in reactive simulations leads to a decrease of the time step typically by a factor 50, which directly impacts the computational cost: explicit computation of the chemical source term is usually one of the most expensive part in a LES code.

With the ultimate goal to run the reactive simulations with the CFL time step, a new time integration method for the chemistry is proposed here. The idea is to take advantage of the simple form of elementary reactions composing the ARC scheme to make an analytical integration of the source terms over the time step. This leads to a time evolution of the concentrations in the form of an exponential function, hence the name of “exponential method”, and allows to substantially increase the time step.

3.1. Principle of the exponential integration

For all what follows, one only considers mass quantities (for source terms, concentrations, etc...).

Consider a species k which is produced and consumed only by elementary first order irreversible chemical reactions. Its total source term $\dot{\omega}_k$ may be recast in the form:

$$\frac{\partial c_k}{\partial t} = \dot{\omega}_k = A_k c_k + B_k, \tag{5}$$

with c_k the concentration of the species k. The functions $A_k c_k$ and B_k are the sum of the contributions to destruction and creation respectively, of the reactions j involving species k:

$$
\begin{aligned}
A_k c_k &= \sum_{j=1}^{M} \nu'_{kj} \dot{r}_j \\
B_k &= \sum_{j=1}^{M} \nu''_{kj} \dot{r}_j
\end{aligned}
\tag{6}
$$

where ν'_{kj}, ν''_{kj} are the stoichiometric coefficients of species k in reaction j and $\dot{r}_j$ the reaction rate.

Assuming A_k^n and B_k^n constant during iteration n, the integration of Eq. (5) is easily found to give at time iteration $n+1$:

$$c_k^{n+1} = \left(c_k^n + \frac{B_k^n}{A_k^n} \right) e^{A_k^n \Delta t} - \frac{B_k^n}{A_k^n} = \frac{B_k^n}{A_k^n} \left(e^{A_k^n \Delta t} - 1 \right) + c_k^n e^{A_k^n \Delta t} \tag{7}$$

where Δt is the time step of the iteration. The obtained solution is correct as long as the assumption of constant A_k^n and B_k^n in the time step stays valid. This introduces a new time step limit, still much higher than the chemical time step, as will be seen in the next sections.

For very small values of A_k^n, i.e., species creation only or non-reacting zone, in order to avoid numerical error, Eq. (7) is rewritten with the second order approximation as:

$$c_k^{n+1} = B_k^n \left(\Delta t + \frac{A_k^n \Delta t^2}{2} \right) + c_k^n \tag{8}$$

The value c_k^{n+1} can then be used to evaluate the source term to be integrated in the equation of transport of c_k as:

$$\dot{\omega}_k = \frac{c_k^{n+1} - c_k^n}{\Delta t} \tag{9}$$

Note that the expression for c_k in Eq. (7) is always positive (provided c_k^0 is positive), so that the approach guarantees positivity of all concentrations. Notice also that this expression exactly holds for first order species only. For second order species, the analytical integration of the source term is still possible but is more complex. As only few reactions involve second order species (10 over 136 in the previously derived ARC), the impact of using first order solution for them is considered negligible and Eq. (7) is still taken as a good approximation.

The calculation of the source term as in Eq. (9) does not guarantee atom conservation, which must be then enforced in a second step. The principle is to correct at each iteration and at each grid point the error on the total mass of each element, by modifying accordingly the local concentrations at iteration $n+1$. To minimize the impact of this correction, it is made on the species of largest concentration. In methane–oxygen flames, three elements are present (H, O, C) and it is chosen to distribute the associated mass corrections among only three species having locally the highest concentration (identified as c_{k_1} to c_{k_3} below).

The mass excess/loss is computed for each element e between iteration n and $n+1$ as:

$$dm_e = \sum_{k=1}^{N_s} (c_k^{n+1} - c_k^n) N_{e,k} \tag{10}$$

where $N_{e,k}$ is the number of element e in species k, and N_s the number of species in the chemical system. Then the corrections $c_{k_e}^{corr}$ of species k_e are calculated by solving the linear system:

$$\begin{pmatrix} n_{H,k_1} & n_{H,k_2} & n_{H,k_3} \\ n_{O,k_1} & n_{O,k_2} & n_{O,k_3} \\ n_{C,k_1} & n_{C,k_2} & n_{C,k_3} \end{pmatrix} \times \begin{pmatrix} c_{k_1}^{corr} \\ c_{k_2}^{corr} \\ c_{k_3}^{corr} \end{pmatrix} = \begin{pmatrix} -dm_1 \\ -dm_2 \\ -dm_3 \end{pmatrix} \tag{11}$$

The corrections c^{corr,k_e} are then used to update the source term in Eq. (9). The linear system may be solved with a simple Gaussian elimination process for example.

The exponential integration algorithm can be summarized as follows:
1 - Compute c_k^{n+1} with Eq. (7) or Eq. (8), where A_k^n, B_k^n use the standard Arrhenius reaction rates.
2 - Compute element mass error dm_e.
3 - Compute concentration corrections c_k^{corr}, for as many species as elements in the chemical system.
4 - Compute the source terms as:

$$\dot{\omega}_k = \frac{c_k^{n+1} + c_k^{corr} - c_k^n}{\Delta t} \tag{12}$$

3.2. Validation in laminar counterflow diffusion flame

The ARC scheme for methane–oxygen combustion, combined with the exponential time integration method is applied here to a laminar 2D counterflow diffusion flame, now computed with a CFD solver. The code AVBP [31–33], developed by CERFACS and benchmarked in many applications [34–37], is used: it solves the compressible Navier–Stokes equations on unstructured meshes with the second order in time and space Lax–Wendroff scheme [38]. The perfect gas equations of state is used. The power-law function is utilized for the molecular viscosity, and constant Schmidt and Prandtl numbers are used for species molecular diffusion and thermal conductivity. The conservation equations for mass, momentum, energy and species write:

$$\frac{\partial \bar{\rho}}{\partial t} + \frac{\partial \bar{\rho} \tilde{u}_i}{\partial x_i} = 0 \tag{13}$$

$$\frac{\partial \bar{\rho} \tilde{u}_j}{\partial t} + \frac{\partial \bar{\rho} \tilde{u}_i \tilde{u}_j}{\partial x_i} + \frac{\partial \bar{P} \delta_{ij}}{\partial x_i} = \frac{\partial}{\partial x_i} \left[\bar{\tau}_{ij} - \bar{\rho} \left(\widetilde{u_i u_j} - \tilde{u}_i \tilde{u}_j \right) \right] \tag{14}$$

$$\frac{\partial \bar{\rho} \tilde{E}}{\partial t} + \frac{\partial \bar{\rho} \tilde{u}_i \widetilde{E}}{\partial x_i} + \frac{\overline{\partial u_i P \delta_{ij}}}{\partial x_i} = \frac{\partial}{\partial x_i} \left[\overline{q_i} - \bar{\rho} \left(\widetilde{u_i E} - \tilde{u}_i \tilde{E} \right) \right] + \overline{\tau_{ij} \frac{\partial u_i}{\partial x_j}} + \bar{\dot{\omega}}_T \tag{15}$$

$$\frac{\partial \bar{\rho} \tilde{Y}_k}{\partial t} + \frac{\partial \bar{\rho} \tilde{u}_i \tilde{Y}_k}{\partial x_i} = \frac{\partial}{\partial x_i} \left[\bar{J}_{k,i} - \bar{\rho} \left(\widetilde{u_i Y_k} - \tilde{u}_i \tilde{Y}_k \right) \right] + \bar{\dot{\omega}}_k \quad \text{for } k = 1, N_s \tag{16}$$

where ρ is the mixture density, u_i stands for the ith-component of the velocity, P the pressure, τ_{ij} the viscous stress tensor, E the total non-chemical energy (including internal and kinetic energy), q_i the ith-component of the heat flux (including heat flux by conduction and species diffusion), $J_{k,i}$ the ith-component of the diffusive flux of species k, $\dot{\omega}_T$ the energy source term and $\dot{\omega}_k$ the chemical source term of species k. δ_{ij} is the Kronecker symbol, equal to 1 if $i = j$ and 0 otherwise. In these notations, the operator $\bar{\cdot}$ represents a Reynolds-averaged variable and the operator $\tilde{\cdot}$ a Favre-weighted variable. For the following laminar flame computations, all the sub-grid scale terms are zero, however they are not in Section 4 where a sub-grid scale model is used.

The opposed jets configuration is set with mass flow rates leading to equal momentum at both sides in order to get the stagnation plane at the center of the domain, where the mesh is the most refined. A small distance ($H = 1$ mm) between both injectors is used to obtain a strain rate in the range of the derived ARC while keeping the flow laminar. With this setup, the targeted mean strain rate is, with $u_F = 0.54$ and $u_O = 0.27$ m/s the fuel and oxidizer velocities respectively:

$$a_{mean} = \frac{u_F + u_O}{H} = 809 s^{-1}. \tag{17}$$

Fig. 6 illustrates the obtained flame for the Fine mesh (see below). Due to the velocity difference of both streams, it is not planar and the solution will be analyzed only along the central axis.

A fine mesh (about $\Delta x = 1$ μm cell characteristic size at the stagnation plane) is first used to assess the accuracy of the exponential integration. Then coarser meshes are used, listed in Table 3, to be more realistic of LES and to demonstrate the capacity of the exponential integration to increase the computational time step. Reference solutions computed with CANTERA are also reported for comparison.

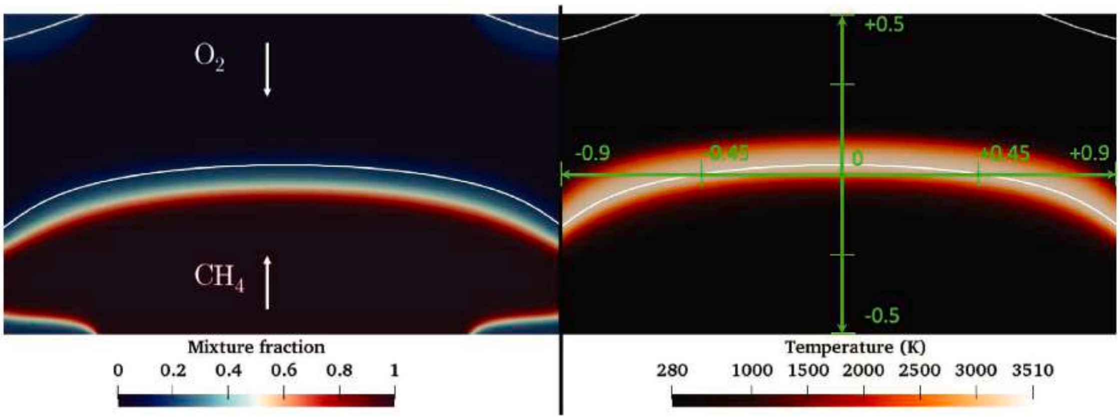

Fig. 6. Laminar counterflow flame in AVBP. Left: mixture fraction field. Right: temperature field. The white line corresponds to the stoichiometric line (Z_{st} = 0.2). Axes in millimeter.

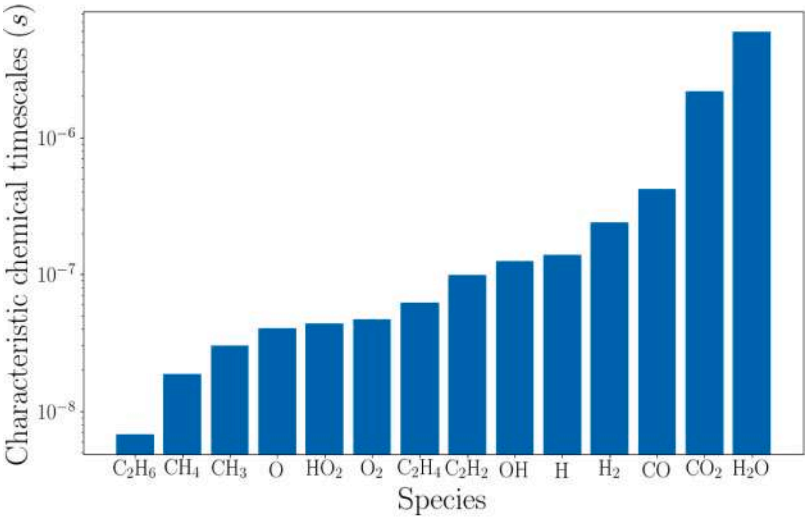

Fig. 7. Characteristic chemical timescales of the methane–oxygen ARC, in the counterflow diffusion flame conditions.

Table 3
Mesh characteristics for the 2D counterflow flame.

Case	Δx[μm]	Δt_{CFL}[ns]
Fine	1	0.194
Coarse 1	10	2.50
Coarse 2	30	5.28

The mesh grid size can be compared to the theoretical thermal flame thickness of a diffusion flame, computed as:

$$\delta_{th} = \sqrt{\frac{\pi D_{th}}{2a_{mean}}} \tag{18}$$

In the present case, δ_{th} = 0.298 mm, so that meshes from Fine to Coarse 2 contain respectively about 300, 30 and 10 points in the thermal flame thickness.

The characteristic chemical time scales $\tau_{chem,k}$ of each species k of the ARC scheme in a diffusion flame at the specified strain rate a_{mean} = 809 s^{-1} are presented in Fig. 7. They are computed as introduced by Eq. (3). It is found that C_2H_6 is the stiffest species with $\tau_{chem,C_2H_6} = 6.8e^{-9}s$. Other radicals are stiff as well, and as already mentioned the fuel itself, CH_4, is also among the stiffest species. Note that these time scales tend to decrease rapidly as the strain rate grows, reaching values about 10e^{-10} - 10e^{-11}s. In practice in the LES code, it is needed to use typically a 1000 times smaller time step than presented in Fig. 7, i.e., much smaller than the time steps Δt_{CFL} for Coarse 1 and Coarse 2 cases of Table 3.

3.2.1. Fine mesh case

Fig. 8 shows the temperature and heat release rate profiles for the fine mesh case, obtained with standard explicit Arrhenius form (referred as "classic") and exponential time integration. An excellent agreement is observed, with exactly the same flame structure. The temperature profiles match perfectly. The difference of total heat release rate is only of 0.11% between the two AVBP computations, and about 2.6% between AVBP and CANTERA simulations. The latter may be attributed to the different numerical solvers and slightly different local strain rate.

Some species profiles, shown in Fig. 9, confirm the excellent behavior of the exponential time integration against the classic one and the excellent agreement with CANTERA. The species profiles perfectly match, with only a slight deviation for CO between AVBP and CANTERA.

In this particular case, it was found that $\Delta t_{chem} > \Delta t_{CFL}$ so that the exponential time integration is not useful. The Fine mesh case was only considered for validation of the exponential time integration. The computational gain is presented in the next section with cases Coarse 1 and Coarse 2 where $\Delta t_{chem} < \Delta t_{CFL}$.

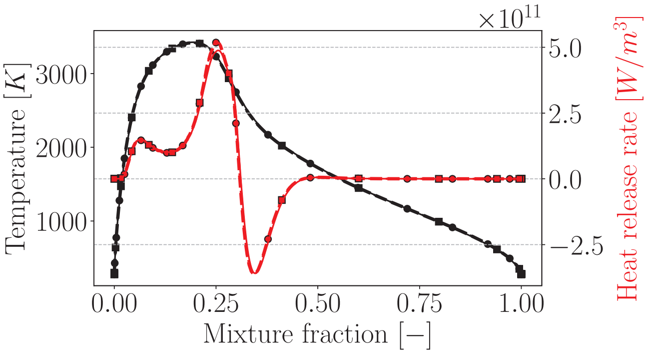

Fig. 8. Strained diffusion flame: evolution with mixture fraction of the temperature (black) and the heat release rate (red). Solid lines: CANTERA (a_{mean} = 809 s^{-1}). Dashed lines with circle markers: classic time integration. Dotted lines with square markers: exponential time integration. Fine mesh case. (For interpretation of the references to color in this figure legend, the reader is referred to the web version of this article.)

3.2.2. Coarse mesh cases and computational gain

Coarse meshes induce numerical diffusion which adds to the laminar diffusion, and artificially increases the scalar dissipation rate at the flame location. This phenomenon, beyond the scope of the present work, was highlighted in [39]. The comparison with CANTERA must be at the same scalar dissipation rate, found to be χ_{st} = 146 s^{-1} and χ_{st} = 209^{-1}, or equivalently in terms of strain rate a_{st} = 930 s^{-1} and a_{st} = 1335 s^{-1} for Coarse 1 and Coarse 2 cases, respectively.

To measure the efficiency of time integration, the quantity κ is introduced as the ratio between the CFL time step and the effective simulation time step:

$$\kappa = \frac{\Delta t_{CFL}}{\Delta t} \tag{19}$$

For both integration methods, coarse mesh cases run with the chemical time step ($\Delta t = \Delta t_{chem}$), leading to κ above 1 as shown in Table 4. Using classic time integration, a reference solution is obtained with a time step 25 times smaller than the CFL time step. The value κ_{min} corresponds to the maximum time step keeping a correct time resolution. As the flow time step Δt_{CFL} is proportional to Δx, κ_{min} increases from 4 for the Coarse 1 case to 10 for the Coarse 2 case. In comparison, the exponential time integration method allows to increase Δt_{chem} (and therefore decrease κ) up to half and fourth the CFL time step for Coarse 1 and Coarse 2 cases, respectively. A reference case with κ = 25 is also computed for exponential integration. As explained in Section 3.1, the constant reaction factors assumption does not allow larger time steps for the exponential method. With the exponential method, the obtained solution has the same accuracy as the solution obtained with the classic approach. This means, concerning the chemical time step, an acceleration factor of 2 and 2.5 for Coarse 1 and Coarse 2 reference solutions, respectively.

Table 4
Efficiency of time integration κ (Eq. (19)) for the classic and exponential time integration for the coarse mesh cases.

Mesh	κ_{ref} (classic)	κ_{min} (classic)	κ_{ref} (expo)	κ_{min} (expo)
Coarse 1	25	4	25	2
Coarse 2	25	10	25	4

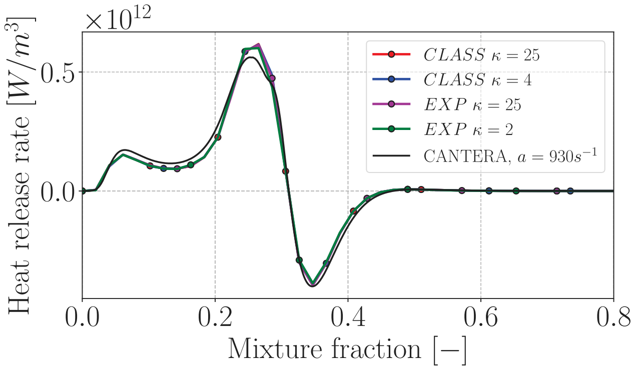

Fig. 10. 1D strained diffusion flame: evolution with mixture fraction of the heat release rate for different time integration methods. Coarse 1 case.

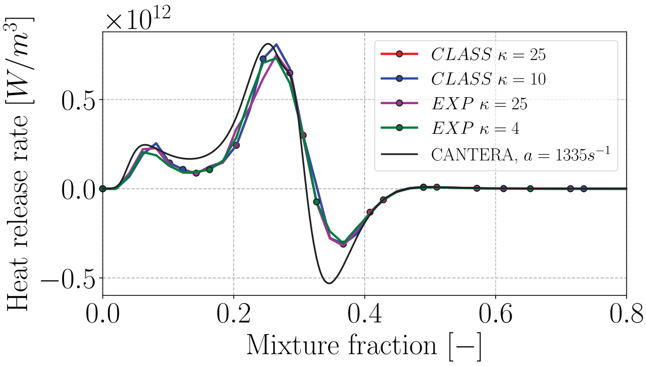

Fig. 11. 1D strained diffusion flame: evolution with mixture fraction of the heat release rate for different time integration methods. Coarse 2 case.

Figs. 10 and 11 compares the solutions obtained with the classic and exponential method, with κ_{ref} and κ_{min}, as well as with the CANTERA solution taken at the appropriate strain rate, for the two coarse meshes.

For Coarse 1 case, the heat release rate profile shows less than 1% discrepancy between all AVBP simulations, and about 2% difference with the CANTERA flame. Discrepancies are larger for Coarse 2 case, linked to the very poor grid resolution with about 10 points to describe the three-peaks flame reaction zone. They stay however very small

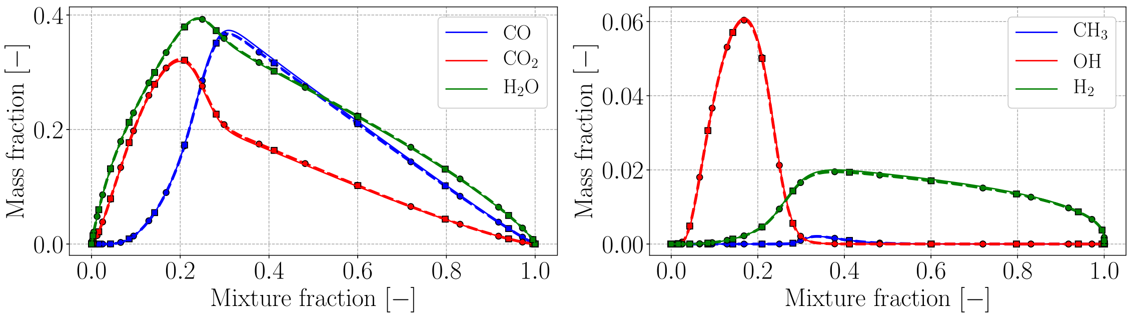

Fig. 9. Strained diffusion flame: evolution with mixture fraction of some species profiles. Solid lines: CANTERA (a_{mean} = 809 s^{-1}). Dashed lines with circle marker: classic time integration. Dotted lines with square markers: exponential time integration. Fine mesh case.

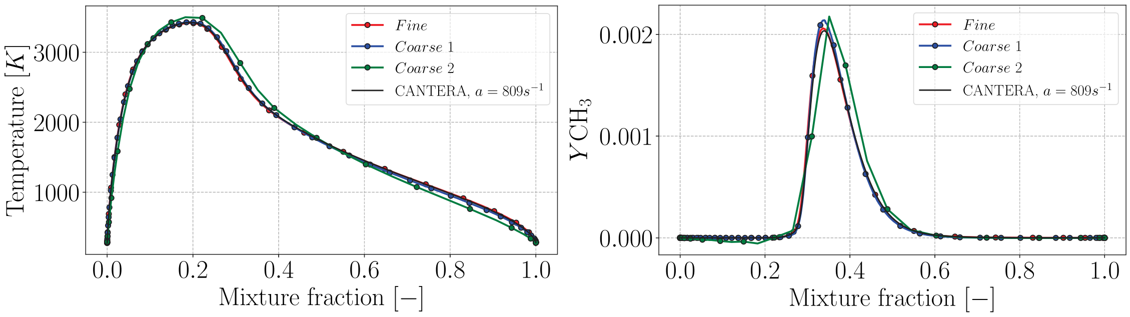

Fig. 12. Strained diffusion flame: evolution with mixture fraction of the temperature and CH_3 mass fraction for the considered meshes compared to CANTERA.

between all AVBP cases, and are more noticeable in the comparison with the CANTERA solution, which does not have this mesh effect. Interestingly, the classic and exponential methods do not respond similarly to the time step increase. While in the classic approach, the solution stays unchanged until the simulation crashes, the increased robustness of the exponential method allows to converge solutions at large time steps, but with an increased error.

The non-conservation of mass of the exponential time integration, described in Section 3.1 is quantified for each element as:

$$dm_{e,rel} = \frac{\sum_{k=1}^{N_s} (c_k^{n+1} - c_k^n) N_{e,k}}{\sum_{k=1}^{N_s} c_k^{n+1} N_{e,k}} \tag{20}$$

In all fine and coarse mesh cases, $dm_{e,rel}$ is found to stay always below 1% in each cell and for all elements, which results in a maximum correction of $\mathcal{O}(1\%)$ on species concentrations. These are maximum values, and most of the simulation does not require such correction. Therefore it is verified *a posteriori* that the mass correction proposed in Section 3.1 remains low and has a very limited impact on the final results. As expected, the mass deviation is directly linked to the temporal resolution: for example in Coarse 1 case with $\kappa = 2$, the maximum correction is about $\mathcal{O}(1\%)$ but with $\kappa = 25$, it decreases down to $\mathcal{O}(0.1\%)$.

Finally, Fig. 12 shows the temperature and the CH_3 mass fraction profiles for the different meshes. The cases Fine, Coarse 1 and the CANTERA reference, all curves almost perfectly match, proving the mesh convergence. The Coarse 2 case logically deviates a bit from the others due its poorer resolution.

4. Application to the Large Eddy Simulation of the CONFORTH test bench

The ARC methane–oxygen scheme and the exponential time integration presented in the previous sections are now used in the LES of a lab-scale combustion chamber representative of LRE conditions, the CONFORTH configuration owned by ONERA. It has been developed for the study of wall heat transfers, with pressure ranging from 20 to 70 bar, and with hydrogen or methane oxy-combustion at different mixture ratios.

4.1. Experimental setup and operating point

The experimental setup is detailed in [26]. The CONFORTH test bench consists of five coaxial injectors: one central and four others placed on an external ring. The chamber is circular and ends with a nozzle. The chosen operating point for the present work is at a pressure of 54 bar with a rich mixture ratio (details are not given for confidentiality reasons). The test rig operates then in supercritical regime. Simulations are run for about two convective times, estimated from the mean injection velocities to be 8.5 ms (see Fig. 13).

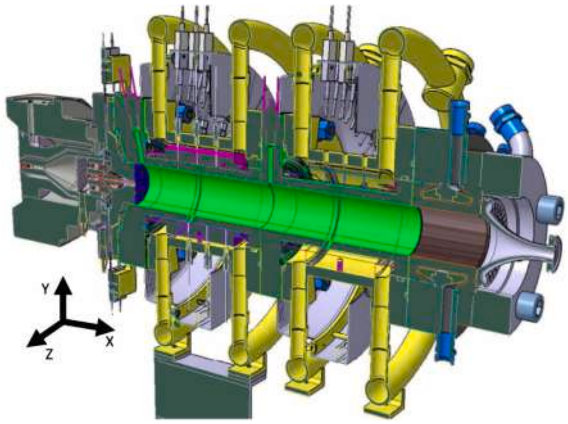

Fig. 13. CAD of the CONFORTH test bench from ONERA [40].

4.2. Numerical setup

4.2.1. Geometry and mesh

The whole 3D combustion chamber (with the five injectors) is simulated except the nozzle. The mesh about 33M cells is fully made of tetrahedral elements, which size from $\Delta x_0 = 40$ μm at the injector lips to $\Delta x_M = 3000$ μm in the domain. At the walls, tetrahedra are also used and y^+ values scale from 40 to 60 along the chamber. There are about 10 points to solve the flame thermal thickness. Fig. 14 shows an overview of the mesh.

4.2.2. Models

The AVBP solver is used, with the same convective scheme and transport coefficients than for the 2D flames. Furthermore, the subgrid-scale turbulence model is the Sigma model [41] and constant turbulent Schmidt and Prandtl numbers (fixed at 0.6 for both) are used for subgrid species and thermal diffusions. The Soave–Redlich–Kwong cubic equation of state is used [42], and local filtering on density and pressure is applied following the LAD approach [43] to avoid spurious numerical perturbations. The main governing equations were recalled from Eq. (13) to (16).

Two simulations are performed: one with the classic time integration (referred to as LES-CLASS), the other with the exponential time integration presented in Section 3 (referred to as LES-EXPO). Similarly to the 2D flame computations shown in Section 3, the diffusion flames which develop in the chamber are artificially thickened by the mesh and do not require further thickening to be resolved. Subgrid-scale flame-turbulence interactions however remain, which in principle should be modeled. In the present case these effects are assumed small in comparison to the resolved turbulence thanks to the refined mesh in the flame zone and are omitted. It will be checked *a posteriori* that the flames are indeed purely non-premixed and that subgrid-scale turbulence is weak.

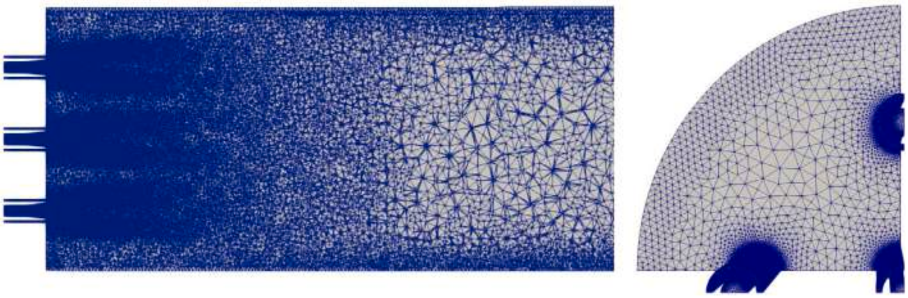

Fig. 14. CONFORTH test bench mesh overview. Left: cut normal to Z-axis. Right: quarter of injection head normal to X-axis.

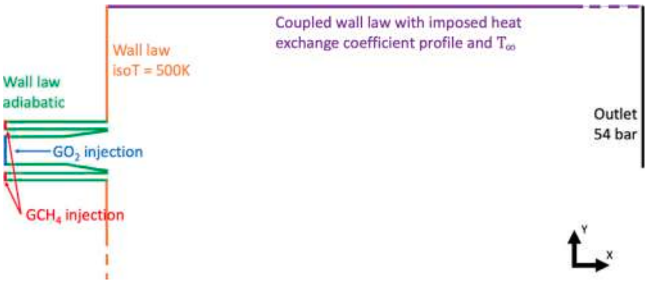

Fig. 15. Boundary conditions: zoom on the top injector (cut normal to Z-axis).

4.2.3. Boundary conditions

The boundary conditions are formulated with the Navier–Stokes Characteristic Boundary Condition (NSCBC) approach [44]. Inlets are set with the recent Non-Reflective Inlets (NRI) method [45] which allows to absorb acoustics while maintaining the injection fluxes. As the nozzle is not computed, the outlet pressure is set at 54 bar. At the GCH_4 and GO_2 inlets, turbulent velocity profiles are imposed. The injector walls including the lip are treated with adiabatic slip conditions with the use of the standard wall-law. The chamber walls make use of the coupled wall law derived by Cabrit [46], which takes into account the high temperature gradients expected between the burnt gases and the walls. The heat transfer through the wall is taken into account by imposing a heat exchange coefficient profile based on experimental results with a reference temperature set at $T_\infty = 280.15$ K. The injector head wall also uses the coupled wall law, with an isothermal condition at T $= 500$ K. All boundary conditions are summarized in Fig. 15.

4.3. Results

4.3.1. Computational cost gain

The CFL time step is $\Delta t_{CFL} = 7.3$ ns while Eq. (3) gives a chemical time step $\Delta t_{chem} = 0.23$ ns, i.e., about 32 times smaller. In practice, the case LES-CLASS runs with $\kappa_{CLASS} = 20$ while the case LES-EXPO runs with $\kappa_{EXP} = 10$, i.e., a 2 times higher chemical integration time step.

4.3.2. Flame shape

All views presented in this Section are cuts across the Z-normal axis. Note that for confidentiality reasons, axes have been non-dimensionalized to new units X', Y', Z', the length $X' = 1$ corresponding to the mean flame length found (see Fig. 16).

Fig. 16 contains various averaged fields to compare the two integration methods, where a typical diffusion flame shape anchored at the lip is easily recognizable. The fields exhibit differences between the central and the side flames because of flame–flame and flame–wall interactions. The central flame is shorter, and it seems that the side flames are slightly bended towards the walls. Also, the main exothermic zone of the side flames is shorter next to the walls, due to the colder area near the walls. Both time integration methods give very similar results, also concerning the flame length.

Figs. 17 and 18 shows instantaneous fields of the temperature with superimposed streamlines. Corner and inter-injector recirculation zones appear with different sizes, extending to about $X' = 0.6$ and $X' = 0.15$ respectively in the axial direction. Short flames and fast thermal expansion lead to a thermally homogeneous flow of hot gases above 3500 K from $X' = 0.9$ and downwards. However looking at Fig. 18, the burnt gases composition is less homogeneous: due to the different relative positions of the flames, CO is trapped in the corner recirculation zone, but entrained downstream by the accelerated flow between the flames.

4.3.3. Flame structure

It is first verified that the flame is purely non-premixed, using the Takeno index [47] ζ weighted by the heat release rate $\dot{\omega}_T$, computed and integrated through the whole domain V, as:

$$\zeta_{HR} = \int_V \zeta \times \dot{\omega}_T \tag{21}$$

It is found that about 73% of the heat is produced in non-premixed conditions. The remaining 27%, therefore burning as premixed, are identified to be at either far from the stoichiometric line, either at the tip of the flame where the resolution is poorer or either located in-between the flames, where the mixture is mainly composed of burnt gas products H_2O, CO and CO_2 but not yet at equilibrium: the mixture continues to react in a premixed mode to establish the correct CO–CO_2 equilibrium.

The flame structure is studied through scatter plots realized in the red box shown in Fig. 16 on the time-averaged solution. As a major control parameter of diffusion flames, strain rate statistics are first shown in Fig. 19. In the LES simulations, the resolved strain rate along the flame is computed as:

$$a_t = (\delta_{ij} - n_i n_j) S_{ij} \tag{22}$$

where n_i, n_j are the components of the flame normal, S_{ij} is the resolved fluid strain rate tensor, and δ_{ij} is the Kronecker symbol.

In the considered area, 75% of the turbulent flame see a strain rate below 5000 s^{-1}, with a peak of the probability around 3000 s^{-1}. At this pressure, the extinction strain rate of a methane–oxygen flame is of the order of 3×10^6 s^{-1}, far above the maximum strain rate observed (of the order of 1.5×10^5 s^{-1}) which means that the present turbulent flame never quenches in the studied zone.

As announced in the model description, the subgrid-scale flame-turbulence interaction is evaluated. To do this the ratio of the turbulent viscosity over the laminar viscosity is shown on Fig. 20. One can see that this ratio is quite low (below 10) in most part of the flame. This is explained by the fine mesh at the flame location, as shown in the top-half of the figure. Towards the flame tip, the mesh coarsens quite rapidly which results in higher values for the viscosity ratio, but at this location most of the heat release has already been produced. This low turbulent viscosity indicates a small flame-turbulence sub-grid

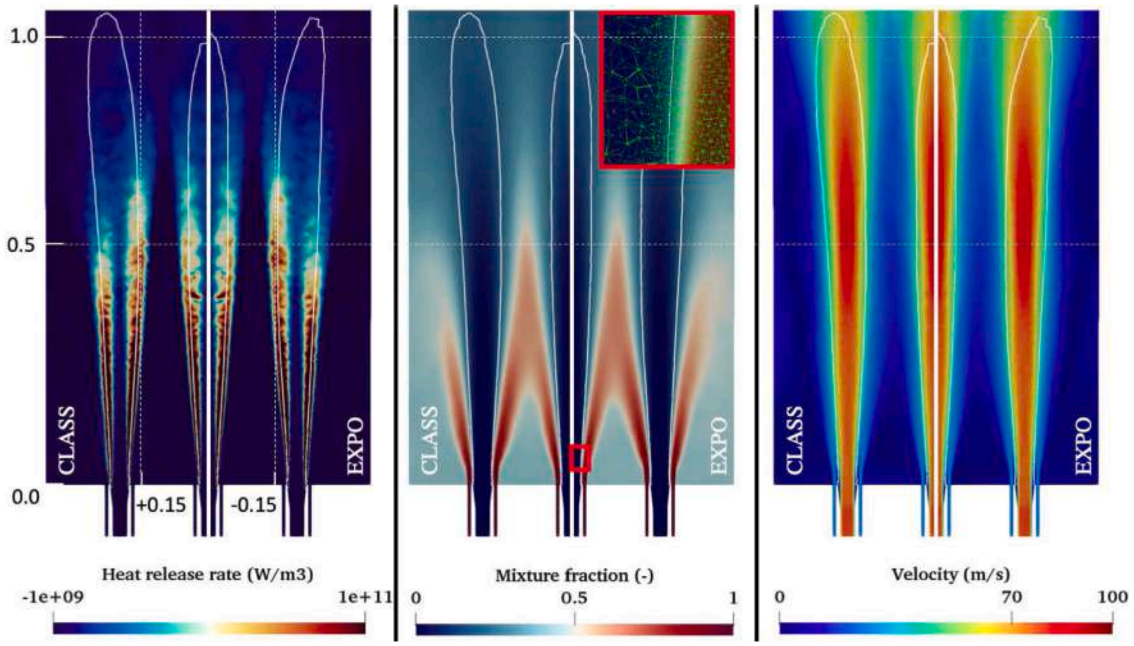

Fig. 16. CONFORTH test bench. Cuts of averaged fields of heat release rate, mixture fraction and velocity obtained with the classic (left half) and the exponential (right half) methods, with the stoichiometric line in white ($Z_{st} = 0.2$). The red box indicates where the scatter plots are realized (see next Section). (For interpretation of the references to color in this figure legend, the reader is referred to the web version of this article.)

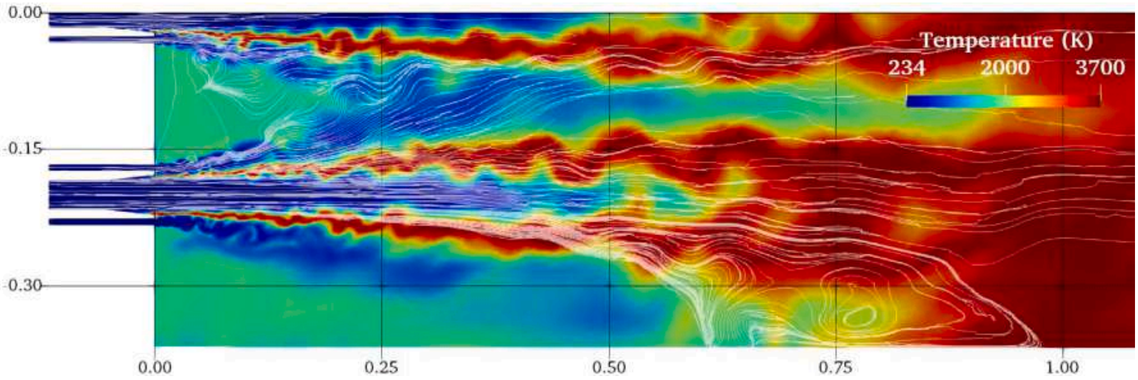

Fig. 17. CONFORTH test bench. Instantaneous temperature field of the classical integration case with streamlines.

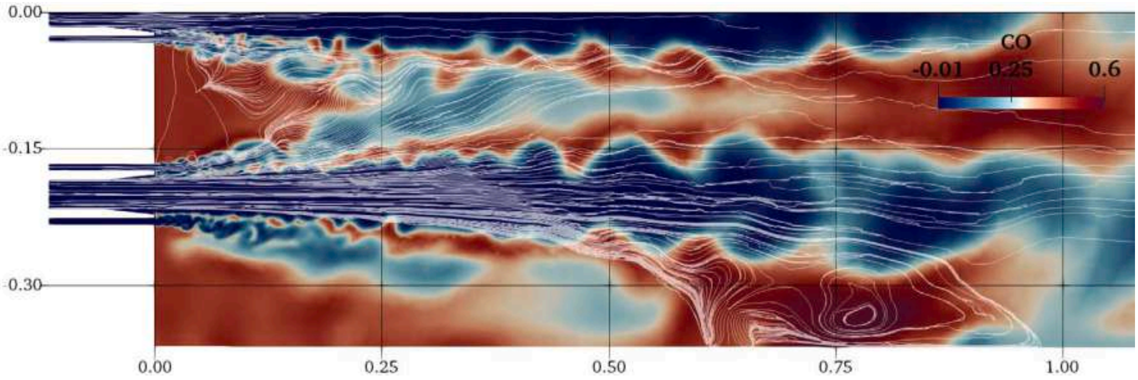

Fig. 18. CONFORTH test bench. Instantaneous CO mass fraction field of the classical integration case with streamlines.

intensity, which can be therefore neglected, following the same idea as in [48].

The maximum temperature gradient in the flame controls the thermal flame thickness which is calculated with Eq. (18) and is found to be between $220 > \delta_{th} > 49$ μm for strain rates of $3000 < a < 30000$ s^{-1}. With a cell size going from 40 to 80 μm in this area, the mesh refinement is considered sufficiently fine to solve correctly this gradient.

To complete these statements about simulation quality, as the computations were long to converge and required many integration time steps, an error accumulation study is performed following the technique

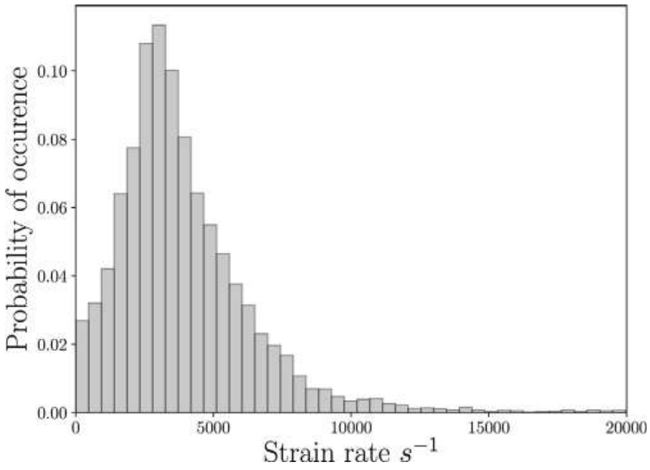

Fig. 19. CONFORTH test bench. Strain rate distribution in the classical integration case.

described in [49]. An average cell size is considered and compared to the domain lengths in each direction, providing a 3D relative integration error. Taking into account the total number of iterations performed, in the case of the LES-CLASS case the accumulation error estimate due to computation duration is found to be less than 2%, which is acceptable.

Scatter plots of temperature with mixture fraction are shown in Fig. 21 for the two cases and compared to the CANTERA solution at strain rate 4000 s^{-1}, which corresponds to the mean value in the zone defined by the red box of Fig. 16. They confirm that the flame is substantially stretched but stays far from quenching. Note that ARC remains valid for strain rates largely exceeding its range of derivation presented in Section 2: this is a known advantage of ARC as demonstrated in [13]. The two AVBP simulations give very same results, which are however different from the laminar CANTERA solution. The maximum temperature is lower in AVBP with about 400 K gap, which can be explained by the fact that the LES flames are simply not adiabatic. It can be noticed that in the rich side of the flame, a group of points seems slightly out of the curves: they are found in the premixed zone, in between the flames.

To go further in the flame structure analysis, statistics of the time-averaged heat release rate in the mixture fraction space are shown in Fig. 22. In the figure, both the time-averaged and the standard deviation in the zone defined by the red box of Fig. 16 are plotted. The two AVBP computations are again very similar. However, due to

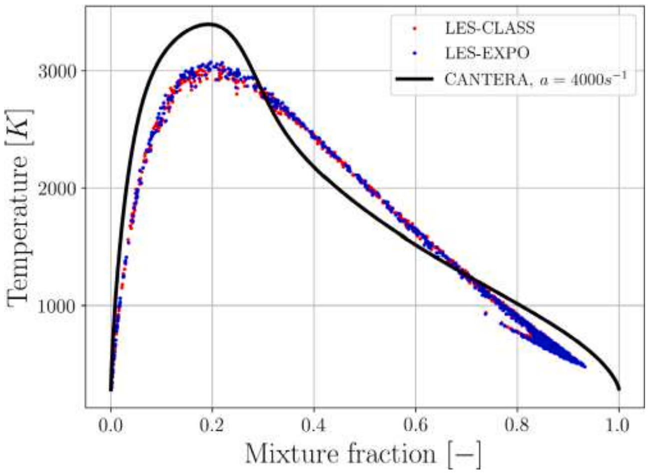

Fig. 21. CONFORTH test bench. Scatter plots of temperature in the zone defined by the red box of Fig. 16 for cases with classical and exponential integration, compared to the temperature profile of a laminar flame at equivalent mean strain rate.

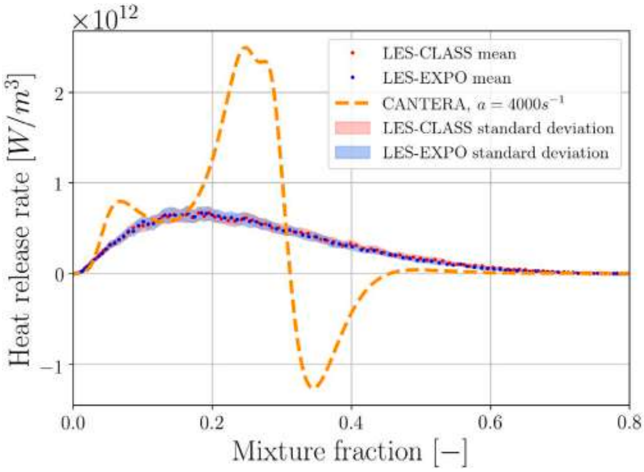

Fig. 22. CONFORTH test bench. Time-averaged heat release rate: mean of the points located in the red box of Fig. 16 and their standard deviation, for cases with classical and exponential integration, compared to heat release rate profile of a laminar flame at equivalent mean strain rate.

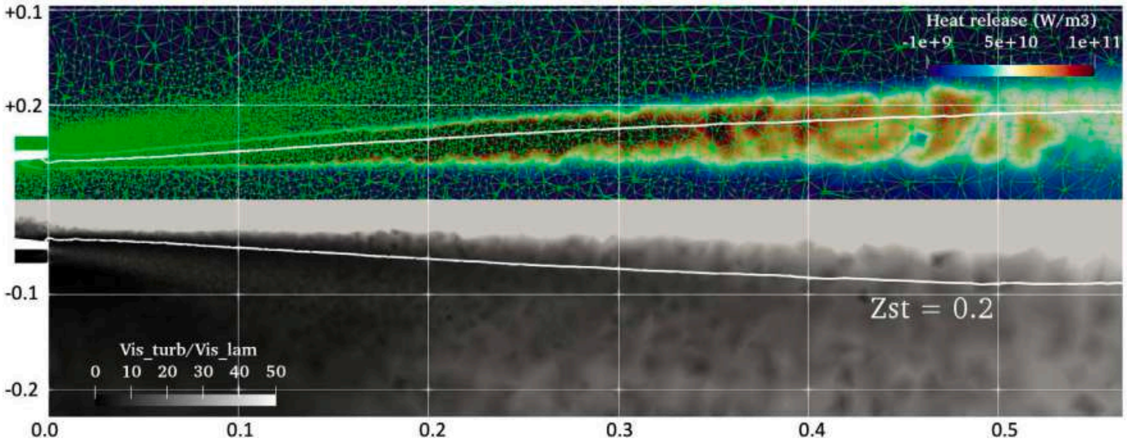

Fig. 20. CONFORTH test bench. Details of the mesh in the central flame (top) and ratio of turbulent over laminar viscosities (bottom) for the averaged solution of the classical integration case. White isoline shows the stoichiometric mixture fractions.

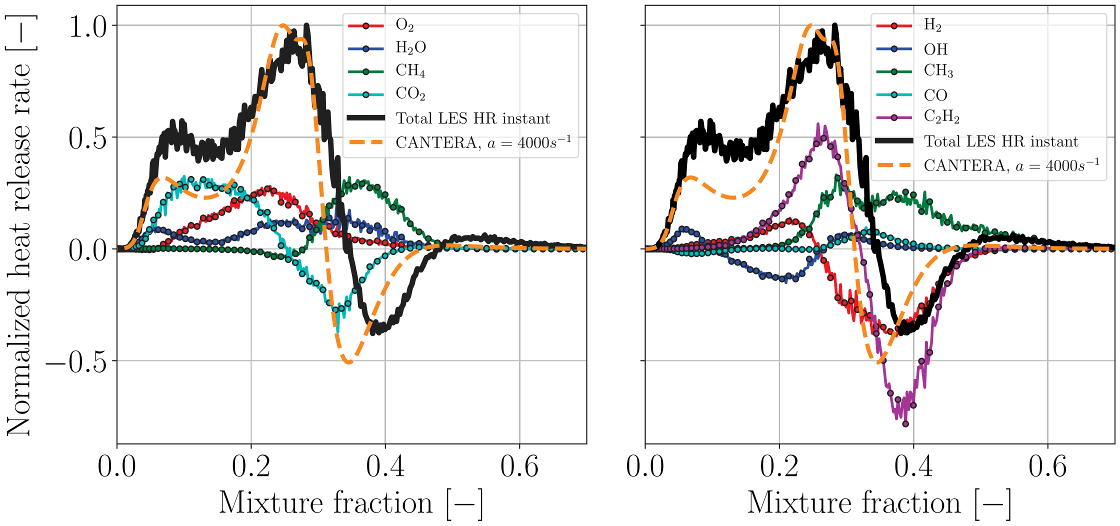

Fig. 23. CONFORTH test bench. Instantaneous heat release rate and species contributions to the heat release (curves fitted on scatter plots in the red box of Fig. 16) for the classical integration case.

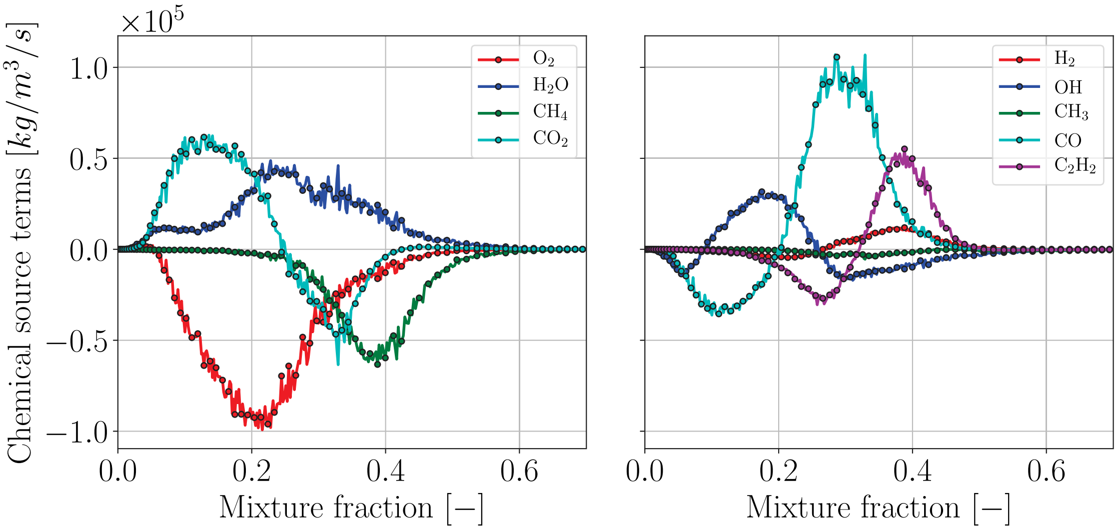

Fig. 24. CONFORTH test bench. Instantaneous chemical source terms (curves fitted on scatter plots in the red box of Fig. 16) for the classical integration case.

the time-averaging operation, the complex shape with two exothermic and one endothermic peaks, as observed in the laminar flame solution at the representative strain rate of $a_{mean} = 4000$ s^{-1}, is not recovered.

To better elucidate the LES flame structure, the instantaneous heat release rate (together with the main species contributions) is plotted against the mixture fraction in Fig. 23. To obtain a typical curve, a reduced number of instantaneous solutions have been used to build scatter plots in the red box of Fig. 16 from which a fitted curve was extracted. Only the LES-CLASS case is shown, as same results were obtained for the LES-EXPO case. The instantaneous LES results clearly recover the whole complex, three-peaks flame structure, which confirms that time-averaging is responsible for the smooth heat release rate profile of Fig. 22. The species contributions explain the origin of the endothermic peak due to the species C_2H_2 and H_2 and, to a less extent, CO_2, while the main exothermic zone is due to C_2H_2 and CH_3. This highlights the importance of some species which are usually not found in simpler chemical schemes.

The flame can also be described in Fig. 24 where instantaneous chemical source terms are plotted (curves fitted on scatter plots). The first exothermic peak in the lean side around $Z = 0.1$ is due to the oxidation of CO in CO_2. The main exothermic peak between $0.2 < Z < 0.3$ corresponds to the consumption of the reactants O_2 and CH_4, the production of H_2O and CO, and the oxidation of radicals such as OH, CH_3 and C_2H_2. Finally the endothermic zone on the rich side is associated to the production of C_2H_2 and H_2 and the consumption of CO_2.

Time-averaged species profiles are plotted in Figs. 25–27. For the propellants CH_4 and O_2, AVBP results fit correctly the CANTERA laminar flame solution, with little dispersion. The main products H_2O, CO and CO_2 show more discrepancies, in particular the CO–CO_2 equilibrium is slightly moved. Smallest species like CH_3 and OH exhibit larger differences compared to the laminar flame. In all those figures, note however the perfect match between the LES-CLASS and LES-EXPO case, demonstrating the validity of the exponential time integration method.

5. Conclusion

An Analytical Reduced Chemistry (ARC) scheme has been derived for a specific range of conditions usually met in lab-scale Liquid Rocket Engines (with here the example of the CONFORTH test bench from ONERA), which allows a strong reduction — and associated computing time gain. The complex structure due to the extreme flow conditions is

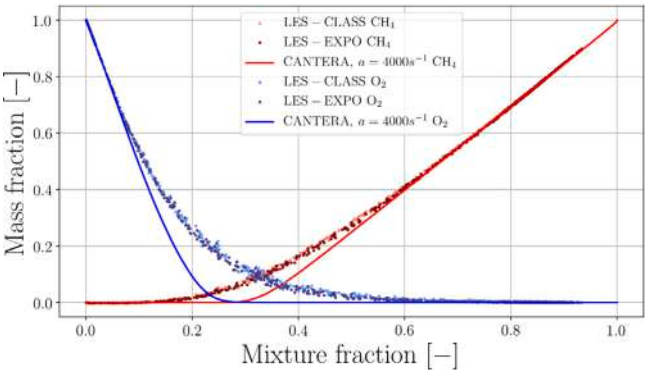

Fig. 25. CONFORTH test bench. Scatter plots of CH_4 and O_2 from the time-averaged solution in the red box of Fig. 16.

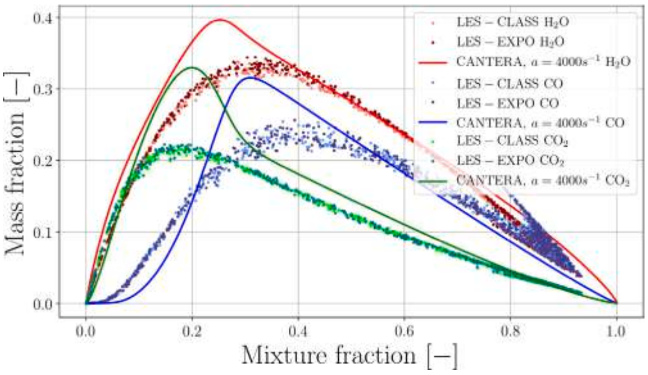

Fig. 26. CONFORTH test bench. Scatter plots of H_2O, CO and CO_2 from the time-averaged solution in the red box of Fig. 16.

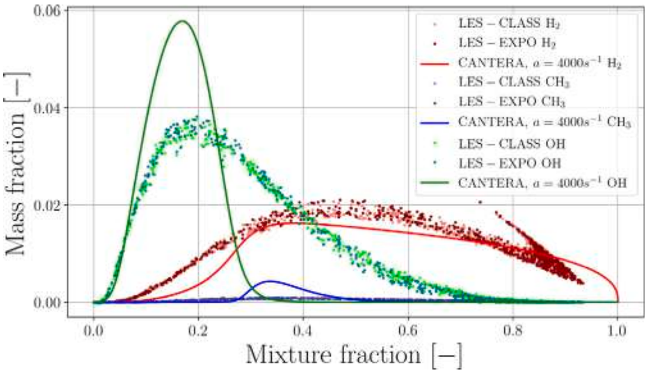

Fig. 27. CONFORTH test bench. Scatter plots of H_2, CH_3 and OH from the time-averaged solution in the red box of Fig. 16.

well retrieved with a minimum number of species and reactions. It is now feasible thanks to the user-friendly derivation code ARCANE.

Even with this reduction, the ARC scheme remains highly stiff due to some intermediate species and the fuel itself that cannot be treated with the Quasi Steady State Assumption. It therefore leads to prohibitively small computational time steps for Large Eddy Simulation (LES). In order to overcome this issue a new integration method for the chemical source terms has been proposed. Based on exponential integration, it ensures positive concentrations and reinforces the simulation stability. It allows to relax the constraint of using a small computational time step, even with stiff ARC chemistry. The mechanism allows to study in details chemistry inside the flame. The flame structure complexity demonstrates the need to use semi-detailed chemistry for this type of configuration. In the presented test cases, the exponential integration allows a significant decrease of the computational cost for the same simulation quality than with the explicit integration. The ARC and exponential integration method described in this paper make it possible to perform LES of methane oxy-combustion with accurate chemistry in realistic Liquid Rocket Engines configurations.

Funding sources

This work has been funded by CNES and ArianeGroup and was performed using HPC resources from GENCI-[TTGC] (Grant 2020-A0052B10157).

Declaration of competing interest

The authors declare that they have no known competing financial interests or personal relationships that could have appeared to influence the work reported in this paper.

Acknowledgments

Thanks to CNES and ONERA for providing the CONFORTH test bench geometry and data. Authors also acknowledge Théo Ogier, Jonathan Wirtz and Antoine Pestre for fruitful discussions and testing about the exponential integration, and Miguel Martin-Benito for the discussions and the feedback about the CONFORTH simulation.

References

[1] H.W. Jones, The recent large reduction in space launch cost, in: 48th International Conference on Environmental Systems, July, 2018, pp. 1–10.

[2] T. Neill, D. Judd, E. Veith, D. Rousar, Practical uses of liquid methane in rocket engine applications, Acta Astronaut. 65 (5–6) (2009) 696–705, http://dx.doi.org/10.1016/j.actaastro.2009.01.052.

[3] D. Preclik, H. Hagemann, K. O., C. Maeding, D. Haeseler, O. Haidn, A. Woschnak, M. DeRosa, LOX/hydrocarbon preparatory thrust chamber technology activities in Germany, in: 41st AIAA/ASME/SAE/ASEE Joint Propulsion Conference and Exhibit, (July) 2005, pp. 1–15, http://dx.doi.org/10.2514/6.2005-4555.

[4] P.G. Sutton, History of Liquid Propellant Rocket Engines, American institute of Aeronautics and Astronautics, 2006, http://dx.doi.org/10.2514/4.868870.

[5] A. Preuss, D. Preclik, C. Mading, J. Gorgen, S. Soller, O. Haidn, M. Oschwald, W. Clauss, R. Arnold, J. Sender, LOX/Methane technology efforts for future liquid rocket engines, in: 5th International Spacecraft Propulsion Conference & 2nd International Symposium on Propulsion for Space Transportation, May, 2008.

[6] G. Lacaze, B. Cuenot, T. Poinsot, M. Oschwald, Large eddy simulation of laser ignition and compressible reacting flow in a rocket-like configuration, Combust. Flame 156 (6) (2009) 1166–1180, http://dx.doi.org/10.1016/j.combustflame.2009.01.004.

[7] T. Schmitt, Y. Méry, M. Boileau, S. Candel, Large-eddy simulation of oxygen/methane flames under transcritical conditions, 33, (1) (ISSN: 15407489) ISBN: 1540-7489, 2011, pp. 1383–1390, http://dx.doi.org/10.1016/j.proci.2010.07.036.

[8] D. Maestro, B. Cuenot, L. Selle, Large eddy simulation of combustion and heat transfer in a single element GCH4/GOx rocket combustor, Flow Turbul. Combust. (2019) http://dx.doi.org/10.1007/s10494-019-00036-w.

[9] B. Ivancic, W. Mayer, Time- and length scales of combustion in liquid rocket thrust chambers, J. Propul. Power 18 (2) (2002).

[10] D. Li, Q. Zhang, Q. Ma, S. Shen, Comparison of explosion characteristics between hydrogen/air and methane/air at the stoichiometric concentrations, Int. J. Hydrogen Energy 40 (28) (2015) 8761–8768, http://dx.doi.org/10.1016/j.ijhydene.2015.05.038.

[11] J.F. Griffiths, Reduced kinetic models and their application to practical combustion systems, Prog. Energy Combust. Sci. 21 (1) (1995) 25–107, http://dx.doi.org/10.1016/0360-1285(94)00022-V.

[12] T. Lu, C. Law, Systematic approach to obtain analytic solutions of quasi steady state species in reduced mechanisms, J. Phys. Chem. A 110 (49) (2006) 13202–13208, http://dx.doi.org/10.1021/jp064482y.

[13] A. Felden, P. Pepiot, L. Esclapez, E. Riber, B. Cuenot, Including analytically reduced chemistry (ARC) in CFD applications, Acta Astronaut. 158 (2019) 444–459, http://dx.doi.org/10.1016/j.actaastro.2019.03.035.

[14] J. Chen, J. Blasco, N. Fueyo, C. Dopazo, An economical strategy for storage of chemical kinetics: Fitting in situ adaptive tabulation with artificial neural networks, Proc. Combust. Inst. 28 (2000) 115–121, http://dx.doi.org/10.1016/S0082-0784(00)80202-7.

[15] V.B. Betelin, B.V. Kryzhanovsky, N.N. Smirnov, V.F. Nikitin, I.M. Karandashev, M.Y. Malsagov, E.V. Mikhalchenko, Neural network approach to solve gas dynamics problems with chemical transformations, Acta Astronaut. 180 (2021) 58–65, http://dx.doi.org/10.1016/j.actaastro.2020.11.058.

[16] M. Cailler, N. Darabiha, D. Veynante, B. Fiorina, Building-up virtual optimized mechanism for flame modeling, 36, (1) (ISSN: 15407489) 2017, pp. 1251–1258, http://dx.doi.org/10.1016/j.proci.2016.05.028.

[17] G. Maio, R. Mercier, M. Cailler, B. Fiorina, Virtual chemistry for prediction of chemical flame structure in non adiabatic combustion, (April) 2017.

[18] T. Lu, C.K. Law, Toward accommodating realistic fuel chemistry in large-scale computations, Prog. Energy Combust. Sci. 35 (2) (2009) 192–215, http://dx.doi.org/10.1016/j.pecs.2008.10.002.

[19] A. Felden, Development of Analytically Reduced Chemistries (ARC) and Applications in Large Eddy Simulations (LES) of Turbulent Combustion, (Ph.D. thesis), Institut National Polytechnique de Toulouse, 2013.

[20] T. Lu, C.K. Law, A criterion based on computational singular perturbation for the identification of quasi steady state species: A reduced mechanism for methane oxidation with NO chemistry, Combust. Flame 154 (4) (2008) 761–774, http://dx.doi.org/10.1016/j.combustflame.2008.04.025.

[21] R.J. Kee, L.R. Petzold, M.D. Smooke, J.F. Grcar, 5 - implicit methods in combustion and chemical kinetics modeling, in: J.U. Brackbill, B.I. Cohen (Eds.), Multiple Time Scales, Academic Press, 1985, pp. 113–144, http://dx.doi.org/10.1016/B978-0-12-123420-1.50010-0.

[22] G.P. Smith, D.M. Golden, M. Frenklach, N.W. Moriarty, M.G. Boris Eiteneer, C.T. Bowman, R.K. Hanson, S. Song, W.C. Gardiner, V.V. Lissianski, Z. Qin, GRI3.0 mechanism website, 1999, URL: http://combustion.berkeley.edu/gri-mech/.

[23] E.L. Petersen, D.F. Davidson, R.K. Hanson, Kinetics modeling of shock-induced ignition in low-dilution CH4/O2 mixtures at high pressures and intermediate temperatures, Combust. Flame 117 (1–2) (1999) 272–290, http://dx.doi.org/10.1016/S0010-2180(98)00111-4.

[24] N.A. Slavinskaya, M. Abbasi, M. Weinschenk, O.J. Haidn, Methane skeletal mechanism for space propulsion applications, in: 52nd AIAA/SAE/ASEE Joint Propulsion Conference, January, 2016.

[25] T. Poinsot, D. Veynante, in: edited by the authors (Ed.), Theorical and Numerical Combustion, Third Edition, edited by the authors, 2012.

[26] G. Ordonneau, L. Vingert, P. Grenard, N. Fdida, A rocket engine under a magnifying glass, Aerospacelab J. (11) (2016) http://dx.doi.org/10.12762/2016.AL11-15.

[27] R.W. Bilger, The structure of turbulent nonpremixed flames, in: Symposium (International) on Combustion, Vol. 22, (1) 1989, pp. 475–488, http://dx.doi.org/10.1016/S0082-0784(89)80054-2.

[28] Q. Cazères, P. Pepiot, E. Riber, B. Cuenot, A fully automatic procedure for the analytical reduction of chemical kinetics mechanisms for computational fluid dynamics applications, Fuel 303 (2021) 121247, http://dx.doi.org/10.1016/j.fuel.2021.121247.

[29] T. Løvås, Model reduction techniques for chemical mechanisms, in: Chemical Kinetics, InTech, 2012, pp. 79–114.

[30] D.G. Goodwin, H.K. Moffat, R.L. Speth, Cantera: An object-oriented software toolkit for chemical kinetics, thermodynamics, and transport processes, 2017, http://dx.doi.org/10.5281/zenodo.170284, Version 2.3.0, http://www.cantera.org.

[31] T. Schönfeld, M. Rudgyard, Steady and unsteady flow simulations using the hybrid flow solver AVBP, AIAA J. 37 (11) (1999) 1378–1385, http://dx.doi.org/10.2514/2.636.

[32] L.Y. Gicquel, N. Gourdain, J.F. Boussuge, H. Deniau, G. Staffelbach, P. Wolf, T. Poinsot, High performance parallel computing of flows in complex geometries, C. R. Mec. 339 (2–3) (2011) 104–124, http://dx.doi.org/10.1016/j.crme.2010.11.006.

[33] N. Gourdain, L. Gicquel, M. Montagnac, O. Vermorel, M. Gazaix, G. Staffelbach, M. Garcia, J.-F. Boussuge, T. Poinsot, High performance parallel computing of flows in complex geometries: I. methods, Comput. Sci. Discov. 2 (1) (2009) 015003, http://dx.doi.org/10.1088/1749-4699/2/1/015003.

[34] L. Selle, G. Lartigue, T. Poinsot, R. Koch, K.U. Schildmacher, W. Krebs, B. Prade, P. Kaufmann, D. Veynante, Compressible large eddy simulation of turbulent combustion in complex geometry on unstructured meshes, Combust. Flame 137 (4) (2004) 489–505, http://dx.doi.org/10.1016/j.combustflame.2004.03.008.

[35] A. Roux, S. Reichstadt, N. Bertier, L. Gicquel, F. Vuillot, T. Poinsot, Comparison of numerical methods and combustion models for LES of a ramjet, C. R. - Mec. 337 (6–7) (2009) 352–361, http://dx.doi.org/10.1016/j.crme.2009.06.008.

[36] A.M. Ruiz, G. Lacaze, J.C. Oefelein, R. Mari, B. Cuenot, L. Selle, T. Poinsot, Numerical benchmark for high-reynolds-number supercritical flows with large density gradients, AIAA J. 54 (5) (2016) 1445–1460, http://dx.doi.org/10.2514/1.J053931.

[37] B. Rochette, F. Collin-Bastiani, L. Gicquel, O. Vermorel, D. Veynante, T. Poinsot, Influence of chemical schemes, numerical method and dynamic turbulent combustion modeling on LES of premixed turbulent flames, Combust. Flame 191 (February) (2018) 417–430, http://dx.doi.org/10.1016/j.combustflame.2018.01.016.

[38] P. Lax, B. Wendroff, Systems of conservation laws, Commun. Pure Appl. Math. 13 (1) (1960) 217–237, http://dx.doi.org/10.1007/978-3-319-31238-5-11.

[39] F. Shum-Kivan, Simulation des Grandes Echelles de flammes de spray et modélisation de la combustion non-prémélangée, (Ph.D. thesis), Institut National Polytechnique de Toulouse, 2017.

[40] J. Pichillou, P. Grenard, L. Vingert, G. Leplat, P. Reulet, Experimental analysis of heat transfer in cryogenic combustion chambers on mascotte test bench, in: 7th European Conference for Aeronautics and Space Sciences, EUCASS, 2017, http://dx.doi.org/10.13009/EUCASS2017-260.

[41] F. Nicoud, H.B. Toda, O. Cabrit, S. Bose, J. Lee, Using singular values to build a subgrid-scale model for large eddy simulations, Phys. Fluids 23 (8) (2011) http://dx.doi.org/10.1063/1.3623274.

[42] G. Soave, Equilibrium constant from a modified redlich-kwong equation of state, Chem. Eng. Sci. 27 (6) (1972) 1197–1203, http://dx.doi.org/10.1016/0009-2509(72)80096-4.

[43] T. Schmitt, Large-eddy simulations of the mascotte test cases operating at supercritical pressure, Flow Turbul. Combust. 105 (1) (2020) 159–189.

[44] T. Poinsot, S. Lele, Boundary conditions for direct simulations of compressible viscous flows, J. Comput. Phys. 99 (2) (1992) 352, http://dx.doi.org/10.1016/0021-9991(92)90227-P.

[45] G. Daviller, G. Oztarlik, T. Poinsot, A generalized non-reflecting inlet boundary condition for steady and forced compressible flows with injection of vortical and acoustic waves, Comput. & Fluids 190 (2019) 503–513, http://dx.doi.org/10.1016/j.compfluid.2019.06.027.

[46] O. Cabrit, F. Nicoud, Direct simulations for wall modeling of multicomponent reacting compressible turbulent flows, Phys. Fluids 21 (5) (2009) 0–29, http://dx.doi.org/10.1063/1.3123528.

[47] H. Yamashita, M. Shimada, T. Takeno, A numerical study on flame stability at the transition point of jet diffusion flames, Symp. (Int.) Combust. 26 (1) (1996) 27–34, http://dx.doi.org/10.1016/S0082-0784(96)80196-2.

[48] P. Breda, M. Hansinger, M. Pfitzner, Chemistry computation without a sub-grid PDF model in LES of turbulent non-premixed flames showing moderate local extinction, in: Proceedings of the Combustion Institute, 2020, http://dx.doi.org/10.1016/j.proci.2020.06.161.

[49] N.N. Smirnov, V.B. Betelin, V.F. Nikitin, L.I. Stamov, D.I. Altoukhov, Accumulation of errors in numerical simulations of chemically reacting gas dynamics, Acta Astronautica 117 (2015) 338–355, http://dx.doi.org/10.1016/j.actaastro.2015.08.013.

Bibliography

[Abramzon and Sirignano, 1989] Abramzon, B. and Sirignano, W. (1989). Droplet vaporization model for spray combustion calculations. *International Journal of Heat and Mass Transfer*, 32(9):1605–1618. 51

[Bae et al., 2019] Bae, H. J., Lozano-Durán, A., Bose, S. T., and Moin, P. (2019). Dynamic slip wall model for large-eddy simulation. *Journal of Fluid Mechanics*, 859:400–432. 100

[Battista et al., 2015] Battista, F., Salvatore, V., Ricci, D., De Matteis, P., De Rose, L., and Ceccarelli, F. (2015). The italian LOX/LCH4 rocket engine technology demonstrator: achievements and outlook. In *66th International Astronautical Congress*, volume 10. 23

[Betelin et al., 2021] Betelin, V. B., Kryzhanovsky, B. V., Smirnov, N. N., Nikitin, V. F., Karandashev, I. M., Malsagov, M. Y., and Mikhalchenko, E. V. (2021). Neural network approach to solve gas dynamics problems with chemical transformations. *Acta Astronautica*, 180:58–65. 58

[Betti et al., 2016] Betti, B., Bianchi, D., Nasuti, F., and Martelli, E. (2016). Chemical Reaction Effects on Heat Loads of CH4/O2 and H2/O2 Rockets. *AIAA Journal*, 54(5):1693–1703. 116, 125

[Bilger, 1989] Bilger, R. W. (1989). The structure of turbulent nonpremixed flames. In *Symposium (International) on Combustion*, volume 22, pages 475–488. 44, 68

[Blanchard et al., 2022] Blanchard, S., Cazères, Q., and Cuenot, B. (2022). Chemical modeling for methane oxy-combustion in liquid rocket engines. *Acta Astronautica*, 190:98–111. 68, 74, 128, 132

[Blanchard and Cuenot, 2019] Blanchard, S. and Cuenot, B. (2019). Large eddy simulation of a single-injector lox/gch4 combustion chamber using analytically reduced chemistry. In *SFB/TRR 40 Summer Program 2019 booklet - Fundamental Technologies for the Development of Future Space-Transport-System Components under High Thermal and Mechanical Loads*, volume 1, pages 69–86. 151

[Blanchard et al., 2021] Blanchard, S., Odier, N., Gicquel, L., Cuenot, B., and Nicoud, F. (2021). Stochastic forcing for sub-grid scale models in wall-modeled large-eddy simulation. *Physics of Fluids*, 33. 101

[Breda et al., 2020] Breda, P., Hansinger, M., and Pfitzner, M. (2020). Chemistry computation without a sub-grid PDF model in LES of turbulent non-premixed flames showing moderate local extinction. In *Proceedings of the Combustion Institute*. 136

[Brent, 1993] Brent, R. (1993). *Algorithms for Minimization without Derivatives, Chapter 4*. Prentice-Hall, Englewood Cliffs. 100

[Bryce Space and Technology, 2017] Bryce Space and Technology (2017). 2017 Global Satellite Economy. Technical report, BryceTech. 17

[Bryce Space and Technology, 2019a] Bryce Space and Technology (2019a). 2019 Orbital Launches Year in Review. Technical report, BryceTech. 16

[Bryce Space and Technology, 2019b] Bryce Space and Technology (2019b). State of the Satellite Industry 2019. Technical report, BryceTech. 15

[Cabrit, 2010] Cabrit, O. (2010). *Modélisation des flux pariétaux sur les tuyères des moteurs à propergol solide*. PhD thesis, Université de Montpellier II. 97, 99

[Cabrit and Nicoud, 2009] Cabrit, O. and Nicoud, F. (2009). Direct simulations for wall modeling of multicomponent reacting compressible turbulent flows. *Physics of Fluids*, 21(5):0–29. 100, 117, 118, 125, 131, 154

[Cailler et al., 2017] Cailler, M., Darabiha, N., Veynante, D., and Fiorina, B. (2017). Building-up virtual optimized mechanism for flame modeling. In *Proceedings of the Combustion Institute*, volume 36, pages 1251–1258. 58

[Candel et al., 2006] Candel, S., Juniper, M., Singla, G., Scouflaire, P., and Rolon, C. (2006). Structure and dynamics of cryogenic flames at supercritical pressure. *Combustion Science and Technology*, 178(1-3):161–192. 23, 127

[Carstensen and Dean, 2007] Carstensen, H.-H. and Dean, A. M. (2007). *The Kinetics of Pressure-Dependent Reactions*, volume 42. Elsevier B.V. 59

[Caudal et al., 2013] Caudal, J., Fiorina, B., Massot, M., Labegorre, B., Darabiha, N., and Gicquel, O. (2013). Characteristic chemical time scales identification in reactive flows. In *Proceedings of the Combustion Institute*, volume 34, pages 1357–1364. 36

[Cazères, 2021] Cazères, Q. (2021). *Analysis and reduction of chemical kinetics for combustion applications*. PhD thesis, Institut National Polytechnique de Toulouse. 72

[Cazères et al., 2021] Cazères, Q., Pepiot, P., Riber, E., and Cuenot, B. (2021). A fully automatic procedure for the analytical reduction of chemical kinetics mechanisms for computational fluid dynamics applications. *Fuel*, 303:121247. 68, 175, 181

[Chapman and Kuhn, 1986] Chapman, D. R. and Kuhn, G. D. (1986). The limiting behaviour of turbulence near a wall. *Journal of Fluid Mechanics*, 170:265–292. 96

[Chen et al., 2000] Chen, J., Blasco, J., Fueyo, N., and Dopazo, C. (2000). An economical strategy for storage of chemical kinetics: Fitting in situ adaptive tabulation with artificial neural networks. *Proceedings of the Combustion Institute*, 28:115–121. 58

[Choi and Moin, 2012] Choi, H. and Moin, P. (2012). Grid-point requirements for large eddy simulation: Chapman's estimates revisited. *Physics of Fluids*, 24(1):1–6. 96

[Chung et al., 1988] Chung, H.-T., Ajlan, M., Lee, L. L., and Starling, K. E. (1988). Generalized Multiparameter Correlation for Nonpolar and Polar Fluid Transport Properties. *Industrial and Engineering Chemistry Research*, 27(4):671–679. 39

[Clift et al., 1978] Clift, R., Grace, J., and Weber, M. (1978). *Bubbles, Drops, and Particles.* Dover Publications, Inc. Mineola, New York. 51

[Colin et al., 2000] Colin, O., Ducros, F., Veynante, D., and Poinsot, T. (2000). A thickened flame model for large eddy simulations of turbulent premixed combustion. *Physics of Fluids*, 12(7):1843–1863. 28, 82, 153

[Colin and Rudgyard, 2000] Colin, O. and Rudgyard, M. (2000). Development of High-Order Taylor-Galerkin Schemes for LES. *Journal of Computational Physics*, 162(2):338–371. 47

[Collin-Bastiani, 2019] Collin-Bastiani, F. (2019). *Modeling and Large Eddy Simulation of Two-Phase Ignition in Gas Turbines.* PhD thesis, Institut National Polytechnique de Toulouse. 52

[Cuenot and Poinsot, 1994] Cuenot, B. and Poinsot, T. (1994). Effects of curvature and unsteadiness in diffusion flames. Implications for turbulent diffusion combustion. In *Symposium (International) on Combustion*, volume 25, pages 1383–1390. 46

[Cuenot et al., 2021] Cuenot, B., Shum-Kivan, F., and Blanchard, S. (2021). The thickened flame approach for non-premixed combustion: Principles and implications for turbulent combustion modeling. *Combustion and Flame*, page 111702. 83

[Dauptain, 2006] Dauptain, A. (2006). *Allumage des moteurs fusées cryotechniques.* PhD thesis, Institut National Polytechnique de Toulouse. 25

[Daviller et al., 2019] Daviller, G., Oztarlik, G., and Poinsot, T. (2019). A generalized non-reflecting inlet boundary condition for steady and forced compressible flows with injection of vortical and acoustic waves. *Computers and Fluids*, 190:503–513. 130, 154

[Desjardins et al., 2008] Desjardins, O., Moureau, V., and Pitsch, H. (2008). An accurate conservative level set/ghost fluid method for simulating turbulent atomization. *Journal of Computational Physics*, 227(18):8395–8416. 26, 49

[Dumont et al., 2021] Dumont, E., Ishimoto, S., Tatiossian, P., Klevansli, J., Reimann, B., Ecker, T., Witte, L., Riehmer, J., Sagliano, M., Giagkozoglou Vincenzino, S., Petkov, I., Rotärmel, W., Schwarz, R., Seelbinder, D., Markgraf, M., Sommer, J., Pfau, D., and Martens, H. (2021). CALLISTO: A Demonstrator for Reusable Launcher Key Technologies. Technical Report 1, DLR, JAXA and CNES. 16

[Ern and Giovangigli, 1994] Ern, A. and Giovangigli, V. (1994). *Mutlicomponent Transport Algorithm.* Springer Verlag, Heidelberg. 38

[Esclapez, 2015] Esclapez, L. (2015). *Numerical study of ignition and inter-sector flame propagation in gas turbine.* PhD thesis, Institut National Polytechnique de Toulouse. 44, 46

[Felden, 2013] Felden, A. (2013). *Development of Analytically Reduced Chemistries (ARC) and applications in Large Eddy Simulations (LES) of turbulent combustion.* PhD thesis, Institut National Polytechnique de Toulouse. 72, 74

[Felden et al., 2019] Felden, A., Pepiot, P., Esclapez, L., Riber, E., and Cuenot, B. (2019). Including analytically reduced chemistry (ARC) in CFD applications. *Acta Astronautica*, 158:444–459. 137

[Foster and Miller, 2010] Foster, J. and Miller, R. S. (2010). Fundamentals of High Pressure Combustion. *High Pressure Processes in Chemical Engineering*, (January 2010):53–75. 59

[Franzelli et al., 2010] Franzelli, B., Riber, E., Sanjosé, M., and Poinsot, T. (2010). A two-step chemical scheme for kerosene-air premixed flames. *Combustion and Flame*, 157(7):1364–1373. 57

[Frassoldati et al., 2009] Frassoldati, a., Cuoci, A., and Faravelli, T. (2009). Simplified kinetic schemes for oxy-fuel combustion. In *1st International Conference on Sustainable Fossil Fuels for Future Energy*, number January, pages 1–14. 57

[Freeman et al., 1997] Freeman, D. C., Talay, T. A., and Austin, R. E. (1997). Reusable launch vehicle technology program. *Acta Astronautica*, 41(11):777–790. 16

[Frohn and Roth, 2000] Frohn, A. and Roth, N. (2000). *Dynamics of Droplets*. Springer Verlag, New York. 50

[Ge et al., 2019] Ge, Y., Li, S., and Wei, X. (2019). Combustion states distinction of the methane/oxygen laminar co-flow diffusion flame at high pressure. *Fuel*, 243(January):221–229. 59

[Ghanbari et al., 2017] Ghanbari, M., Ahmadi, M., and Lashanizadegan, A. (2017). A comparison between Peng-Robinson and Soave-Redlich-Kwong cubic equations of state from modification perspective. *Cryogenics*, 84(September):13–19. 33

[Gicquel and Poinsot, 2011] Gicquel, L. and Poinsot, T. (2011). *The AVBP HandBook*. 47

[Gicquel et al., 2011] Gicquel, L. Y., Gourdain, N., Boussuge, J. F., Deniau, H., Staffelbach, G., Wolf, P., and Poinsot, T. (2011). High performance parallel computing of flows in complex geometries. *Comptes Rendus Mecanique*, 339(2-3):104–124. 29, 47

[Gilbert et al., 1983] Gilbert, R. G., Luther, K., and Troe, J. (1983). Theory of Thermal Unimolecular Reactions in the Fall-off Range. II. Weak Collision Rate Constants. *Berichte der Bunsengesellschaft für physikalische Chemie*, 87(2):169–177. 60

[Giovangigli, 1999] Giovangigli, V. (1999). *Mutlicomponent Flow Modeling*. Modeling and Simulation in Science, Engineering and Technology. Birkauser, Boston. 38

[Goodwin et al., 2017] Goodwin, D. G., Moffat, H. K., and Speth, R. L. (2017). Cantera: An object-oriented software toolkit for chemical kinetics, thermodynamics, and transport processes. `http://www.cantera.org`. Version 2.3.0. 29, 69

[Gourdain et al., 2009] Gourdain, N., Gicquel, L., Montagnac, M., Vermorel, O., Gazaix, M., Staffelbach, G., Garcia, M., Boussuge, J.-F., and Poinsot, T. (2009). High performance parallel computing of flows in complex geometries: I. methods. *Computational Science & Discovery*, 2(1):015003. 29, 47

[Grenard et al., 2019] Grenard, P., Fdida, N., Vingert, L., Dorey, L.-h., Pichillou, J., Grenard, P., Fdida, N., Vingert, L., Dorey, L.-h., and Selle, L. (2019). Experimental investigation of heat transfer in a subscale liquid rocket engine at high mixture ratio. *Journal of Propulsion and Power*, 35:544–551. 23, 127

[Habiballah et al., 2006] Habiballah, M., Orain, M., Grisch, F., Vingert, L., and Gicquel, P. (2006). Experimental studies of high-pressure cryogenic flames on the mascotte facility. *Combustion Science and Technology*, 178(1-3):101–128. 23, 127

[Halter et al., 2020a] Halter, F., Chen, Z., Dayma, G., Bariki, C., Wang, Y., Dagaut, P., and Chauveau, C. (2020a). Development of an optically accessible apparatus to characterize the evolution of spherically expanding flames under constant volume conditions. *Combustion and Flame*, 212:165–176. 61

[Halter et al., 2020b] Halter, F., Dayma, G., Serinyel, Z., Dagaut, P., and Chauveau, C. (2020b). Laminar flame speed determination at high pressure and temperature conditions for kinetic schemes assessment. In *Proceedings of the Combustion Institute*, volume 000, pages 1–9. Elsevier Inc. 28, 61

[He et al., 2011] He, B., Nie, W. S., Feng, S. J., and Li, G. Q. (2011). A modified implicit iterative difference algorithm for stiff chemical kinetic equations in complex combustion system. *Advanced Materials Research*, 295-297:2333–2340. 73

[Hickey and Ihme, 2013] Hickey, J. and Ihme, M. (2013). Supercritical mixing and combustion in rocket propulsion. *Center for Turbulent Research*, pages 21–36. 26, 27

[Hirschfelder et al., 1969] Hirschfelder, J., Curtiss, C., and Bird, R. (1969). *Molecular theory of gases and liquids*. Wiley-Blackwell. 37

[Hirt and Nichols, 1981] Hirt, C. and Nichols, B. (1981). Volume of Fluid (VOF) Method for the Dynamics of Free Boundaries. *Journal of Computational Physics*, 39:201–225. 26, 49

[Hopfinger, 2001] Hopfinger, E. (2001). Atomisation d'un jet liquide par un jet de gaz coaxial : un bilan des connaissances acquises. In Cepadues, editor, *Combustion dans les moteurs fusee*, pages 33–47. CNES. 156

[Jamet, 1995] Jamet, D. (1995). Numerical description of a liquid-vapor interface based on the second gradient. *Fluid Mechanics Research*, 22. 27

[Jofre and Urzay, 2021] Jofre, L. and Urzay, J. (2021). Transcritical diffuse-interface hydrodynamics of propellants in high-pressure combustors of chemical propulsion systems. *Progress in Energy and Combustion Science*, 82. 26, 27

[Jones, 2018] Jones, H. W. (2018). The Recent Large Reduction in Space Launch Cost. In *48th International Conference on Environmental Systems*, number July, pages 1–10. 15, 16

[Jones and Lindstedt, 1988] Jones, W. P. and Lindstedt, R. P. (1988). Global reaction schemes for hydrocarbon combustion. *Combustion and Flame*, 73(3):233–249. 158, 160

[Joo et al., 2013] Joo, P. H., Charest, M. R., Groth, C. P., and Gülder, Ö. L. (2013). Comparison of structures of laminar methane-oxygen and methane-air diffusion flames from atmospheric to 60atm. *Combustion and Flame*, 160(10):1990–1998. 59

[Kader, 1981] Kader, B. A. (1981). Temperature and concentration profiles in fully turbulent boundary layers. *International Journal of Heat and Mass Transfer*, 24(9):1541–1544. 99

[Kays and Crawford, 1993] Kays, W. and Crawford, M. (1993). *Convective heat and mass transfer*. McGraw-Hill. 115

[Kee et al., 1985] Kee, R. J., Petzold, L. R., Smooke, M. D., and Grcar, J. F. (1985). 5 - Implicit Methods in Combustion and Chemical Kinetics Modeling. In Brackbill, J. U. and Cohen, B. I., editors, *Multiple Time Scales*, pages 113–144. Academic Press. 74

[Kitano, T. and Kaneko, K. and Kurose, R. and Komori, S., 2016] Kitano, T. and Kaneko, K. and Kurose, R. and Komori, S. (2016). Large-eddy simulations of gas- and liquid-fueled combustion instabilities in back-step flows. *Combustion and Flame*, (170):63–78. 28

[Kolmogorov, 1941] Kolmogorov, A. (1941). The local structure of turbulence in incompressible viscous fluid for very large Reynolds numbers. *Proceedings of the Royal Society of London. Series A: Mathematical and Physical Sciences*, 434(1890):9–13. 39

[Kraus et al., 2018] Kraus, C., Selle, L., and Poinsot, T. (2018). Coupling heat transfer and large eddy simulation for combustion instability prediction in a swirl burner. *Combustion and Flame*, 191:239–251. 28

[Kwak and Mansoori, 1986] Kwak, T. Y. and Mansoori, G. a. (1986). Rules for Cubic Equations. *Chemical Engineering Science*, 41(5):1303–1986. 33

[Lacaze, 2009] Lacaze, G. (2009). *Simulation aux Grandes Echelles de l'allumage de moteurs fusees cryotechniques*. PhD thesis, Institut National Polytechnique de Toulouse. 25

[Lamarque, 2007] Lamarque, N. (2007). *Schémas numériques et conditions limites pour la simulation aux grandes échelles de la combustion diphasique dans les foyers d ' hélicoptère*. PhD thesis, Institut National Polytechnique de Toulouse. 47

[Larsson et al., 2016] Larsson, J., Kawai, S., Bodart, J., and Bermejo-Moreno, I. (2016). Large eddy simulation with modeled wall-stress: recent progress and future directions. *Mechanical Engineering Reviews*, 3(1):15–00418. 96

[Launder and Spalding, 1974] Launder, B. E. and Spalding, D. B. (1974). The numerical computation of turbulent flows. *Computer Methods in Applied Mechanics and Engineering*, 3(2):269–289. 98

[Laurent et al., 2018] Laurent, C., Esclapez, L., Maestro, D., Staffelbach, G., Cuenot, B., Selle, L., Schmitt, T., Duchaine, F., and Poinsot, T. (2018). Flame-wall interaction effects on the flame root stabilization mechanisms of a doubly-transcritical LO2/LCH4cryogenic flame. In *Proceedings of the Combustion Institute*, volume 000, pages 1–8. Elsevier Inc. 59

[Laurent et al., 2021] Laurent, C., Staffelbach, G., Nicoud, F., and Poinsot, T. (2021). Heat-release dynamics in a doubly-transcritical LO2/LCH4 cryogenic coaxial jet flame subjected to fuel inflow acoustic modulation. In *Proceedings of the Combustion Institute*, volume 38, pages 6375–6383. Elsevier Inc. 59

[Lax and Wendroff, 1960] Lax, P. and Wendroff, B. (1960). Systems of conservation laws. *Communication on pure and applied mathematics*, 13(1):217–237. 47, 76, 94, 129, 153

[Le Touze et al., 2020] Le Touze, C., Dorey, L. H., Rutard, N., and Murrone, A. (2020). A compressible two-phase flow framework for Large Eddy Simulations of liquid-propellant rocket engines. *Applied Mathematical Modelling*, 84:265–286. 27

[Legier et al., 2000] Legier, J. P., Poinsot, T., and Veynante, D. (2000). Dynamically thickened flame LES model for premixed and non-premixed turbulent combustion. In *Proceedings of the Summer Program, Centre for Turbulence Research*, pages 157–168. 28

[Lemmon and Penoncello, 1994] Lemmon, E. W. and Penoncello, S. G. (1994). The Surface Tension of Air and Air Component Mixtures. *Advances in Cryogenic Engineering*, 39:1927–1934. 155

[Løvås, 2012] Løvås, T. (2012). Model Reduction Techniques for Chemical mechanisms. In *Chemical Kinetics*, pages 79–114. InTech. 68

[Lu and Law, 2006] Lu, T. and Law, C. (2006). Systematic approach to obtain analytic solutions of quasi steady state species in reduced mechanisms. *Journal of Physical Chemistry A*, 110(49):13202–13208. 58

[Lund, 2003] Lund, T. S. (2003). The Use of Explicit Filters in Large Eddy Simulation. *Computers and Mathematics with Applications*, 46(4):603–616. 40

[Maestro, 2018] Maestro, D. (2018). *Large Eddy Simulations of the interactions between flames and thermal phenomena: application to wall heat transfer and combustion control*. PhD thesis, Institut National Polytechnique de Toulouse. 100, 175

[Maestro et al., 2019] Maestro, D., Cuenot, B., and Selle, L. (2019). Large Eddy Simulation of Combustion and Heat Transfer in a Single Element GCH4/GOx Rocket Combustor. *Flow, Turbulence and Combustion*. 59, 68, 72, 95

[Maio et al., 2017] Maio, G., Mercier, R., Cailler, M., and Fiorina, B. (2017). Virtual chemistry for prediction of chemical flame structure in non adiabatic combustion. In *8th European Combustion Meeting*, number April. 58

[Mari, 2015] Mari, R. (2015). *Influence des transferts thermiques sur la structure et la stabilisation de flamme à haute pression dans les moteurs fusées cryothechniques*. PhD thesis, Institut National Polytechnique de Toulouse. 61

[Marmottant and Villermaux, 2004] Marmottant, P. H. and Villermaux, E. (2004). On spray formation. *Journal of Fluid Mechanics*, 498(498):73–111. 157

[Martin-Benito, 2019] Martin-Benito, M. (2019). Note synthèse calculs WP2000 2019. Technical report, CNES. 131, 179

[Martinez, 2009] Martinez, M. G. (2009). *Development and validation of the Euler-Lagrange formulation on a parallel and unstructured solver for large-eddy simulation*. PhD thesis, Institut National Polytechnique de Toulouse. 54

[Mathew et al., 2003] Mathew, J., Lechner, R., Foysi, H., Sesterhenn, J., and Friedrich, R. (2003). An explicit filtering method for large eddy simulation of compressible flows. *Physics of Fluids*, 15(8):2279–2289. 48

[Mazas, 2010] Mazas, A. (2010). *Etude des flammes prémélangées enrichies en oxygéne: analyse des effets de dilution par la vapeur d'eau et le dioxyde de carbone*. PhD thesis, Ecole Centrale Paris. 61

[Meyer et al., 2017] Meyer, S. E., Heister, S. D., Slabaugh, C., Lucht, R. P., Pratt, A., Gejji, R. M., Bedard, M., and Lemcherfi, A. (2017). Design and development of the high pressure combustion laboratory at Purdue University. *53rd AIAA/SAE/ASEE Joint Propulsion Conference, 2017*, (July):1–9. 61

[Muscatello and Santiago-Maldonado, 2012] Muscatello, A. C. and Santiago-Maldonado, E. (2012). Mars In Situ Resource Utilization technology evaluation. *50th AIAA Aerospace Sciences Meeting Including the New Horizons Forum and Aerospace Exposition*, (January):1–13. 22

[Muto et al., 2018] Muto, D., Daimon, Y., Shimizu, T., and Negishi, H. (2018). Wall modeling of reacting turbulent flow and heat transfer in liquid rocket engines Downloaded. In *2018 AIAA Joint Propulsion Conference*, pages 1–9. 117

[Muto et al., 2019] Muto, D., Daimon, Y., Shimizu, T., and Negishi, H. (2019). An equilibrium wall model for reacting turbulent flows with heat transfer. *International Journal of Heat and Mass Transfer*, 141:1187–1195. 117, 125

[NASA, 2004] NASA, G. R. C. (2004). A History of the Rocket Engine Test Facility at the NASA Glenn Research Center. Technical report. 23

[Nayigizente et al., 2021] Nayigizente, D., Schmitt, T., Ducruix, S., Nayigizente, D., Schmitt, T., and Ducruix, S. (2021). Development of an interface thickening method for the direct numerical simulation of compressible liquid-vapor flows in the framework of the Second Gradient theory. *Physics of Fluids*, 33(5). 27

[Nicoud and Ducros, 1999] Nicoud, F. and Ducros, F. (1999). Subgrid-scale stress modelling based on the square of the velocity gradient tensor. *Flow, Turbulence and Combustion*, 62(3):183–200. 42, 100

[Nicoud et al., 2011] Nicoud, F., Toda, H. B., Cabrit, O., Bose, S., and Lee, J. (2011). Using singular values to build a subgrid-scale model for large eddy simulations. *Physics of Fluids*, 23(8). 43, 100, 129, 153

[Nikuradse, 1933] Nikuradse, J. (1933). Strömungsgesetze in rauhen rohren. *Forschungsheft auf dem Gebiete des Ingenieurwesens*. 115

[Oefelein and Yang, 1998] Oefelein, J. C. and Yang, V. (1998). Modeling high-pressure mixing and combustion processes in liquid rocket engines. *Journal of Propulsion and Power*, 14(5):843–857. 59

[Ordonneau et al., 2016] Ordonneau, G., Vingert, L., Grenard, P., and Fdida, N. (2016). A Rocket Engine under a Magnifying Glass. *Aerospacelab Journal*, (11). 68, 127, 128

[Oschwald et al., 2006] Oschwald, M., Cuoco, F., Yang, B., and Rosa, M. D. (2006). Untersuchungen zur Zerstäubung und Verbrennung in kryogenen LOx/H2- und LOx/CH4-Sprayflammen. Technical report, DLR. 23

[Palerm et al., 2015] Palerm, S., Bonhomme, C., Petitot, S., Jn, C., and Dreyer, S. (2015). CNES Future Preparation for Liquid Propulsion. In *51st AIAA/SAE/ASEE Joint Propulsion Conference*, pages 1–7. 127

[Patureau de Mirand et al., 2020] Patureau de Mirand, A., Bahu, J. M., and Gogdet, O. (2020). Ariane Next, a vision for the next generation of Ariane Launchers. *Acta Astronautica*, 170(February):735–749. 17

[Pelletier, 2019] Pelletier, M. (2019). *Diffuse interface models and adapted numerical schemes for the simulation of subcritical to supercritical flow.* PhD thesis, Université Paris-Saclay, Centrale Supélec. 26, 49

[Peng and Robinson, 1976] Peng, D. Y. and Robinson, D. B. (1976). A New Two-Constant Equation of State. *Industrial and Engineering Chemistry Fundamentals*, 15(1):59–64. 33

[Perakis et al., 2017] Perakis, N., Celano, M. P., and Haidn, O. J. (2017). Heat flux and temperature evaluation in a rectangular multi-element GOX / GCH 4 combustion chamber using an inverse heat conduction method. In *7th European Conference for Aeronautics and Space Sciences (EUCASS)*. 23, 151

[Perakis et al., 2020] Perakis, N., Haidn, O. J., and Ihme, M. (2020). Investigation of CO recombination in the boundary layer of CH4/O2 rocket engines. In *Proceedings of the Combustion Institute*, volume 000, pages 1–9. Elsevier Inc. 116, 117, 125

[Pestre et al., 2021] Pestre, A., Cuenot, B., and Riber, E. (2021). Evaluation of numerical methods for explicit chemistry integration and application on DNS of turbulent kerosene ignition at high altitude conditions. In *European Combustion Meeting*. 81, 175

[Petersen et al., 1999] Petersen, E. L., Davidson, D. F., and Hanson, R. K. (1999). Kinetics modeling of shock-induced ignition in low-dilution CH4/O2 mixtures at high pressures and intermediate temperatures. *Combustion and Flame*, 117(1-2):272–290. 60, 68, 158, 181

[Pichillou et al., 2017] Pichillou, J., Grenard, P., Vingert, L., Leplat, G., and Reulet, P. (2017). Experimental analysis of heat transfer in cryogenic combustion chambers on Mascotte test bench. In *7th European Conference for Aeronautics and Space Sciences (EUCASS)*. 23, 127

[Piomelii et al., 1991] Piomelii, U., Cabot, W. H., Moin, P., and Lee, S. (1991). Subgrid-sclae backscatter in turbulent and transitional flows. *Physics of Fluids*, pages 1766–1771. 42

[Piomelli, 2008] Piomelli, U. (2008). Wall-layer models for large-eddy simulations. *Progress in Aerospace Sciences*, 44(6):437–446. 96

[Pitzer, 1955] Pitzer, K. S. (1955). The Volumetric and Thermodynamic Properties of Fluids. I. Theoretical Basis and Virial Coefficients. *Journal of the American Chemical Society*, 77(13):3427–3433. 34

[Poinsot and Lele, 1992] Poinsot, T. and Lele, S. (1992). Boundary conditions for direct simulations of compressible viscous flows. *Journal of Computational Physics*, 99(2):352. 130, 154

[Poinsot and Veynante, 2012] Poinsot, T. and Veynante, D. (2012). *Theorical and Numerical Combustion, third edition.* edited by the authors. 31, 44, 45, 58, 60, 68, 69

[Potier, 2018] Potier, L. (2018). *Large Eddy Simulation of the combustion and heat transfer in sub-critical rocket engines.* PhD thesis, Institut National Polytechnique de Toulouse. 24, 49, 55, 100, 117, 155, 173, 175

[Potier et al., 2018] Potier, L., Cuenot, B., Saucereau, D., Pichiliou, J., and Grenard, P. (2018). Modeling liquid injection in cryogenic rocket engine simulation. unpublished. 156

[Powell et al., 1998] Powell, R. W., Lockwood, M. K., and Cook, S. a. (1998). The Road from the NASA Access-to-Space Study to a Reusable Launch Vehicle. In *49th International Astronautical Congress.* 16

[Preclik et al., 2005] Preclik, D., Hagemann, H., O., K., Maeding, C., Haeseler, D., Haidn, O., Woschnak, A., and DeRosa, M. (2005). LOX/hydrocarbon preparatory thrust chamber technology activities in Germany. In *41st AIAA/ASME/SAE/ASEE Joint Propulsion Conference and Exhibit*, number July, pages 1–15. 23, 68

[Preuss et al., 2008] Preuss, A., Preclik, D., Mading, C., Gorgen, J., Soller, S., Haidn, O., Oschwald, M., Clauss, W., Arnold, R., and Sender, J. (2008). LOX/Methane Technology Efforts for Future Liquid Rocket Engines. In *5th International Spacecraft Propulsion Conference & 2nd International Symposium on Propulsion for Space Transportation*, number May. 23

[Proch et al., 2017] Proch, F., Domingo, P., Vervisch, L., and Kempf, A. (2017). Flame resolved simulation of a turbulent premixed bluff-body burner experiment. part ii: A-priori and a-posteriori investigation of sub-grid scale wrinkling closures in the context of artifcially thickened flame modeling. *Combustion and Flame*, (180):340–350. 28

[Ranz and Marshall, 1952] Ranz, W. and Marshall, W. (1952). Evaporation from drops. *Chem. Eng. Prog.*, 4. 52, 53

[Ranzi et al., 2014] Ranzi, E., Frassoldati, A., Stagni, A., Pelucchi, M., Cuoci, A., and Faravelli, T. (2014). Reduced kinetic schemes of complex reaction systems: Fossil and biomass-derived transportation fuels. *International Journal of Chemical Kinetics*, 46(9):512–542. 61

[Rezaeiravesh et al., 2019] Rezaeiravesh, S., Mukha, T., and Liefvendahl, M. (2019). Systematic study of accuracy of wall-modeled large eddy simulation using uncertainty quantification techniques. *Computers and Fluids*, 185(October):34–58. 100

[Ribert et al., 2017] Ribert, G., Petit, X., and Domingo, P. (2017). High-pressure methane-oxygen flames. Analysis of sub-grid scale contributions in filtered equations of state. *Journal of Supercritical Fluids*, 121:78–88. 58

[Rocchi, 2012] Rocchi (2012). *Simulations Aux Grandes Echelles De La Phase D'Allumage Dans Un Moteur Fusee Cryotechnique.* PhD thesis, Institut National Polytechnique de Toulouse. 83

[Rochette et al., 2020] Rochette, B., Riber, E., Cuenot, B., and Vermorel, O. (2020). A generic and self-adapting method for flame detection and thickening in the thickened flame model. *Combustion and Flame*, 212:448–458. 28, 83

[Sagaut, 2006] Sagaut, P. (2006). *Large Eddy Simulation for Incompressible Flows.* Springer. 39, 40

[Sankaran et al., 2007] Sankaran, R., Hawkes, E. R., Chen, J. H., Lu, T., and Law, C. K. (2007). Structure of a spatially developing turbulent lean methane-air Bunsen flame. In *Proceedings of the Combustion Institute*, volume 31 I, pages 1291–1298. 58

[Savard et al., 2015] Savard, B., Xuan, Y., Bobbitt, B., and Blanquart, G. (2015). A computationally-efficient, semi-implicit, iterative method for the time-integration of reacting flows with stiff chemistry. *Journal of Computational Physics*, 295:740–769. 74

[Schlichting and Gersten, 1979] Schlichting, H. and Gersten, K. (1979). *Boundary-Layer Theory*. Springer Berlin Heidelberg. 97

[Schmitt, 2020] Schmitt, T. (2020). Large-Eddy Simulations of the Mascotte test cases operating at supercritical pressure. *Flow, Turbulence and Combustion*, 105(1):159–189. 48, 58, 129, 153

[Schönfeld and Rudgyard, 1999] Schönfeld, T. and Rudgyard, M. (1999). Steady and unsteady flow simulations using the hybrid flow solver avbp. *AIAA Journal*, 37(11):1378–1385. 29, 47

[Shum-Kivan, 2017] Shum-Kivan, F. (2017). *Simulation des Grandes Echelles de flammes de spray et modélisation de la combustion non-prémélangée*. PhD thesis, Institut National Polytechnique de Toulouse. 79, 82, 153

[Silvestri et al., 2016] Silvestri, S., Celano, M. P., Schlieben, G., and Haidn, O. J. (2016). Characterization of a Multi-Injector GOX/CH4 Combustion Chamber. In *52nd AIAA/SAE/ASEE Joint Propulsion Conference*, pages 1–14. 23, 116, 151

[Silvestri et al., 2014] Silvestri, S., Celano, M. P., Schlieben, G., Kirchberger, C., and Haidn, O. J. (2014). Characterization of a GOX-GCH4 Single Element Combustion Chamber. In *Space Propulsion 2014*, volume 1. 23, 151

[Silvestri et al., 2017] Silvestri, S., Winter, F., Garulli, M., Celano, M. P., Schlieben, G., Haidn, O., Knab, O., and München, G. (2017). Investigation on Recess Variation of a Shear Coaxial Injector in a GOX - GCH4 Rectangular Combustion Chamber with Optical Access. In *7th European Conference for Aeronautics and Space Sciences (EUCASS)*. 26

[Silvestry et al., 2018] Silvestry, S., Kirchberger, C., Schlieben, G., CEelao, M. P., and Haidn, O. (2018). Experimental and Numerical Investigation of a Multi-Injector GOX-GCH4 Combustion Chamber. *Transactions of the Japan Society for Aeronautical and Space Sciences, Aerospace Technology Japan*, 16(5):374–381. 116

[Simontacchi et al., 2018] Simontacchi, P., Edeline, E., Blasi, R., Sagnier, S., Ravier, N., Espinosa-Ramos, A., and Breteau, J. (2018). Prometheus: Precursor of new low-cost rocket engine family. In *Proceedings of the International Astronautical Congress, IAC*, volume 2018-Octob, pages 1–12. 22

[Singla et al., 2005] Singla, G., Scouflaire, P., Rolon, C., and Candel, S. (2005). Transcritical oxygen/transcritical or supercritical methane combustion. In *Proceedings of the Combustion Institute*, volume 30 II, pages 2921–2928. The Combustion Institute. 23

[Slavinskaya et al., 2016] Slavinskaya, N. A., Abbasi, M., Weinschenk, M., and Haidn, O. J. (2016). Methane Skeletal Mechanism for Space Propulsion Applications. In *52nd AIAA/SAE/ASEE Joint Propulsion Conference*, number January. 68

[Slotnick et al., 2014] Slotnick, J., Khodadoust, A., Alonso, J., Darmofal, D., Gropp, W., Lurie, E., and Mavriplis, D. (2014). CFD Vision 2030 Study: A Path to Revolutionary Computational Aerosciences. Technical Report March, NASA. 23

[Smagorinsky, 1963] Smagorinsky, J. (1963). General Circulation Experiments With the Primitive Equations. *Monthly Weather Review*, 91(3):99–164. 42

[Smirnov et al., 2015] Smirnov, N. N., Betelin, V. B., Nikitin, V. F., Stamov, L. I., and Altoukhov, D. I. (2015). Accumulation of errors in numerical simulations of chemically reacting gas dynamics. *Acta Astronautica*, 117:338–355. 136

[Smith et al., 2016] Smith, G., Tao, Y., and Wang, H. (2016). Foundational Fuel Chemistry Model Version 1.0 mechanism website. 60

[Smith et al., 1999] Smith, G. P., Golden, D. M., Frenklach, M., Moriarty, N. W., Boris Eiteneer, M. G., Bowman, C. T., Hanson, R. K., Song, S., Gardiner, W. C., Lissianski, V. V., and Qin, Z. (1999). GRI3.0 mechanism website. 60, 68

[Soave, 1972] Soave, G. (1972). Equilibrium constant from a modified Redlich-Kwong equation of state. *Chemical Engineering Science*, 27(6):1197–1203. 33, 129, 153

[Son et al., 2017] Son, M., Radhakrishnan, K., Yoon, Y., and Koo, J. (2017). Numerical study on the combustion characteristics of a fuel-centered pintle injector for methane rocket engines. *Acta Astronautica*, 135(January):139–149. 59

[Song and Sun, 2016] Song, J. and Sun, B. (2016). Coupled numerical simulation of combustion and regenerative cooling in lox/methane rocket engines. *Applied Thermal Engineering*, 106:762–773. 59

[Spalding, 1953] Spalding, D. B. (1953). Combustion of liquid fuels. *Symposium (international) on combustion*, 4:847–864. 51

[Strakey and Eggenspieler, 2010] Strakey, P. and Eggenspieler, G. (2010). Development and validation of a thickened flame modeling approach for large eddy simulation of premixed combustion. *J. Eng. Gas Turb. and Power*, 7(132). 28

[Strauss, 2020] Strauss, J. (2020). Development of Global Chemical Reaction Scheme for Methane and Oxygen in Rocket Applications to be Used in Large-Eddy Simulation. Technical report, CERFACS. 157, 184, 213

[Tancin et al., 2019] Tancin, R. J., Mathews, G. C., and Goldenstein, C. S. (2019). Design and application of a high-pressure combustion chamber for studying propellant flames with laser diagnostics. *Review of Scientific Instruments*, 90(4). 61

[Tatiossian et al., 2017] Tatiossian, P., Desmariaux, J., and Garcia, M. (2017). CALLISTO project - reusable first stage rocket demonstrator. In *7th European Conference for Aeronautics and Space Sciences (EUCASS)*. 16

[Urbano et al., 2016] Urbano, A., Selle, L., Staffelbach, G., Cuenot, B., Schmitt, T., Ducruix, S., and Candel, S. (2016). Exploration of combustion instability triggering using Large Eddy Simulation of a multiple injector liquid rocket engine. *Combustion and Flame*, 169:129–140. 28

[Vingert et al., 2019] Vingert, L., Fdida, N., and Mauriot, Y. (2019). Experimental Investigations of Liquid Oxygen / Methane Combustion at Very Low Mixture Ratio at the Mascotte Test Facility. In *32nd ISTS & 9th NSAT Joint Symposium*, pages 1–7. 23, 127, 149

[Von Sethe et al., 2019] Von Sethe, C. B., Soller, S., and Haidn, O. J. (2019). Experimental investigation of a single element LOX / GCH4 heat-sink combustion chamber. In *EUCASS 2019*, number July. 23, 151, 152

[Wartha et al., 2020] Wartha, E. M., Bösenhofer, M., and Harasek, M. (2020). Characteristic Chemical Time Scales for Reactive Flow Modeling. *Combustion Science and Technology*, 00(00):1–26. 36

[Wasserman, 2018] Wasserman, M. (2018). An efficient implicit scheme for the simulation of supersonic combustion. In *58th Israel Annual Conference on Aerospace Sciences, IACAS 2018*, pages 1735–1764. 74

[Whealan George, 2019] Whealan George, K. (2019). The Economic Impacts of the Commercial Space Industry. *Space Policy*, 47:181–186. 15

[Wilhelm et al., 2021] Wilhelm, S., Jacob, J., and Sagaut, P. (2021). A New Explicit Algebraic Wall Model for LES of Turbulent Flows Under Adverse Pressure Gradient. *Flow, Turbulence and Combustion*, 106(1). 96

[Woodward et al., 2006] Woodward, R. D., Pal, S., Farhangi, S., and Santoro, R. J. (2006). LOX/GH2 shear coaxial injector atomization studies at large momentum flux ratios. In *AIAA/ASME/SAE/ASEE 42nd Joint Propulsion Conference*, volume 11, pages 8431–8450. 156

[Yamashita et al., 1996] Yamashita, H., Shimada, M., and Takeno, T. (1996). A numerical study on flame stability at the transition point of jet diffusion flames. *Symposium (International) on Combustion*, 26(1):27–34. 135, 170

[Yang et al., 2017] Yang, S., Ranjan, R., Yang, V., Menon, S., and Sun, W. (2017). Parallel on-the-fly adaptive kinetics in direct numerical simulation of turbulent premixed flame. *Proceedings of the Combustion Institute*, 36(2):2025–2032. 74

[Yang et al., 2004] Yang, V., Habiballah, M., Hulka, J., and Popp, M. (2004). *Liquid Rocket Thrust Chambers: aspects of modeling, analysis, and design.* AIAA. 20, 25

[Zhang, 2019] Zhang, C. (2019). *Amélioration de Loi de Paroi de Simulation aux Grands Échelles pour des Applications Aéroacoustiques.* PhD thesis, Université de Sherbrooke. 96

[Zhukov, 2019] Zhukov, V. P. (2019). The impact of methane oxidation kinetics on a rocket nozzle flow. *Acta Astronautica*, 161(January):524–530. 59

[Zips et al., 2019] Zips, J., Traxinger, C., Breda, P., and Pfitzner, M. (2019). Assessment of presumed/transported probability density function methods for rocket combustion simulations. *Journal of Propulsion and Power*, 35(4):747–764. 58